Non-Classical Crystallization Pathways in Eutectic-Forming Systems

by

Saman Moniri

A dissertation submitted in partial fulfillment
of the requirements for the degree of
Doctor of Philosophy
(Chemical Engineering)
in The University of Michigan
2020

Doctoral Committee:

Assistant Professor Ashwin J. Shahani, Chair
Professor Nicholas A. Kotov
Professor Emmanuelle Marquis
Professor Robert M. Ziff

Saman Moniri

moniri@umich.edu

ORCID iD: 0000-0003-0723-5091

To my family and friends

Acknowledgements

A large number of mentors, peers, and staff played a pivotal role and offered invaluable support throughout my graduate degree. First among them is my advisor Professor Ashwin Shahani. I joined Ashwin's research group in November 2016 as his first student, shortly after he started his independent career as an assistant professor and a few months after I had obtained my master's degree in my home department (chemical engineering). As I have progressed through my doctoral research, my experiences working under his mentorship have been overwhelmingly positive, and I am very grateful for the helpful feedback that he has given me all along the way. There are many descriptive examples that I could choose from of how these interactions have been instrumental in helping me to develop new skills in both experimental and computational realms, as well as to maintain a strong curiosity for science. Throughout the years, Ashwin provided direct guidance while also giving me the independence to explore different avenues. Given that much of the methods we pursued are novel, our weekly individual meetings consisted of not only updates but also a critical examination of our experimental results. He set a great example for a faculty member to excel in both research and teaching. I am very lucky to have Professor Shahani as my mentor and advisor, and I will forever be grateful to him

for helping me grow my career.

I also want to thank my committee members Professors Nicholas Kotov, Emmanuelle Marquis, and Robert Ziff for providing feedback and guidance on my dissertation. Their flexibility in the past couple of months is much appreciated, especially during the disrupted times of the COVID-19 era and for attending my defense talk virtually. I would also like to thank Professor Lola Eniola-Adefeso for providing feedback on my research work early on, and together with Professors Mark Burns, Nicholas Kotov, and Robert Ziff for writing recommendation letters in support of my postdoctoral applications.

I would also like to thank every member of the Shahani lab for their friendship and help, and making the years in the lab immensely enjoyable. Having been a part of the group will always serve as a source of pride. Beginning with the other three early members of the lab, Dr. Nancy Senabulya Muyanja (currently an Instrument Scientist at $(MC)^2$), Insung Han (next to graduate), and Mushfequr Rahman (a master's alum and currently a Data Analyst at a software company in Ann Arbor), to the present members Dr. Ning Lu and Dr. Hadi Parsamehr (postdocs); Jiwoong Kang, Geordie Lindemann, Paul Chao, Matthew Higgins, Caleb Reese (PhD students); and Yeqing Wang (visiting PhD student) – thank you all. It has been very rewarding to work with you, and words cannot express my gratitude. I have also enjoyed our spontaneous conversations about science, politics, and random topics. Extended thanks to the eutectic subgroup - Geordie, Paul, and Yeqing - for work on some exciting projects that have been quite insightful. And thanks to all who lent a helping hand during the synchrotron experiments. I also want to thank the former

master's students Megan Wiltse and Zhucong Xi for their contributions.

I have had the pleasure of working with a number of talented undergraduate students, beginning with Ron Keinan who stayed an extra year in the group through the SUGS program and is currently at Raytheon in Arizona, Che Chan, Matthew Rodeman, and Tianxiang Lu. Working with them helped me improve as a mentor and reminds to pay it forward for those who helped me gain a love of science. Their contributions helped me juggle several projects at a time, and that allowed me to accomplish more than I could have otherwise. I am happy that these students felt comfortable to ask questions without hesitations and seek guidance not only about the research projects they were working on, but also other professional development matters. I hope they also gained some skills and scientific knowledge along the way.

I am very grateful to the research scientists at Argonne, Brookhaven, and Oak Ridge National Laboratories for their assistance during research visits. In particular, I would like to thank Francesco De Carlo and Pavel Shevchenko at the Argonne X-ray Science Division (Advanced Photon Source); Mingyuan Ge, Wah-Keat Lee, and Xianghui Xiao at Brookhaven Photon Sciences (National Synchrotron Light Source II); Lawrence Allard, David Cullen, Karen More, and Raymond Unocic at Oak Ridge Electron and Atom Probe Microscopy group (Center for Nanophase Materials Sciences). Thanks to collaborators Hrishikesh Bale and Tobias Volkenandt in Carl Zeiss Microscopy for helping me overcome some of the equipment-related challenges in the spirals project.

I am also indebted to the wonderful staff that make the University of Michigan the great place that it is. Among them are the Chemical Engineering Graduate

Coordinator Susan Hamlin; the Coordinator of Graduate Programs in the College of Engineering Andria Rose; the Assistant Director of Graduate Programs in the College of Engineering Tiffany Porties; the Director of Undergraduate Studies, Chief Undergraduate Program Advisor, and wonderful mentor Dr. Susan Montgomery; the Materials Science and Engineering Graduate Coordinator Renée Hilgendorf; Michael Africa, Connie Bacus, Pamela Bogdanski, Jennifer Downey, Shelley Fellers, Heather Guenther, Catrina Hamilton, Dana Jackson, Keith McIntyre, Barbara Perry, Todd Richardson, Kelly Raickovich, Mary Beth Westin. As manager of lab supplies and primary contact on a number of new equipment purchases, I would like to thank Chris Cristian, Ellen Hou, Debbie Johnson, and Kevin Worth for all of their help (and patience!) with ordering equipment and supplies. The staff at $(MC)^2$, Drs. Allen Hunter, Bobby Kerns, Haiping Sun, Kai Sun, Nancy Senabulya Muyanja, and Ms. Deanna Wendel, all keep $(MC)^2$ as vibrant as it is in serving the broader campus community as well as non-Michigan and non-academic users. Much of the success of these research activities lies on the users' interactions with the center's staff members, so thank you for all your mentoring and assistance.

A huge thanks to all of my friends outside the lab who have been there for me throughout graduate school and supporting me in all times. You know who you are. I especially want to thank Abdulla A., Lydia A., Ramin A., Simon A., Adarsh B., Bruna B., Calvin B., Zach B., David C., Kathleen C., Sarah C., Steven C., Ben D., Martin D., Megan D., Bobby G., Mario G., Alex H., Nahal H., Hannah K., Patrick K., Prashant K., Genesis L., Jeff L., Sam L., Connor M., Doug M., Soroush M., Tejas N., Max P., Hanieh S., Jake S., Jon S., Phil S., Harry V., and Zixuan W.

Also thanks to the more than 45 people who joined my virtual defense, and all their positive thoughts and support.

I gratefully acknowledge financial support from the Air Force Office of Scientific Research Young Investigator Program (award no. FA9550-18-1-0044), the National Science Foundation CAREER program (award no. 1847855), and the the U-M College of Engineering. I also thank additional support from the U-M Rackham Graduate Student Research Grant program. I am thankful for receiving the Rackham Conference Travel Grant and the Gordon Conference Fellowship for me to present parts of this work at external conferences. I also thank the Chemical Engineering Department for recognizing me with the Excellence in Teaching Award (2017) and the Excellence in Research Award (2019), as well as the College of Engineering for the Richard F. and Eleanor A. Towner Prize for Distinguished Academic Achievement (2020).

Lastly, I would like to thank my mom, Mansoureh, and dad, Mojtaba. They have been my role models in life and in science, and they have have made countless sacrifices and always encouraged me to follow my passion. Throughout my whole life they have supported me unconditionally, uplifted me at difficult times, and kept me grounded. Where I am today is, in greatest part, a reflection of their resilience.

Table of Contents

List of Figures

Figure

List of Tables

Table

Abstract

Crystallization is the central process of synthesizing materials across length scales, with ubiquitous examples in synthetic, biogenic, and geologic environments. During crystallization a continuum of patterns could emerge due to the interplay of growth kinetics, material or solution chemistry, and crystallographic defects. In particular, solidification of eutectic alloys, characterized by the proximity of their compositions to a nonvariant point in the phase diagram, produces multi-phased micro- and nanostructures with diverse morphologies. This spontaneous pattern formation lies among the broader self-organization strategies that can be easily scaled to large areas, potentially enabling higher throughput and lower cost than serial processes.

This dissertation sheds new light on non-classical pathways for eutectic crystallization, perplexing characteristics that cannot be satisfactorily explained nor predicted by classical nucleation and growth models. The scope of this work entails a platform combining advanced experimental techniques – precise synthesis along with multiscale, three-dimensional, and time-resolved measurements – and computational methods – computer vision and machine learning – for tracking eutectic formation at temperature and their structural evolution under external stimuli. The first thrust of this dissertation focuses on crystallization in the presence of chemical modifiers,

and the second thrust on the emergence of two-phase metastable spirals and their response in extreme environments.

Thrust one demonstrates cases in which the interaction of the modifier with the growing crystal is either synergistic, illustrated in a case study of Al-Si and Al-Ge eutectics, or antagonistic, shown in the growth of primary Si crystals. Thrust two focuses on spiral growth in the Zn-Mg system, and their behavior at elevated temperatures. These spirals are thermodynamically metastable, so their successful synthesis requires steering the system down certain kinetic pathways on intermediate time-scales. Collectively, our multi-modal characterization studies provide the necessary benchmark data for simulations of complex self-organization patterns, thus expanding the horizon for the design of next-generation alloys with superior properties.

Part I

Motivation and Background

Chapter 1

Motivation

1.1 Crystallization-Mediated Synthesis of Materials Across Scales

Materials design and crystal growth lie at the heart of all branches of natural sciences, and indeed the development of a sustainable economy. Scalable design and development of materials with enhanced or novel physiochemical properties have and continue to build upon the progress of a wide range of technological applications, from structural metallic-based materials paving the path of human civilization in the fields of energy conversion, construction, communication, health, and transportation, to functional materials for emerging applications in health, energy, and transportation.

Methods for creating materials across length scales include physical techniques (*e.g.,* spray-based [1] and spin-coating [2]), and chemical techniques (*e.g.,* heat treat-

ment [3] and electrochemical [4]). Crystallization (solidification) is among the most studied phenomena for both fundamental and technological reasons. The advantage of crystallization and other solution-based strategies for growth of materials lies in their scalability in manufacturing in a wide range of areas – including pharmaceutical and protein crystallization [5, 6], semiconductor and polymer processing [7, 8], single crystal production [9], and process metallurgy [10] including additive manufacturing [11, 12, 13].

Crystallization refers to the nucleation of a precursor phase in solution, and the subsequent growth of the nuclei into an eventual ordered structure (detailed treatment of crystallization is provided in Section 2.1). These structures could be hierarchical in nature and composed of multiple phases (termed composites), which is the focus of this dissertation and elaborated in the subsequent Chapters. This Section aims to illustrate the centrality of crystallization in a diverse range of natural sciences as evident from multiples lines of research. For example, the concept of nucleation has been invoked to explain phenomena such as the formation of bacterial appendages, initiation of divers' decompression sickness and neuro-degenerative diseases [14], earthquakes, volcano eruptions, and the formation clouds as well as black holes [15]. The importance of nucleation is rooted in its description of the transition from a stochastic regime dominated by thermal fluctuations to a deterministic regime where growth occurs through an interplay of thermodynamic and kinetic control (as expounded later).

In crystal growth, this description aims to disentangle the diverse set of pathways by which crystals nucleate and grow from a parent solution in both synthetic and

natural (*e.g.,* biogenic and geologic) systems. Crystal growth is a pervasive phenomenon not just in technological settings, but also in the environment - both in the geochemical reservoirs in soil and in the atmosphere - and in biology - both in the 'soft' side and in organisms that produce mineralized tissues such as bones and teeth in humans. At the intersection of biogenic and geologic systems, crystallization plays a central role in the global carbon cycle: Coccolithophores, phytoplankton whose blooms are visible as turquoise-colored patches in satellite images such as the one in Fig. 1.1 (a), use carbon dioxide to grow and release carbon dioxide when they create their array of calcium carbonate (calcite) shells shown in Fig. 1.1 (b). Carbonates in general are most important for what they represent, namely interactions between biology and Earth over the past 220 million years [16, 17]. Calcite in particular constitutes the largest carbon source on the planet [16]. When carbon resides within calcite, it is absent in the atmosphere as carbon dioxide that would otherwise warm the world, as shown schematically in Fig. 1.1 (c). Understanding how calcium carbonate turns into various minerals could help scientists control its formation to keep carbon dioxide from getting into the atmosphere. In 2019, the nanoscale-level three-dimensional (3D) structure of calcite shells on coccolithophores was revealed by synchrotron X-ray techniques (X-ray nano-tomography, described and utilized later in this dissertation) [18]. The technique is well-suited to image coccospheres of 1–7 μm size and to determine the mass of individual coccoliths. Thanks to its high resolution, this technique can access not only the thickness of coccoliths but all morphological features of these calcareous plates even within a single coccosphere [18].

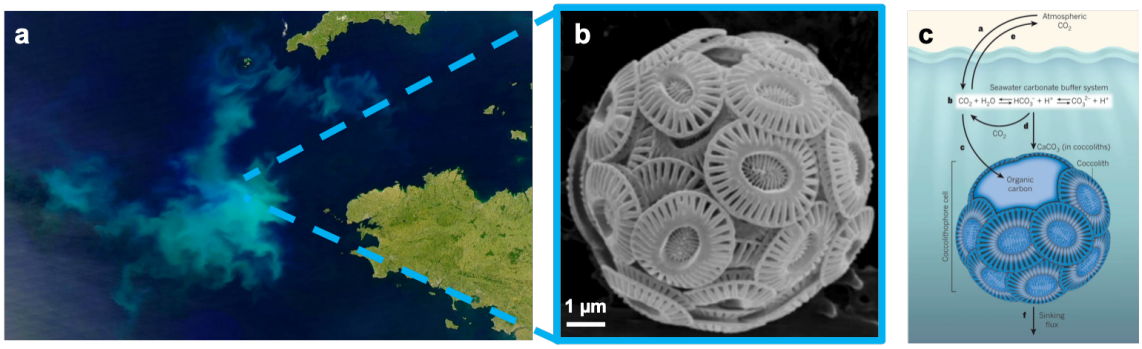

Figure 1.1: Crystallization and the global carbon cycle. (a) Bloom of coccolithophores visible from space. (b) Scanning electron micrograph of a coccolithophore showing the calcite crystals (coccolith plates) lying in specific locations. Figure adapted from ref. [17]. (c) Coccolithophore carbon chemistry. Figure adapted from ref. [16].

Crystal growth is also a central phenomenon in synthetic environments. Figure 1.2 shows recent (2015-2019) examples from literature of both inorganic (Fig. 1.2(a-c)) and organic (Fig. 1.2(d)) crystals ranging in size from nano-, to meso-, and to macro-scales. Fig. 1.2(a) displays highly anisotropic, shape-engineered gold (Au) nanorods for distinct optical responses one nanocrystal at a time. The authors used triangular templates to direct the assembly of Au nanorods along the edges of an equilateral triangle, and these assemblies exhibit rotation- and polarization-dependent hybridized optical response, which can be further modulated with geometrical symmetry breaking through variations in nanorod size, position, and orientation.

Figure 1.2(b) shows highly-branched nanowires that defy expectations based on crystal symmetry in titanium dioxide (TiO_2), a semiconducting oxide. The inset displays that each branch of the nanowire occurs on a set of twin boundaries, an important class of grain boundaries along which two crystals share the same lattice sites and intergrow through certain symmetry operations. Figure 1.2(c) shows the synthe-

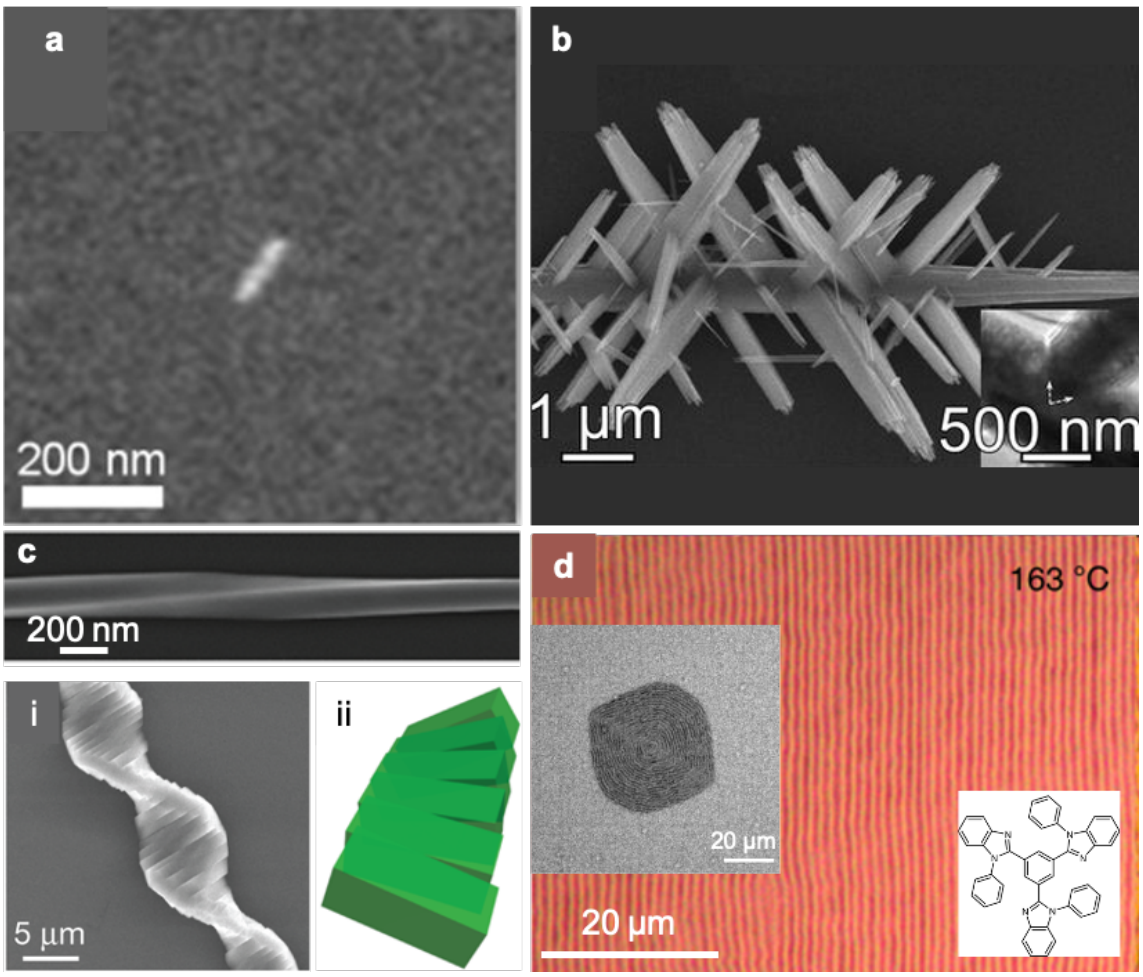

Figure 1.2: Crystal growth and assembly across. (a) An individual gold nanorod. The structure demonstrates synthetic ability to create anisotropic, shape-engineered nanocrystals. (b) Branched nanowire of rutile (TiO_2). Branching occurs on twin boundaries (inset). (c) Helical van der Waals crystals with discretized twist in GeS. Inset (i) shows the twisting morphology across scale, and (ii) a schematic illustration of twisting between successive layers. (d) Periodic pattern formation in TPBi films. Molecular structure and the *in situ* optical microscopy of the crystallization of a single crystalline grain are shown in the insets. Figures adapted from from refs. [19, 20, 21, 22].

sis of van der Waals structures with various twisting morphologies and topologies. The ability to manipulate the twisting topology of van der Waals structures offers a new degree of freedom for tailoring their electrical and optical properties. Using germanium sulfied (GeS), a layered IV–VI monochalcogenide, the authors demonstrate that the twisting topology can be tailored by controlling the radial size of the structure, and that these twisted crystals can be grown from nanoscale to mesoscale and macroscale. These particular GeS van der Waals crystals exhibit discretized mesoscopic twisting between the successive layers, as displayed schematically in sub-panel (ii).

Pattern formation phenomena such as those described above are not limited to only metallic and semi-metallic structures; numerous organic analogues have also been reported. Figure 1.2(d) shows periodic pattern formation in 2,2′,2″-(1,3,5-benzinetriyl)-tris(1- phenyl-1-H-benzimidazole) (TPBi, chemical structure shown in inset), a small-molecule organic semiconductor commonly used in organic light-emitting devices (OLEDs). The authors reported a crystallization-mediated mechanism in which aligned, periodic surface structures form along the amorphous-to-crystal transformation front during annealing of single-layer thin films of TPBi. The periodicity of these micrometer-scale structures can be tuned from 800 nm to 2,400 nm by varying the film thickness and annealing temperature, and the structures exhibit promising thermal stability as they occur with a transition to a crystalline phase. Additionally, this pattern formation occurs directly in the active semiconductor and thus avoids the need for further processing steps, making this self-organizing approach promising for the large-area fabrication of photonic devices and scattering

layers in optoelectronics.

1.1.1 Crystallization of Multi-Phase Materials and Composites

Modern materials research is shifting focus toward the design of multiphase, multicomponent materials with enhanced physiochemical properties and/or multifunctionality. This shift is motivated, in part, by the desire to create materials for emerging technological applications such as those in medicine and health, energy, and transportation. As such, the conventional trial-and-error synthesis approaches become very inefficient. Rational design of materials for these and other targeted applications requires a clear understanding of their formation mechanism, which then paves the way for creating a plethora of desired morphologies and properties for specific behavior and functions.

This dissertation focuses on crystallization pathway of eutectic composites from multi-component environments. Eutectic crystallization naturally leads to phase-separated solid patterns (thus a composite); a further treatment of eutectics, including the classical theories of growth, are presented in Section 2.3. For the introductory purpose of this Section, it suffices to state that eutectic composites are promising materials for both structural and functional applications. For instance, Fig. 1.3(a) shows directionally-solidified intermetallic Cr-Cr_3Si eutectic which shows improved fracture toughness for high-temperature structural applications. The results of long-term (1728 hours) annealing (bottom panel in the figure) shows the "ductile-phase-toughened" *in situ* intermetallic composites possess a high thermal

stability as they retain their microstructures without spheroidization, making these structures suitable candidates for applications that require creep resistance at elevated temperatures.

Figure 1.3(b) shows localized enhanced optical transmittance and absorption-induced transparency (AIT) in the near-infrared and terahertz (THz) ranges using templates from directionally-solidified metal-dielectric eutectics. This report was the first experimental demonstration of AIT at THz frequencies. The eutectics were prepared with starting compositions NaCl-LiF, followed by a series of etching and metal-coating steps as demonstrated schematically in the figure. The resulting structures are arrays of holey metallic films perforated with dielectric or polaritonic micropillars filling or towering over the holes, such as those displayed in the micrograph in the figure. In broader terms, this and other [23, 24, 25] studies suggest that directional solidification of eutectics belongs to the inexpensive, scalable class of self-assembling procedures to fabricate photonic structures and metamaterials. This serves as motivation for Part III of this dissertation (Chapters 7 and 8), where we uncover the growth and thermal stability of two-phase spiral eutectics with the results establishing a potential pathway toward bottom-up synthesis of chiral materials with an inter-phase spacing comparable to the wavelength of infrared light.

Eutectic semiconductor composites have shown promise also for use in hydrogen production *via* photoelectrochemical cells (PECs). While many PEC electrode designs suffer from either poor stability or low energy conversion efficiency (thus hindering commercialization), a eutectic system consisting of titanium dioxide and strontium titanate (TiO_2-$SrTiO_3$) [28] as the active photoanode material for wa-

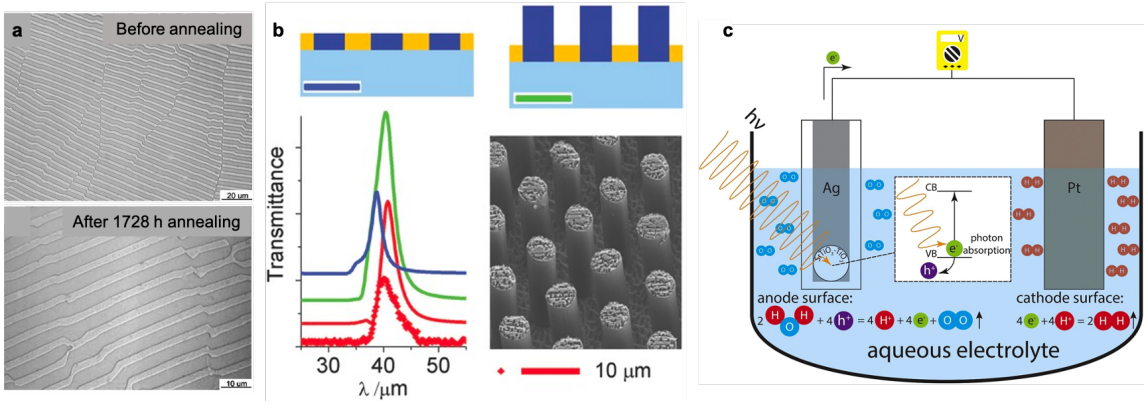

Figure 1.3: Multiphase eutectic composites for structural and functional applications. (a) Directionalldy-solidified intermetallic eutectic composites for high-temperature structural applications. Optical micrographs show that the Cr-Cr_3Si eutectic has a high fracture toughness during long-term (1728 hours) annealing at 1200 °C. (b) Micropillar Templates for Dielectric Filled Metal Arrays and Flexible Metamaterials. Directionally-solidified KCl-LiF eutectics were used as templates for creating holey metallic films perforated with dielectric or polaritonic micropillars that show localized enhanced optical transmittance and absorption induced transparency in the near-infrared or THz ranges. (c) TiO_2-$SrTiO_3$ eutectic composite-based PEC cell. The schematic displays the principle of water splitting using this eutectic system as the active photoanode in a PEC cell. Figures adapted from refs. [26, 27, 28].

ter splitting, shown schematically in Fig. 1.3(c), performs competitively to other state-of-the-art systems comprising TiO_2 and $SrTiO_3$. Among the advantages of this eutectic multiphase composite are the low transport and recombination losses due to its sharp interfacial contacts and high crystallinity. These structures also show strong resistance to photocorrosion in aqueous electrolytes, as demonstrated by 30 hours of stability testing under 600 $\frac{mW}{cm^2}$ of solar irradiation to boost potential photocorrosion.

These few examples point to the abundance of potential of eutectic-based composite materials for a variety of technological purposes. Accordingly, a detailed understanding of the crystallization pathway used to synthesize these (perhaps hierarchical) structures is key to realizing desired functionalities.

1.2 Rational Design Guided by Illuminating the Mechanism of Crystallization

In crystallization-mediated synthesis of materials, a grand challenge revolves around the interplay of free-energy landscapes (thermodynamics) and reaction dynamics (kinetics), as expounded in greater detail in Section 2.1. Given the structural diversity of the building blocks involved, a predictive description must cross length- and time-scales to connect molecular details with macroscopic behavior. Directly influencing nanoscale assembly at solid-liquid interfaces are structures of solution and solids (size, shape, and composition), as well as interactions among solid particles, growth modifiers, or ions in confined regions of solution. The dynamic nature of the assembly process – the movement of particles in solution – causes a continuous change

of the local structure and corresponding forces, taking the particles from a regime of long- to short-range interactions and, eventually, leading to particle-attachment (growth) events along specific crystallographic directions.

A molecular-level understanding of both the free-energy landscape that dictates the thermodynamically preferred route of the assembly process, and the dynamic events such as particle diffusion and relaxation that influence whether such set of thermodynamic preferences or, instead, kinetically-controlled pathways, ensue could provide key insights into that question. Such an elementary step-level understanding of the interface-driven processes involved in crystallization and other phase transformation-based methods of creating materials could be utilized to form hierarchical structures with enhanced or novel physiochemical properties for the motivations that abound, from eutectics to semiconductors to biomimetic composites.

1.3 Dissertation Outline

This dissertation is organized into four main Parts. The remainder of the present Part (Chapters 2, 3) serves to introduce the theoretical framework behind crystallization science and eutectics, namely classical nucleation theory as well as the coupled growth theories of eutectics. The development of these frameworks dates back to the mid-1900s; the intention of this introduction is a survey of the key underlying concepts. This Part also provides an overview of the morphological diversity of eutectics and concludes by highlighting the innovations in experimental methodology used for the experiments in this dissertation. Detailed experimental procedures are provided at

the end of corresponding Chapters in Parts II and III.

Part II is divided into three Chapters (4-6), which explore the origins of morphological and topological evolution of anisotropic Al-Ge and Al-Si eutectics as well as primary Si crystals in the presence of small concentration of chemical modifiers. Parts of these results are reported in references [29, 30]. The remainder will be reported in forthcoming publications.

Part III is divided into two Chapters (7 and 8), which unearth the growth and thermal response of two-phase spiral eutectics in the Zn-Mg. Part of these results is reported in references [25], with the remainder in a forthcoming publication.

Part IV, composed of two Chapters (9 and 10), concludes this dissertation and provides an outlook into potential future directions. A complete list of bibliography is provided in Part V.

Chapter 2

Background

The majority of technological materials are crystalline, from pharmaceuticals to semiconductors. Living systems exploit crystallization to produce biominerals such as bones and teeth. The interplay between living systems and the environment often takes place through crystal formation and dissolution. At this interface, oxygen in the atmosphere is produced through iron reduction and oxidation reactions by microbes. The vast volume of carbonates in modern-day oceans are a product of the relationship between biota and minerals dating back to one billion years ago. These phenomena impact global seawater chemistry and the flux of CO_2 into and out of the atmosphere.

This Chapter provides an overview of the theoretical framework behind crystallization science, beginning with the thermodynamic principles proposed by J.W. Gibbs in the 1870s [31] which have come to be known as "classical nucleation theory" (CNT, Section 2.1). This view of nucleation has persisted for more than a century,

but a number of discoveries since the end of the 20^{th} century have revealed a richer, more complex set of hierarchical nucleation pathways than classical predictions, for instance those that involve transient crystalline or amorphous phases [20].

Despite this complexity which might initially seem chaotic, the pathways that lead to nucleation can be described within a common context by a holistic framework that is rooted in classical concepts, but which takes into account the coupled effects of perturbations in free-energy landscapes (thermodynamics) and the impact of dynamical (kinetic) factors. This holistic framework lays a solid conceptual foundation underneath all of the variety of crystallization processes that have been observed to take place in different systems, and thus moves us closer toward a predictive model of nucleation.

This Chapter also provides an overview of the relevant theories for the second step of crystallization, *i.e.,* growth. Given the focus of this dissertation on eutectic composites, this discussion focuses on the coupled-growth theories of eutectics (Section 2.3) and is divided into two main parts, beginning with the classical work of Jackson and Hunt for 'regular' eutectics developed in the 1960s, followed by the analysis of Kurz and Fisher for 'irregular' eutectics in the 1980s. This Chapter concludes by illustrating the various eutectic interface morphologies reported in the literature (Section 2.4).

Before proceeding to the theoretical framework, it must be noted that the habit of a crystal is given by its internal structure and the external growth conditions. During the crystallization process, small differences in concentration and temperature are generated and, under the influence of gravity, these result in buoyancy-driven

convection which in turn affects the mass and heat transfer. In diffusion-controlled crystal growth and when supersaturation is high, the isoconcentration or isosupersaturation curves are not uniformly distributed around the growing crystal ("Berg effect"). Interferometric measurements reveal that supersaturation is highest at corners and edges of the growing crystal [32]. Therefore, nucleation of new layers occurs at the edges and corners of the crystal, and hopper growth becomes dominant. Hopper growth is characterized by the spreading of layers at the crystal surface and laterally-moving steps. The results and growth modes presented in this dissertation, including spiral formation, are not a manifestation of the Berg effect, given the relatively low supersaturation levels considered. While a further analysis of the Berg effect is beyond the present scope, examples of hopper growth due to the Berg effect can be found in, *e.g.,* refs. [33, 34].

2.1 Classical Nucleation Theory

Crystallization starts with nucleation, a phenomenon that J.W. Gibbs explained for the first time in terms of thermodynamic principles in the 1870s [31]. Although Gibbs was considering the formation of raindrops through the condensation of water from humid air into droplets, the principles of what has come to be known as "classical nucleation theory" (CNT) is applied to crystal formation through both experimental and computational methods, *e.g.,* refs. [35] and [36], respectively. Gibbs' key insight was that nucleation is not a spontaneous process even when the chemical potential change in producing the new phase is negative. Instead, there is a free-energy

barrier ΔG that must be overcome before a nascent crystal nucleus can grow into a macroscopic size. This barrier exists because the appearance of the solid phase (nucleus) also creates a phase boundary with a surface tension, and although the chemical potential drop associated with the transfer of ions, atoms, or molecules from the solution to the solid nucleus contributes to a negative change in free energy, the creation of the phase boundary contributes to a positive change.

In this perspective, homogeneous nucleation has a high thermodynamic energy barrier ΔG_{hom} that originates from the high surface-to-volume ratio of the nucleus, and has a contribution of a surface energy (capillary) term and a volume term: Given the surface energy per area γ_s and the bulk energy per volume ΔG_v of a spherical nucleus with radius r, the resulting homogeneous barrier can be approximated as

$$\Delta G_{hom} = 4\pi r^2 \gamma_s - \frac{4}{3}\pi r^3 \Delta G_v \tag{2.1}$$

As Eq. 2.1 indicates, the positive change in ΔG_{hom} stemming from the creation of the phase boundary scales with surface area, which dominates at small size due to the r^2 factor. Conversely, the negative change in ΔG_{hom} scales with volume, which dominates at large size due to the r^3 factor. These two competing effects imply that nucleation is only possible because of the inherent thermal fluctuations in density that raise the free energy *locally*, as it is impossible to move a system uphill in free energy *globally*.

From the condition $\frac{d[\Delta G_{hom}(r)]}{dr} = 0$, the critical radius, $r^* = \frac{-2\gamma_s}{\Delta G_v}$ is derived. Only the nuclei with $r \geq r^*$ can spontaneously grow into larger particles ($\frac{d[\Delta G_{hom}(r)]}{dr} < 0$) whereas those with $r < r^*$ will dissolve in the solution.

Figure 2.1 shows the possible nucleation pathways that can occur during crystallization; Fig. 2.1(a) shows the the framework of CNT, namely the presence of both an uphill free-energy barrier and a critical nucleus size. Figure 2.1(b) shows the simultaneous occurrence of multiple crystalline clusters in the unstable supercooled liquid. This scenario is often labeled as spinodal decomposition and, as the Figure shows, transformation to the crystal proceeds in a barrierless fashion. Spinodal decomposition does not pertain to this dissertation and its further analysis is beyond the present scope.

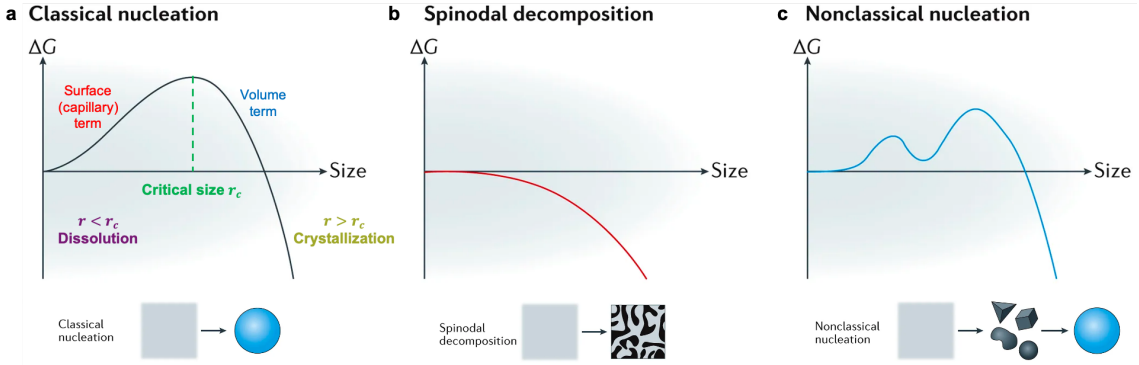

Figure 2.1: Energetics of nucleation pathways. Plots of the free-energy change as a function of nucleus size in (a) classical nucleation, (b) spinodal decomposition, and (c) non-classical nucleation models. Schematic illustrations of each pathway is also displayed. Figure adapted form ref. [37].

Within CNT, the rate of nucleation J depends exponentially on ΔG_{hom}, reflecting the collective behavior of the system in exploring its possible configurations, including those that are microscopically and transiently out of equilibrium. Moreover, J is also influenced by a second barrier E_a, which represents the activation energy for atomistic processes, such as desolvation or binding, that limit the rate of any chemical transformation independent of a free-energy barrier. Importantly, the

exponential dependence of J on ΔG implies that even subtle relative variations in free-energy *barriers* of nucleation for different phases such as in crystallization from multi-component environments, as is the focus of this dissertation, could manifest in large differences in nucleation *rates*.

CNT also comprises the theoretical framework for heterogeneous nucleation, that is, nucleation that occurs on account of the presence of a foreign phase, grain boundaries, dislocations, or impurities. Nucleation in liquids occurs heterogeneously more often than not, with a free energy barrier ΔG_{het} that is often significantly lower than that of homogeneous nucleation. Heterogeneous nucleation is customarily formulated within the CNT framework in terms of geometric arguments [38]. Specifically, $\Delta G_{het} = \Delta G_{hom} \cdot f(\theta)$, where $f(\theta) \leq 1$ is the shape factor, a quantity that accounts for the extent to which the crystalline nucleus wets the foreign surface. In other words, the contact angle θ determines whether and how much it could be easier for a critical nucleus to form in heterogeneously. Several factors could define the effectiveness of nucleants in promoting heterogeneous nucleation. Indeed, the selection of suitable nucleants, *e.g.,* for commercial applications, remains an empirical exercise [39].

For eutectic solidification, nucleation dynamics can play a key role on the establishment of the eutectic structure. The early theories of nucleation and growth of eutectic alloys assume, either implicitly or explicitly, that the equilibrium relationships between the phases hold from the onset of nucleation and thereafter [40]. These theories also assume that when the eutectic liquid is undercooled to slightly below the equilibrium eutectic temperature, a nucleation center promotes the growth of

one of the phases in the form of a plate. As this plate grows, the liquid adjacent to it becomes enriched in the second component and the second eutectic phase then nucleates sympathetically on one side of the plate of the first phase, leading to a process of edgewise growth and sidewise nucleation. These classical models of eutectic nucleation are reviewed in ref. [40]. The pioneering work on eutectic nucleation in Al–Si alloys by Crosley and Mondolfo [41], as well as several recent reports [42, 43], have demonstrated that nucleation dynamics can vary widely depending on the composition of the alloy, resulting in widely different spatial evolution of the eutectic phases.

2.2 Non-Classical Nucleation Pathways: A Brief Overview

For more than a century, the view of nucleation was shaped largely by the basic predictions of CNT – namely that the transition from liquid to solid occurs through a single step with a free-energy barrier to nucleation, fluctuations take the system over that barrier, and that the nucleation rate depends exponentially on that barrier. However, the field of nucleation is undergoing somewhat of a renaissance as numerous recent publications for last approximately 20 years have revealed more complex processes at work [44, 45, 46, 20, 37]. These studies report many systems that do not exhibit the simple process of sequential addition of monomeric species. Instead, they report pathways of nucleation that are hierarchical, either involving the addition of a more complex species, such as multi-ion complexes [47] and oligomers [48], or

passing through transient metastable states, including dense liquids [49], amorphous solids [50] and poorly crystalline polymorphs. In yet other systems, particularly those exhibiting complex stoichiometry (*e.g.,* calcium phosphates) or lattice structure (*e.g.,* zeolites), nucleation is accompanied by chemical transformations that lead to compositional evolution as the nucleus grows.

In non-classical pathways the energetics are somewhere in between the two extremes of high energy barrier in CNT and no barrier in spinodal decomposition [51, 52]. In non-classical nucleation, unlike what is assumed in CNT, γ and ΔG_v are not constant with respect to nucleus size. Rather, there are intermediate structures with lower surface and/or bulk energy, which provide alternative pathways to circumvent the high energy barrier of homogeneous nucleation, as shown schematically in Fig. 2.1(c).

The details of these processes are beyond the scope of this dissertation and can be found in many excellent papers such as refs. [20, 46, 38, 37], among others. In particular, the review article by J.J. De Yoreo *et. al.* [20] demonstrates the mounting evidence for these non-classical pathways from both observational and computational techniques. The more recent article by J.F. Lutsko [46] reports results from the combination of recent advances in classical density functional theory with stochastic process theory and rare event techniques to formulate a theoretical description of nucleation, including crystallization, that can predict non-classical nucleation pathways based on no input other than the interaction potential of the particles making up the system.

2.3 Coupled Growth Theories for Eutectic Composites

Thus far this Chapter has summarized the key conceptual framework underlying our understanding of how materials begin to form, *i.e.,* nucleation, which is mostly a thermodynamic consideration. This Section aims to highlight the kinetics of growth as they relate to eutectic composites. An important element of studying composite systems is describing interfaces, in this case solid-solid eutectic interfaces and the solid-liquid crystallization interface. As outlined in Section 1.1, eutectics often exhibit outstanding electromechanical properties because their microstructures act as natural or *in situ* composite material. A fundamental understanding of the growth process allows tuning the eutectic structures to these and other technological demands.

Away from equilibrium solids may crystallize into highly ordered eutectic patterns. This pattern formation has been observed in organic [53, 54], metallic [55], and semi-metallic [56]. The resulting eutectic morphologies are typically classified into either 'regular' or 'irregular,' depending on whether the arrangement of lamellae is periodic or not, respectively. Eutectic systems comprised of non-faceted components, such as fully-metallic alloys, exhibit regularity; those systems that contain at least one faceted phase, such as Si and other semiconductors, are irregular or degenerate. The irregular (non-periodic) arrangement of lamellae in the latter category results from the directional covalent bonding of the faceted phase and its defect-mediated growth mechanism [57, 58] that limits its growth to certain well-defined

directions [59, 29]. Growth models of regular and irregular eutectics are provided below. An overview of the morphological diversity of eutectic systems, both regular and irregular, is presented in Section 2.4.

2.3.1 Jackson-Hunt Model for Regular Eutectics

In 1966 Jackson and Hunt provided the first model of regular eutectic growth [55]. In this analysis of a binary system, they approximated the interface shape as planar and assumed (i) equal undercooling of both solid phases growing in a coupled mode from a melt of eutectic composition, as shown schematically in Fig. 2.2, and (ii) isothermal solid-liquid front. The α phase rejects B solute, and the β phase rejects A solute. This process results in the increase of solute concentration in the liquid ahead of the solid α and β phases and hence to lateral diffusive transport of solute through the liquid. This is also why growth of eutectics is often referred to as "coupled growth."

By solving the diffusion problem due to composition gradients of A and B at the solid-liquid interface during eutectic growth, Jackson and Hunt found the following relationship between the total undercooling ΔT of the eutectic front which is the thermodynamic driving force required to drive the growth front at rate V with an interphase spacing λ,

$$\begin{aligned} \Delta T &= \Delta T_c + \Delta T_r \\ &= K_c V \lambda + \frac{K_r}{V} \end{aligned} \tag{2.2}$$

The first terms in Eq. 2.2 is the solutal undercooling relating to the solute

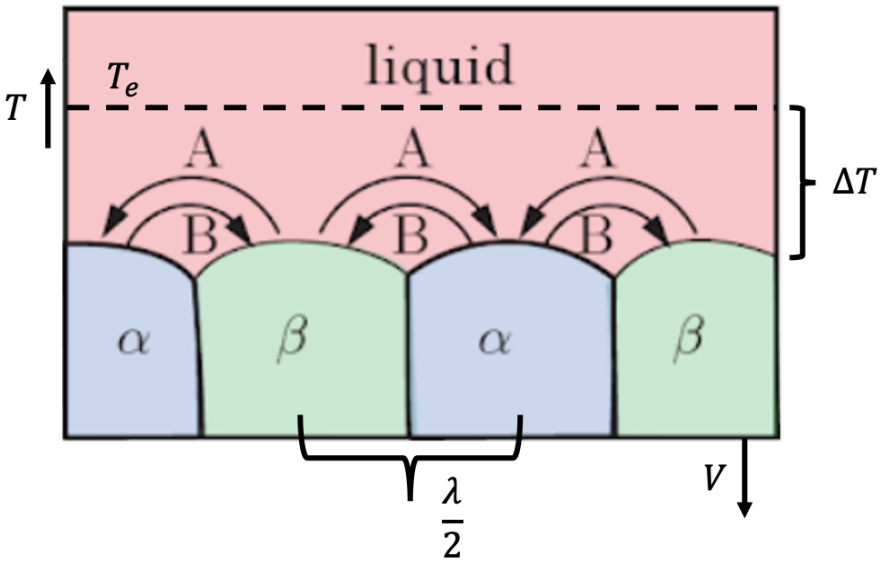

Figure 2.2: Coupled growth of a regular eutectic. A schematic diagram of the coupled-growth of α- and β- lamellae during the eutectic reaction. Figure adapted from ref. [60].

distribution field, *i.e.,* associated with the solute composition departure from the eutectic composition. The second term is the capillary undercooling associated with the curvature at the solid-liquid interface. Kinetic undercooling is negligible for metallic eutectics. In one dimension, curvature scales with $\frac{1}{\lambda}$. Assuming the so-called "extremum criterion," wherein the eutectic growth grows at minimum undercooling, the following relationships are derived:

$$\lambda_{ext}^2 V^* = \frac{K_r}{K_c}, \tag{2.3a}$$

$$\frac{\Delta T}{\sqrt{V^*}} = 2\sqrt{K_r K_c}, \tag{2.3b}$$

$$\lambda_{ext}\Delta T = 2K_r \tag{2.3c}$$

Equations 2.3a-2.3c can be used when the undercooling or growth velocity is set. These equations also provide key intuition into ways of tuning some properties of eutectic crystals by modifying only the growth conditions of a fixed alloy chemistry. For instance, under steady-state growth, Eq. 2.3a implies that fast rates of heat removal (high V^*) leads to small inter-phase spacing λ and *vice versa*. Indeed, the inter-phase spacing can be tuned over a wide range, from tens of nanometers to hundreds of microns, for the same material system by changing only the growth conditions (velocity and undercooling).

2.3.2 Kurz-Fisher Model for Irregular Eutectics

Irregular eutectics may have a mean interphase spacing that is much larger than the extremum value λ_{ext} derived above. This increase in interphase spacing can be rationalized by the branching of the faceted lamellae as the growth is localized to certain well-defined directions [53].

In 1980 Kurz and Fisher provided the first model of irregular eutectic growth [53]. From their consideration of an organic irregular system, they deduced that the growth front is non-isothermal, and that the faceted and non-faceted phases have unequal undercoolings. As shown schematically in Fig. 2.3, they observed that the faceted phase has a lower undercooling and therefore extends deeper into the melt.

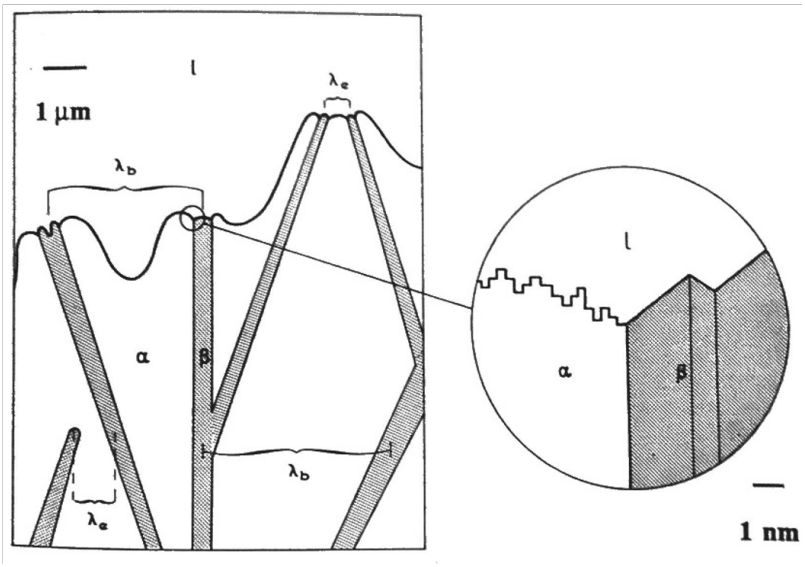

Figure 2.3: Coupled growth of an irregular eutectic. Growth of an irregular eutectic, where the diffuse α phase can grow easily while the faceted β phase is more sluggish. Figure adapted from ref. [53].

2.3.3 Competitive Growth Principle

A eutectic reaction is the direct transformation of the liquid into two or more solid phases, $L \rightarrow \alpha + \beta + ...$. Eutectic crystals have two or more chemical components for which a liquid and two or more solid phases coexist in equilibrium at the eutectic temperature and composition, T_E and C_E, respectively. However, metastable phases which are not predicted from equilibrium thermodynamics may still appear in alloys. This bifurcation in the crystallization pathway is commonly referred to as the competitive growth principle. According to this principle, crystallization at a given velocity produces the growth form with the lowest undercooling (*i.e.,* highest interfacial temperature), rationalizing the observation of metastable phenomena such as the formation of dendritic Al in Al-Si eutectics [61] and, as will be shown in Chap-

ter 7, metastable spiral eutectics in Zn-Mg alloys [25]. We note that solidification could also entail a competition in nucleation processes, *e.g.,* stable and metastable solidification pathways in cast iron [62].

The competitive growth of dendrites and eutectics gives rise to what has come to be known as the "coupled zone," which represents the range of growth conditions (*e.g.,*, alloy composition, growth rate) within which the structure is wholly eutectic. In regular eutectic systems the coupled zone is symmetric about the eutectic composition; in irregular eutectic systems the coupled zone is skewed towards the faceted phase. The skewness can be rationalized by the more sluggish kinetics of the faceted phase relative to the non-faceted one, and the resulting need for an undercooling that increases faster with velocity [60]. In directional solidification, wherein crystallization occurs at a constant velocity V in a decoupled unidirectional thermal gradient G, the coupled zone is sensitive to G: At high G, the solutal undercooling is suppressed, so dendrites are less likely to grow below the eutectic temperature. For this reason, the coupled zone broadens with increasing G.

2.4 Morphological Diversity and Technological Promise of Eutectic Composites

During solidification of a eutectic melt, the liquid phase-separates into two distinct solid phases α and β. The simultaneously solidifying phases organize into motifs consisting of alternating layers with diverse morphologies. Beyond the simpler lamellar and rod-like morphologies, more unique and complex structures such as spirals,

nodular, and split-ring resonators have also been observed.

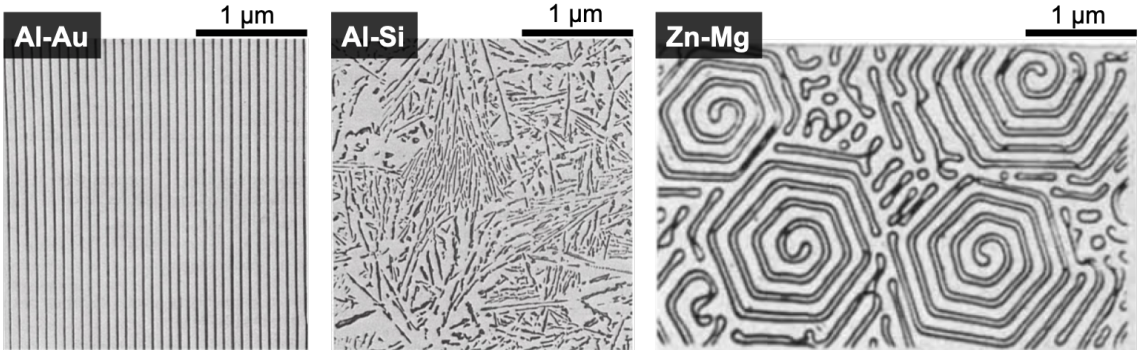

Figure 2.4: Diversity of eutectic interface morphologies. Regular Al-Au eutectic observed in a longitudinal section. Irregular Al-Si eutectic observed in a transverse section. Spiral Zn-$MgZn_2$ eutectic observed in a transverse section. Figures adapted from refs. [60, 63].

Figure 2.4 shows three representative eutectic morphologies. The fully-metallic Al-Au system is comprised of highly periodic, parallel lamellae. For this reason, metallic systems are fully isotropic. In contrast, the Al-Si system displays highly non-periodic arrangement of lamellae because the Si phase is faceted and hence has a highly anisotropic growth behavior. The Zn-Mg system shows spirals; the spiral eutectics are made of metallic Zn and intermetallic $MgZn_2$ [64, 65, 25]. The spiral morphology is explored exclusively in Part III (Chapters 7, 8) of this dissertation.

Broadly, the morphology of the eutectic interfaces is governed by the confluence of anisotropy (*i.e.,* faceting) and the volume fraction of the two phases. Materials for which $\frac{\Delta S_m}{R} > 2$, where ΔS_m is the entropy of fusion and R is the ideal gas constant, usually have a large anisotropy in solid-liquid interfacial energy and are therefore faceted (the ratio $\frac{\Delta S_m}{R}$ is commonly referred to as the Jackson α-factor). Conversely, materials with the Jackson α factor of less than 2 are non-faceted. The

various combinations of materials lead to different morphologies for the $\alpha-\beta$ eutectic. Figure 2.5 provides a schematic illustration of the eutectic interface morphologies for a binary eutectic $\alpha - \beta$ where at least one of the phases (here α) is non-faceted.

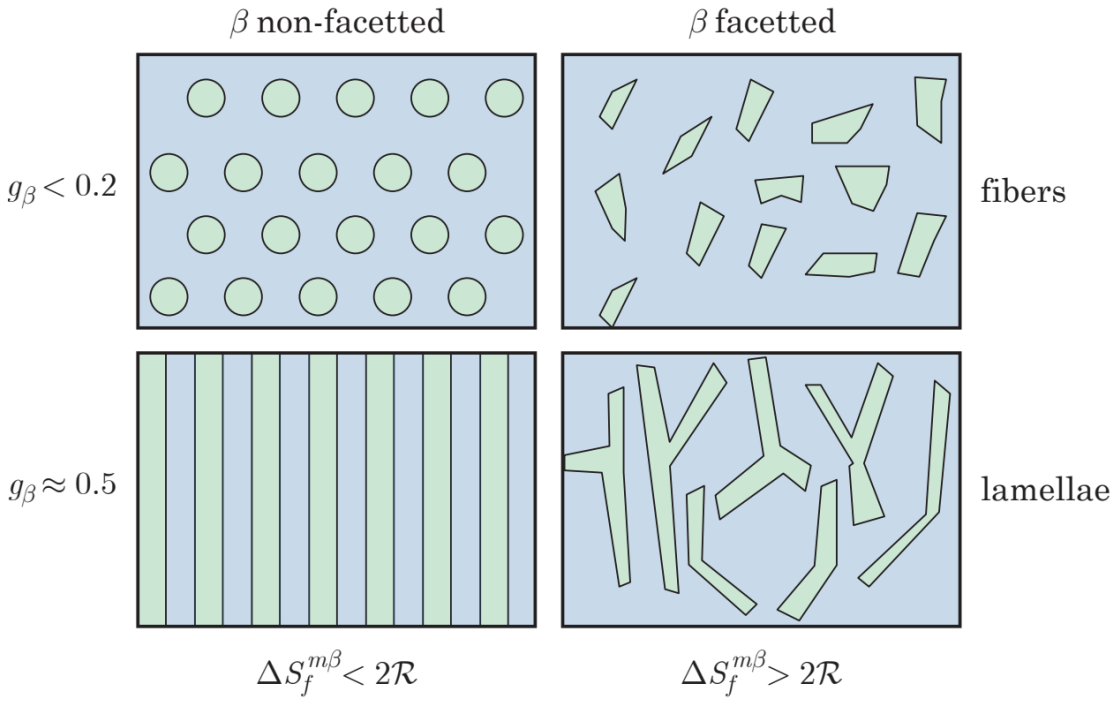

Figure 2.5: Classification of eutectic interface morphologies. Eutectic interface morphologies that can be obtained when the α phase is non-faceted and the β phase is either non-faceted (left) or faceted (right). This is shown for two volume fractions of the β phase. The eutectic is growing in a thermal gradient perpendicular to the page. Figure from ref. [60].

Eutectic crystallization stands out as a self-assembly - hence bottom-up and scalable - procedure to fabricate composite structures and, in the future, metamaterials. Eutectic systems such as Al-Si are the predominant alloys used in light-weight applications such as automotive and aerospace due to their low density, good castability,

low cost, and favorable mechanical properties (ductility and strength). Other metal-dielectric systems could also find use in metamaterial applications, which require one phase of the system to have a metallic character. Part II of this dissertation focuses on irregular Al-Ge and Al-Si eutectics, and Part III focuses on spiral eutectics in the Zn-Mg system.

Chapter 3

Methods

This Chapter provides an overview of the major experimental techniques used for most of the work reported in this dissertation. Detailed experimental procedures are provided at the end of the respective chapters for each project in Parts II and III (Chapters 4-8).

3.1 Crystallographic Texture Analysis *via* Electron Backscatter Diffraction

The macroscale properties of many crystalline solids, including minerals, ceramics, semiconductors, superconductors, and metals, depend very strongly on the arrangement of the atomic planes of their component units inside a volume of the crystal relative to a fixed frame. Electron backscatter diffraction (EBSD) allows peering into the crystallographic orientation of crystalline solids, for instance characterizing

the grain misorientation and the network of grain boundaries. The use of EBSD to measure grain-specific orientations and misorientations was first recorded in the mid-1980s [66].

Grain boundaries are classified according to the misorientation of neighboring grains and the inclination of the grain boundary plane [67, 68, 69]. Misorientation encompasses both the angle and axis of rotation that would bring the two grains in overlap, as shown schematically in Fig. 3.1(a). In orientation mapping misorientation is recognized by the orientation difference, above a preset threshold level, between pixels. Orientation mapping with EBSD for grain boundary-related investigations offers the advantage of obtaining directly the misorientation between grains. The main shortfall of the misorientation approach to boundary structure is that only three of the five macroscopic degrees of freedom required to describe a boundary and and the geometry of an interface are supplied. The remaining two degrees of freedom denote the crystallographic orientation of the boundary plane, as shown schematically in Fig. 3.1(b), which are not readily available from EBSD data acquired from either side of a boundary because the location of the boundary surface within the opaque material is not revealed from the position of its trace on a single section through the specimen. Additional steps such as calibrated serial sectioning are required to ascertain the position of the boundary plane.

The coincidence site lattice (CSL) distribution is a popular analysis tool for grain boundaries using grain boundary misorientation statistics (angle and axis pair). CSLs arise due to overlapping lattices at the interface of two grains, such as twin boundaries (*e.g.,* red line in 3.1(a)). In the CSL model grain boundaries are cate-

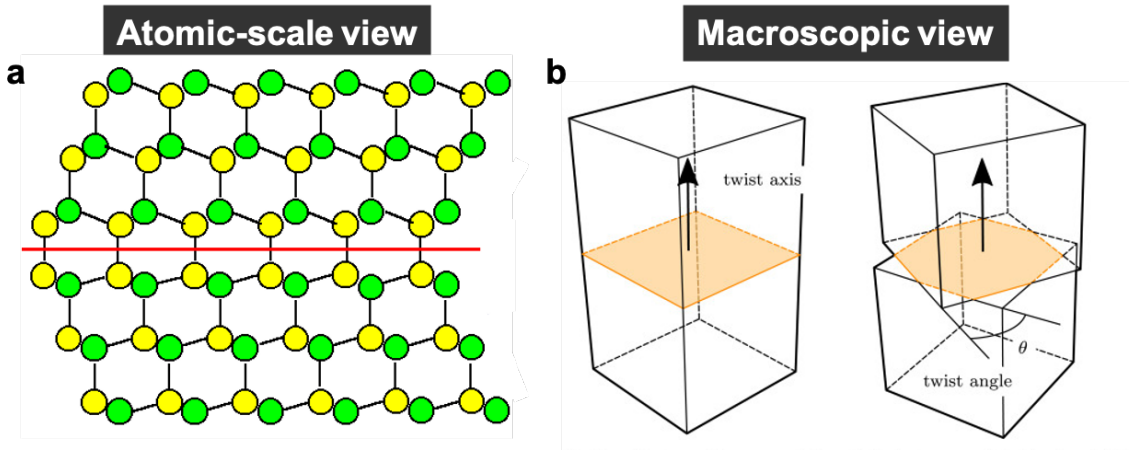

Figure 3.1: Characterization of grain boundaries. (a) Atomic-scale schematic of a twin boundary (red line). (b) Macroscopic view of a twin boundary (orange plane). Figures adapted from refs. [70, 71].

gorized according to the reciprocal density of coinciding lattice sites, Σ. Schematic examples of Σ3 and Σ5 boundaries are shown in Figs. 3.2(a,b), respectively: Σ3 boundary is a 60° rotation about the $< 111 >$ direction, and Σ5 boundary is a 36.9° rotation about the $< 100 >$ direction.

3.1.1 Conventional Two-Dimensional (2D) EBSD

In typical EBSD experiments, performed in a scanning electron microscope, a beam of electrons is directed at a point of interest on a tilted crystalline sample. The atoms in the sample cause an inelastic scattering of a fraction of the incoming electrons (*i.e.,* a small loss of their kinetic energy) to form a divergent source of electrons close to the surface of the sample. Some of these electrons are incident on atomic planes at angles that satisfy the Bragg equation $n\lambda = 2dsin\theta$, where n is the order of diffraction (typically only the first order is considered), λ the wavelength of the electrons, d the

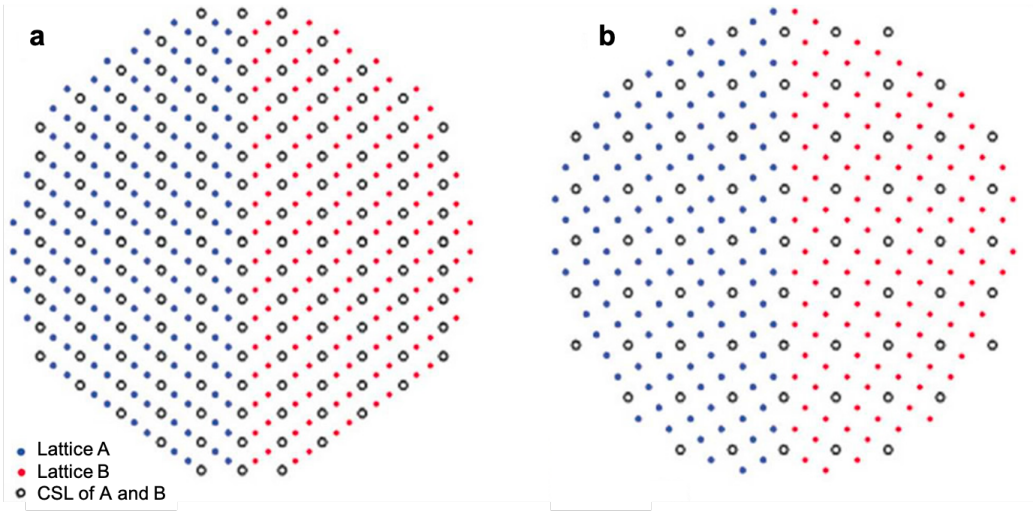

Figure 3.2: Schematic illustration of CSL boundaries. (a) $\Sigma 3$ grain boundary. (b) $\Sigma 5$ grain boundary. Blue and red circles denote lattice grains A and B, respectively; CSLs of A and B are shown with empty black circles. Figures adapted from ref. [72].

spacing of the diffracting plane (*i.e.,* the interplanar spacing), and θ the angle of incidence of the electrons on the diffracting plane. The diffracted electrons then form a set of paired large-angle cones that correspond to each diffracting plane. The image produced on the phosphor screen contains characteristic Kikuchi bands which are formed where the regions of enhanced electron intensity intersect the screen. The Kikuchi diffraction patterns are then indexed by comparing them to a dictionary of such patterns, and the result of this indexing is often displayed by inverse pole figure (IPF) orientation maps that use a basic RGB coloring scheme. For example, for cubic crystals full red, green, and blue are assigned to grains whose $< 100 >$, $< 110 >$, and $< 111 >$ axes, respectively, are parallel to the projection direction of the IPF (typically, the surface-normal direction). Intermediate orientations are colored by an RGB mixture of the primary components.

3.1.2 Three-Dimensional (3D) EBSD

EBSD-based orientation microscopy is, by its nature, a 2-dimensional technique that reveals the crystallographic texture close to the surface of the sample. By combining this technique with successive serial sectioning in a dual-beam focused ion beam and scanning electron microscope (FIB-SEM), as shown schematically in Fig. 3.3(a), a 3D approach is developed. Although this technique is destructive, it provides a quantitative measure of the crystallographic texture of a volume of a sample by performing orientation analysis of individual slices, as displayed schematically in Fig. 3.3(b).

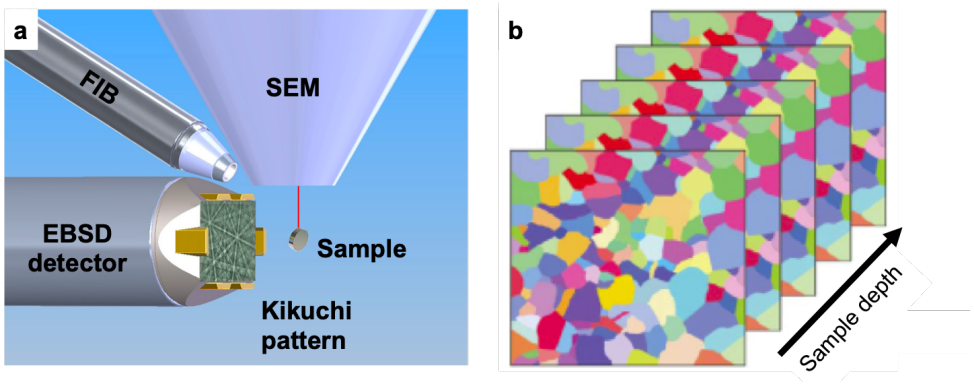

Figure 3.3: chematic illustration of 3D EBSD experimental setup in a dual-beam SEM-FIB. (a) Sample is placed in the field-of-view of both the SEM and FIB beam paths. (b) Illustration of orientation mapping of the serial-sectioned slices. Figure adapted from [72].

3.2 Synthesis *via* Directional Solidification

Directional solidification (DS) is a well-known technique in the field of materials science that, by decoupling the solidification parameters into two independently-

tunable parameters - namely a thermal gradient G and interface velocity V, can cause instabilities in pattern-forming systems such as dendritic and eutectic solidification. Many exmaples of morphological control of steady-state patterns formed at the crystal-melt interface have been reported [58, 73, 74]. For instance, for the the transparent organic crystal succinonitrile (SCN) doped with the laser dye coumarin, it has been shown that, under rapid solidification, the smooth solid– liquid interface becomes unstable and transforms to a pattern of shallow cells, deep cells, or an array of dendrites with sidebranch structure [74].

The Bridgman–Stockbarger method is a DS technique that allows solidification at constant V in a decoupled G. The Bridgman configuration allows controlling the rate of solidification, which in turn controls the characteristic interphase spacing λ, according to Eqs. 2.2-2.3. As stated earlier (Section 2.4), the ability of tuning the length-scale λ of (periodic) eutectic structures enables adjusting the wavelengths of light that an optically-active eutectic material interacts with.

Figure 3.4 shows an annotated picture of the three-zone Bridgman furnace used in the synthesis of some of the work reported later in this dissertation (spiral eutectics, Chapter 7). In this setup, the sample is placed inside a crucible (typically made of boron nitride) sitting atop a crucible holder. The crucible holder itself is mounted on a support rod that is moved down *via* the controller unit for sample loading and unloading, and moved up for directional solidification experiments. When the support rod is fully up, the sample is stationary inside the processing tube passing through the heating zones. The furnace is equipped with three individually controlled heating modules which allows each heating zone to be operated at distinct temperatures T_1,

T_2, and T_3. Assuming a positive thermal gradient G, the temperature of the top zone T_1 is higher than that of the bottom zone T_3. The processing tube is made of high-purity alumina, a ceramic material that helps reduce thermal shock during operation at elevated thermal gradients. The furnace allows growing ingots up to one-inch diameter.

A typical DS synthesis involves heating a stationary (fixed in the laboratory frame) material above its melting point, followed by imposing a fixed G *via* independently programming the temperature-time profile of the furnace zones; the furnace zones move up across the height of the sample at a fixed V that can be adjusted by the user. The sample then experiences this motor-driven temperature gradient and thus solidifies into a pattern that can be tuned by adjusting G and V.

Figure 3.4: Photo of the Bridgman furnace used in this dissertation. The equipment consists of three heating zones, which can be controlled independently to impose a range of thermal gradients. The controller at right allows tuning the velocity of the moving heating zones and their temperature.

3.3 Morphological Observation *via* Three-Dimensional X-Ray Nano-Tomography

3.3.1 Principles of X-Ray Transmission Microscopy (TXM)

X-ray microscopy (XRM) enables non-destructive 3D investigation of a variety of materials across length-scales. Driven by the development of advanced X-ray optics such as Fresnel zone platee, nanoscale XRM, with a resolution of tens of nanometers, has been implemented at synchrotron radiation sources. More recently, lab-scale instruments have also been developed; the resolution achieved by these sources can often compete with that achieved by synchrotron facilities. The most common way of producing magnified full-field images of an object on the detector is to use Fresnel zone plates (FZPs) as the high-resolution objective. Figure 3.5 shows a wide range of attenuation and phase contrast imaging techniques with sub-micron spatial resolution; ref. [75] provides an excellent review of the status, capabilities, and limitations of high-resolution imaging of both synchrotron and laboratory X-ray systems and considers future developments.

Sub-micron X-ray tomography, commonly referred to as X-ray nano-tomography (nTXM), stands out as a technique for 3D imaging of nanoscale features in metallic samples. Sub-50 nm resolution nTXM capability has been demonstrated recently based on FZPs using both laboratory and synchrotron X-rays. Part of this dissertation research, Chapters 7 and 8, harnesses these new developments in nTXM, using laboratory and synchrotron X-ray sources, respectively. Optical schematic of a lab-scale nTXM setup is shown in Fig. 3.6(a). This instrument focuses a high-brightness

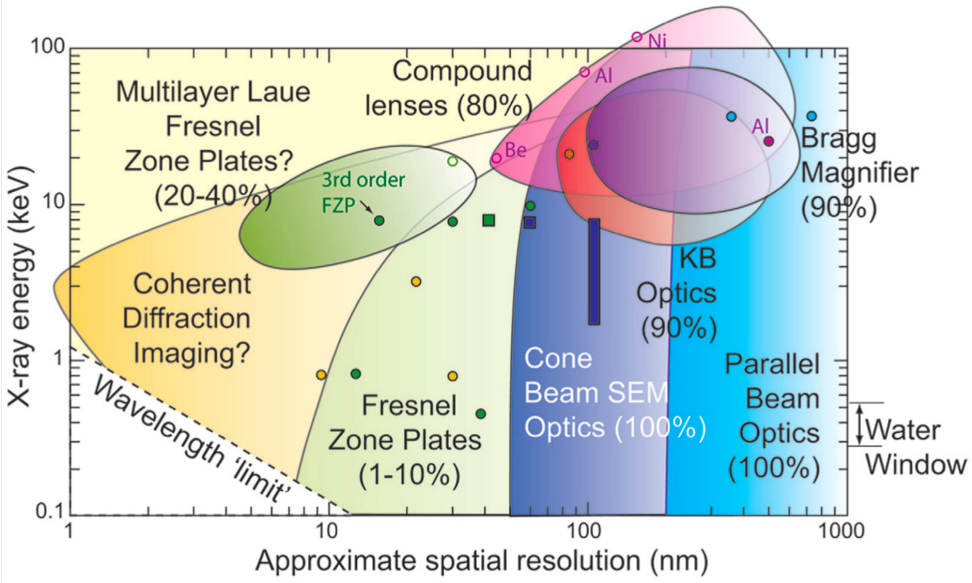

Figure 3.5: Schematic summary of a wide range of attenuation and phase contrast imaging techniques extending in resolution below the micron mark. The highest resolution systems currently available are limited by FZP technology. Current capabilities are marked with points, and potential for further developments are indicated with colored regions. Calculated resolutions are shown with open symbols, measured ones with filled symbols of the appropriate color, circles correspond to synchrotrons and squares to lab sources. Figure adapted from ref. [75].

X-ray source onto the sample by a high-efficiency capillary condenser. The transmitted beam then passes through a Fresnel zone plate to form a magnified image of the sample on the detector. Optionally, an optical phase ring can be placed in this path as shown in the schematic to achieve Zernike phase contract, which would aid visualizing features with low-absorbing or low-absorption-difference phases. The continuous rotation of the sample over a range of angles during the acquisition of projections enables a 3D tomographic reconstruction of the dataset. Due to the low-flux of the labscale nTXM instruments, their 3D data acquisition times are on

the time scale of hours. At the high-flux sources of synchrotron facilities, a full 3-D tomography data set can be acquired in one minute.

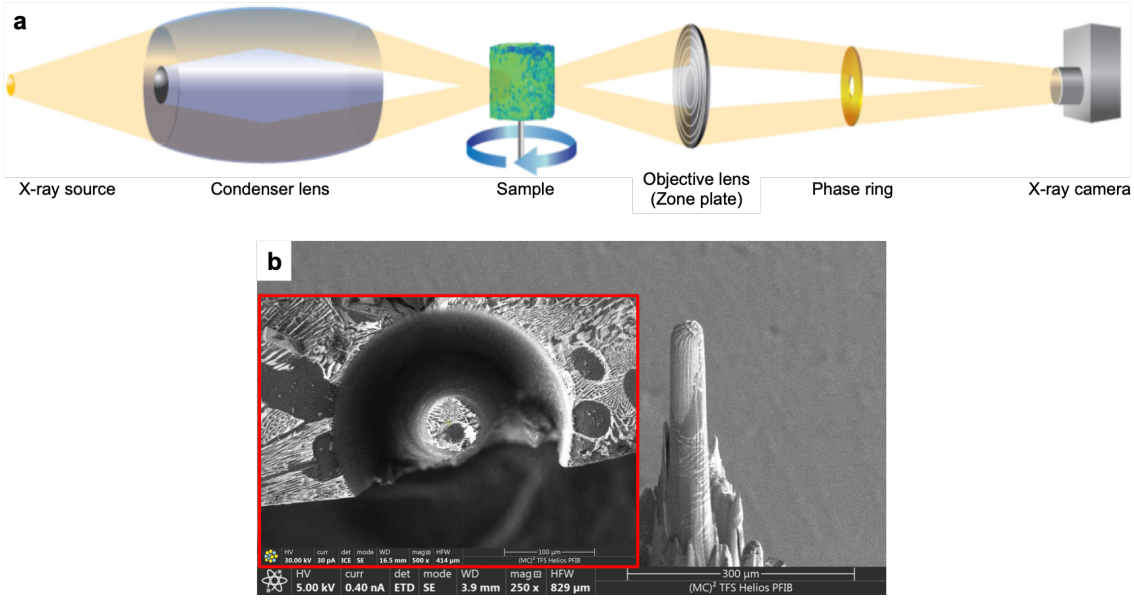

Figure 3.6: Optical setup and typical sample used in X-ray nano-tomography. (a) Optical setup schematic courtesy of Zeiss. (b) Micropillar sample prepared by plasma FIB (PFIB) for X-ray nano-tomography experiments. Inset in (b) shows a top-view of the region of interest before ablating its neighborhood with the PFIB.

3.3.2 Overview of Recent *In Situ* nTXM Capabilities

In 2018, the Full-field X-ray Imaging beamline at National Synchrotron Light Source-II in Brookhaven National Laboratory presented a demonstration of one-minute nTXM with sub-50 nm spatial resolution [76]. This achievement was made possible with an in-house designed and commissioned TXM instrument at the beamline, and it represents an order of magnitude decrease in the time required for studying sam-

ple dynamics with tens of nanometer spatial resolution. More recently, in fall 2019, the beamline designed and fabricated a compact high-temperature furnace optimized for *in situ* experiments with transmission X-ray microscope. The furnace has high temperature stability and minimal heat footprint to the ambient environment that are critical to high-quality experiments. This recent beamline addition provides an unprecedented opportunity to probe dynamic events such as phase transformations at high spatial and temporal resolutions.

3.3.3 Sample Preparation Using Plasma Focused Ion Beam

Typical X-ray energies in nTXM are around 8-10 keV, so it is imperative that the sample is sufficiently thin (typically around 30-50 μm for metallic samples). In order to prepare high-symmetry samples of this in this range of thickness for metallic systems, a focused ion beam can be used to prepare micropillars which will then be imaged along their height. Continuous rotation of this cylindrical-shaped samples during the acquisition of projections would facilitate the reconstruction of the dataset (*i.e.,* uniform center for the 2D cross-section slices). An example of a micropillar of a Zn-Mg alloy, used for the work reported in Chapter 7, is shown in Fig. 3.6(b). The micropillar was prepared with a Xe plasma FIB (PFIB, Thermo Fisher Helios G4 PFIB UXe), which has higher throughput and milling rate than conventional Ga-ion FIB sources.

In a typical micropillar preparation routine, the bulk, directionally-solidified sample (1 mm diameter) is first mechanically ground and polished to a sharp, wedge geometry (tip thickness approximately 300-400 μm). The sharpened sample is then

inserted into the PFIB chamber, and a region-of-interest (ROI) is identified. The ROI is then positioned at the center of two concentric circle patterns of desired depth defining the milling geometry. The sample is milled with circle patterns of progressively smaller outer and inner diameters until a desired diameter and depth are achieved.

3.4 Dislocation Analysis *via* Electron Microscopy

Dislocations are extended line defects that play crucial roles in both the mechanical response and growth of crystalline structures [77]. They may also strongly influence the electronic properties of semiconductors because they act as scattering centers for charge carriers or as non-radiative recombination centers in light-emitting devices and solar cells. Typically dislocations are studied in relation to the mechanical properties of materials since they allow plastic deformation to occur at lower applied stresses by permitting the glide of one entire crystal plane over the one below it in a discrete, rather than coherent, way. The role of dislocations in mechanical response of crystals are comparatively well-understood. For instance, the motion, multiplication, and interaction of dislocations cause strain hardening, a common phenomenon in which continued deformation increases the strength of a crystal. Furthermore, dislocations control the strength and ductility of crystals. What is less commonly appreciated is that dislocations are also important for crystal growth. For instance, screw dislocations offer non-vanishing growth steps on the otherwise flat surface allowing the growth to advance in a spiral manner without the need for

nucleation of a new layer [78].

Evidently, the characterization of dislocations is of significant interest to understand material properties and crystal formation processes. This Section provides a brief introduction to the concept of dislocations followed by experimental analysis of dislocations by electron microscopy.

3.4.1 Dislocations in Crystals

The atoms in a crystal containing dislocations are displaced from their perfect lattice sites, and the resulting distortion produces a stress field in the crystal around the dislocation. Dislocations are therefore sources of internal stress in crystals. There are two basic extreme types of dislocations, edge and screw, that can occur. Often dislocations in crystalline solids are a hybrid of the edge and screw forms.

Broadly, a dislocation is the boundary between the deformed and undeformed regions in a crystalline structure. In this sense, the dislocation line represents the slip front of the propagation of a dislocation (a line defect). The Burgers vector, which is commonly used to define dislocations in crystals, represents the length and direction of the slip. The magnitude of the Burgers vector is a characteristic discontinuity of the displacement the the dislocation has caused. To find the Burgers vector, an atom-to-atom circuit is drawn around the suspected dislocation until the starting point is reached again. Each step of the circuit is associated with a step in a perfect, dislocation-free crystal of the same structure. If the circuit fails to close, then it must enclose one or more dislocations, and the vector needed to complete this circuit is the Burgers vector of the dislocation. In other words, the Burgers vector is

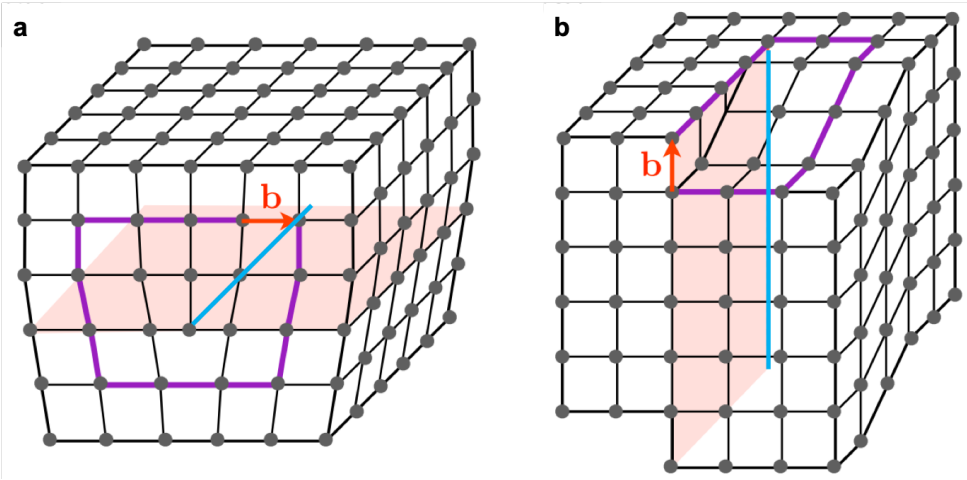

Figure 3.7: Schematic representation of edge and screw dislocations. (a) Edge dislocation. (b) Screw dislocation. Filled circles denote the crystal lattice, **b** is the Burgers vector, pink area and blue line illustrate the slip plane and dislocation line, respectively, and the purple paths are the Burgers circuits. Figure adapted from ref. [79].

the closure failure of a Burgers circuit around the dislocation.

Figure 3.7 shows a schematic representation of the Burgers analysis. The distinction between the two extreme cases of dislocations, edge and screw, is related to the relative orientation between the Burgers vector and dislocation line. When the Burgers vector is perpendicular, parallel or arbitrarily oriented with respect to the dislocation line, the corresponding dislocation is of edge, screw or mixed character, respectively. Figure 3.7(a) shows that, in edge dislocations, an extra half-plane of atoms is introduced into the crystal lattice. This extra half-plane of atoms causes the region above it to be in compression and the region below to be in tension, so the inter-atomic bonds are significantly distorted in the immediate vicinity of the dislocation line. Figure 3.7(b) shows that screw dislocations can be visualized as a

cutting a crystal along a plane and slipping one half across the other by a Burgers vector.

The Burgers vector $\mathbf{b}$ of dislocations can be determined on the basis of the $\mathbf{g}\cdot\mathbf{b} = n$ criterion in a transmission electron microscope (TEM) by setting up different two-beam diffraction conditions with an imaging vector $\mathbf{g}$. Based on the reciprocity theorem in optics by which an electron source and a detector can be reversely arranged to obtain the same image intensity, scanning transmission electron microscopy (STEM) can also be applied for defect characterization. However, STEM has been less frequently used up to now because, historically, the specimen orientation could not be precisely controlled due to the lack of cameras to acquire on-axis transmission electron diffraction patterns and double-tilt TEM specimen holders that are necessary to orient specimens in a two-beam condition. These accessories have become available more recently. In STEM, owing to the use of transmitted electron beams, one can obtain bright-field images similar to those in TEM. This similarity is proved by the reciprocity theorem in optics, and diffraction contrast images of dislocations, phase contrast of lattice images, and structure images in TEM are similarly observed in STEM. This Section concludes by highlighting sample considerations for dislocation analysis (both $\mathbf{g}\cdot\mathbf{b}$ in TEM and direct visualization in STEM). The recent developments of aberration correctors in has led to a dramatic improvement in spatial resolution in STEM for imaging dislocations at atomic resolution.

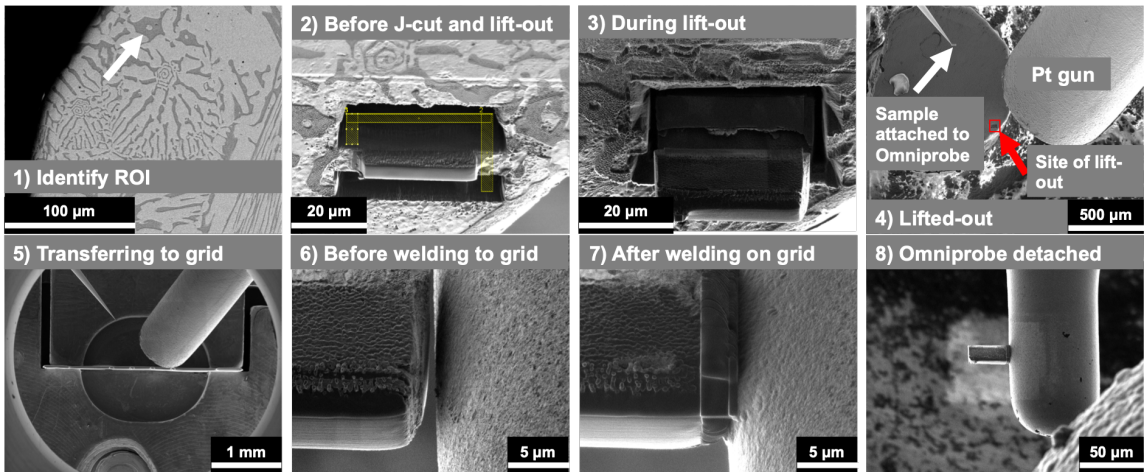

Figure 3.8: Illustration of lift-out sample preparation. The region of interest is indicted by the white arrow in the first image.

3.4.2 Lift-Out Sample Preparation

Precise, site-specific preparation of S/TEM samples is afforded by a series of steps, denoted collectively as "lift-out" in the following, in a dual-beam FIB-SEM. FIB enables deposition and ablation of materials, and SEM enables monitoring of the steps. At a broad level, the lift-out procedure consists of seven major steps: (1) Deposition of a protective layer of Pt on the region of interest (ROI) in a bulk sample, (2) Bulk-out cut around the ROI, (3) J-shaped of the ROI from the bulk sample, (4) Lift-out of the freed ROI, (5) Mounting on the TEM grid, (6) Thinning, and (7) Cleaning. A step-by-step guide of a typical lift-out experiment is shown in Fig. 3.8. The starting cross-sectional region is typically around 1.5 μm. Target final thickness is 60-100 nm (depending on the concentration of 'heavy' elements in the sample), with minimal amorphous material for high resolution imaging. Total time for the lift-out process is 1-4 hours depending on skill level.

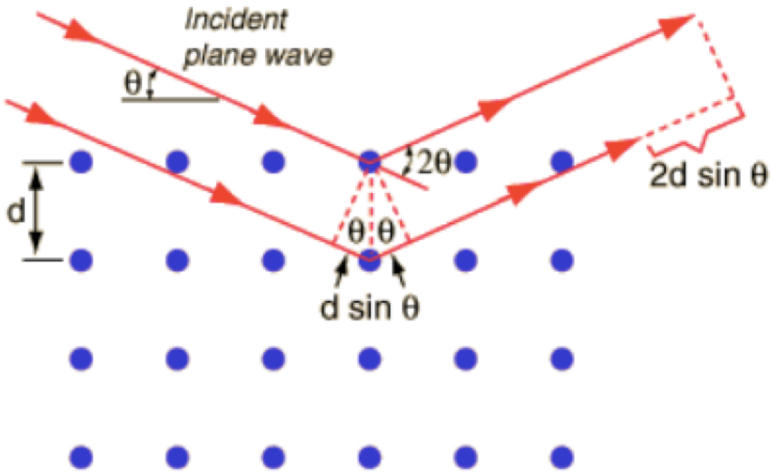

Figure 3.9: Relationship between Bragg diffraction and lattice images. The schematic shows that satisfying the Bragg conditions leads to diffraction contrast observed during TEM imaging. Figure adapted from ref. [80].

3.4.3 Two-Beam TEM Imaging

Obtaining lattice fringes in TEM requires an interference between the direct and Bragg-diffracted waves from a crystalline specimen. Electron diffraction occurs when an electron wave is incident on a crystalline specimen; the diffracted waves exit from the crystal with an angle of $2\theta_{hkl}$, according to the Bragg formula $2dh_{hkl}sin\theta = n\lambda$, where d is the lattice spacing, the integers h, k, l are the Miller indices in crystallography, θ is the glancing angle, n is the order of diffraction, and λ is the wavelength of the incident wave. Bragg's law provides a scalar description of diffraction, and is shown schematically in Fig. 3.9.

In a TEM, electron diffraction can be obtained by converging the incident beam to a spot on sample, or from a selected area of the sample using parallel beam. This technique provides crystallographic information of, *e.g.,* crystal structure, orienta-

tion, strain, and defects including dislocations, through a local modulation of the amplitude and phase of primary and diffracted beams. Diffraction maxima (spots) occur only when Bragg's condition is satisfied (constructive interference).

Bragg's law is an algebraic description of diffraction in real-space. Rearrangement of Bragg's law, $\frac{sin\theta_{hkl}}{\lambda} \sim \frac{1}{2d}$, shows that distance and angle have a reciprocal relation. The 'reciprocal lattice' construction and Ewald's sphere constitute a useful way of visualizing dislocations. The Ewald construction integrates the scalar (Bragg) and vector (Miller index) description of diffraction. This integration demonstrates the diffraction relationship in reciprocal lattice, and it provides a visual way to understand which lattice points are in diffraction condition. The Ewald sphere has a radius of $\frac{1}{\lambda}$ and is centered at the crystalline specimen, as sketched in Fig. 3.10(a). As the Figure shows, for a diffraction point in reciprocal space to be in diffraction condition, it must lie on the *surface* of the sphere. An axial incidence of electrons to the crystal does not realize the exact Bragg condition because of curvature of the Ewald sphere.

In the diagrams in Fig. 3.10(a), the electron beam comes from the left. The unscattered (direct) beam passes through the crystal, and the point where it reaches the sphere surface is the origin of reciprocal space. The electron diffraction pattern is the 2D projection of the reciprocal lattice of a crystal that intersects with Ewald's sphere, as shown in Fig. 3.10(b). The angle between the incident and diffracted beams is 2θ, and the vector connecting the origin of the reciprocal space and the diffraction point is the diffraction vector $\mathbf{g}$. The length of $\mathbf{g}$ is the reciprocal of the spacing between the planes ($\frac{1}{d}$); by construction, $\mathbf{g}$ is perpendicular to the planes that

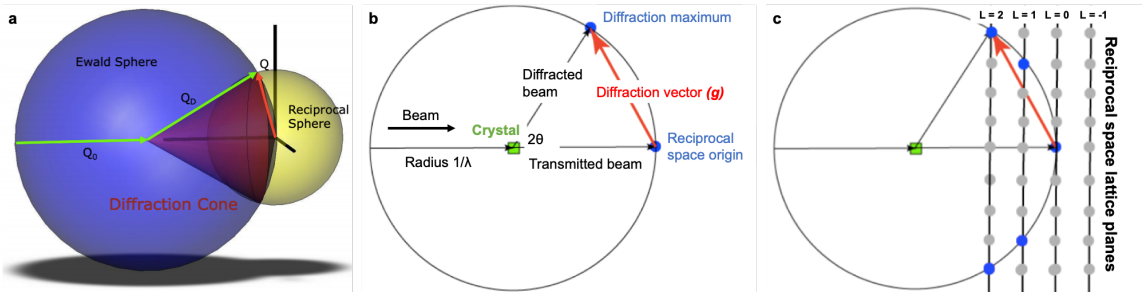

Figure 3.10: Schematic illustration of diffraction in reciprocal space using the Ewald. (a) Ewald and reciprocal spheres. (b,c) Condition for diffraction as explained in the text. Figures adapted from ref. [80].

originate diffraction in Bragg's law. The reciprocal space is the map of diffraction pattern, displayed in Fig. 3.10(c), where only the diffraction points that lie on the surface of the Ewald sphere meet the diffraction condition.

When some Bragg-diffracted waves are incorporated into an objective lens in a TEM, the wave converges on the image plane. Near the image plane interference fringes form with the direct beam and the selected Bragg-diffracted waves. This phenomenon gives rise to the diffraction contrast that lies at the heart of imaging in TEM, which can then be used to study defects, grain boundaries, strain field, precipitates.

The diffraction contrast depends on several parameters, including (1) Excitation error: Is the Bragg condition met *exactly* (dynamic case, Fig. 3.11(a)) or *approximately* (kinematic case, Fig. 3.11(b))? (2) The diffraction condition: Is the Bragg condition met for many diffraction vectors **g**, *e.g.*,, Fig. 3.12(a), two, *e.g.*,, Fig. 3.12(b), or none? (3) Imaging mode: Is the *primary* beam used for imaging (bright field) or *diffracted* beam (dark field)?

Dislocation analysis with TEM is mediated by the two-beam condition, namely

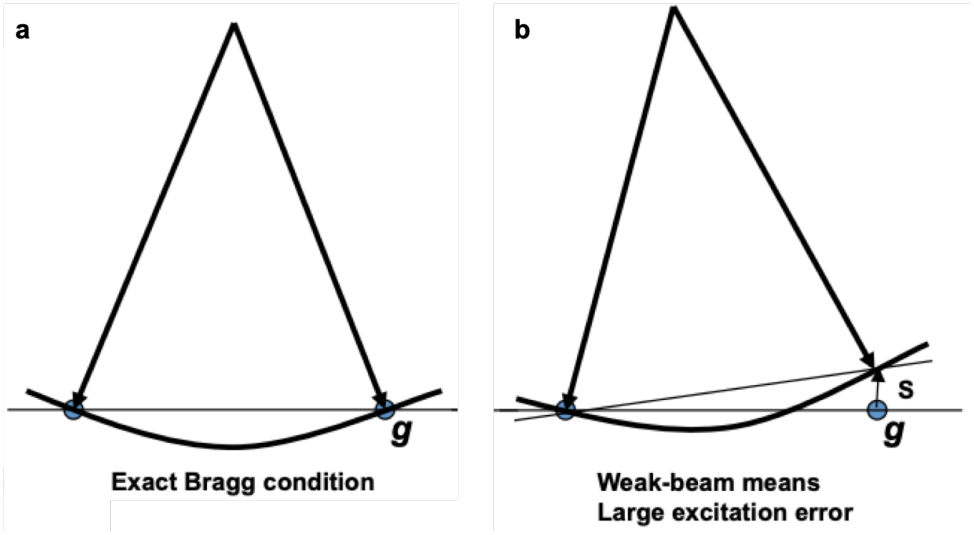

Figure 3.11: Excitation error in diffraction-contrast TEM imaging. Dark-field weak-beam can offer very high resolution, but needs long exposure time and stable instruments. Figure adapted from ref. [81].

by imaging the same dislocation with different $\mathbf{g}$ and observing the contrast. For this reason, a double-tilt TEM specimen holder must be used. Dislocations are invisible (or have a very weak contrast) if $\mathbf{g} \cdot \mathbf{b} = 0$, the so-called "invisibility criterion." In two-beam experiments, dislocations are perceived with the greatest contrast when $\mathbf{g}$ and $\mathbf{b}$ are parallel. A schematic illustration of the $\mathbf{g} \cdot \mathbf{b}$ rule in two-beam experiments is shown for an edge-dislocated sample in Fig. 3.13.

Two-beam observation of dislocations relies on collecting diffraction pattern in the zone axis pattern (ZAP). As shown schematically in Fig. 3.14, this process involves satisfying the diffraction condition with the incident beam along a lattice direction $[uvw]$. Electron diffraction then "lights up" $\mathbf{g}_{hkl}$ spots that are perpendicular to $[uvw]$, *i.e.,* when $hu + kv + lw = 0$.

STEM has been less frequently considered for defect characterization mostly be-

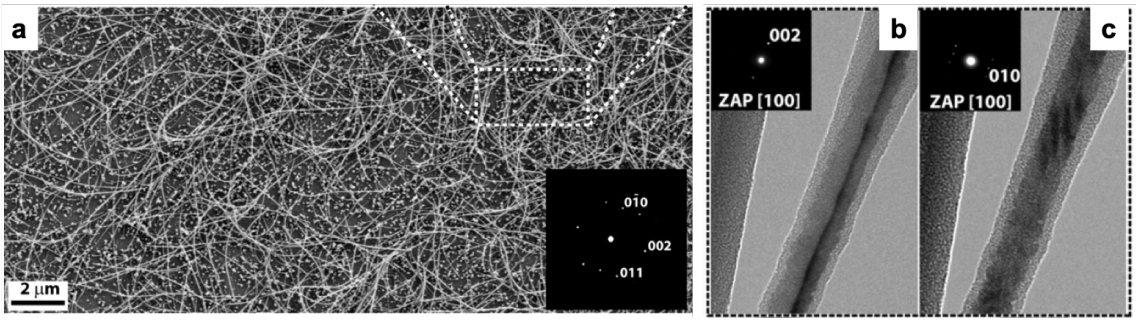

Figure 3.12: Diffraction conditions in TEM imaging.. TEM observation of solution-grown zinc oxide nanotubes and nanowires. (a) Low-magnification and electron diffraction patterns of a region in the sample. (b,c) TEM observation of screw dislocations within ZnO nanowires by two-beam TEM imaging. Figures adapted from ref. [82].

cause the specimen orientation could not be precisely controlled. In particular, while electron microscopy techniques have allowed atomic-scale characterization of edge dislocations from the conventional end-on view, for screw dislocations the atoms are predominantly displaced parallel to the dislocation line (3.7(b)). Hence, the screw displacements are parallel to the electron beam and become invisible when viewed end-on. More recent developments in double-tilt specimen holders have enabled direct imaging of dislocations, including screws, using STEM [84, 85, 25].

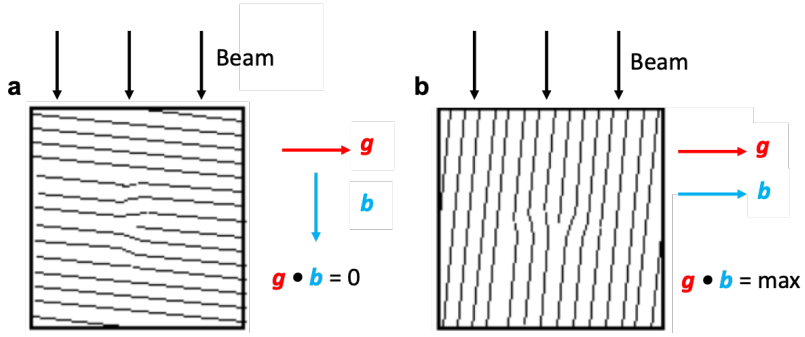

Figure 3.13: Schematic illustration of two-beam TEM imaging for a sample with edge dislocation. A $\mathbf{g} \cdot \mathbf{b}$ analysis can be implemented to determine the direction of the dislocation, as described in the text. In (a), $\mathbf{g} \cdot \mathbf{b} = 0$ and thus the dislocation appears invisible. In (b), $\mathbf{g} \cdot \mathbf{b}$ attains its maximum value since the two vectors are parallel, and the dislocation will have a bright contrast during imaging. Figures adapted from ref. [83].

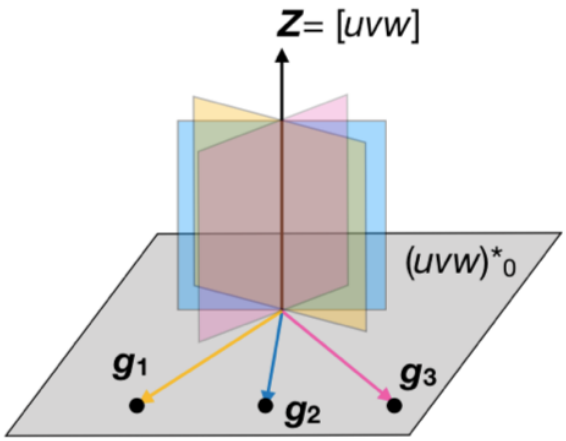

Figure 3.14: Schematic illustration of several zone-axis patterns in a crystalline sample. Diffraction pattern taken with incident beam along lattice direction $[uvw]$ are shown. Electron diffraction "lights up" $\mathbf{g}_{hkl}$ spots that are perpendicular to $[uvw]$, *i.e.,* when $hu + kv + lw = 0$. Figure adapted from ref. [80].

Part II

Crystallization in the Presence of Chemical Modifiers

Chapter 4

Chemical Modification of Degenerate Eutectics

This chapter is based on the review article published in *Journal of Materials Research* [29].

4.1 Introduction

4.1.1 General Features of Degenerate Eutectics

Eutectic solidification results in multi-phase patterns with diverse morphologies. Owing to their unique appearances, they have been given descriptive names such as lamellar, Chinese script, spiral, nodular, etc. Since two or three of these morphologies can coexist in the same system (due to, *e.g.*, differences in the solidification pathway), there are yet other ways to classify the eutectic structures beyond their

morphologies. Following Fredriksson *et al.*, one way is to classify the eutectic as either 'normal' (also known as 'regular') or 'degenerate' (also known as 'irregular') based on its ability to establish cooperation between the phases during growth [86]. In particular, such a classification holds for two-phase eutectics, such as those considered in this review. In a normal eutectic reaction, such as that between two elemental metals, there is a close cooperation between the two phases. Cooperation (also known as coupled growth) implies that the growth of the two phases is sustained by the side way inter-diffusion of the rejected components ahead of the advancing interface [59, 60], as discussed in Section 2.3. The two phases grow into the melt with a common planar solid–liquid interface and a well-defined interphase spacing, leading to the formation of lamellar or rod-like microstructures.

By contrast, a degenerate eutectic reaction proceeds with little to no cooperation between the phases, and the eutectic spacing varies. This situation occurs when one of the two phases grows faster than the other. Consequently, the growth mechanism of the single "leading" phase determines the structure of the eutectic. Such is the case in semi-metallic eutectics wherein one of the two phases is faceted (*e.g.*, Si or β in Fig. 2.3) while the other is non-faceted (*e.g.*, Al or α in Fig. 2.3). The faceted phase possesses a certain stiffness due to the nature of its covalent bonding and thus is only capable of growing along well-defined, "fast growth" directions [59, 58, 57]. In these directions, the faceted phase grows with the assistance of defects such as twin boundaries and screw dislocations. Detailed analysis of the total undercooling of the eutectic growth front by Kurz and Fisher in 1980 shows that the faceted phase leads the growth process, *i.e.*, it has lower undercooling and extends deeper into the

melt [87]. Thus, the eutectic growth front is non-isothermal (see also Fig. 2.3 for a schematic illustration).

4.1.2 Modification of Degenerate Eutectics

The brittleness of the coarse and faceted Si crystals in untreated Al–Si eutectics is the main reason for its poor mechanical properties, such as premature crack initiation and fracture in tension [88, 89, 90]. However, to our advantage, the growth mechanism of the faceted phase is fairly complex, and thus its microstructure (as well as that of the overall eutectic) can be influenced in various ways. One option is to tune the solidification parameters, *e.g.*, growth velocity and thermal gradient, in directional experiments [58, 91]. The resulting microstructure can vary from flake-like to fibrous depending on the growth conditions and the volume fractions of the constitutive elements, see Refs. [58, 92, 39] for further details. A second route is to tune the alloy chemistry by introducing trace concentrations of a metallic element, a process known as chemical modification.

In 1921, Aladar Pacz was granted a US patent for the discovery that the treatment of Al–Si alloys containing between 8 and 15% Si (*i.e.*, near the eutectic composition) with alkali fluoride flux before casting into the finished form yields improved tensile strength and ductility [93]. Pacz wrote of the modified alloy, "If now the metal be cast, it will be found that the fracture instead of being coarse, dark, and glassy, is fine-grained, light and dense. The physical properties have undergone a most remarkable change, the tensile strength rising to a point between 23,000 and 2788 pounds per square inch [from 15,000 to 18,000 pounds per square inch] and the elon-

gation to a point between 3.5 to 6.25% [from 0.5%]" [93]. Although Pacz' discovery of eutectic modification predates the Second World War, it was not until after the War had ended that dramatic advancements in the aluminum casting industry were made. The booming aerospace industry in the 1960s provided the necessary stimulant for the production of new, light-weight aluminum alloys that complied with engineering requirements. Similarly, the energy crisis of the early 1970s inspired the replacement of heavy cast iron and steel with light-weight aluminum alloys. Many of these aluminum-based components were castings, among which Al-Si alloys constituted ∼90% of the total parts produced [94]. Since then, chemical modification of this alloy has been widely practiced in the aerospace and automotive sectors as a viable route to enhance the mechanical properties of Al–Si castings. For instance, additions of only a few hundred ppm of Sr or Na are more than sufficient to modify the eutectic Si microstructure in Al–Si castings from coarse flake-like into fine fibrous; such microstructural changes have favorable effects on both strength and ductility [89, 41]. The critical levels of modifier necessary to produce significant changes in the microstructure are addressed in Section 4.2 below.

The remainder of our review is concerned with the types and mechanisms of this chemically induced modification. More specifically, we will address the following two questions: (i) What are the microstructural signatures commonly associated with modification; and (ii) Where do these signatures come from? As will be shown in Section 4.2, chemical modification carries many connotations, depending in part on the perspectives of the beholder. Furthermore, as described in Section 4.3, modification may originate during solidification (*i.e.*, nucleation and growth of the eutectic

phases) and/or subsequent annealing of the cast alloy. Finally, in Section 4.4, we will address challenges and future developments needed to move the field forward.

4.2 The Signatures of Chemical Modification

The effects or signatures of modification are multi-fold. As alluded to in the previous paragraph, chemical modifiers may (i) alter the length-scale of the eutectic microstructure. More specifically, modification results in a structural refinement, *i.e.*, a decrease in the average interlamellar spacing . It is important to reiterate that refinement can also be achieved by solely increasing the growth velocity v in directional solidification experiments since according to the generalized Jackson–Hunt model [59, 93, 55] (*cf.,* Section 2.3.1). Chemical modifiers may also (ii) change the morphology of the faceted phase from flake-like to fibrous, see Fig. 4.1. The fibrous form of Si in modified Al–Si alloys minimizes stress concentration effects and therefore improves ductility substantially [95]. Such morphological transitions are thought to be related to (iii) changes in the defect density. That is, the increased flexibility of the growth habit in the modified eutectic is made possible by a very high frequency of multiple twinning in the Si phase. For instance, Hellawell has reported that the twinning probability in Sr-, Ba-, Ca-, and Yb-treated eutectics—defined as the ratio of the twin spacing to the Si{111} interplanar spacing—is two to three orders-of-magnitude higher than in the unmodified Al–Si casting [96]. However, experimental evidence by other groups has been put forward that contradicts this claim and suggests instead that twins are not present in the modified structure [97]. These

opposing viewpoints are expounded in detail below. It is also well known that trace metal additions are accompanied by (iv) increased porosity in the casting, such that it negates any of the beneficial refining (i) or morphological (ii) effects discussed above [98, 99]. Some investigators have found the porosity so detrimental that they have abandoned chemical modification of Al–Si eutectics [98, 99]. Finally, chemical modifiers may (v) alter the topology (*i.e.*, connectivity) of the eutectic phases, as first deduced from three-dimensional tomographic reconstructions by Moniri *et al.* [30]. Whereas unmodified eutectics contain a network of interconnected Si flakes,5 its modified counterpart consists of isolated domains of Si that are surrounded by Al. This topological transition occurs (for the same volume fractions of Si and Al) because the non-faceted phase leads at the solidification front in the modified alloy, and eventually engulfs the faceted phase in its wake [30]. In all, modification brings about a host of changes in the eutectic microstructure, including length-scale, morphology, defect density, porosity, and topology.

Figure 3 illustrates the potency of various elements for the modification of eutectic Si in Al–Si alloys, using data published in the literature in the period from May 1963 to May 2018 [102, 103, 104, 105, 106, 107, 108, 109, 110, 111, 112, 113, 114, 115, 116, 56, 117, 118, 119, 120, 121, 42]. We note that "modification" is not always uniquely defined in the community (see also Section 4.1.2), so we attempt to avoid any potential ambiguity by designating whether a particular modifying agent brings about only refinement and/or morphological change, or whether an increased density of twins is also observed. Due to these inconsistencies, we believe that it would be instructive for the community to agree upon a specific metric for reporting

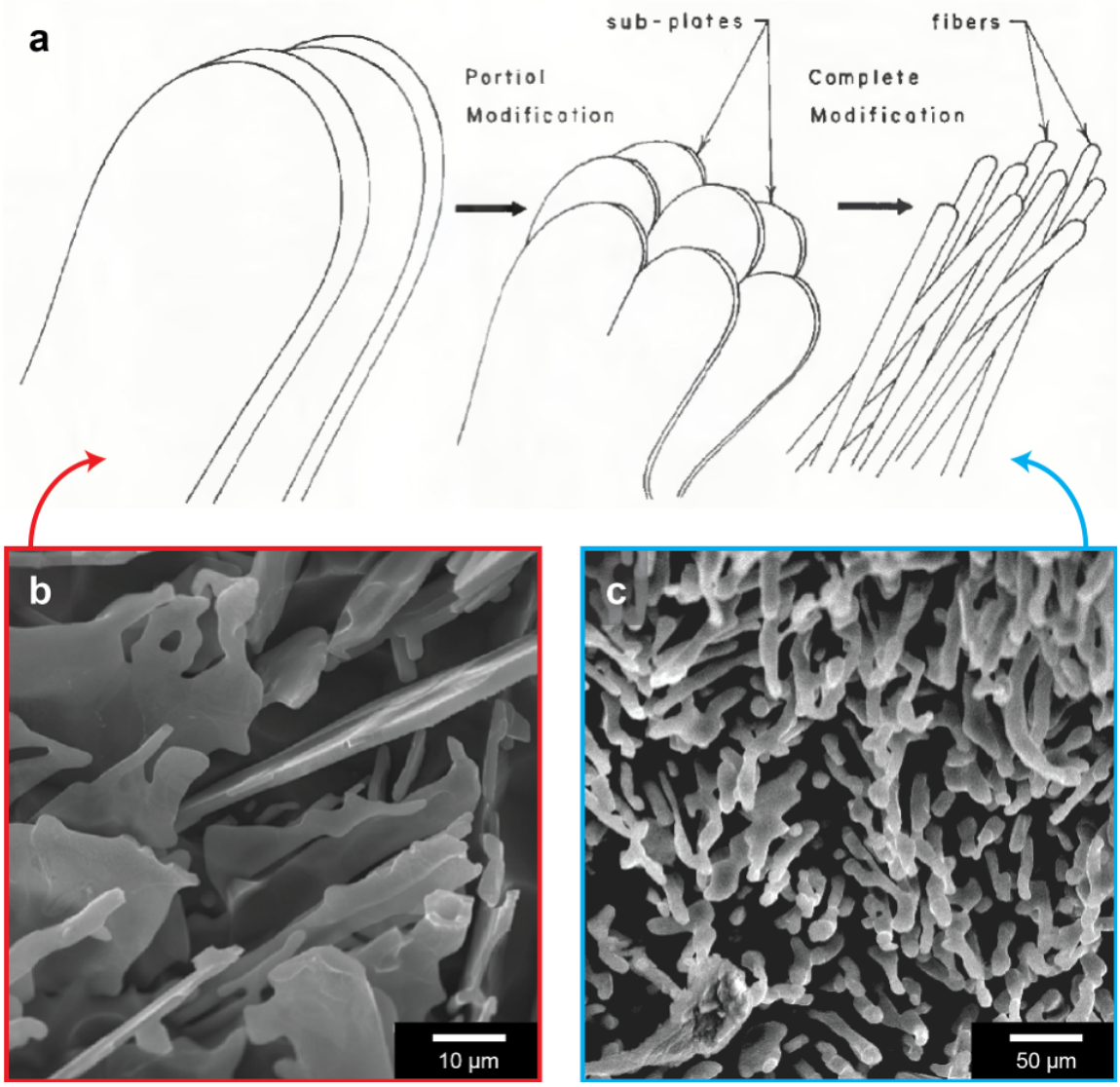

Figure 4.1: Morphological transitions upon chemical modification. (a) Schematic representation of the different eutectic Si morphologies attained with varying degrees of chemical modification. In the unmodified or "chill cast" alloy, Si takes the form of coarse flakes; on the other hand, in the completely modified or "Na-treated" alloy, Si is typically found as fine fibers. Reprinted with permission from American Welding Society [100]. Example high-resolution scanning electron images corresponding to the (b) unmodified and (c) modified microstructures shown in (a). In both cases, the Al-rich phase has been chemically removed. (b) Figure adapted from [91] and (c) from [101].

"modification". Figure 3 is intended to provide a bigger picture of which elements have been used to modify eutectic Si in Al–Si alloys, and to what extent. It is evident that a vast majority of Group I and II, Lanthanides, and the nitrogen family (Group 15) elements cause refinement and morphological change. A few transition metals have also been reported to cause refinement/morphological change. Of note is that only a limited subset of all the elements investigated have been reported to also cause an increase in twinning, namely, Na, Sr, Sc, and Eu. Some elements have been reported to have neutral effect on modification. The reason for the varying degree of modification—from none for some elements, to morphological for most, and crystallographic for only a few—remains to be determined.

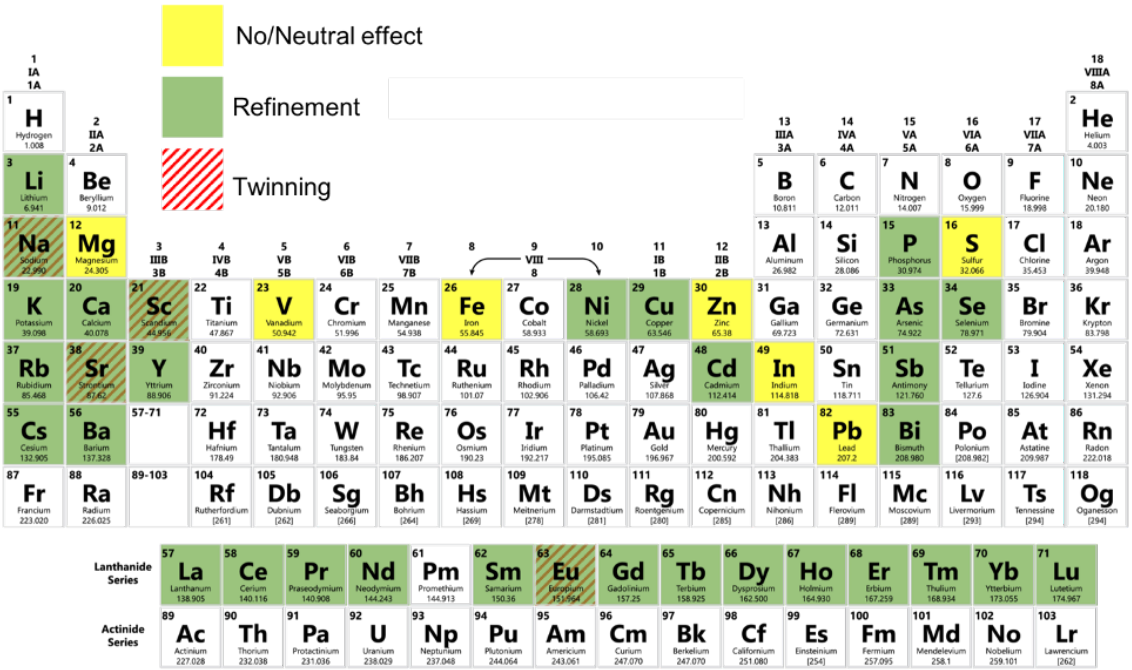

Figure 4.2: Summary of the modification potency of elements for eutectic Si in Al–Si alloys from the literature in the period from May 1963 to May 2018. Elements that bring about only a morphological change and/or refinement are shaded green, while those that also induce twinning are hatched with red lines. Elements that have been found to be neutral are illuminated as yellow. Data compiled from Refs. [102, 103, 104, 105, 106, 107, 108, 109, 110, 111, 112, 113, 114, 115, 116, 56, 117, 118, 119, 120, 121, 42].

4.3 The Origins of Chemical Modification

4.3.1 Modification During Nucleation

The first school of thought on the origins of modification concerns eutectic nucleation, and particularly that of the faceted phase (*e.g.*, Si). In the mid-1960s, Crosley and Mondolfo conducted pioneering metallographic investigations on nucleation phenomena in Al–Si alloys [41]. Their conclusions were 2-fold: (i) Eutectic Al is not affected by trace metal additions, while nucleation of eutectic Si is highly sensitive to the type and amount of modifiers present. In commercial unmodified alloys, eutectic Si is most likely to be nucleated by AlP particles that pre-exist in the melt. That is, the critical undercooling required for the nucleation of eutectic Si by the primary α (Al) phase is higher than that by the AlP particles. We note that P is an unavoidable trace element in Al–Si castings. (ii) Modification of Al–Si by Na results in a "neutralization" of the AlP particles such that easy nucleation of Si is prevented. The evidence for the latter effect is manifested in a depression of the critical nucleation temperature for eutectic Si in cooling curves of the Na-modified alloy. The undercooling required for Si nucleation in the presence of Na was recorded as 6–12 °C, versus 5–7 °C in the unmodified, hypoeutectic Al–Si alloy [41].

Support for Crosley and Mondolfo's theory of modified nucleation comes from the recent body of work by Dahle and coworkers [42, 122]. Through electron backscatter diffraction (EBSD) of the solidified specimens, they determined that the eutectic Al shares an epitaxial relationship to the primary α (Al) dendrites in unmodified Al–Si alloys, while in Sr- and Sb-modified alloys, the eutectic Al has multiple orientations

unrelated to the surrounding dendrites [42]. This suggests independent nucleation and growth in the Sr- and Sb-modified alloys. Moreover, Dahle and coworkers detected AlP particles located at the center of polyhedral Si. Selected area diffraction patterns in the transmission electron microscope (TEM) show that there is no lattice mismatch between the 111 planes of AlP and the Si crystal. The authors took this result to mean that AlP is a good nucleant for eutectic Si [42]. Both AlP and Si have cubic crystal structures with nearly identical lattice parameters (5.421 Å [123] and 5.431 Å [124], respectively). The modification of the Al–Si alloy is then thought to be due to the fact that the AlP nuclei are saturated with Sr-containing intermetallics, *e.g.*, Al_2Si_2Sr; this contributes to an increased "nucleation difficulty" for eutectic Si (*i.e.*, higher nucleation undercooling and also lower nucleation frequency) [42]. Further high-resolution evidence was provided by Schumacher and coworkers [125]. They report that P, in the form of AlP particles, is located not only at the center of primary Si but also at the interface between eutectic Si and eutectic Al, see Fig. 4.3 [125]. During the eutectic reaction, the AlP forms at the surface of Al, and thereby provides favorable conditions for the heterogeneous nucleation of eutectic Si on eutectic Al. Direct experimental verification showing the "poisoning" of these such particles by Sr or Na is still lacking. Nevertheless, it is clear that the potency of AlP as an innoculant must be critically considered in unmodified and modified Al–Si alloys alike.

At low concentrations of P, the AlP particles may also nucleate on oxide bifilms that are folded into the liquid phase, as suggested by Campbell and Tiryakioğlu and others [98, 126]. In the absence of any modifier species, the Si phase precipitates on

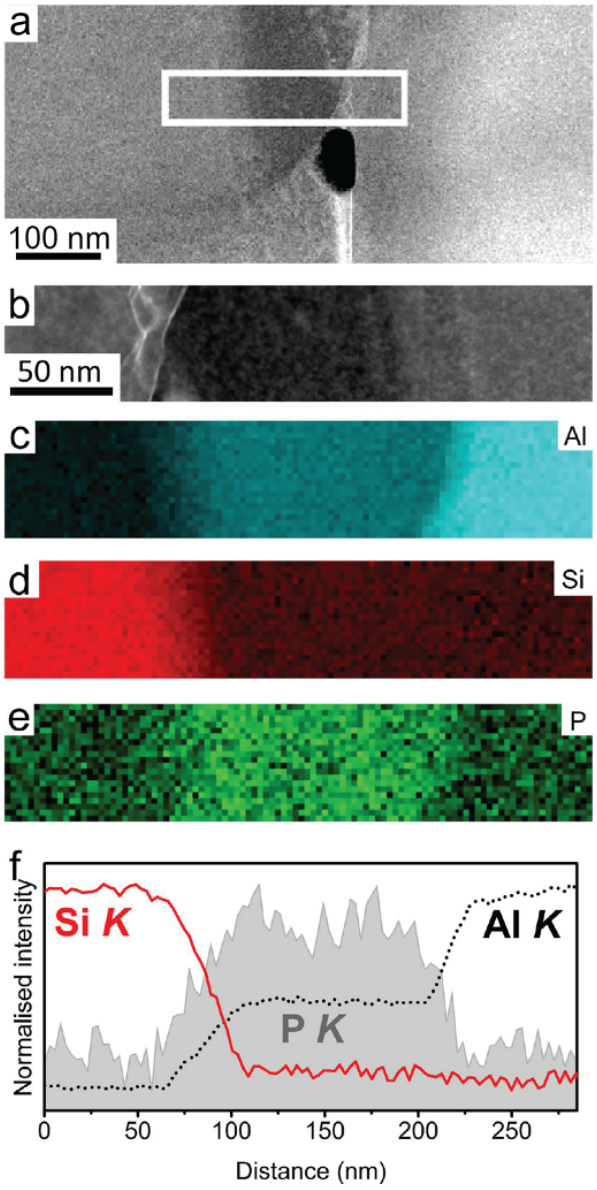

Figure 4.3: Structural features of P-modified Al-Si alloys.(a,b) High-resolution HAADF STEM images; corresponding EELS maps of (c) Al, (d) Si, and (e) P; and (f) line scanning analysis of Al, Si, and P in an Al–18Si–0.03P mater alloy. The AlP particle was observed at the interface between Al and Si. Figure from ref. [125].

these crumpled bifilms (decorated with the AlP particles). The planar growth of the Si phase straightens the bifilms, thereby creating cracks along the long axis of the Si particles. That is, the Si particles reflect the length of the straightened-out bifilms. From the preceding analysis, Sr deactivates the AlP nucleation sites and hence also the oxide bifilm as a growth substrate for Si. In modified alloys, then, the bifilms are no longer sequestered into Si particles and are now in free suspension in the liquid. To accommodate the solidification shrinkage upon freezing, the bifilm opens and a shrinkage cavity (pore) is initiated. This mechanism of porosity development in modified alloys is predicted by the fact that the oxide bifilm is a double film, unbonded between its two halves [98].

Through phase-field (PF) simulation linked to CALPHAD databases, Eiken *et al.* showed that critical threshold amounts of P and Sr are needed for the pre-silicon formation of AlP and Al_2Si_2Sr, respectively [121]. The threshold for P was found to be between 3.2 and 3.8 ppm, where the lower-bound was obtained from PF simulations due to the additional consideration of nucleation undercooling. Thus, the minimum P level to form AlP is indeed well below the commercial purity standards of Al–Si alloys. Meanwhile, thermodynamic calculations revealed a critical Sr threshold of approximately 80 ppm to form Al_2Si_2Sr. In corresponding PF simulations with subcritical Sr levels [Fig. 4.4(a)], AlP was not neutralized by Al_2Si_2Sr, and thus eutectic Si nucleated with high frequency on AlP with minimal undercooling [121]. The solidification pathway for supercritical Sr levels [Fig. 4.4(b)] is notably different: Al_2Si_2Sr poisons the AlP particles, which results in a retarded nucleation of eutectic Si. Moreover, the nucleation frequency was found to be significantly less (*e.g.*, one

nuclei in the modified alloy versus four per unit volume in the unmodified alloy, see Fig. 4.4) [121]. The refinement and structural modification of the eutectic Si lamellae result from this reduced nucleation rate and will be dealt with below.

It should be mentioned that the details surrounding the influence of the modifier species on the nucleation rate are not universally agreed upon. According to Liao and coworkers, the decrease of nucleation temperature in modified alloys only suggests that the required nucleation undercooling is increased [127]. In other words, the addition of the Sr modifier species makes the nucleation process more difficult at higher temperatures. Liao and coworkers comment that the driving force for nucleation increases with the Sr content, and in addition, "other nucleation sites are activated, although they do not have the power to operate at higher temperatures" [127]. Consequently, the higher driving force and the operation of these nucleation sites actually leads to an increased rate of nucleation of the modified eutectic. Thus, the number of nuclei per unit volume per unit time increases with respect to the unmodified alloy. Support for this alternative viewpoint comes from micrographs showing eutectic grain refinement in Al–Si alloys containing Sr and B [127]. Furthermore, not all modifier elements impact the nucleation rate in the same way: For instance, StJohn and coworkers demonstrated that Cu and Mg increased the nucleation density of Al–Si eutectic grains in unmodified and Sr-modified alloys, whereas Fe decreased the nucleation density in the same master alloys [103].

What is the influence of the modified nucleation density (either positive or negative) on the resultant Si morphology? In the early 1980s, Flood and Hunt provided one of the pioneering attempts to answer this question [128]. They reasoned that for

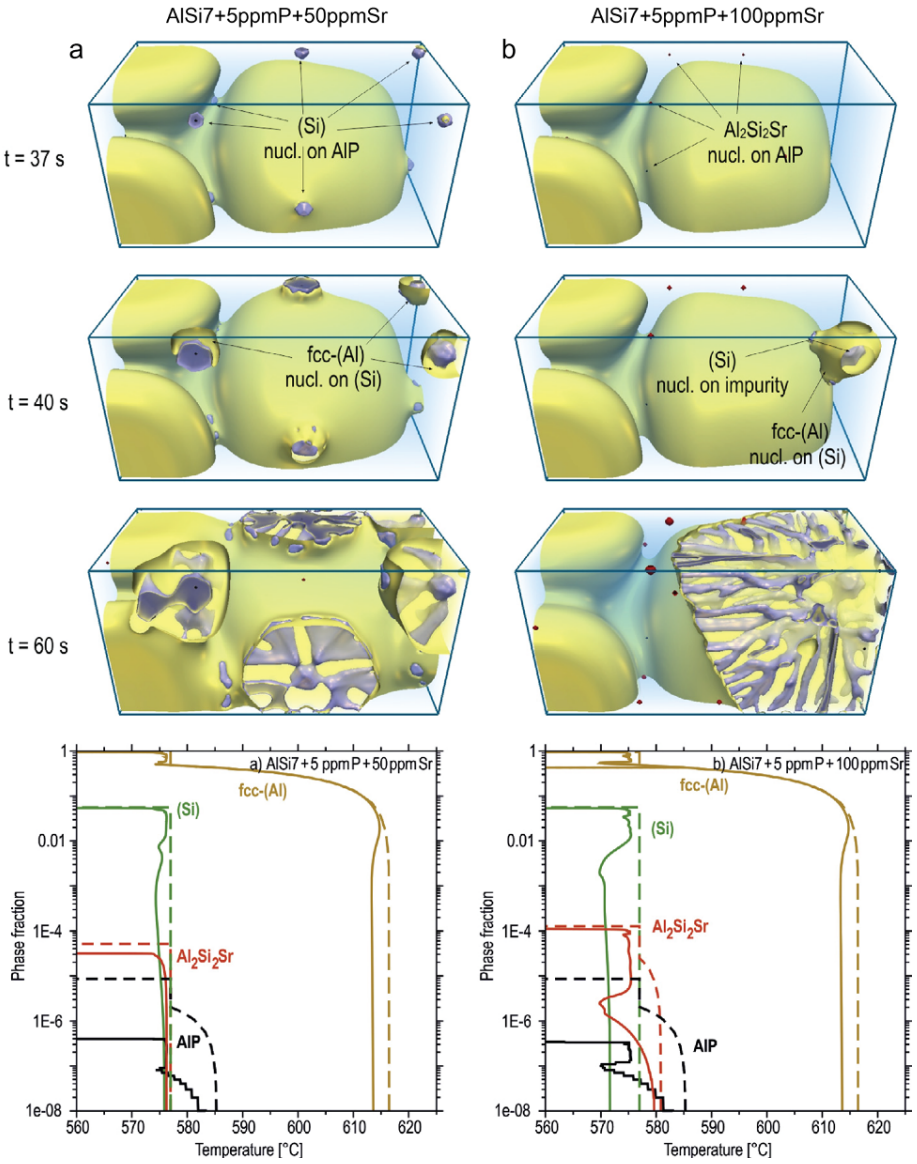

Figure 4.4: Phase field simulation results for solidification in AlSi7 + 5 ppm P with two different Sr contents. (a, left column) 50 ppm Sr, and (b, right column) 100 ppm Sr. The first three rows show different time-steps during the microstructural evolution. In (a), eutectic Si nucleated on AlP and grew as plates while in (b) Al_2Si_2Sr first nucleated on AlP, deactivating the nucleation sites of Si. The latter forms at higher growth undercooling in a fibrous morphology. The bottom row shows the phase fractions versus temperature, evaluated from PF (solid lines), and Scheil prediction (dashed lines) for both alloy compositions. Figures adapted from ref. [121].

a given rate of heat extraction, the factor controlling the growth velocity of the eutectic is the solid–liquid interfacial area, which is directly controlled by the nucleation frequency. For a constant rate of heat extraction , the growth velocity v will vary inversely with the total solid–liquid surface area A of the system. That is, , where L f is the latent heat of fusion per unit volume. Therefore, the more eutectic grains that nucleate, the larger the interfacial area A and the lower the growth velocity v [128]. In the context of Fig. 4.4, then, this analysis indicates that growth velocities are higher in the Sr-modified alloy. Additionally, due to kinetic roughening [129], Si tends to be non-faceted at these higher velocities. Flood and Hunt proposed that the morphological transition from plate-like to fibrous Si occurs at the same time as the transition from faceted to non-faceted growth [128]. However, Dahle and coworkers argued that the increase in velocity in the Sr-modified alloy is not large enough to induce the flake–fiber transition in Si [122].

An alternative explanation has been put forth by StJohn and coworkers to explain the influence of nucleation density on the Si morphology in chemically modified alloys [103]. During the growth of a eutectic grain, the modifier species is rejected by both eutectic phases into the melt and gradually piles up ahead of the solid–liquid interface. This solute segregation results in the formation of a constitutionally undercooled zone. The constitutional driving force for growth is related to the solute concentration gradient ahead of the interface,

$$\frac{dC_l}{dz}$$

, where C_l is the liquid concentration and z is the distance [59]. Such constitutional

effects in modified alloys can be better understood by considering Fig. 4.5: As two solid eutectic grains grow toward each other, their solute fields overlap and thus the constitutional driving force for growth decreases. After the driving force begins to decrease, the velocity decreases to a value where the Si morphology changes from fibrous to flake-like. This occurs at a point referred to as the "critical overlap" (see Fig. 4.5) [103]. Thus, a decrease in the spacing of nuclei (due to a high nucleation rate) causes the solute fields to overlap sooner. In this case, a higher proportion of eutectic grains grow with a fibrous morphology [103].

4.3.2 Modification During Growth

The second school of thought contends that the modifier species influences growth and not nucleation of the eutectic phases. Among the various "modified growth" theories that have been proposed from the 1960s and onwards, the three that have gained the most traction are (i) the twin plane re-entrant edge (TPRE) mechanism [130, 131], (ii) the poisoning of the TPRE mechanism [132], and (iii) impurity-induced twinning (IIT) [96]. These three mechanisms are thought to be valid under different growth conditions. For instance, at slow cooling rates in unmodified alloys, the TPRE mechanism becomes activated and the Si lamellae assume a plate-like morphology with closely spaced twins aligned parallel to the longer axis. Detailed reviews of TPRE and its variants can be found elsewhere [133, 134], but the key idea is that the growth of new layers of the crystal occurs preferentially at the re-entrant edges, *i.e.*, where the twin boundary intersects the solid–liquid interface. The first account of TPRE was described in faceted Ge dendrites by Wagner and

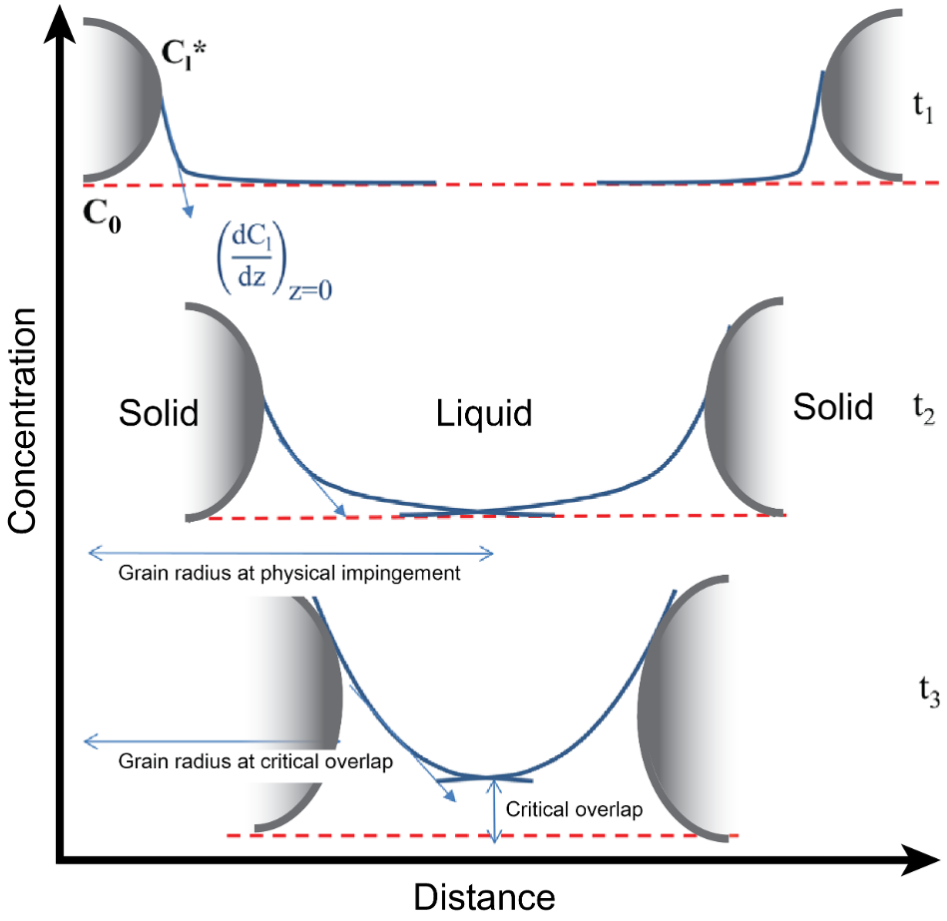

Figure 4.5: Schematic illustration showing changes in the concentration gradient (and hence the constitutional supercooling) as two solid eutectic grains impinge on one another during solidification. $C_1^\star$ is the equilibrium liquid concentration at the interface ($\star$), C_0 is the far-field liquid concentration, z is the distance, and t is the time. At time-step t_1, the diffusion fields of the solids do not overlap. Eventually, the diffusion fields overlap, see time-step t_2. Finally, at time-step t_3, solute accumulation in the overlap region attains a critical value at which the growth velocity decreases to trigger the morphological change to flake-like Si. Figure adapted from ref. [103].

Hamilton and Seidensticker in 1960 [130, 131]. It is worth mentioning that TPRE also occurs in chemically modified alloys, although the twins are no longer parallel to the long axis: According to Shamsuzzoha and Hogan's viewpoint [Fig. 4.6(a)], the twins marked AB in the bottom left give rise to branches in the form of twins BC [135]. Further branching produces AB twins on the surface marked C. This process of multiple twinning perpetuates and generates the entire Si fiber, which grows in a net [001] direction [135]. Based on the observations of Wagner and Hamilton and Seidensticker, as well as the concept of surface adsorption, Day and Hellawell advanced the poisoning of the TPRE mechanism in 1968 [132]. It was assumed that the modifier retards Si growth by adsorbing at the re-entrant edges, thereby deactivating the TPRE mechanism and forcing the Si to grow in a more isotropic manner. Finally, in 1987, Li and Hellawell proposed that the modifier atoms are adsorbed on the {111} step-surfaces of Si, and the associated change in the stacking sequence facilitates the formation of frequent crystallographic twins, a process they termed IIT [96]. The IIT mechanism makes two key assumptions: (i) the faceted phase has an FCC crystal structure; and (ii) only modifier elements that meet the 'ideal' atomic radius ratio $\frac{r_i}{r} \approx 1.646$ enable twin formation. Here, r_i is the atomic radius of the modifier element and r is that of the faceted phase. The arguments made by Lu and Hellawell to reach this conclusion were purely geometric. Yet some elements that do not satisfy this criterion (*e.g.*, Sr and Na) still modify the eutectic Si microstructure to a significant extent by increasing the twin density (see Fig. 4.2). Thus, there are likely other factors beyond atomic radius that are critical for modified growth. Taken altogether, both poisoning of TPRE and IIT involve modifier adsorption on

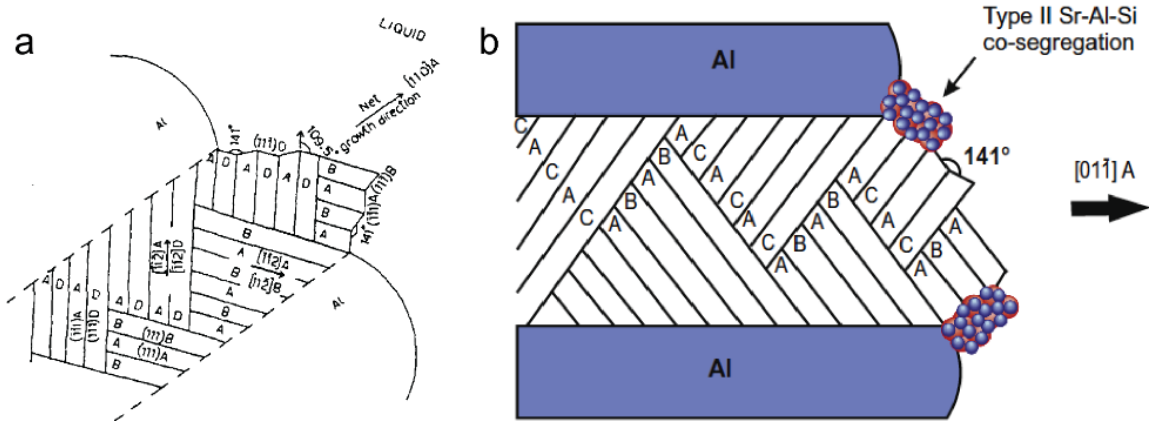

Figure 4.6: Schematic representation of (011) plane projection of Sr-modified eutectic Si phase. (a) Schematic of a fully modified Si fiber with an effective [110] growth axis in the Al–14% Si–0.18% Sr alloy. The fiber contains intersecting twins with re-entrant edges in contact with the liquid phase. (b) These edges are "poisoned" by Sr–Al–Si (type-II) co-segregations that prevent the attachment of Si to the growing fiber. (a) Figure from ref. [135] and (b) with from ref. [61].

Si at the growth front; however, the two mechanisms differ in two important aspects: (a) the location of interfacial poisoning (*i.e.*, re-entrant grooves versus facet planes), as well as (b) the consequence of it (twin suppression versus twin formation).

Recently, Schumacher and colleagues have found direct experimental support for the poisoning of TPRE and the IIT mechanisms through high-resolution high angle annular dark field (HAADF) scanning transmission electron microscopy (STEM) [136]. Their results on the diverse roles of trace Eu additions on the growth of eutectic Si in Al–Si alloys are summarized in Fig. 4.7. In some cases (see top row), Eu atoms are located approximately between every two Si atomic columns at the TPRE. These images point to the poisoning of the TPRE mechanism. DFT calculations performed by the same team show that structures with mixed Eu–Si occupation at the twin boundary, akin to Fig. 4.7(a), are energetically preferred (*i.e.*,

they possess a more negative segregation energy compared to other configurations) [136]. On the other hand, Eu atoms can also be located at the intersection of Si facets and twins (see middle row), thereby suggesting that the IIT mechanism is also operative. Finally, Schumacher and colleagues observed the entrainment of continuous layers of Eu within Si (bottom row). The authors propose that during solidification of eutectic Si, Al and Eu will segregate ahead of the growth front (the partition coefficients $k_{Al} < 1$ and $k_{Eu} < 1$); during continued growth, the {111} planes of Si fold on each other, resulting in solute impingement and entrainment of the segregation fields [136, 137]. No significant twinning was observed in the Si phase adjacent to the entrained Eu layer, indicating that this layer did not result from either the poisoning of TPRE nor the IIT mechanisms.

The poisoning of the TPRE mechanism has also been used recently to explain the EBSD results of Liu *et al.* on a Sr-modified Al–Si alloy [138]. The authors suggested that modification *via* poisoning can occur in two distinct ways: Sr can block the Si growth on one initial {111} twin plane and force the formation of (i) new twins with the same misorientation and inclination as the first, or (ii) new twins with different orientations and inclinations. The latter scenario leads to a change in the growth direction, resulting in a more isotropic growth and thus the appearance of "quasi-equiaxed" Si crystals [138]. The authors suppose that due to this Sr-induced deceleration of the Si crystal in the original growth direction, the growth velocities of both eutectic phases become comparable, *i.e.*, Si no longer leads at the growth front. However, this conclusion is impossible to verify through *ex situ* experimental probes like EBSD. To conclusively determine the structure of the solid–liquid interfaces, one

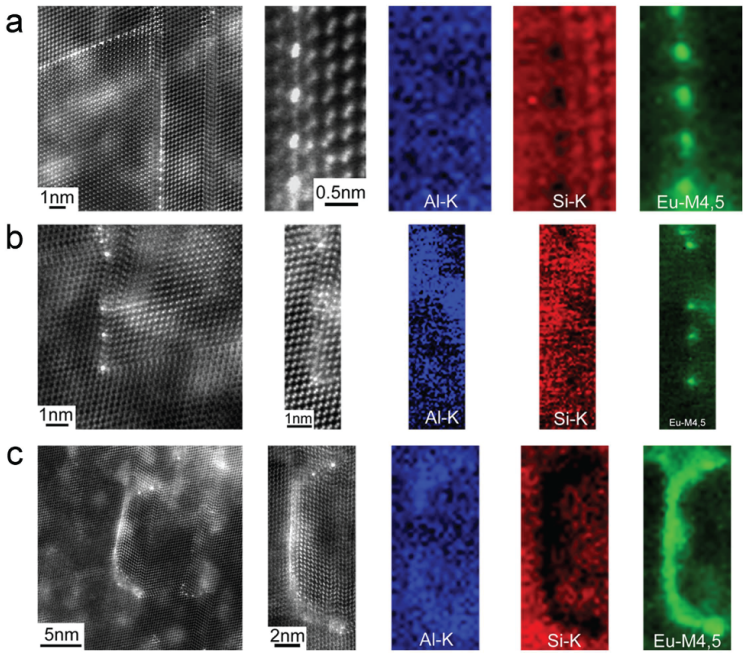

Figure 4.7: Diverse roles of trace Eu additions on the growth of eutectic Si in Al–Si alloys. High-resolution HAADF STEM images and EELS maps of Al, Si, and Eu in an Al–5Si–0.05Eu alloy: (a) Eu atoms are located at the TPRE, indicating that poisoning of the TPRE mechanism is active; (b) Eu-rich atomic columns are located at the intersection of Si facets and twins, indicating that the IIT mechanism is active; (c) Eu atoms are located in a continuous Eu-rich layer, indicating that a solute entrainment occurs within eutectic Si. See text for descriptions of each mechanism. Figure from ref. [136].

would require nondestructive and 3D imaging of eutectic solidification as it proceeds in real-time. To meet this need, Moniri and coworkers have illustrated through *in situ* X-ray tomography that the retardation is indeed more dramatic than predicted by Liu *et al.* The growth velocities are not comparable; instead, it is the eutectic Al phase that leads at the growth front, such that steady-state coupled growth between the eutectic phases can no longer be maintained [30].

Growth modification may be due to not only single modifier atoms but also intermetallic compounds that pre-exist in the liquid phase, as first suggested by Banhart and coworkers in 2012 [61]. Their atom probe tomography (APT) investigation revealed that the Sr modifier co-segregates with Al and Si within the eutectic Si phase, as well as at the eutectic Si/Al interface (Fig. 4.8) [61]. Interestingly, the chemical compositions of the co-segregations derived from the APT proximograms [see, *e.g.*, Fig. 4.8(c)] correspond to Al_4Si_33Sr and Al_2Si_88Sr, and not Al_2Si_2Sr as seen in previous investigations. Nevertheless, both of these former compounds have negative Gibbs free energies of formation at the Al–Si equilibrium eutectic temperature of 577 °C, suggesting that their existence at this temperature is thermodynamically plausible. Such co-segregations interact with the eutectic phases in two distinct ways: (i) By adsorbing at the Si {111} growth steps and promoting a change of stacking sequence of the propagating Si phase; and (ii) by adsorbing along the re-entrant edges and hence preventing a further attachment of Si atoms to the growing crystal [61]. The first possibility represents a revision of the IIT mechanism, where it is not Lu and Hellawell's geometrical size factor that plays a major role in modification but rather the chemistry of the co-segregate [61]. Meanwhile, the latter

scenario is a generalization of the poisoning of the TPRE mechanism and is depicted schematically in Fig. 4.6(b). Synchrotron-based X-ray nano-diffraction and X-ray fluorescence (XRF) elemental mapping have also been used to confirm the presence of intermetallic Sr phases in Sr-modified Al–Si alloys [139]. According to Schumacher and coworkers, such nanoscale co-segregates (clusters) are likely sub-critical nuclei, and the local ordering of the melt would be that of fluctuating clusters [140]. Stable clusters would require heterogeneous substrates or high undercooling. Thus, during solidification of eutectic Si, two processes are dominant, that of (a) segregation of Sr and Al out of Si, and (b) heterogeneous nucleation of Sr–Al–Si clusters at the propagating Si growth front [140]. By contrast, one may view clusters only as an artefact of solute entrainment (described above), and not a leading cause of eutectic modification. Proponents of this viewpoint contend that elements such as Ca and Yb are commonly found in Al_2Si_2Ca and Al_2Si_2Yb phases, respectively, yet these elements do not necessarily modify the eutectic Si morphology [137]. Whether it is single modifier atoms or modifier-containing clusters that induce the multiplication of crystallographic defects remains to be determined. However, both cases have in common the interaction between the modifier and eutectic Si during the growth process.

4.3.3 Modification During Subsequent Annealing

The last and most recent school of thought takes the view that eutectic modification occurs in the solid-state, *i.e.*, following nucleation and growth and upon annealing of the fully solidified specimen [141]. This is the principal assessment of Kothleitner and

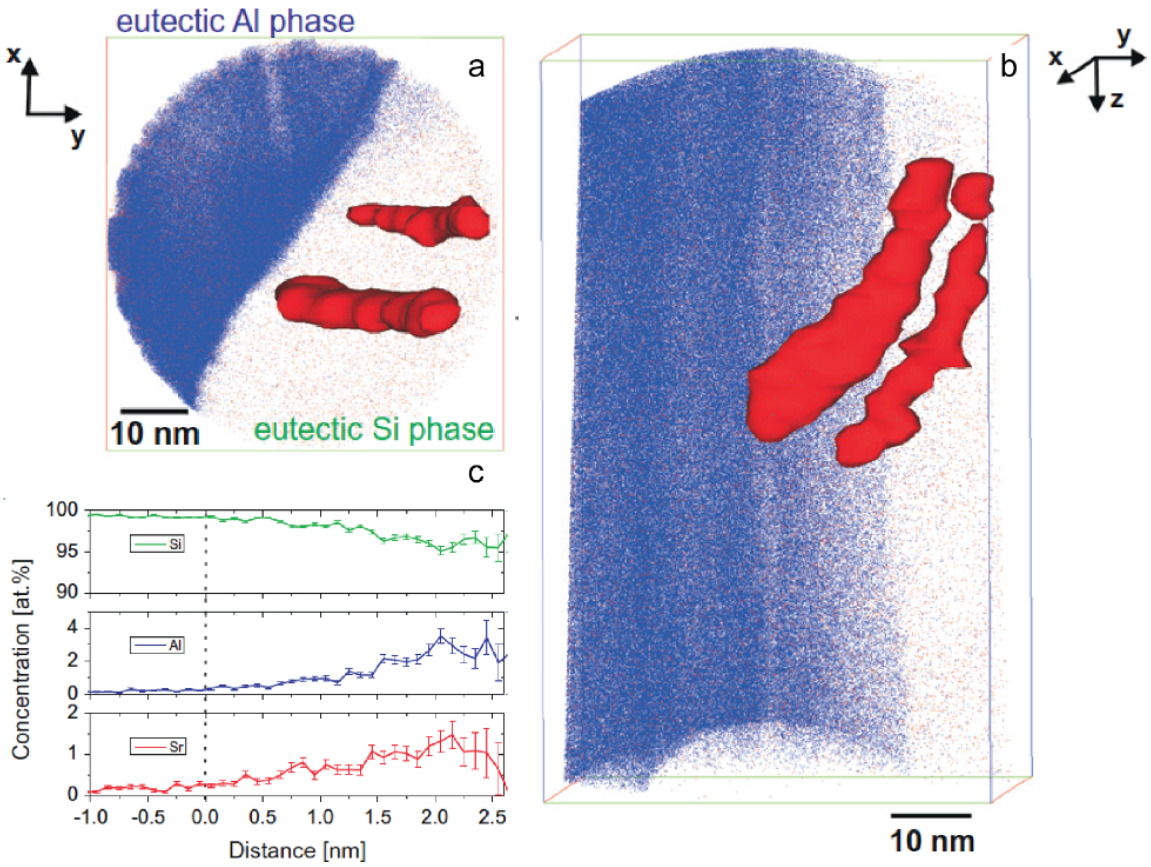

Figure 4.8: APT results of the eutectic Al/Si interface in an Al–10 wt% Si–0.1 wt% Fe alloy modified by 200 ppm Sr. (a) Top and (b) side views of 3D reconstruction of Sr (red) and Al (blue) atom positions in analyzed region-of-interest (ROI) of size 58 x 56 x 93 nm^3. Si atoms have been omitted for clarity. The rendered isosurfaces represent 0.17 Sr atoms nm^{-1} in both views. (c) Proximogram showing Sr, Al, and Si concentration as a function of distance to the Si/Sr-Al-Si co-segregation interface. Figures from ref. [61].

coworkers, whose work is procedurally very similar to that of Schumacher *et al.*: The team used STEM together with DFT simulations to lend support to their theory of solid-state modification. Through STEM of a Sr-modified hypoeutectic Al–Si alloy, they observed that $< 110 >$ interstitial Sr columns are located preferentially at the re-entrant groove of the twin boundaries [141]. Unlike the poisoning of the TPRE mechanism described above, however, Sr could not be detected along the twin defect in the growth direction.

Kothleitner and coworkers also performed *ab initio* DFT simulations to understand why Sr self-organizes into $< 110 >$ interstitial columns and whether this configuration of Sr at the twin boundaries is energetically favorable. Fig. 4.9 shows the variation in the system energy with distance between Sr atoms in the same column when aligned in several different crystallographic directions [141]. Both substitutional and interstitial Sr were considered. From these data, the team deduced that a binding energy between Sr atoms exists only when the column is aligned in the $< 110 >$ direction. If Sr is substitutional, the strongest binding is in the second nearest-neighbor position; and if Sr is interstitial, the strongest binding occurs in the nearest-neighbor position and hence interstitial Sr columns are composed entirely of Sr [141]. This result corroborates their STEM findings mentioned above. The team also compared the system energies of (i) a Si lattice with two successive twins, (ii) the same structure with two $< 110 >$ interstitial Sr columns located at the twin boundaries, and (iii) a perfect Si lattice without the twins but with the same Sr columns as in (ii). Out of the three cases, the energetic cost of (ii)—introducing a twin boundary and a Sr column located on it—was the lowest. This indicates

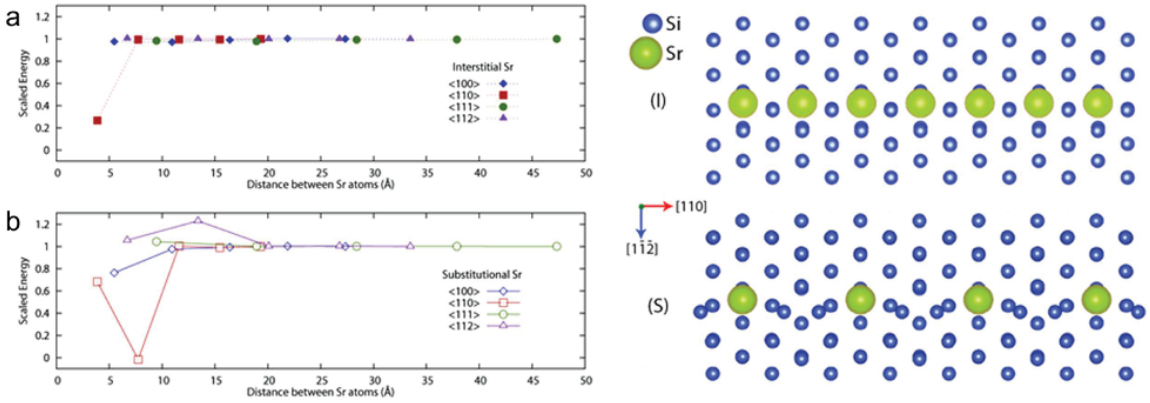

Figure 4.9: Variation of the system energy with distance between Sr atoms in the directions indicated in the legend. The vertical axis represents the excess energy above the pure Si lattice energy. This excess energy is scaled by the long-distance limit for each of the defects, which is 2.296 ± 0.072 eV for ((a), top row) the interstitial case and $1.203 \pm 0.100eV$ for ((b), bottom row) the substitutional case. Error bounds result from different k-point grids. The atomic configurations at right show the lowest energy states for interstitial (I) and substitutional (S) $<$ 110 $>$ Sr columns. Figure from ref. [141].

that it is thermodynamically favorable for Sr to diffuse to a twin boundary, once the twin has already formed (presumably during solidification, *i.e.*, a growth twin) and the Sr is located away from it. Conversely, the formation of a twin starting exactly from a Sr column is also thermodynamically favorable [141]. Despite the elegance of their DFT results, assessing whether such columns are kinetically likely to occur within eutectic Si requires further analysis of nucleation barriers, solid-state diffusion mechanisms, *etc.*

4.4 Challenges and Opportunities

4.4.1 Outlook for Experimental Studies

External probes such as photons or electrons can be used to interact with matter in the eV and meV energy ranges, respectively, to gain insights that allow for characterizing and identifying materials. The proliferation of advanced characterization tools in recent years for *ex situ* nanoscale investigations of quenched modified eutectics has revealed some limitations of the classical models of modification and shed new light on the role of various modifier agents [137, 61, 141]. Of relevance is electron energy loss spectroscopy (EELS), which provides the electronic fingerprint of the different constituents of a material and hence can provide atomically resolved mapping of the local composition within a sample [142]. For instance, in Eu-modified Al–Si alloys, Schumacher and coworkers observed nanoscale Al_2Si_2Eu intermetallic clusters or continuous Eu-rich layers located ahead of the Si twins *via* EELS (see above in Section 4.3.2) [136]. The authors also complemented the EELS maps with high-resolution STEM images that display the spatial distribution of Eu atoms in relation to the atomic columns of Si. Altogether, their results support the simultaneous occurrence of the IIT as well as poisoning of the TPRE growth mechanisms.

Given the typical concentrations ($< 100 - 1000$ ppm) of modifying agents used in Al–Si alloys [99], the success of analytical methods to investigate the local spatial distribution of the modifying agent relies on some key factors: (i) the chemical identity (atomic number) of the modifier, (ii) the susceptibility of the modifier to electron-beam irradiation, and (iii) the resolution limit of the analytical method to

be used (spatial and, if applicable, energy resolutions). Of significance among these factors is the chemical identity of the modifying agent. While Sr has been found to be amenable to a suite of analytical methods such as imaging (direct observation) *via* STEM [137, 61, 143], elemental analysis *via* X-ray energy dispersive spectroscopy (EDS) [61], and EELS in STEM (STEM-EDS, STEM-EELS), as well as XRF microscopy [144], the detection of trace amounts of Na—first used by Pacz in 1921 and still among the most common modifier species—remains an experimental bottleneck. We note that of the two modifiers, Na is more potent as it produces more uniform fibrous structure at lower concentrations (typically 0.005-0.01%); meanwhile, Sr modification requires somewhat higher concentrations (0.01-0.02%) [145]. Considering only the influence of the modifier species on growth (see Section 4.3.2 above), this behavior is to be predicted by the IIT mechanism. In other words, Na is predicted to produce more growth twins in Si as compared to Sr [96]. Only recently was the distribution of Na atoms within eutectic Si in Al–Si observed by laser-assisted APT [146]. Other considerations for electron microscopy-based techniques include the possible knock-on damage in light elements (*e.g.*, Na) as well as susceptibility to electron-beam irradiation. Another way forward is *in situ* TEM studies of Al–Si alloys [147, 148], providing an alternative method to perform future solidification experiments with high chemical and spatial resolutions. Continuing advances in the design of analytical tools for high-resolution characterization of materials containing light elements as well as those prone to beam irradiation will aid further analysis of the atomic distribution of Na in future studies. Of note are recently developed STEM designs [149] with enhanced annular bright field, a new imaging technique

that facilitates the observation of light elements in part by their ability to operate at accelerating voltages as low as 30 kV.

4.4.2 Outlook for Computational Studies

According to the adsorption-and-entrapment model for modified growth discussed in Section 4.3.2, the solutal entrapment likely forms an aggregation of Al–Si–X within, as well as in the vicinity of, the eutectic Si phase. Assuming that the chemical composition of these Al–Si–X clusters can be determined using analytical methods, it would in principle be possible to also derive an estimate of the free energy of formation for these intermetallic compounds at the eutectic equilibrium temperature to rationalize their thermodynamic stability, as in Ref. [61]. A plausible means to accomplish this task is to use the CALPHAD method, which provides a realistic thermodynamic assessment of alloys based on all available information on the phase equilibria and thermochemical properties of a given system. However, the free energy curves might only be defined over a finite range of composition that may not necessarily coincide with those investigated in solidification studies. Therefore, a problem arises in cases where the free energies of the phases become undefined or discontinuous. We note that, in the phase field community, methods have been recently reported that eliminate such characteristics while largely retaining the free energy values [150].

Hecht *et al.* have reviewed the advances in phase field modeling of multiphase solidification [151]. Other reviews [23, 152] and research articles [153, 154], as well as references therein, provide additional examples of how PF modeling and other theoretical methods can be used to understand the physical mechanisms controlling

the microstructural development. However, in a phase field simulation, the interface is diffuse and thus the incorporation of interfacial energy anisotropy requires careful consideration. Such is the case for the eutectic Si constituent considered here, which forms sharp facets with a discrete set of orientations (below its roughening transition). When the anisotropic interfacial energy is sufficiently strong, the unregularized Cahn–Hilliard equations become ill-posed. To remove the ill-posedness, a number of regularization strategies have been introduced, see, *e.g.*, Refs. [155, 156].

4.5 Summary

Since Pacz' discovery of eutectic modification in 1921, several elements have been reported to induce varying degrees of modification (*e.g.*, refinement, morphological change, and twinning; see Section 4.2). Much of this research has been, and continues to be, motivated from both a scientific interest—establishing direct links between microscopic building blocks and macroscopic performance limits—and technological relevance—developing aluminum-based alloys for engineering applications.

Our current understanding of the process of eutectic modification by (metallic) species is largely based on the physical models developed from a geometric point of view (*e.g.*, impurity-induced-twinning; see Section 4.3.2). In these conventional pictures, the modifying agents of "optimum" radius (relative to the Si matrix) force a monolayer step to miss one regular close packed position, thereby altering the stacking sequence and creating or suppressing coherent $\Sigma 3$ twin defects. While the above-discussed conventional mechanisms have, to a large extent, guided the field,

recent reports on partially and fully-solidified specimens have provided great insights into the structure and crystallography of chemically modified degenerate eutectics. Furthermore, the rich variety of growth forms that are experimentally observed calls into question our conventional wisdom surrounding eutectic modification.

The emerging synchrotron X-ray imaging methods, which enable spatially and temporally resolved investigation of structural materials under relevant growth conditions, have displayed the capability to offer unprecedented insights into the growth forms of this and other classes of materials under relevant conditions [157, 158, 159]. Key opportunities reside in integrating this and other relevant real-time imaging tools with advanced *ex situ* analytical methods (*e.g.*, EELS; see Section 4.4.1) to draw direct comparisons against the unmodified alloys to elucidate conclusively the role of modifier species. Linking the microstructural and topological evolution, as measured recently in three dimensions [30], to the crystallographic features of, as well as the local spatial distribution of the modifier atoms in, fully solidified samples can help move us closer to a unifying theory of chemical modification of degenerate eutectics.

Such insights can be readily extended to a vast array of other materials systems in which elemental modifiers play a critical role. An example is the additive manufacturing of technologically useful classes of alloys. It was recently demonstrated [11] that chemical modification of the feedstock alloy with grain refining nanoparticles for additive manufacturing can achieve previously incompatible high-strength aluminum alloys that are crack-free, equiaxed, and fine-grained. It is reasonable to assume that chemical modification by trace metal additions—a lesson from casting—can vastly

expand the range of compatible metallic materials for future development of additively manufactured alloys, representing landscape-changing advances across multiple sectors such as aerospace, automotive, and biomedical.

Chapter 5

Topological Transitions of Eutectic Microstructures Upon Chemical Modification

This chapter is based on the article published in *Scientific Reports* [30].

5.1 Introduction

Impurities, whether intentionally introduced to modify a product or unavoidably present in the growth medium, have been shown to play important roles during all stages of solidification in areas as diverse as pharmaceutical and protein crystallization [5, 6], semiconductor and polymer processing [7, 8], single crystal production [9], and process metallurgy [10] including additive manufacturing [11, 12, 13]. In the latter case, it has been demonstrated recently that chemical modification of the feed-

stock alloy by impurities can vastly expand the range of compatible metallic materials that can be processed [11], which could lead to landscape-changing advances across multiple sectors such as aerospace, automotive, and biomedical. The specificity of impurities for either inhibition, by poisoning the nucleation sites, or promotion, by lowering the barriers of nucleation, often leads to a rich variety of growth forms that are distinct from the equilibrium habit of the pure crystal.

A manufacturing process that is of both scientific interest and technological relevance is the crystallization of eutectic alloys in the presence of trace, often metallic impurities. During eutectic solidification, a parent liquid phase transforms simultaneously into two or more solid phases [40]. One important class of eutectics is the irregular eutectic, which consists of at least one faceted (*e.g.*, Si or Ge) and one non-faceted (*e.g.*, Al or Ag) phase. Due to the 'stiff' covalent bonding of the faceted phase [59], irregular eutectics possess a non-periodic arrangement of lamellae and a non-isothermal growth front. Among these are low density Al-Si alloys of eutectic composition, which are used widely in many engineering applications, such as automotive and aerospace [99]. Ever since the discovery of eutectic Si modification in Al-Si alloys by Pacz in 1921 [93] (*cf.*, Section 4.1.2) — who incorporated a small amount of NaF (as well as separate treatments with a few other alkali halides) into the alloy melt before solidification — chemical modification as a phenomenon has been widely investigated. Various modifier species (*e.g.*, Na, Sr, Eu, Ba, Ca, Y, Yb) have been reported to yield refinement, *i.e.*, a change in the length scale (smaller inter-lamellar spacing), as well as favorable changes in the eutectic morphology, typically from a coarse, plate-like network into a finer, more fibrous one

[146, 110, 160, 42, 161, 61, 136, 96, 162, 101, 112]. Such chemical modification is of technological interest as it improves the mechanical properties (*e.g.*, strength and ductility) of the as-cast alloy product [99, 96, 163].

A question of critical importance for the structure-property relationship of impurity-modified alloys is related to the microscopic origin of modification itself. In turn, a fundamental understanding of chemical modification will enable manufacturers to tune the complex microstructures to technological demands. Several models have been proposed since the 1960s and onwards to explain the mechanisms leading to refinement and morphological evolution in the impurity-modified alloys, but in more recent years the utilization of advanced characterization tools for *ex situ* nanoscale investigations has revealed some limitations of these classical models and shed new light on the role of impurities [61, 136, 141].

Broadly, the classical models fall into one of two categories: (i) modified nucleation, or (ii) modified growth. In the former perspective, Thall and Chalmers [164] proposed that the modifier species suppresses eutectic nucleation and shifts the eutectic composition toward higher Si content, relative to the unmodified Al-Si alloy. According to Crosley and Mondolfo [41], the reason for this behavior might be that the modifier species poisons the Si nucleation sites, thereby causing the observed morphological changes. Additionally, these authors suggested that there is a reversal of leading roles (Al leading Si at the growth front in the modified alloy), due to a reduction in the rate of Si diffusion in the liquid in the presence of the modifying agent as well as a change in the surface tension of liquid Al. Differences in the growth rates between Al and Si results in complete encasement of Si by Al in the modified

alloy, such that the Si phase is forced to continuously re-nucleate as films along the boundaries of eutectic colonies [41]. We note that Si re-nucleation would then imply a change in the topology (*i.e.*, connectivity) of the eutectic Si, as will be expounded in detail below. In the latter (growth) perspective, the proposed models are largely based on geometric considerations of the impurity atoms and the faceted phase. The twin plane re-entrant edge (TPRE) growth mechanism describes the growth of the faceted (Si) phase facilitated by {111} $\Sigma 3$ twins [131, 130]. According to the poisoning of the TPRE mechanism, growth of the faceted phase is more isotropic due to selective adsorption of the modifier atoms at the twin-liquid interface (*i.e.*, deactivating the advantage of the TPRE mechanism) [132]. In the impurity-induced twinning (IIT) mechanism, the modifier atoms adsorb instead at the 111 Si step surfaces, and the associated change in the stacking sequence facilitates the formation of frequent crystallographic twins and locally enables growth in multiple $< 112 >$ directions [96]. The IIT mechanism, which assumes an FCC crystal structure for the faceted phase, projects that only the elements that meet the 'ideal' atomic radius ratio $\frac{r_i}{r} \sim 1.646$ (where r_i is the atomic radius of the impurity element, and r is that of the host phase) cause modification [96]. The ideal radius ratio is calculated based on the assumption that impurity atoms of appropriate size force a monolayer step to miss one regular close packed position and alter stacking sequence [96]. While the IIT model has gained some traction in the crystal growth community, several of its shortcomings have been reported, including by the original proposers [96] and others [112, 165, 106]. We note that while quenching in the absence of modifying agents can produce fibrous, as opposed to flake-like, Si in Al-Si alloys, it does not change

the twin density of Si [101].

In the contemporary literature, for cases that chemical modification does result in increased twinning, the twinning mechanisms remain a subject of debate. In Eu-modified Al-Si alloys [136], Schumacher and colleagues observed frequent twinning within eutectic Si as well as the formation of nanoscale Al_2Si_2Eu intermetallic clusters or continuous Eu-rich layers located ahead of the Si twins. These authors' high-resolution scanning transmission electron microscopy results support the simultaneous occurrence of the IIT as well as poisoning of the TPRE growth mechanisms [136, 96, 131, 130]. Additionally, the authors attribute the formation of such impurity-containing moieties as "artifact" of the adsorption and entrapment of the modifying agent within eutectic Si during growth [136], rather than as enabler of modification as suggested previously by others [161, 61]. On the other hand, in the case of Sr-modified Al-Si alloys, Kothleitner and colleagues [141] have recently reported that prolific twinning in Si arises in the solid state, upon subsequent annealing of the as-grown eutectic microstructure. In this picture, the modifier (here Sr) atoms diffuse interstitially into the fully-solidified Si, self-organizing into ¡100¿ interstitial columns. According to these authors' work, twin boundaries subsequently originate in the vicinity of the interstitial Sr columns.

The above and many other *post mortem* studies of fully-solidified alloy samples have provided great insights into the structure and crystallography of impurity-modified irregular eutectics. However, the oft-employed 'quench-and-look' approach is inherently limited in scope and can only provide mechanistic inferences in limited situations. Quenching can distort the morphology of the solid-liquid interface com-

pared to that seen during crystallization. It is also worth noting that at the typical concentrations of impurities used for chemical modification ($\sim$ 100 ppm), analytical methods do not possess the necessary sensitivity for conclusive determination of the local spatial distribution of the modifying element. In the contemporary viewpoints surveyed above, no *in situ* reports are available to the best of our knowledge, and no comparisons are drawn against the corresponding unmodified alloys. Evidently, a unified theory of eutectic modification — that can fully describe the microstructural and topological complexities that arise during solidification — remains elusive due to the dearth of 3D space- and time-resolved information.

In the present study, we employ an integrated imaging approach in an effort to understand the role of impurities on eutectic solidification. In particular, we examine the solidification pathways of an Al-51.6 wt.%Ge eutectic with trace metal impurities (0.1 wt.% Na) and draw comparisons with the unmodified Al-Ge alloy reported recently by Shahani and coworkers [57]. We note that Ge behaves in a similar fashion to Si discussed above, *e.g.*, both materials have covalent bonding, high entropies of fusion, highly anisotropic Wulff shapes, and only modestly different self-diffusion coefficients at their respective melting points [166, 167]. By non-destructively monitoring the solidification process *in situ via* synchrotron-based X-ray microtomography (4D XRT), we tracked the evolution of directionality and topology in the eutectic constituents for the first time. To link these dynamical events to crystallographic features, we conducted electron backscatter diffraction (EBSD) experiments on the fully-solidified specimens. On the basis of our integrated characterizations, we find that the growth of the faceted phase is retarded by the trace impurities, leading

to orientational changes and topological singularities during crystallization. The resulting eutectic microstructure belongs to its own topological class, distinct from the unmodified alloy.

5.2 Results and Discussion

5.2.1 Nucleation and Growth Observations

The synchrotron experiment was guided by the equilibrium phase diagram of the unmodified Al-Ge eutectic (black solid lines in Fig. 5.1(a)), with the anticipation that chemical modification leads to higher nucleation undercooling [96, 164]. Initially the sample was heated in a resistive furnace to 440 ° – which is well above the eutectic temperature, 425 °, of Al-Ge – and allowed to equilibrate. The oxide skin layer, grown by thermal oxidation, contained the molten specimen and prohibited the diffusion of the Na out of the sample bulk. Then, the sample was cooled to 417 ° and held at this temperature for 5–10 min for homogenization. Subsequently, the sample temperature was dropped down to 416 ° and was held isothermally at this temperature while X-ray projections were recorded (see Methods). In Fig. 5.1(a), we also provide kinetic boundaries due to Na modification (red dashed lines), according to our direct experimental observations of the solidification pathway, see Fig. 5.1(b).

We observe that primary Al (in the form of equiaxed dendrites; an example marked by the arrow in Fig. 5.1(b)) forms at $\sim$ 417–418 °C and continues to grow and coarsen until a sufficiently low temperature (416 °C) is reached, at which point the

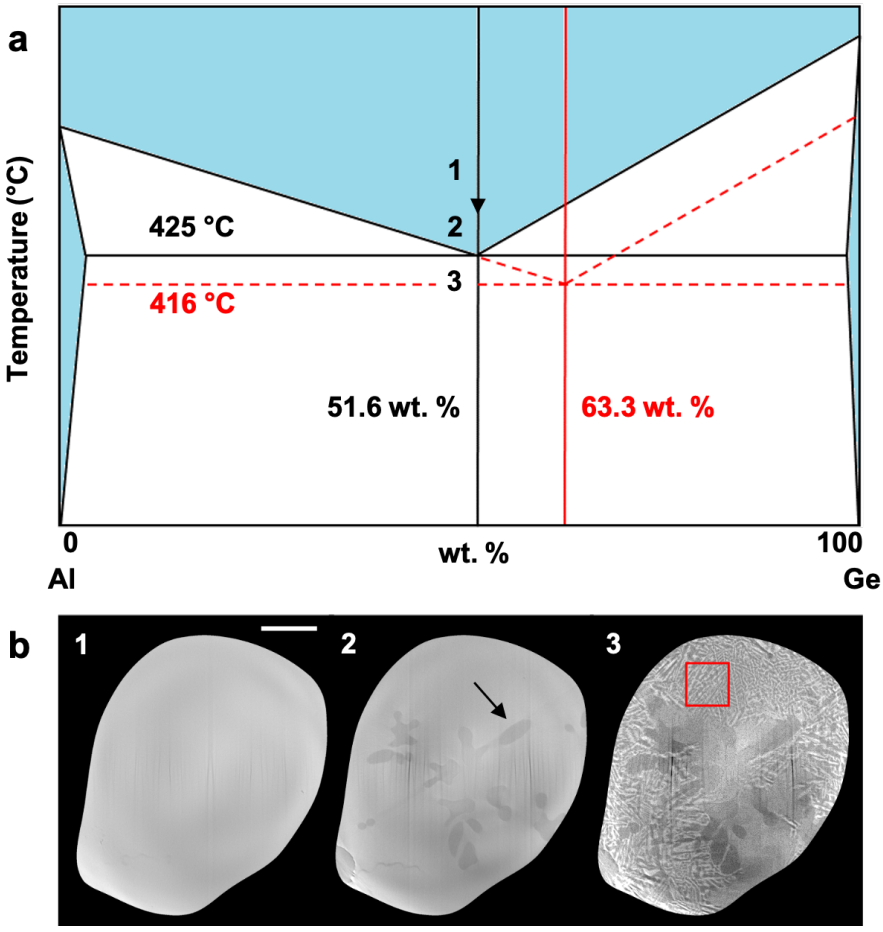

Figure 5.1: Solidification pathway. (a) The equilibrium phase diagram of the unmodified Al-Ge eutectic (black solid lines) is shown together with kinetic arrests in the modified Al-Ge-Na alloy (red dashed lines). The eutectic composition shifts to the Ge side (63.3 wt.%) in the modified alloy. (b) Representative 2D slices of the 3D reconstruction show the progression of solidification. The absorption contrast between the constituents allows distinguishing between the three coexisting phases: the liquid (light gray), eutectic Ge (white), and eutectic Al (dark gray). In panel (1) the sample is fully liquid (corresponding to region 1 in (a)). Upon cooling below the Al-Ge eutectic temperature (425 °), the sample consists of primary Al dendrites in the melt, seen as dark, bulbous features in panel (2) (corresponding to point 2 in (a); one marked by arrow as example). Through further cooling to 416 °, development of the Al-Ge eutectic microstructure is observed, as in panel (3), corresponding to point 3 in (a). The red box in panel (3) shows the region-of-interest isolated for subsequent analysis. Scale bar: 100 μm.

nucleation of eutectic Ge in the presence of the Na modifier species occurs. Given that the primary Al phase was detected first, and immediately below the Al-Ge eutectic temperature, we expect that the Al liquidus is unaffected by chemical modification (see the oblique dashed red line in Fig. 5.1(a)); a similar argument is presented in ref. [164] based on the analysis of cooling curves. Rather, our results indicate that it is exclusively the Ge liquidus which is depressed in the Na-modified alloy, in agreement with the observation of Hanna *et al.* [119]. In comparison, in the unmodified alloy, Al and Ge phases nucleate at the same temperature and subsequently grow in a loosely-coupled manner [57]. Ultimately, the critical undercooling for the nucleation of the modified eutectic is $\sim$ 9 °C, which is approximately three times higher than that of the unmodified Al-Ge eutectic [57]. Interestingly, the nucleation of the modified Al-Ge eutectic does not occur heterogeneously on the pre-existing Al dendrites, but rather on the Al_2O_3 oxide skin of the sample, in agreement with *ex situ* observations of Dahle *et al.* [42]. The sample temperature was maintained at 416 °C throughout the *in situ* XRT experiment, allowing for the Al-Ge eutectic to grow with minimal undercooling.

5.2.2 Tomographic Reconstructions

For subsequent analysis, we analyze the dynamics of eutectic crystallization within a region-of-interest (ROI) that does not contain Al dendrites. The selected ROI provides a 'good' statistical representation of the eutectic microstructure because its composition (53 wt. % Ge, assessed in the fully-solidified state) matches very closely to that of the bulk alloy (51.6 wt. % Ge). A snapshot of the ROI at 260 s after the

start of solidification is shown in Fig. 5.2.

In the 3D rendering, Ge lamellae are shown in red, and Al in yellow. The liquid phase is rendered transparent. Some Ge lamellae are observed to have highly curved solid-solid interfaces, which is anomalous for a faceted phase. As noted in Introduction, the equilibrium and kinetic shapes of semiconductor crystals tend to be fully faceted due to their strong and directional covalent bonds [166]. This curvature might arise due to the interaction of the Ge constituent with Na segregations ahead of the solidification front. To further investigate these qualitative observations, we track the growth of the eutectic region of interest in 4D. Figure 5.3 shows microstructural evolution during growth of the eutectic ROI at five representative time-steps. At each time-step, three views of the region are provided. Interestingly, and as indicated by the arrows in the side views of Fig. 5.3(c,d), the Al phase leads at the growth front, and eventually envelopes the lagging Ge phase. Because the Ge phase cannot keep pace with the Al phase, steady-state growth is not possible in the modified Al-Ge system. This morphological instability is shown to cause a marked change in the topology of the eutectic constituents, which is discussed in the next section.

5.2.3 Characterization of Topology

We quantify the connectivity of the eutectic constituents during the growth process by computing the topological characteristics of the microstructure [168]. In the present study, we examine three topological characteristics within the region of interest, across time: the number of independent bodies, *i.e.*, solid 'voids', v; the

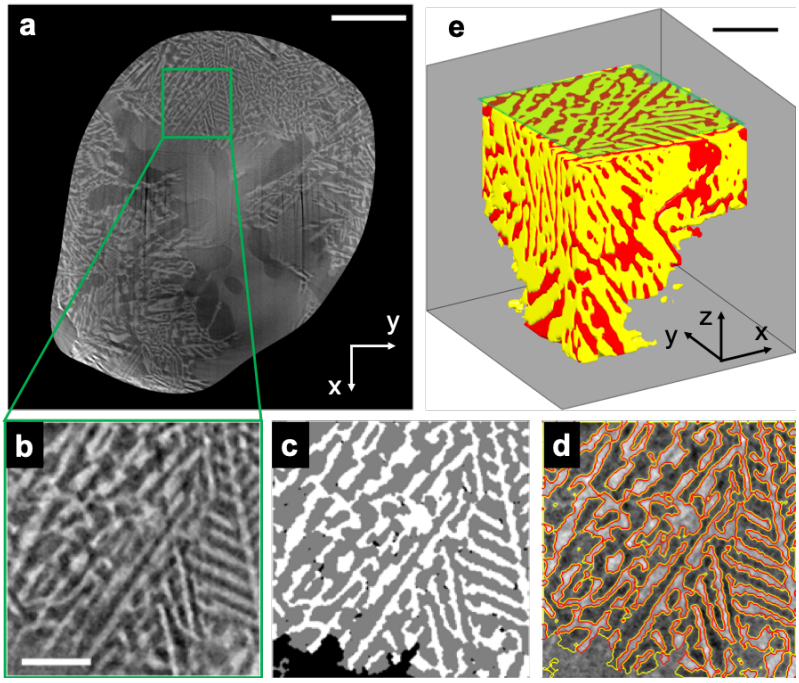

Figure 5.2: Segmentation and visualization of tomographic data. (a) A representative ("raw" grayscale, 260 s after the start of solidification) 2D slice of the 3D reconstruction serves as the input for computer vision algorithm. For subsequent analysis, a region of interest (green box) was extracted. Scale bar: 200 μm. (b) A magnified version of the region-of-interest is shown. The eutectic Ge lamellae appear as brighter features while the eutectic Al phase appears as darker gray. Scale bar: 50 μm. (c) Segmented (output) image corresponding to the same "raw" (grayscale) image in (b). The eutectic Ge phase is shown as white, and the eutectic Al is displayed gray. (d) The edges of the segmentation output are overlaid on top of the raw (grayscale) image. Edges of eutectic Ge are red, and those of eutectic Al are yellow. The segmentation result shows great agreement with the structures underneath. (e) Three-dimensional reconstruction of the region-of-interest at this particular time-step. The eutectic Ge phase is shown in red, Al in yellow. The melt is rendered transparent. The 2D slice in (a) corresponds to the top side of the 3D reconstruction in (e). Scale bar: 200 μm.

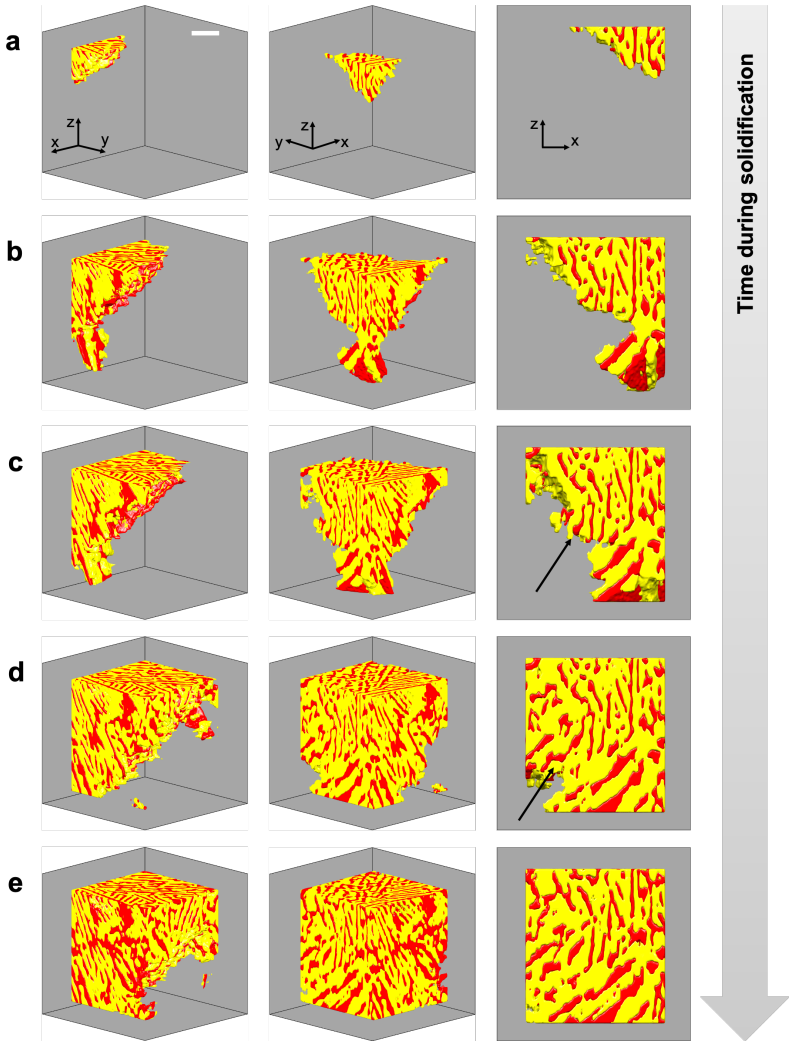

Figure 5.3: Microstructural evolution during eutectic crystallization. Three views of 3D reconstructions are shown at five representative time-steps after the start of solidification: (a) 180, (b) 220, (c) 240, (d) 280, and (e) 300 s. The Al phase is represented in yellow, and Ge is shown in red (the melt is rendered transparent). The arrows in the side views of (c,d) point to regions where the Al phase leads at the growth front, advancing deeper into the melt and eventually engulfing the lagging Ge phase. This morphological instability is shown to cause a marked change in the topology of the eutectic constituents. Scale bar: 100 μm.

genus, g; and the total number of loops, *i.e.*, handles, h [168, 169]. The genus is approximately related to the number of holes or gaps in an object: for instance, a donut or torus has a genus of one. For any object, the genus is related to the number of handles and voids according to Eq. 5.1:

$$g = h - \nu \tag{5.1}$$

It is therefore evident that, for structures with no voids, the genus and handle have the same values. More importantly, if the number of voids exceeds the number of handles, then the genus assumes a negative value, indicating that the solid bodies are disjoint. In the context of crystallization, this situation might be encountered during the early stages of nucleation, wherein the nuclei are small and far apart. During growth the nucleated solid bodies may coalesce, giving rise to continuous handles in the microstructure and a correspondingly higher value of genus (Eq. 5.1). In eutectic microstructures, the genera of the phases may depend on each other given the intertwined pathways available for growth.

To circumvent the potential ambiguity in the calculation of genus related to the parts of the microstructure that contact the bounding box (*i.e.*, any of six sides of the ROI), we obtain the upper and lower bounds of genus, g_{max} and g_{min}, respectively [168]; computational details are provided in Methods. The true value of the genus g for each phase i is then in between the g^i_{min} and g^i_{max} limits. The maximum and minimum genera of Al and Ge, scaled by the corresponding solid volume, are shown in Fig. 5.4(a). We define the reference (zero) time as the time-step during the tomographic experiment when the Ge phase is first observed (we note that this is

not the precise moment of nucleation of Ge, given the 20-second temporal resolution of the tomographic experiment, nor is it necessarily the same time-step at which eutectic Al nucleates). At the reference time, several small and disjoint solid Ge domains exist. Thus, the genus of Ge is negative (both g_{max} and g_{min}). We also observe that the Al phase attains a positive genus and already encases the Ge phase in a few locations (*cf.,*. Fig. 5.3).

In order to eliminate the effect of the increasing length-scale of the system during the growth process, we scale the volume-normalized genus by the inverse of the surface area per unit volume [169], S_V^{-3}. This scaling yields a dimensionless topological quantity $\frac{g}{S_V^{-3}}$ that is independent of both volume and length-scale differences of the growing microstructure over time. The dimensionless upper and lower bounds of genus for both Al and Ge are shown in Fig. 5.4(b). While the unscaled (but volume-normalized) genus of Ge and Al have roughly the same value in the second half of the growth process, the scaled genus of Ge is approximately an order of magnitude smaller than that of Al (a manifestation of the greater S_V^{-1} of Al compared to Ge), indicating that the eutectic Al phase engulfs the eutectic Ge phase. That is, the many holes in the Al phase (contributing to a relatively high value of $\frac{g_{Al}}{S_V^{-3}}$) are filled with independent Ge solids that are unable to grow through the solid metal layer. We note that this direct topological analysis is only possible using the 4D synchrotron data.

Full topological details of the eutectic Ge phase are shown in Fig. 5.4(c,d). Using the upper and lower bounds for genus as defined above, together with Eq. 5.1, upper and lower bounds for the number of handles were calculated. Figure 3c shows the

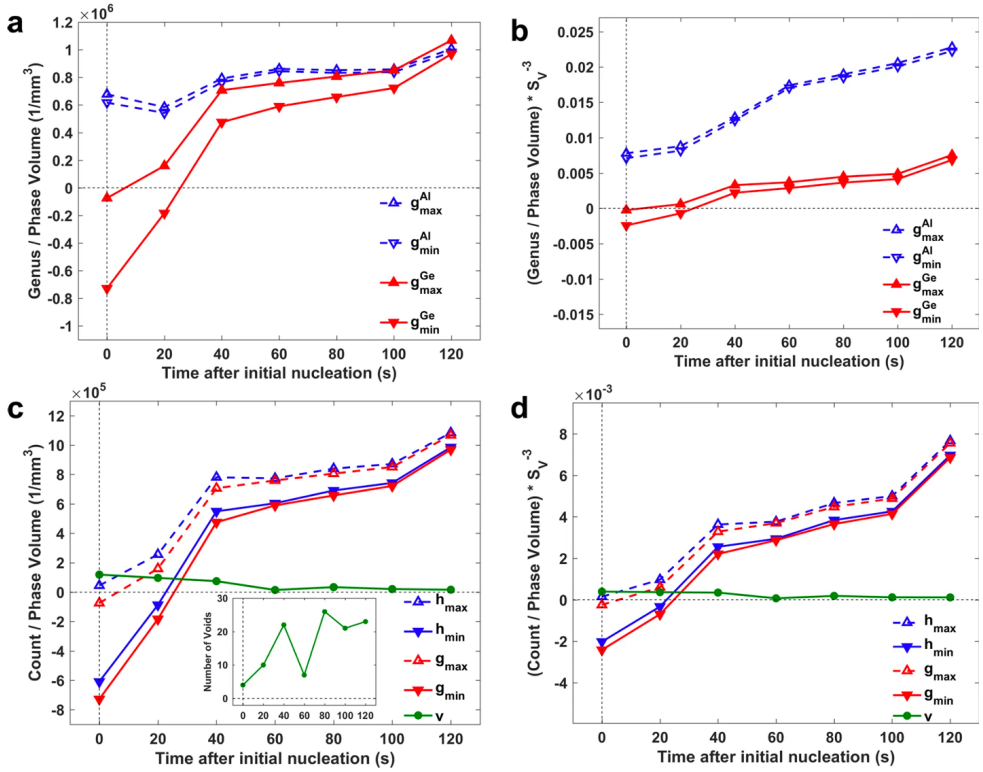

Figure 5.4: Topological distinctions between the eutectic phases. (a) The upper (upward arrows) and lower (downward) bounds of genus for the Al (open symbols) and the Ge (filled) phases are measured from the tomographic reconstructions. The genera are normalized by the corresponding solid phase volumes. The reference (zero) time as defined in the text is indicated by a dashed vertical line for clarity. At this time, the genus of Ge is negative (both g_{max} and g_{min}), while that of Al is positive. Therefore, the Al phase already encases the Ge phase. (b) The scaled (dimensionless) genera (see text) of the two eutectic constituents are displayed over time. The scaled genus of Ge is approximately an order of magnitude smaller than that of Al. (c) Volume-normalized topological characteristics of the eutectic Ge phase are shown, calculated by applying Eq. 5.1 (in the text) on the mesh representation of the Ge phase. The number of solid Ge voids (inset) does not have an appreciable contribution to the topology of the microstructure, as the genus and number of handles are roughly equal. (d) The scaled topological characteristics of the Ge phase are displayed.

evolution of the unscaled (*i.e.*, only phase volume-normalized) characteristics during the growth process, while Fig. 5.4(d) shows the scaled (*i.e.*, dimensionless) topological parameters. Clearly, the number of solid Ge voids does not have an appreciable contribution to the topology of the microstructure, as the genus and number of handles are roughly equal. However, it is interesting to observe that topological parameters are not necessarily monotone during the growth process. For instance, the number (absolute count) of solid Ge voids (shown in the inset in Fig. 5.4(c)) initially increases over time, followed by a sudden drop by $> 50\%$ and subsequently a quick rise. In order to verify that this drop and rise in the number of voids is inherent to the data and not an artifact of the image segmentation algorithm, the connected components of the Ge phase were examined. Broadly, a connected component is defined as several interconnected structures, as opposed to a single, isolated structure [170]. As shown in Fig. 5.5, immediately before the drop in the number of voids, there are several small and large Ge connected components. At the time-step at which the drop in the number of voids occurs, coalescence of those connected components is observed, justifying the decrease in the number of solid voids (fewer Ge connected components). At the following time-step, in addition to the growth of the merged connected component, several new (small) connected components (hence solid voids) are present, justifying the corresponding rise in the number of solid voids. The new Ge connected components arise due to the high undercooling (and consequently, high nucleation power) of the modified Al-Ge eutectic.

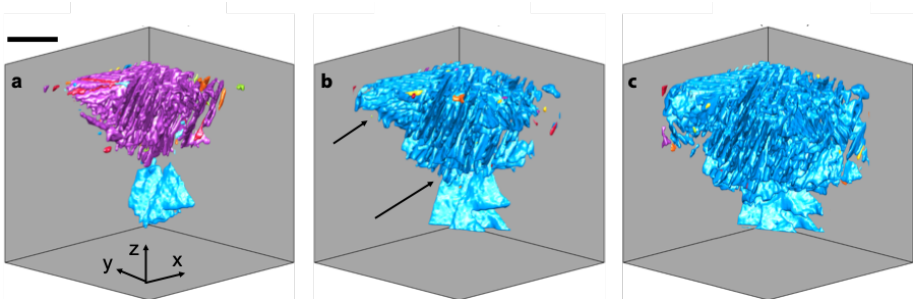

Figure 5.5: Coalescence of Ge lamellae during the growth process. (a) Several solid voids (connected components) of eutectic Ge phase are present, varying from small to large sizes. The solid voids are illuminated by different colors so that no two neighboring connected components have the same color. Scale bar: 200 μm. (b) Upon growth, the Ge lamellae coalesce, reducing the number of solid Ge voids, as observed in the inset of Fig. 5.4(c). The arrows point to coalescence events of the Ge connected components. (c) The coalesced Ge voids (connected components) grow while new, smaller solid voids appear, giving to the rise in the total number of solid Ge voids (see the inset of Fig. 5.4(c)).

5.2.4 Characterization of Directionality

Figure 5.6(a–c) shows the 3D microstructures of the Ge phase superimposed at two different time-steps (represented by red and pink colors). As described earlier, the *in situ* XRT results reveal significant curvature in the solid-solid interfaces of Ge, which is anomalous for the covalently-bonded faceted phase. Points of significant curvature and branching are shown with arrows in Fig. 5.6(b,c). The degree of directionality of the microstructure is quantified by calculating stereographic projections of the orientations (normals) of patches of interface in the microstructure. Stereographic projections collapse the three-dimensional spatial orientation of the microstructure into a two-dimensional representation that facilitates the detection of any preferential directionality in the microstructure. Upon scaling the stereographic projections with the interfacial patch area, the probability of locating an interfacial patch with a

particular spatial orientation is represented. We note that this so-called interface normal distribution (IND) is constructed in the reference (*i.e.*, laboratory) frame, not the crystallographic frame. Thus, due to the many independent Ge lamellae in the bulk microstructure, the IND represents a superposition of many single crystal patterns.

The IND of the 3D microstructure of Ge for the two time-steps during growth are shown in Fig. 5.6(d,e). The Ge facets correspond to sharp peaks in the IND, indicating a high degree of directionality of the shown lamellae. The poles of high probability present in the IND of the microstructure at earlier time-step (Fig. 5.6(d)) disappear in the later time-step (Fig. 5.6(e)), indicating loss of directionality during growth, that come about due to the curving and branching of the Ge lamellae between the two time-steps. Over time, we predict the stereographic projection to be uniformly distributed as the Ge lamellae explore the full extent of the orientation space.

5.2.5 Characterization of Crystallographic Texture

Motivated by the unique directionality and topology of the eutectic Ge phase observed during the *in situ* XRT results, we investigated the individual crystallographic orientations of the fully-solidified microstructure. The microtexture (*i.e.*, conjunction of microstructure and crystallographic texture) investigation was performed by means of electron backscatter diffraction (EBSD), on both the unmodified Al-Ge and modified Al-Ge-Na samples for sake of comparison. Analysis of a sufficiently large ROI in both cases is important to ensure statistical significance of the results. To

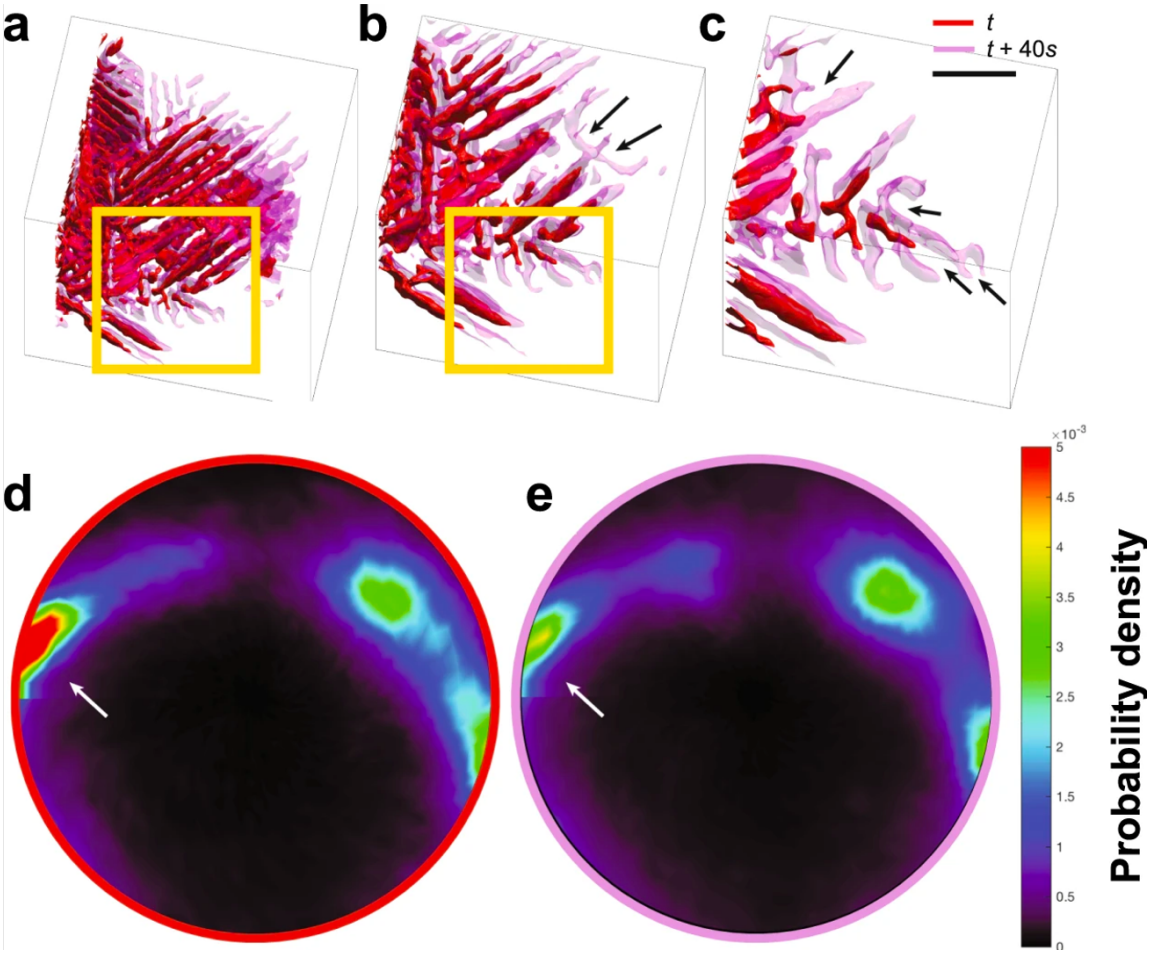

Figure 5.6: Directionality of eutectic Ge during growth. (a–c) Shown are the 3D microstructures of the Ge phase at two different time-steps, superimposed on each other. The structure at the earlier time is colored red, while that at the later time is colored pink. The two time-steps are 40 s apart. Curvature and branching events are shown with arrows in (b,c). Scale bar: 30 μm. (d) The interface normal distribution (IND; see text for definition) of the earlier time-step contains poles of high probability (marked by the arrow) that indicate anisotropy in growth. (e) The IND of the later time-step shows a diminished pole intensity compared to the earlier time-step (shown by the arrow), indicating loss of directionality during growth.

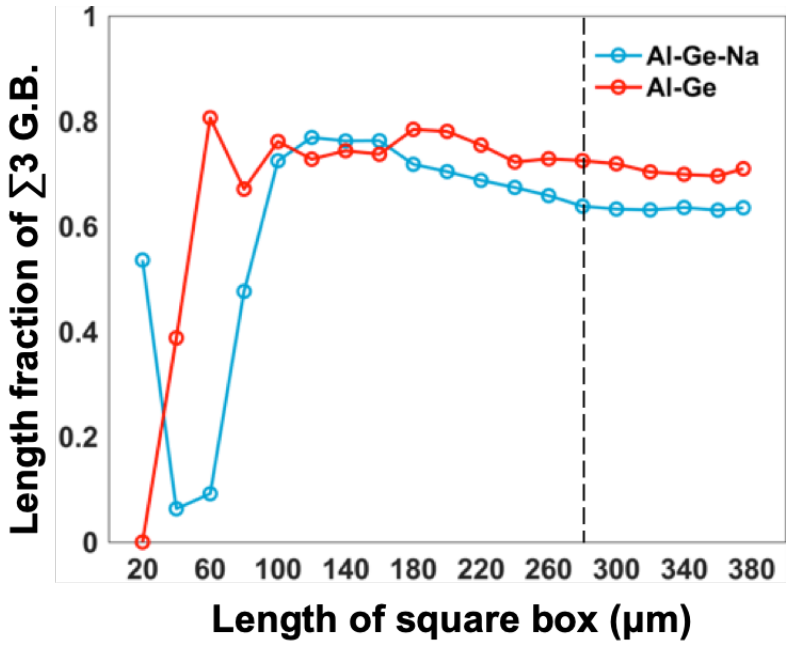

Figure 5.7: EBSD convergence tests. The length fraction of $\Sigma 3$ grain boundary (G.B.) as a function of EBSD scan area was used as the metric of statistical convergence. Convergence was achieved for a minimum scan area of 280 μm x 280 μm (indicated by the vertical dashed line in figure) for both Al-Ge-Na and Al-Ge EBSD patterns, as the $\Sigma 3$ length fraction for each alloy reached its steady-state value. All EBSD results reported in the text satisfy this convergence condition.

this end, the EBSD results presented herein satisfy the convergence criterion shown in Fig. 5.7.

Representative orientation maps of the two alloys are shown as insets in Fig. 5.8(a). The mean crystallographic orientation of each grain of eutectic Ge is colored according to the standard stereographic triangle on the top-right of the Al-Ge orientation map, while non-indexed regions, belonging to the Al phase, are depicted as black. The orientation maps provide only a qualitative intuition about the degree of crystallographic twinning as well as inter-lamellar spacing, both of which appear to

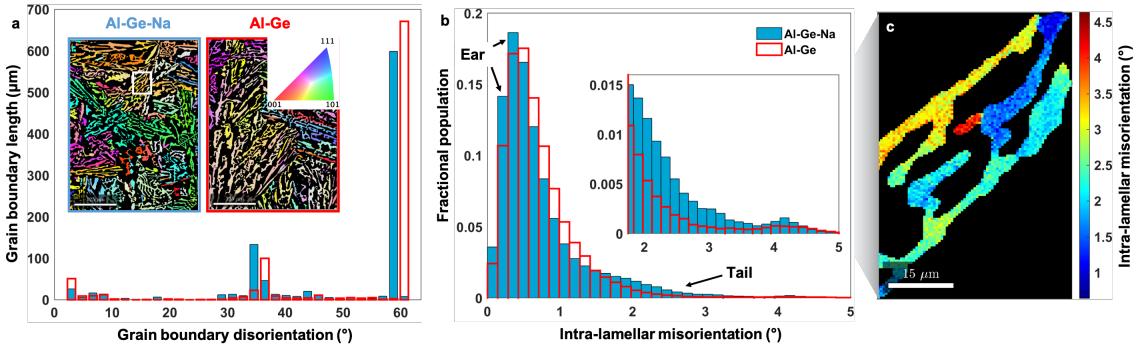

Figure 5.8: Crystallographic texture of the Ge lamellae. (a) Angle distribution of grain boundary disorientations (defined in main text) of eutectic Ge in both the modified (blue bars) and unmodified (red) alloys are displayed. The degree of twinning (high-probability peak at 60°) in both cases is practically equivalent. Insets show the mean crystallographic orientation of the Ge lamellae, colored according to the standard stereographic triangle in the inset. The non-indexed regions, belonging to the Al phase, are depicted as black. Scale bar: 125 μm. (b) Distribution of intra-lamellar misorientation of the Ge lamellae in both the modified and unmodified alloys are shown. Two features of the distributions are marked as the "ear" and the "tail"; see text for details. A significant fraction of the Ge grains in Al-Ge-Na exhibits greater intra-lamellar misorientation at higher angles (2–5°), as displayed in the inset. (c) Example of intra-lamellar misorientation is illustrated in a single Ge lamella of Al-Ge-Na boxed in (a).

be roughly insensitive to chemical modification by Na. Quantitative analyses of the grain boundary and intra-lamellar characteristics are discussed below.

The angle distribution of grain boundary disorientations is shown in Fig. 5.9(a). The disorientation angle refers to the minimum of all crystallographically equivalent misorientation angles. The distribution below 2° has a value of zero, as that is the threshold used to define the boundary between two distinct orientations. For both alloys, there are obvious peaks at roughly 4°, 35°, and 60°. The near-zero peak in the angle distribution stems from the low-angle, intra-lamellar misorientation (discussed further below). The misorientation axes distribution corresponding to

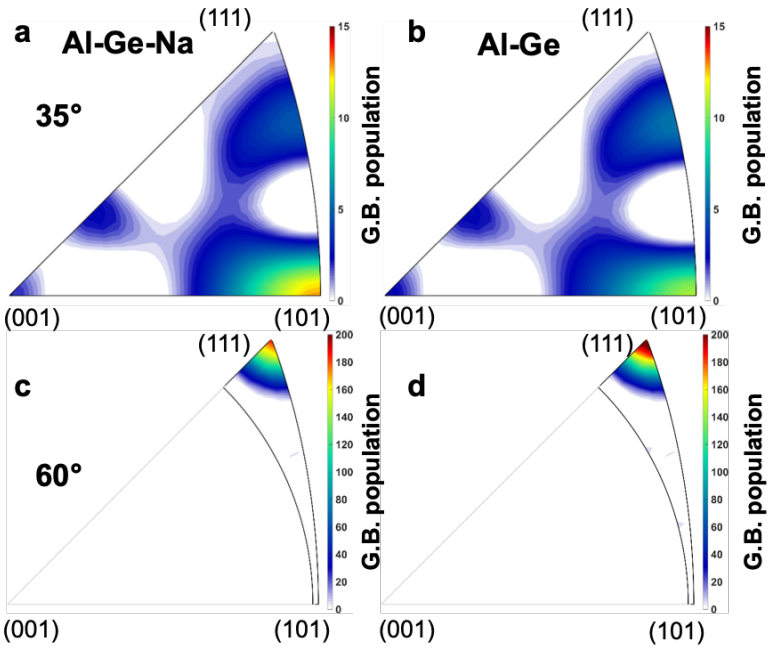

Figure 5.9: Disorientation axis distributions corresponding to peaks in angle distributions. (a) The axis distribution of 35° misorientation in Al-Ge-Na. The combination $35°/< 101 >$ corresponds to the $\Sigma 9$ coincident site lattice (CSL); see Supplementary Note 1. (b) The axis distribution of 35° misorientation in Al-Ge. (c) The axis distribution of 60° misorientation in Al-Ge-Na. The combination $60°/< 111 >$ corresponds to the $\Sigma 3$ CSL. (d) The axis distribution of 60° misorientation in Al-Ge. No significant differences are observed in the axis distribution of misorientation in the modified and unmodified alloys.

the two latter peaks in the angle distribution are shown in Fig. 5.9. In the panels corresponding to the 35° misorientation angle (panels (a,b)), minor peaks are present at the $< 110 >$ axes of the Al-Ge-Na sample, which are absent in unmodified Al-Ge. There are several Σ CSL boundaries in this angular region: $\Sigma 5$ at $36.86°/< 100 >$, $\Sigma 9$ at $38.94°/< 110 >$, $\Sigma 27$a at $31.59°/< 110 >$, and $\Sigma 27$b at $35.43°/< 210 >$. Clearly, the combination $35°/< 110 >$ cannot be assigned to $\Sigma 5$ because the axes distribution (Fig. 5.9(a)) displays a peak at $< 110 >$, not $< 100 >$. In practice, a CSL grain boundary can deviate slightly from the 'correct' CSL orientation due to dislocations in the lattice. In 1966, Brandon developed a criterion which showed that only boundaries with a maximum deviation $\Delta\theta_m$ given by Eq. 5.2 persist as CSL boundaries [171].

$$\Delta\theta_m \leq \frac{15°}{\sqrt{\Sigma}} \tag{5.2}$$

We note that the use of Brandon criterion is a common practice in assigning Σ values, see, *e.g.,* refs. [172, 173]. According to the Brandon criterion, the only valid combination for the $35°/< 110 >$ angle-axis pair is $\Sigma 9$ CSL.

Overall, the modified and unmodified alloys exhibit similar grain boundary characteristics. The high-probability peak at 60° in the angle distribution corresponds to the $< 111 >$ misorientation axes (Fig. 5.9(c,d)). The combination $60°/ < 111 >$ represents the coherent twist $\Sigma 3$ grain boundary [174, 175, 172]. We observe that the degree of twinning in the unmodified and modified eutectic Ge is practically equivalent, unlike the predictions from the IIT and poisoning of TPRE models discussed above. For instance, if the twinning density were significantly higher in the modified

alloy, this would suggest that IIT is operative; on the other hand, a reduction in the number of $\Sigma 3$ boundaries might suggest that the re-entrant grooves were poisoned by the modifier species during crystallization.

In addition, we analyze the intra-lamellar misorientation of the Ge lamellae in both the modified and unmodified alloys, *i.e.*, the pairwise orientation difference between points (pixels) in each Ge lamella in reference to the mean orientation of the corresponding lamella, surveyed over all lamellae inside the EBSD scan area. These results are displayed in Fig. 5.8(b). A significant fraction of the Ge grains of the modified Al-Ge-Na displays greater intra-lamellar misorientation at higher angles (2–5°), as shown in the inset of Fig. 5.8(b). To visualize the intra-lamellar misorientation in the Al-Ge-Na alloy, we extract the lamella boxed in the inset of Fig. 5.8(a). This lamella was chosen since it possesses the maximum grain orientation spread (GOS), which is calculated by averaging the deviation between the orientation of each point (pixel) in a grain and the average orientation of that grain. This single Ge lamella of Al-Ge-Na is shown in Fig. 5.8(c), illuminated according to the degree of misorientation within it. We note that a noticeable length fraction of the lamella possesses misorientation $< 3°$, with some region of the sample having misorientation close to 5°.

Comparison of the distributions of intra-lamellar misorientation, shown in Fig. 5.8(b), with the bivariate histogram in Fig. 5.10 relating the Ge GOS and grain size in Al-Ge-Na demonstrates that the distributions differ in two important aspects, termed the "ear" and "tail" regions [176]: While the "ear" of the distribution corresponding to the modified alloy is characterized by grains of smaller size with lower intra-

lamellar misorientation, the "tail" of the same distribution encompasses larger grains that have developed higher intra-lamellar misorientation. The "ear" can be explained using classical nucleation theory [164, 41]: The larger nucleation undercooling of the modified eutectic (three times that of the unmodified eutectic; see above) provides a greater driving force for the formation of more Ge (and Al) nuclei per volume per time [127]. In turn, these new but smaller Ge solids do not experience the same temporal duration to grow into larger bodies that would then possess higher intra-lamellar misorientation. Meanwhile, the larger "tail" in the modified distribution reflects errors in the stacking sequence of the Ge phase during the growth process, resulting in a higher GOS; see Discussion. That is, both eutectic nucleation and growth are impacted in the modified alloy, as exemplified by differences in intra-lamellar misorientation.

5.2.6 Discussion of Modification Mechanism and Topological Classification of Eutectic Microstructures

It is well-established that eutectic constituents upon modification exhibit refinement (change in length scale) [93, 110, 165] as well as favorable morphological changes (*e.g.*, flake to fiber transition) [96, 41, 119]. Direct interrogation of the time-resolved 3D results demonstrate uniquely that chemical modification also brings about significant changes in the topology (*i.e.*, connectivity) of the eutectic constituents, the reasons for which are discussed in detail below.

By monitoring the phase transformation in real-time, we found that the nucleation undercooling of the Al-Ge eutectic in the presence of Na is more than three

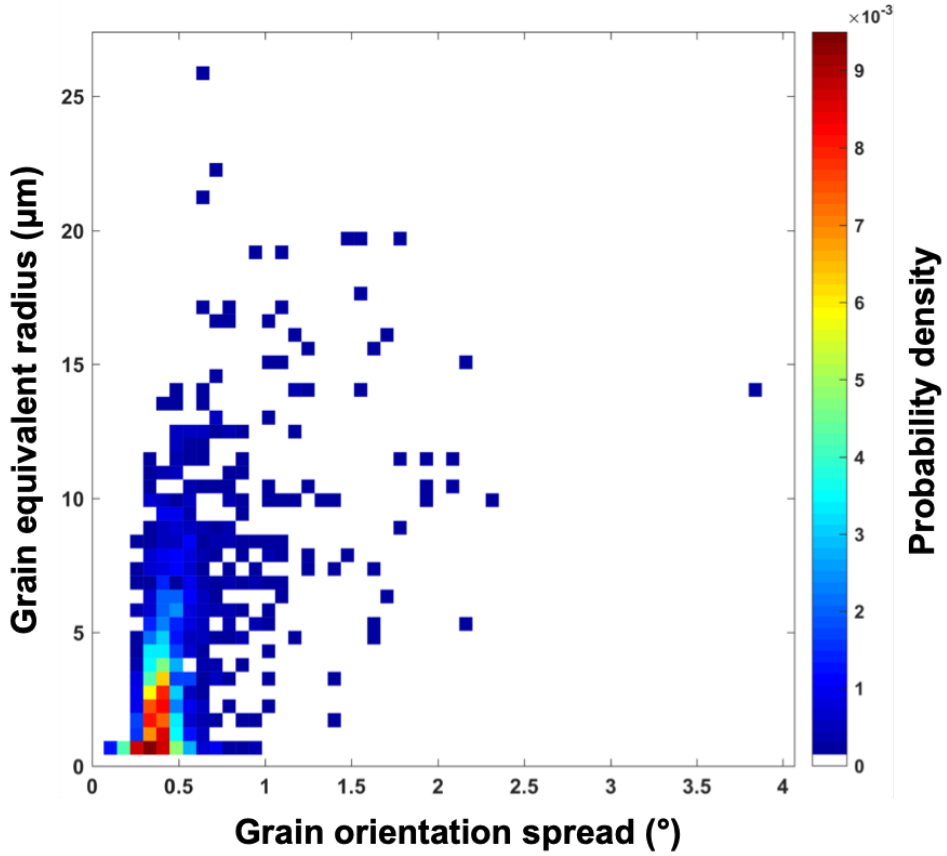

Figure 5.10: Grain size *vs.* orientation spread of eutectic Ge in Al-Ge-Na. The bivariate histogram relating the Ge grain orientation spread (defined in text) and grain size in Al-Ge-Na demonstrates that smaller Ge grains tend to possess smaller grain orientation spreads. The data can be used to interpret the trends in the intra-lamellar misorientation shown in Fig. 5.8b.

times that of the unmodified alloy. This suggests that trace amounts of Na have a profound influence on the nucleation kinetics of the Al-Ge eutectic. In particular, primary Al dendrites nucleate prior to the faceted Ge phase, indicating that Ge is more strongly impacted than Al. Such a depression of the eutectic temperature due to chemical modification of the faceted phase is in agreement with the prediction of Thall and Chalmers [164]. Furthermore, observation of the selective affiliation of the modifier species with the faceted phase agrees with Hellawell's prediction [162] and is attributed to the lower activity of Na in the Al melt [177].

During growth of the modified Al-Ge eutectic, the faceted Ge phase trails behind the non-faceted Al phase. Eventually, the Ge constituent is fully engulfed in holes (gaps) within eutectic Al (Fig. 5.3). Therefore, growth of the Ge phase is retarded with respect to the Al phase, pointing to the influence of Na on the growth kinetics of Ge. The idea of Al enveloping Ge is consistent with previously observed over-modification bands of Al when an excess ($>$ 100 ppm) of Na is added [41, 97]. The engulfment of Ge inside Al domains implies important topological behaviors of the eutectic constituents. In particular, the scaled (dimensionless) genus of Ge is about an order of magnitude lower than that of Al throughout the growth process (Fig. 5.4(b)), indicating that the Ge phase exists as independent bodies (connected components) inside holes within the Al matrix (Fig. 5.11(c)). This change of lead also has important technological significance: The brittle phase (Ge) is embedded in a ductile matrix (Al), thus contributing to the enhanced mechanical properties that have been documented previously [99]. We note that the exact opposite roles of Al and Ge (Fig. 5.11(b)) were recently observed during the growth of the unmodified

Al-Ge eutectic: In the latter, the Al bulbs were observed to grow through holes caused by crystallographic twinning within the Ge plates (*i.e.*, in-plane mosaicity); subsequently, the Al bulbs spread across the exposed Ge 111 facet planes [57]. Thus, in the unmodified microstructure, the genus of Ge would be greater than that of Al. In addition, the topology of the modified eutectic is markedly different from that expected for organic irregular eutectics, *e.g.*, camphor-napthalene and succinonitrile-borneol systems [59] (Fig. 5.11(a)). In this scenario, the genera of both phases would be comparable due to the duplex structure of the growth front (the number of disjoint Al components is roughly the same as the that of Ge).

Whereas eutectics have been traditionally classified in terms of entropies of fusion and constitutive volume fractions [39], we suggest an alternative classification based on the relative magnitudes of the phase topologies. In our schema, there are three topological classes for eutectic microstructures, that come about due to variations in alloy composition and defect density. For example, when defect densities and impurity concentrations are low, one might expect to see the classical picture shown in Fig. 5.11(a). On the other hand, in low stacking-fault-energy semiconductors, twinning is rampant (especially at high growth rates [96, 178]), and one might instead obtain a microstructure akin to Fig. 5.11(b). Lastly, when impurities selectively modify the growth kinetics of the faceted phase, the most probable scenario is that of Fig. 5.11(c). More broadly, the higher degrees of freedom in the univariate eutectic reaction (*i.e.*, three components and two solid phases) bring about morphological and topological transitions that are not seen in nonvariant eutectics [151]. Thus, interfacial topology represents a signature of the structural complexity in each case.

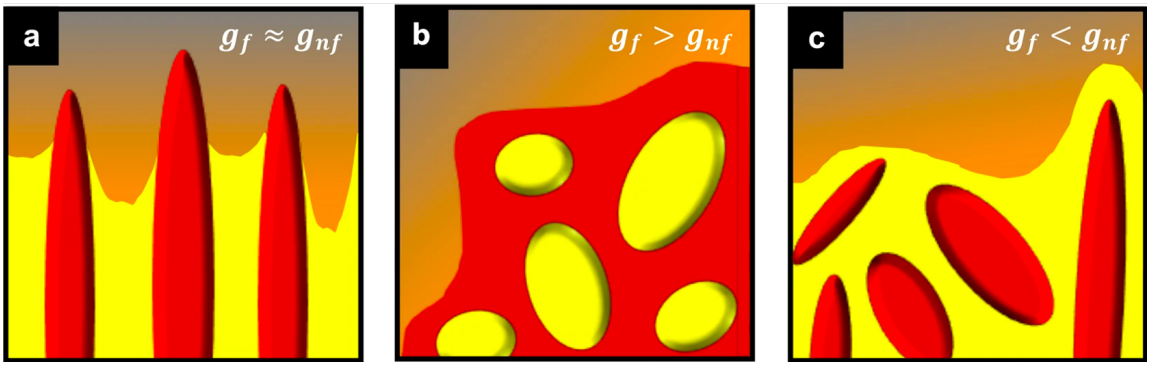

Figure 5.11: Topological classification of eutectic microstructures. (a) The schematic shows crystal systems with high stacking-fault energy. Due to the duplex structure of the growth front, the number of disjoint faceted components (red) would be roughly the same as the that of the non-faceted components (yellow). Thus, the genus of the faceted phase (g_f) is comparable to that of the non-faceted phase (g_{nf}). (b) A depiction of crystal systems with low stacking-fault energy, such as in elemental semiconductors, is shown. There, bulbs of the non-faceted phase were observed to grow through holes caused by crystallographic twinning within plates of the faceted phase [57]. In this case, the genus of faceted phase is greater than that of the non-faceted phase. (c) The schematic illustrates crystal systems solidified in the presence of impurities. The non-faceted phase (here Al) leads at the solidification front and eventually collapses on the faceted phase (Ge), prohibiting the latter's steady-state propagation and resulting in a reversal of the ordering of their genera. Note that all three cases (a–c) show approximately the same volume fractions of the non-faceted (nf) and faceted (f) eutectic phases.

The reason for this remarkable topological modification remains to be determined. While our observation of Al leading and encasing the Ge at the growth front agrees with studies done by Thall and Chalmers and Crosley and Mondolfo [164, 41], we propose that the root cause of this effect is not the 're-nucleation' of Ge. If that were the case, the introduction of the new independent bodies, *i.e.*, solid voids, of Ge would cause a decrease in the genus of Ge (Eq. 5.1). However, in the present study the genus of Ge is observed to increase over time (Fig. 5.4). Instead, the most compelling reason for the retardation of the growth of Ge is that Na interferes with the stacking sequence of Ge, leading to the greater intra-lamellar misorientation of Ge, as we show in Fig. 5.8(b). This intra-lamellar misorientation in turn facilitates the development of curved solid-solid interfaces, enabling the Ge phase to grow without ever attaining its fully-faceted shape. Importantly, Na does not satisfy the geometric condition of Hellawell's IIT mechanism [96] nor increase the twinning frequency in Ge (Fig. 5.8(a)). Yet, as discussed above, Na modification is demonstrated to cause a marked change in both the morphology and the topology of the eutectic constituents. It is therefore evident that the conventional growth mechanisms of IIT, TPRE, as well as poisoning of TPRE are limited in scope. The former model is overly deterministic in that it assumes that the impurity atoms fit perfectly in the Ge lattice so as to create coherent $\Sigma 3$ twin defects [96]. In reality, adsorbed impurities can give rise to a range of interfacial configurations, grain orientations, and misorientation angles beyond 60°.

Our results support and generalize the chemical modification model proposed by Schumacher and colleagues [136, 179, 165], wherein the segregation and/or adsorption

and subsequent entrapment of the impurity species (here Na) during growth of the faceted (here Ge) phase lead to modification. In this picture, the Na and Al segregate ahead of the growing Ge phase (where the partition coefficients $k_{Na} < 1$ and $k_{Al} < 1$, respectively); then, during continuous Ge growth, the adsorption of Na atoms on the exposed Ge facets may occur, forcing a change in the stacking sequence of the faceted phase at the growth front. Total-energy minimization calculations, as well as vibrational spectroscopy results, show that the adsorption of Na on Ge surfaces does give rise to new vibrational states, forming adatom-surface bonds [180]. Finally, the overgrowth of Ge leads to a solute entrapment within the eutectic Ge phase [136, 179]. We note that entrapment should not be confused with solute trapping, wherein solute atoms are "frozen" in the liquid state. Given that our *in situ* tomographic experiment was conducted with minimal undercooling, solidification rates ($\sim 1 \frac{\mu m}{s}$) are not high enough to physically trap the trace impurity atoms.

The aforementioned solutal entrapment likely forms an aggregation of Al-Ge-Na within, as well as in the vicinity of, the eutectic Ge phase. In the present study, we aimed to map the atomic distribution of Na in the fully-solidified specimen using high-resolution (scanning) transmission electron microscopy together with energy-dispersive spectroscopy as well as electron energy loss spectroscopy. However, our chemical mapping efforts did not yield conclusive insights, due to the high overlap of the peak from Ge L2,3 absorption edge (1217–1248 eV) and the small peak from the Na K-edge (1072 eV), given the trace atomic content of the latter (¡0.2 at. %), in the HR-STEM images. Continuing advances in the design of analytical tools for high-resolution characterization of materials containing light elements as well as those

prone to beam irradiation, will aid further analysis of the atomic distribution of Na in future experiments.

5.3 Summary

In summary, by employing a multi-modal imaging approach, we tracked the growth behavior of a modified irregular eutectic alloy and analyzed the physical characteristics of the fully-solidified specimen. We illustrated that the trace presence of the modifier species has a profound influence on the kinetics of both nucleation, as manifested in higher undercooling compared to the unmodified alloy, and growth, as expressed in the marked difference in the morphological and topological properties. These trends can be rationalized by noting that the impurity species selectively alters the stacking sequence of the faceted phase, as indicated by the higher intralamellar misorientation of the faceted phase in the impurity-modified alloy (over a two-fold increase). This result supports the notion that during growth, the faceted phase rejects the modifier atoms; subsequently, the modifier species adsorbs onto or in the vicinity of the faceted phase, thereby acting as "obstacles" to its continued propagation. Consequently, the non-faceted phase supersedes the faceted phase during growth, leading to a topological transition (complete encasement of the faceted phase). Collectively, our findings demonstrate a comprehensive understanding of the role of trace impurities during eutectic crystallization.

Although our results concern eutectic systems, nothing precludes the immediate extension of our techniques to materials classes that involve the interaction of

impurities and other building blocks. Exploiting analogies with interactions among impurities and other building blocks, aided by powerful computational schemes, can help derive design rules that span across a vast array of materials systems. As an example, the newly investigated Al-Ce alloys demonstrate castability, structure, and mechanical strength similar to the near-eutectic Al-Si alloys modified by Sr; as a result, the Al-Ce alloys have been rated positively for laser additive manufacturing (no cracking or porosity) [181]. It is reasonable to assume that chemical modification, a lesson from a much older manufacturing process, namely casting, will provide unique pathways toward future design of alloys – including Al-Ce – by additive manufacturing.

5.4 Materials and Methods

5.4.1 Experimental Design

An integrated imaging approach, comprised of 4D (3D space- and time-resolved) synchrotron X-ray microtomography (4D XRT) was employed to directly observe the solidification pathways and interfacial dynamics of an irregular eutectic system in the presence of trace metallic impurities. We illustrate our findings on the Al-51.6 wt.%Ge eutectic with 0.1 wt.% Na as the impurity species ('modifier'). Direct comparisons are drawn against the unmodified Al-Ge alloy reported recently [57]. Microstructural and topological evolution as measured in the reconstructed volumes are linked to the crystallographic features of post-growth samples using electron backscatter diffraction.

5.4.2 Sample Preparation

Alloy buttons of nominal composition Al-51.6 wt.%Ge-0.1 wt.%Na were cast *via* vacuum arc-remelting at the Materials Preparation Center at Ames Laboratory (Ames, IA, USA), using 99.999% purity Al, 99.999% purity Ge, and ¿99.9% purity Na. We note that the composition of Ge (51.6 wt.%) in the present study is the same as that in the recent report of the unmodified, fully eutectic alloy investigated in ref. [57]. For the synchrotron X-ray tomography (XRT) experiments, the as-prepared alloy buttons were cut in the shape of cylindrical rods of 1 mm diameter by 5 mm length *via* electrical discharge machining.

5.4.3 Beamline Setup

The XRT experiments were conducted at Sector 2-BM at the Advanced Photon Source in Argonne National Laboratory (Argonne, IL, USA). The polychromatic 'pink' X-ray beam was focused on the samples and a 20 μm thick LuAg:Ce scintillator converted the transmitted X-rays to visible light. High-resolution imaging was accomplished utilizing a PCO Edge CMOS camera equipped with a 10x magnifying objective to provide isotropic pixel sizes of 0.65 mm x 0.65 mm. The tomographic field-of-view measured 2,560 x 600 pixels (*i.e.*, 1,664 mm in width by 390 mm in height). The camera frame rate and exposure time were 50 Hz and 14 ms, respectively. Due to the small penetration depth through the 'heavy' element Ge (51.6 wt.%), relatively long exposure times were required to ensure high signal-to-noise images. Given the 1 mm diameter of each sample, the temperature distribution was assumed to be uniform within the sample. Our beamline setup follows closely that

of ref. [57]. During acquisition, the sample was rotated continuously at a rate of 6° per second. During each 180° rotation of the sample, 1,500 projections were collected. The large number of projections recorded (in addition to the high exposure time of 14 ms) guaranteed high-quality images. This combination of acquisition parameters optimally allowed for a temporal discretization of 20 s between consecutive 3D reconstructions. Data were collected for roughly 450 s, resulting in 22,500 total projections and 15 total reconstructions.

5.4.4 Data Visualization

Reconstruction of the tomographic data was performed using TomoPy, a Python-based open source framework [182]. Within TomoPy, the X-ray projections were first normalized by the dark- and white-field images to account for beam instabilities. Additional correction for "ring" artefacts was made *via* combined wavelet-Fourier filtering [183]. Subsequently, the data were reconstructed *via* the direct Fourier-based Gridrec algorithm [184]. The reader is referred to ref. [182], and references therein, for further details on these algorithms. A representative grayscale 2D slice of 3D reconstruction, parallel to the axis of rotation of the cylinder-like sample, is given in Fig. 5.2(a). The strong absorption contrast between the constituents allows one to easily distinguish between the three coexisting phases: eutectic Ge (white), eutectic Al (dark gray), and the liquid (light gray). The reconstructed image also features bulbous Al dendrites (also dark gray). One eutectic region free of dendrites (Fig. 5.2(b)) is boxed and isolated for subsequent analysis. In order to enhance the contrast between the solid and liquid phases, and minimize any systematic im-

age artefacts, reconstructions of the fully-liquefied sample were subtracted from all other reconstructions. Subsequently, the grayscale reconstructions of this region were segmented, *i.e.*, transformed into a computable representation of their parts (liquid, eutectic Ge, and eutectic Al). Our segmentation algorithm, implemented in the Image Processing Toolbox^{TM} of MATLAB R2016a, comprised of (i) multi-level thresholding, (ii) edge-based methods for finding the boundaries of 'objects' (Ge and Al) within images, and (iii) morphology-based methods (*e.g.*, dilation and erosion) in order to remove speckle noise (small objects) as well as to smooth the border of large objects [185]. Figure 5.2(c) shows the segmentation output of the region in Fig. 5.2(b), wherein eutectic Ge is indicated with white, eutectic Al with gray, and air (pore) with black. In Fig. 5.2(d), edges of the segmentation output are overlaid on the original grayscale reconstruction (edges of Ge are red, and those of Al are yellow), showing excellent agreement with the eutectic structures underneath. The segmented 2D images were then stacked along the third spatial dimension to reveal the 3D microstructures. Fig. 5.2(e) shows the 3D eutectic structure corresponding to the region of interest (boxed). The slice shown in Fig. 5.2(a) corresponds to the top-most surface of the 3D visualization in Fig. 5.2(e).

For subsequent (topological and directional) analysis of the 3D microstructures, we represented the interphase interfaces using a triangular mesh, wherein sequences of vertices and triangular faces comprise the solid-liquid and solid-solid interfaces. To remove any 'staircase' artifacts, the triangular meshes were smoothened *via* mean curvature flow [186]. The 3D visualization in Fig. 5.2(e) is an example of the smoothed structure (triangular faces and vertices are rendered colorless).

5.4.5 Topological Calculations

The topological parameters were calculated from the triangular mesh representation of the segmented interphase interfaces as an input. The mesh consists of n nodes, e edges, and f faces. In these calculations, the genus g was computed according to Eq. 5.3:

$$g = 1 - \frac{\chi}{2} \tag{5.3}$$

$$\chi = n - e + f \tag{5.4}$$

χ is the Euler characteristic, which relates the number of nodes (n), edges (e), and faces (f) of a polygonal mesh to the genus g of the underlying object [187]. Since the genus is a topologically-invariant property, it does not depend on the fineness or smoothness of the mesh representation of the object. Subsequently, Eq. 5.1 (main text) was used to compute the contributions of handles h and voids v to the genus g. We computed and report upper and lower bounds for genus, g_{max} and g_{min}, respectively. These two distinct boundary conditions are determined by treating the parts of the microstructure that contact the bounding box. To obtain g_{max}, we assume that all such parts of the microstructures cross the boundary and connect to an external node, as illustrated in Fig. 5.12(a). To obtain g_{min}, we assume that those parts of the microstructure are 'capped' at the bounding box, as shown in Fig. 5.12(b), so that there is no point of contact between the microstructure and the bounding box. In our digital (mesh) representation of the 3D microstructures,

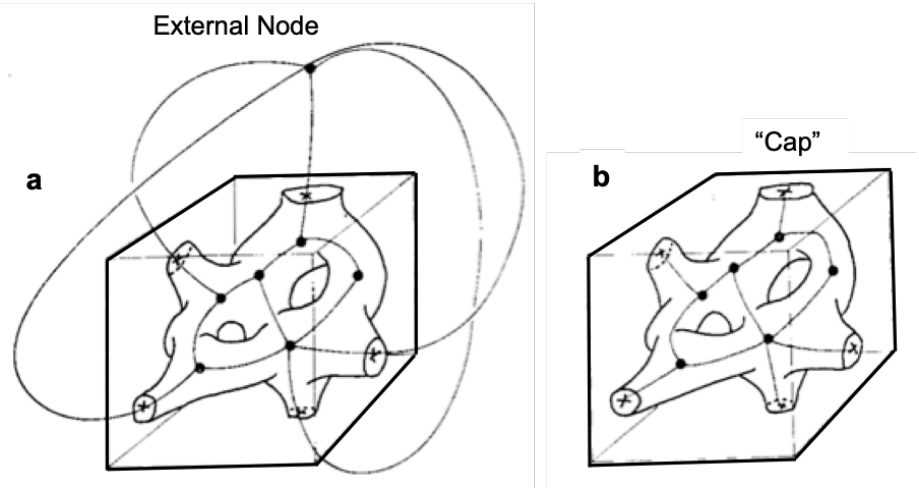

Figure 5.12: Boundary conditions for genus calculations. Boundary conditions for genus calculations. (a) The parts of the solid phase that contact the bounding box of the ROI are assumed to cross it and meet at an external node. This assumption provides an upper bound for the genus g_{max} of the solid phase. (b) The parts of the solid phase that would contact the bounding box are capped, so that there is no longer a point of contact between the two. This configuration yields a lower bound of the genus g_{min} of the solid phase. Figure adapted from ref. [168].

the latter is accomplished by padding all six sides of the bounding box by arrays of zeros.

5.4.6 *Ex Situ* Characterization

The XRT experiment was complemented with *ex situ* characterization studies. Crystallographic investigation of the as-solidified Al-Ge and Al-Ge-Na eutectics by means of electron backscatter diffraction (EBSD) was performed using the field-emission gun scanning electron microscope Tescan MIRA3 at the University of Michigan campus. For this purpose, a small cut of the high-purity alloy button was thermally annealed at 550 °C for 4 hours, and mechanically ground and polished so as to obtain scratch-

free surface. For the EBSD experiments, the beam voltage was adjusted to 10 kV; the working distance, tilt, and step size were set to 20 mm, 70° relative to normal incidence, and 0.5 μm, respectively. Analysis of the texture data was performed using the MATLAB toolbox MTEX [188] in order to generate orientation maps and misorientation distributions.

5.5 Data Availability

The raw XRT projection data are publicly available in the University of Michigan Deep Blue Data repository at `https://doi.org/10.7302/Z2154F89`.

5.6 Acknowledgments

We gratefully acknowledge financial support from the University of Michigan College of Engineering. We also acknowledge additional support from the University of Michigan Rackham Graduate Student Research Grant program. This research used resources of the Advanced Photon Source, a U.S. Department of Energy (DOE) Office of Science User Facility operated for the DOE Office of Science by Argonne National Laboratory under Contract No. DE-AC02-06CH11357. We thank Ron Keinan for experimental assistance and Pavel Shevchenko (ANL) for assistance in sample preparation. We also thank Professor Amit Misra for the fruitful discussions. This research was supported in part through computational resources and services provided by Advanced Research Computing at the University of Michigan, Ann Arbor. We also acknowledge the University of Michigan College of Engineering for

financial support and the Michigan Center for Materials Characterization for use of the instruments and staff assistance. We thank Dr. Kai Sun for assistance in STEM and EELS.

Chapter 6

Singly-Twinned Growth of Si Crystals Upon Chemical Modification

This chapter is based on the article under review (revision stage) as of April 2020.

6.1 Introduction

Understanding the relationship between the distribution of chemical impurities and microstructural defects – including grain boundaries – in crystals is of paramount importance for engineering new or improved materials for a wide variety of applications, including structural [189, 190], electronic [191, 192], and energy [193]. An important class of grain boundaries is the twin plane along which two crystals share the same lattice sites and intergrow through certain symmetry operations, and re-

cent works provide key insights into the twin forming process [194] and its impact on grain growth [195]. The use of growth modifiers in natural, biological, and synthetic crystallization is a common strategy to control growth and achieve more desirable physicochemical properties [196, 197, 198, 143, 30]. For structural materials, such as eutectic alloys, chemical modification through the addition of trace, typically metallic elements to the feedstock alloys during crystallization often improves the mechanical properties of growing crystals from a melt, for instance ductility and strength [42, 61, 161, 137, 165, 141] of cast alloys. This is due to a combination of structural refinement [42, 179] as well as morphological and topological changes during solidification [30]; Ref. [29] provides a review on the microstructural effects of chemical modification. While it is known that impurities such as those deliberately added [197, 198, 30, 61, 45] through chemical modification tend to segregate to grain boundaries [189, 199] with dramatic consequences for the physical behavior of the material [196, 30, 29], the origins behind such drastic microstructural changes upon crystallization remain elusive.

Several models have been proposed since the 1960s and onwards to explain the mechanisms behind chemically-modified crystallization. These models are often in relation to the growth of eutectic Si in Al Si alloys whose brittleness and coarse microstructure in pristine (unmodified) state is the main reason for the poor mechanical properties of the as cast alloy, such as premature crack initiation and fracture in tension [145]. Among these proposed models are those that describe the growth of the faceted Si phase largely based on geometric considerations involving the impurity atoms. The twin plane re-entrant edge (TPRE) growth mechanism (*vide infra*) de-

scribes the growth of the faceted phase facilitated by 111 $\Sigma 3$ twins [130, 131]. TPRE is thought to dominate for slow cooling rates in unmodified alloys. According to the poisoning of the TPRE mechanism, growth of the faceted phase is more isotropic due to selective adsorption of the modifier atoms or clusters at the twin-liquid interface (i.e., deactivating the advantage of the TPRE mechanism) [132]. In the impurity-induced twinning (IIT) mechanism, the modifier atoms adsorb instead at the 111 step surfaces of the faceted phase, and the associated change in the stacking sequence facilitates the formation of frequent twins and locally enables growth in multiple $< 112 >$ directions [96]. That is, both IIT and the poisoning of TPRE involve adsorption of the modifier at the Si-liquid interfaces; however, the former leads to twin formation and the latter to twin suppression.

The TPRE growth model for crystallization of a twinned diamond cubic crystal was independently proposed by Wagner [130] and Hamilton and Seidensticker [131], hereafter referred to as WHS. The model is based on enhanced nucleation at the $\Sigma 3$ twin-liquid interface. According to this model, nucleation occurs at the 141° concave basin, termed type I re entrant groove, which is formed by the intersection of 111 interfaces on either side of the twin defect. Fig. 1(a) shows the shape of a faceted crystal with a single twin plane, which contains three such re entrants along ¡211¿ growth directions. Nucleation of new solid layers occurs readily at these re entrants compared to the $< 111 >$ flat surfaces, given that adsorption is more favorable on the groove (local coordination number of four) than on the 111 plane (coordination number three). Therefore, growth occurs preferentially along the three re entrant grooves and terminates upon the disappearance of the re entrants, and the crystal

attains triangular 60° corners, as shown in Fig. 6.1(b).

The above mechanism alludes to the requirement of a multiply twinned interface that mediates growth until, *e.g.,* depletion of the melt. The WHS growth model of a 111 bounded crystal with two parallel twin planes, shown schematically in Fig. 6.1(c-e), entails rapid growth at the type I re entrant corner similar to the above description of a crystal with one twin. The nucleated layer propagates to the neighboring, parallel twin and subsequently forms a new re entrant corner with an angle of 109.5° termed a type II re entrant. The type II re entrant groove alleviates the shortage of nucleation sites brought about by the formation of ridge (convex) structures during growth, thus enabling a continuous propagation of the crystal (Fig. 6.1(d)) until the solid attains its original shape (Fig. 6.1(e)). Such concerted growth mediated by the two parallel twins proceeds in all three ¡211¿ directions. The key distinction between the growth of parallel twinned and singly twinned interfaces is that the type II re entrant in the former enables the cyclic, steady state growth to proceed in the ¡211¿ directions with a non-vanishing type I re entrant.

Here, we investigate whether the formation of Si crystals in an Al-Si-Cu liquid follows the classical models mentioned above in the presence of trace modifiers. We do so by utilizing *in situ* X-ray microtomography to follow the evolution of solid-liquid interfaces as a function of time. In comparison, most previous assessments of Si modification are based on quenched specimens. Our 4D (time and 3D space resolved) data reveal that the particles attain a more convex geometry during growth, from an initially concave-like curvature. We attribute this morphological instability to the selective poisoning of the concave re entrant groove by the modifying agent,

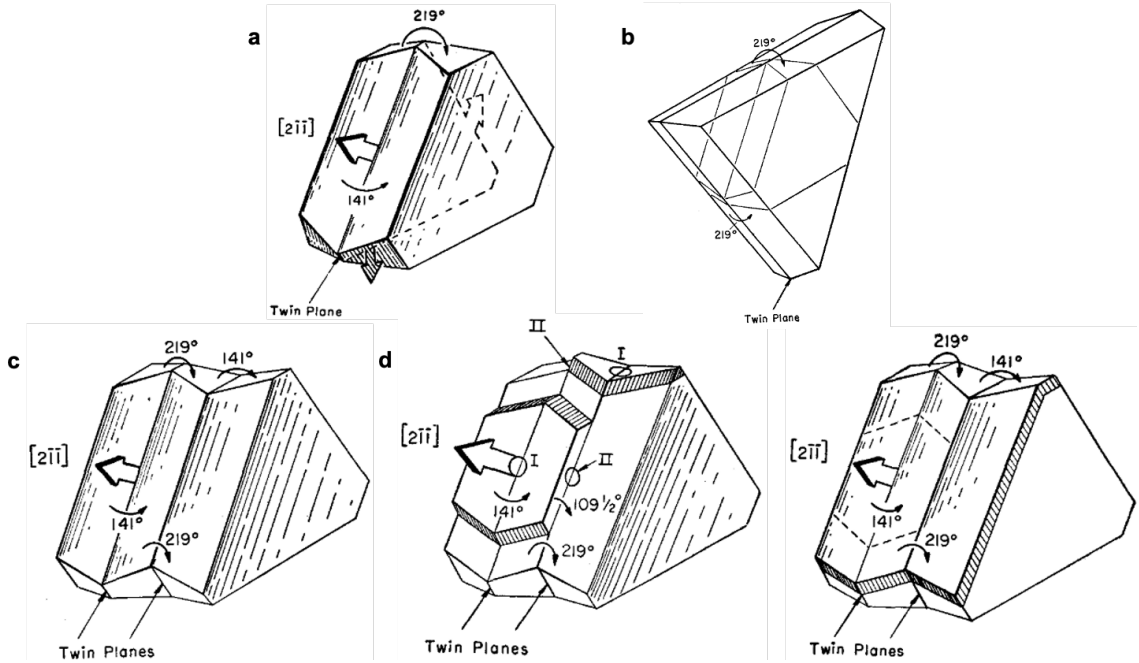

Figure 6.1: Schematics of faceted crystal growth with singly- and doubly-twinned interface, according to Wagner [130] and Hamilton and Seidensticker [131]. (a,b) Growth of a crystal with a single twin boundary. (a) The crystal is bounded by 111 habit planes, and a 141° re-entrant corner (type I) appears where the twin intersects the solid-liquid interface. Growth proceeds in $< 112 >$ directions (arrows) upon nucleation at the re-entrant groove, compared to the flat 111 habit planes. (b) Growth terminates by the vanishing of the re-entrant grooves and subsequent formation of a triangular mound projecting into the melt. (c-e) Growth of a crystal with two parallel twin planes. (c) The doubly twinned crystal is bounded by 111 habit planes and contains a type I re-entrant groove. Nucleation readily occurs at the re-entrant groove as opposed to the flat 111 planes, similar to the case of singly-twinned crystal in (a). (d) At the neighboring twin the new layer creates a second re-entrant corner (type II) with an angle of 109.5°. (e) The type II corner enables the continuous propagation of the crystal in the ¡$< 112 >$¿ direction. Unlike in the singly-twinned interface in (a), the type I corner does not disappear during growth and no triangular mounds appear upon the termination of growth. Figure reproduced with permission from ref. [131].

suggesting that the poisoning of TPRE mechanism is operative. In itself, the variable convexity of Si particles during growth provides evidence that growth does not occur under steady state conditions. Subsequent investigations of grain boundary characteristics and twinned interface of fully solidified Si particles in both modified and unmodified alloys show that chemical modification allows non-steady state growth to occur with a single twin boundary at the center of the Si particle. For unmodified Si, steady state growth proceeds through the formation and persistence of doubly twinned interface between the grains of Si [133]. We find that modifier clusters can readily nucleate at the re-entrant groove, owing to a nucleation barrier that is $\sim$50% smaller than on 111 habit planes, thereby blocking the continuous propagation of the twin boundary. Taken altogether, these insights shed new light on the impact of dopants and impurities on the growth of crystals as well as their defect distributions.

6.2 Results and Discussion

6.2.1 Growth Behavior of Si Particles

The dynamics of chemically modified Si crystallization was captured by *in situ* μXRT. Four representative snapshots during the growth process are shown in Fig. 6.2(a-d), where only the Si particles are colored and the Cu enriched liquid is rendered transparent for clarity. The particles nucleate heterogeneously on the oxide skin (translucent gray) and grow into the melt. Qualitative comparison of the solid liquid interfaces during the early (panels (a,b)) and late times (panels (c,d)) indicates a transition from a relatively flat morphology to one that features a triangular

mound projecting into the melt. For subsequent analysis, we focus on the crystallization dynamics of the Si particle that forms first and which is boxed yellow in Fig. 6.2(a). A closer examination of the growth dynamics of this particle, shown in Fig. 6.2(e), indicates a continuum of polycrystalline growth forms that Si attains, undergoing a morphological instability toward an eventual convex geometry that resembles a triangular mound projecting into the melt. This morphological instability, quantified in the next section, is hypothesized (and verified below) to be the result of the disappearance of the concave re entrant groove, and an indication of the non-steady state growth of Si in chemically modified alloy. We note that the Si particle is not devoid of twins altogether, else its kinetic Wulff shape should resemble an octahedron bounded by 111 habit planes [200].

It is worth pointing out the difference between our 3D results and those of Ref. [133]. In the pristine (unmodified) crystallization of Si, it was observed [133] that the type I re entrant (concave interface) persists during growth, suggesting a steady state pathway afforded by the presence of two parallel twin planes and in which the lateral growth rate and the re entrant nucleation rate proceed in concert. This finding illustrates that the WHS mechanism (Fig. 6.1(c-e)) agrees with the growth of pristine Si [130, 131]. The same cannot be said about the present work, *cf.* Fig. 6.2. At the macroscale, such differences in crystallization mechanisms amount to the distinction in the morphology of fully solidified Si: flat interfaces with wide terraces in the pristine crystals, and triangular corners at the growth tips in chemically modified crystals.

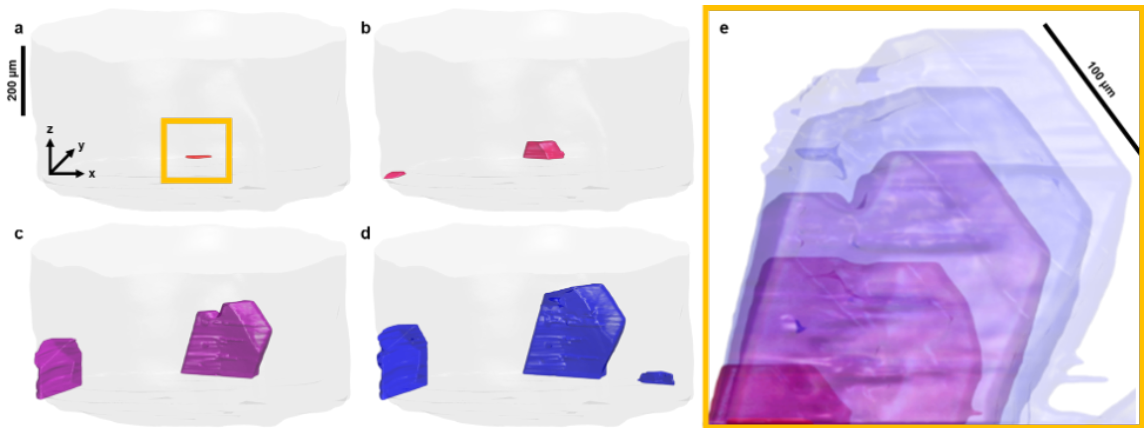

Figure 6.2: 3D growth behavior of the Si particles from X-ray tomographic reconstructions. (a-d) The Si particles are visualized at 912, 907, 884, 879 °C (22.5, 27.5, 69, 89 min after imposing a cooling rate of 1 °C/min to the melt at 934 °C), respectively. The transparent gray wall represents the oxide skin that contained the molten specimen. The Cu enriched liquid is rendered transparent for clarity. Si particle color reflects crystallization time, with early times in red and late times in blue. (e) A closer examination of the particle boxed in (a) suggests that Si undergoes a morphological instability during growth to attain, eventually, a convex geometry with a triangular mound projecting into the melt (*cf.* Fig. 6.1(b)). Shown are the Si particle at six time-steps: 912, 907, 890, 884, 879, 873 °C (22.5, 27.5, 44, 69, 89, and 120 min from start of cooling).

6.2.2 Morphology of Si Particles

We quantify the observed morphological evolution of the Si crystals by computing the degree of concavity of the crystals during the late stages of growth from μXRT reconstructions. We treat concavity as a structural signature of the re-entrant groove, i.e., where the twin boundary intersects the solid-liquid interfaces (see Fig. 6.1). That is, the presence of a re entrant groove implies that the Si crystals have a geometry that is at least partially concave. Our analysis involves generating the convex hull of the Si crystal – the intersection of all convex sets containing the crystal – and measuring the maximum normal distance from the convex hull to the crystal surface (arrow in inset (ii) of Fig. 6.3). We note that, given the crystals grows principally along their height, this choice of distance for quantifying concavity is reasonable. We limit our analysis to the same Si crystal as in Fig. 6.3(e). The concavity of the Si particle during growth is plotted in Fig. 6.3. Included in the inset are the 3D visualization of both the Si crystal (red) and the corresponding convex hull (light blue) at the three indicated time steps during growth. As the data show, the concavity initially increases and subsequently decreases as the crystal attains a more convex geometry. The initial rise in concavity distance can be explained by invoking the "growth accident" hypothesis [201], which postulates that growth twins are formed by errors in the stacking of 111 planes. Twinning, in turn, will lead to re-entrant grooves at the growth front. We postulate that the subsequent drop in concavity is due to the poisoning of the newly created re entrant groove by the impurity Sr atoms or clusters. Upon termination of the growth process, the Si crystal is fully convex, as indicated by the "filling" of the convex hull (concavity distance of zero). The non-constant concavity distance

indicates that the Si geometry is not self similar during growth, and that growth proceeds in a non-steady state manner.

6.2.3 Twinning Profile of Fully-Solidified Si Particles

To confirm the grain boundary characteristics and twinned interface of the fully solidified Si particles, we conducted electron backscatter diffraction (EBSD) on both the unmodified and modified Si crystals for comparison. Representative orientation maps of the two alloys are shown in Fig. 6.5. The mean crystallographic orientation of each grain of Si is colored according to the standard stereographic triangle on the top left of Fig. 6.5(a) while non-indexed regions, belonging to the Al phase and the surrounding eutectic matrix, are depicted as black. While the orientation maps provide only a qualitative intuition about the degree of crystallographic twinning as well as inter-lamellar spacing, they point a key striking difference in the twinning profile of the two systems: In the absence of chemical modification (Fig. 6.5(a,b)), the Si crystals consist of two parallel twin planes that run along the long axes of the crystals and intersect the solid liquid interface at the crystal edges. In the chemically modified crystal (Fig. 6.5(c,d)), only a single twin boundary runs along the crystal that then intersects the solid liquid interface at the crystal edges. The major distinction in the multiplicity of the twinned interface – doubly in unmodified Si, singly in modified Si – further supports the idea that the growth of modified Si crystals involves the selective poisoning of the re entrant grooves that are formed by the intersection of the 111 $\Sigma 3$ twin planes with the surface.

Quantitative analysis of the grain boundary character involves the computation of

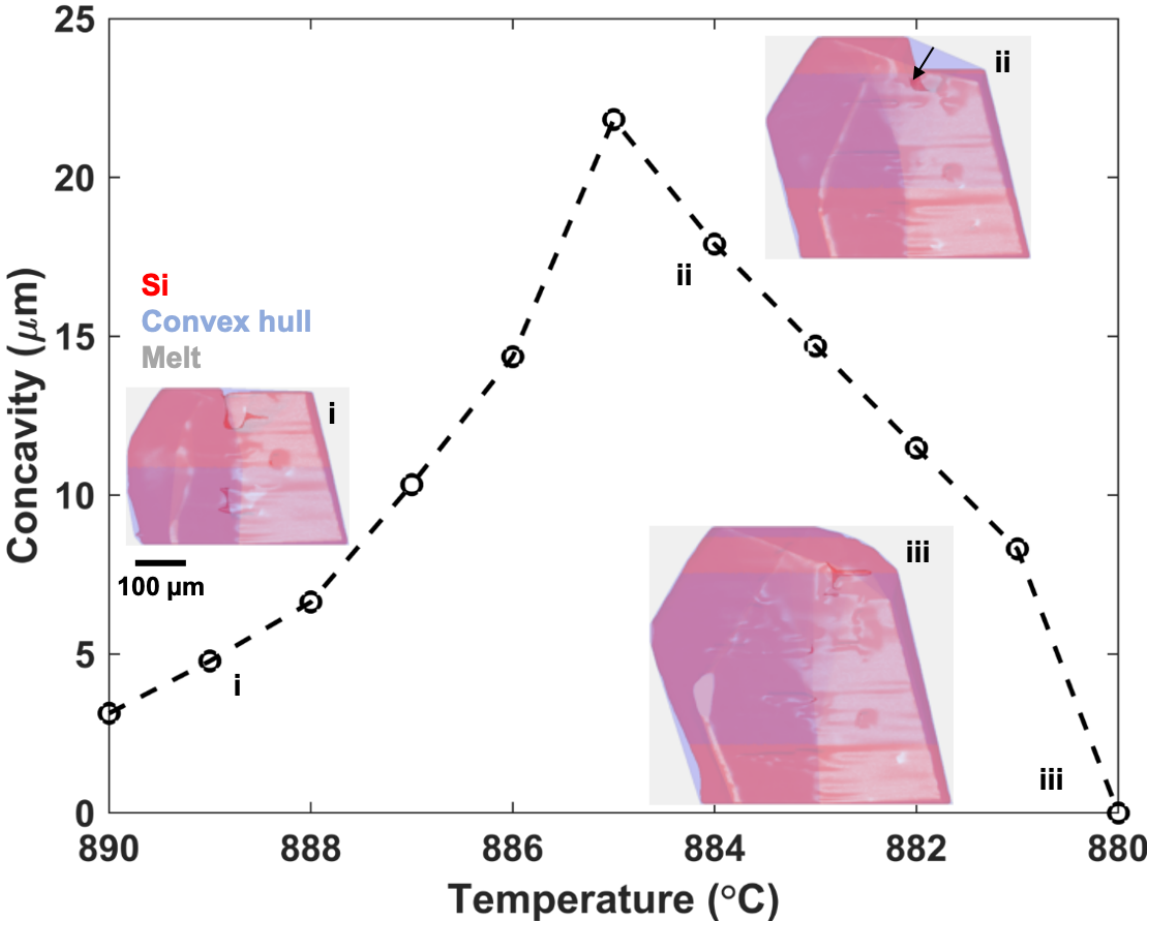

Figure 6.3: Evolution of Si morphology during growth. Concavity was calculated from the μXRT results as the length of the normal vector projected from the convex hull to the crystal surface (see arrow in inset (ii)). The analysis is limited to the single Si particle shown in Fig. 6.2(e), and the early times in growth are omitted due to the small size of particle at time step labeled i). The concavity initially increases and subsequently decreases as the crystal attains a more convex geometry. The latter suggests a disappearance of the concave re entrant groove. Inset: Si particle (red) and its corresponding convex hull (light blue) at the three indicated time steps (denoted i, ii, and iii) during growth showing that the crystal is fully convex as growth terminates, thus "filling" its convex hull.

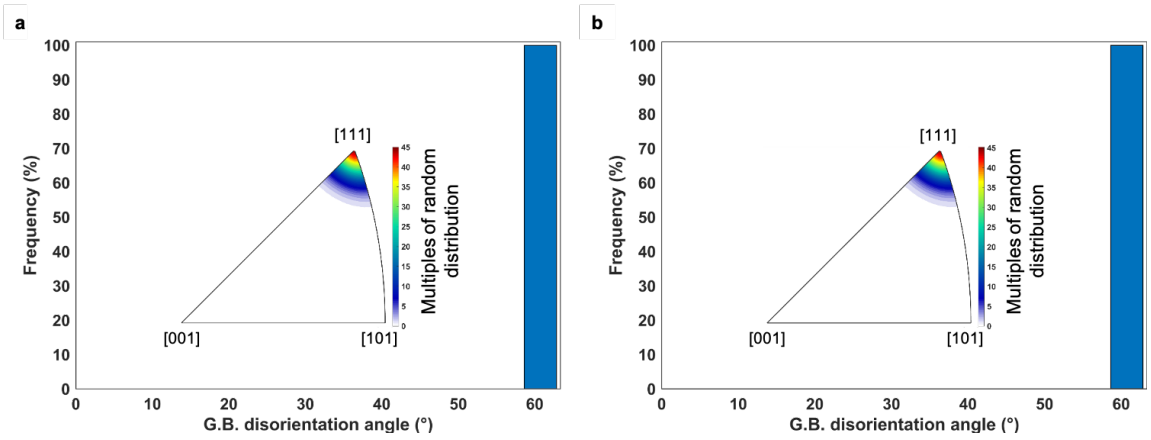

Figure 6.4: Uncorrelated misorientation distribution function of Si crystals. (a) Unmodified and (b) modified Si. MODF is represented as the distributions of the angle and axis (inset) of misorientation. In both cases, the only grain boundaries are the coherent Σ3 {111} twins.

the uncorrelated misorientation distribution function (MODF) using the discretized EBSD data taken from the interior region of a representative Si crystal (see Fig. 6.4).

In this analysis, only individual crystals were considered to avoid the potential ambiguity that would otherwise result if considering the entire collection of Si crystals in the fully solidified microstructure which might not have an orientation relationship. The MODF for both unmodified and modified Si is represented in Fig. 6.4 as the distribution of both angle and axis of misorientation. In both the unmodified and modifies Si, we observe only a single misorientation angle at 60° corresponding to the $< 111 >$ misorientation axis (cf. misorientation angle plot and axis (insets) in Fig. 6.4). This combination of $60°/< 111 >$ represents the Σ3 111 coherent twin boundary, demonstrating the high incidence of coherent twins in polycrystalline Si particles independent of chemical modification [173]. Thus, chemical modification influences not the character of the twin boundaries but rather their *multiplicity*.

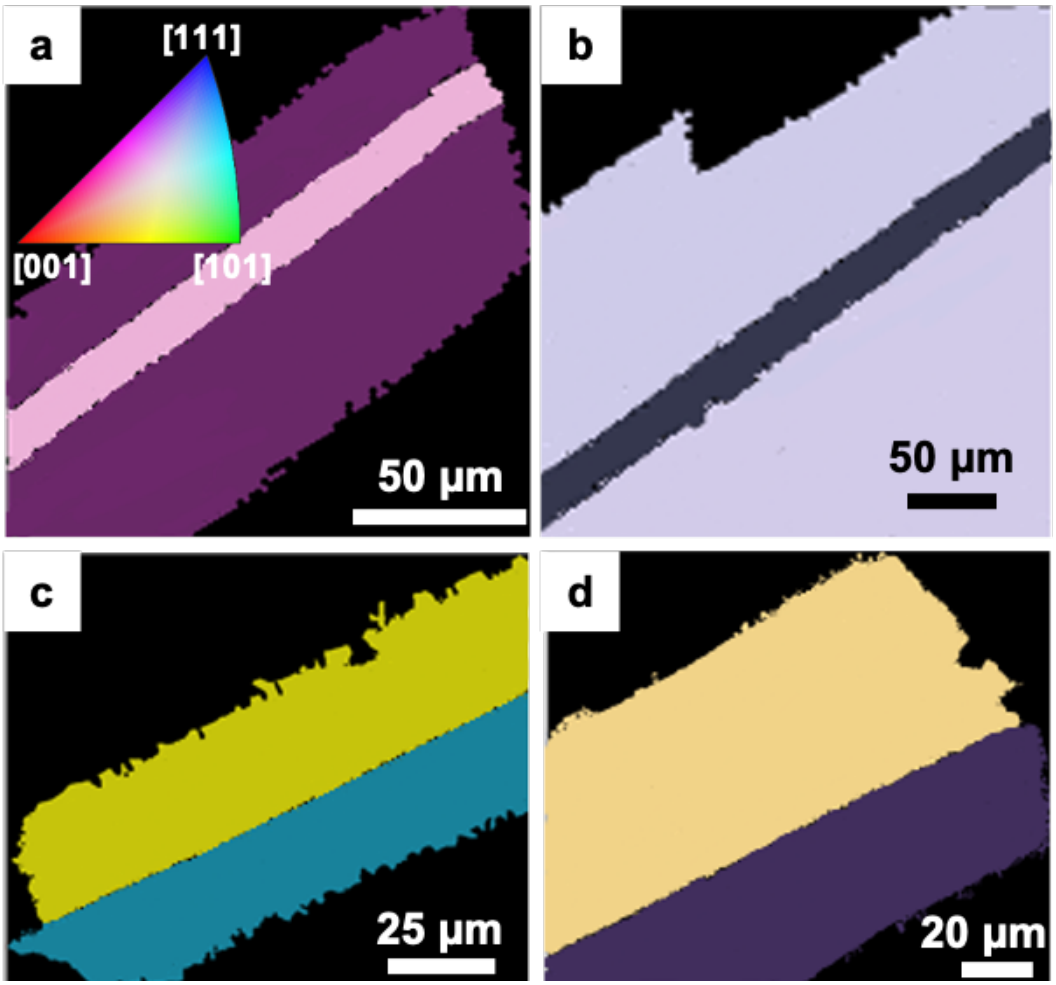

Figure 6.5: The impact of chemical modification on the twinning behavior of fully-solidified, primary Si particles. (a,b) EBSD orientation maps of two representative unmodified Si particles show the existence of two parallel twin planes running across the length of the Si particles and intersecting the solid liquid interface at the edges of the particles. (c,d) Orientation maps of two representative chemically modified Si particles display singly twinned interface. Similar to the unmodified case, the twin plane intersects the solid liquid interface at the edge of the particle. In all maps, the mean crystallographic orientation of each grain of Si is colored according to the standard stereographic triangle on top left of (a); the surrounding eutectic matrix is depicted black.

6.2.4 Nucleation of Impurity Clusters on the Si Crystal Surfaces

The morphological instability of Si crystals during growth (Figs. 6.2, 6.3) as observed through *in situ* μXRT experiments, together with the absence of parallel twins in chemically modified Si crystals as confirmed by EBSD texture analysis (Fig. 6.5), point to the poisoning of the re entrant groove in Si upon chemical modification. To verify this hypothesis, we calculate the nucleation barrier of an arbitrary impurity cluster as a function of wetting strength for a re entrant groove, a ridge, and a flat surface (*cf.,* Fig. 6.1(c)), according to classical nucleation theory (CNT) [202] (*cf.,* Section 2.1); a brief sketch is outlined below:

The inset in Fig. 6.6 displays a Sr-containing cluster with a (semi)spherical embryonic form nucleated on Si. This embryonic form is based on the assumption of isotropic surface free energies of the phases involved. Plotted in Fig. 6.6 is the ratio of the barriers of the heterogeneous ("het") and homogeneous ("hom") nucleation. This ratio can be computed as the ratio of the volumes of the corresponding nuclei: the nucleus partially "buried" by the Si surface in the heterogeneous case and the "isolated" nucleus in the homogeneous case [202, 203],

$$\frac{\Delta G^{\star}_{het}}{\Delta G^{\star}_{hom}} = \frac{V^{\star}_{c,het}}{V^{\star}_{c,hom}} \tag{6.1}$$

In the homogeneous case, the volume is that of a sphere of radius r (isotropic

approximation):

$$V_{c,hom} = \frac{4}{3}\pi r^3 \tag{6.2}$$

According to Sholl and Fletcher [202], the heterogeneous volume $V^{\star}_{c,het}$ can be found by integrating over the line of intersection of the curved part of the nucleus surface and the area of the interface between the nucleus and one of the two planes of the step (see also inset of Fig. 6.6). We refer subsequently to the derivation by Sholl and Fletcher [202] for that derivation; here we invoke their integrated expression for the volume $V^{\star}_{c,het}$ of the heterogeneous nucleus as a function of step angle η and contact angle α (labeled in inset of Fig. 6.6):

$$V^{\star}_{c,het} = \frac{r^3}{r}[cos\alpha sin^2\alpha sin\phi - cos\alpha(3 - cos^2\alpha)\phi + 4sin^{-1}(sin\frac{\phi}{2}sin\frac{\eta}{2})] \tag{6.3}$$

where ϕ is given by

$$cos\frac{\phi}{2} = cot\alpha cot\frac{\eta}{2} \tag{6.4}$$

Combining Eqs. 6.1-6.4 yields the following expression plotted in Fig. 6.6:

$$\frac{\Delta G^{\star}_{het}}{\Delta G^{\star}_{hom}} = \frac{cos\alpha sin^2\alpha sin\phi - cos\alpha(3 - cos^2\alpha)\phi + 4sin^{-1}(sin\frac{\phi}{2}sin\frac{\eta}{2})}{4\pi} \tag{6.5}$$

We note that η takes on three discrete values depending on the local geometry of

a {111}-faceted Si particle: (1) the re-entrant groove has $\eta = 2\pi - 2cos^{-1}[\frac{1}{3}(111) \cdot (\overline{1}\overline{1}1)] \approx 141°$; (2) a ridge has $\eta = 2\pi - 2cos^{-1}[\frac{1}{3}(111) \cdot (11\overline{1})] \approx 219°$; (3) a {111} facet plane is devoid of steps and thus $\eta = 180°$. The notation $a \cdot b$ indicates the dot product between vectors a and b.

The results of the calculation sketched above is plotted in Fig. 6.6, and they indicate that impurity nucleation is more favorable at the re entrant groove for all contact angles θ relative to the twin plane. A schematic of the nucleus and nucleant geometry is provided as inset in Fig. 6.6. We point out that the spherical impurity cluster effectively "caps" the twin boundary, thereby blocking its continued propagation. This geometry is different from that of [204], which assumes that the nucleus itself is twinned. We note also that the concavity distance, as defined above, scales with the cosine of the half-angle $\frac{\eta}{2}$ of the crystal step angle η. Thus, for a flat facet ($\eta = 180°$) concavity is identically zero; grooves and ridges ($\eta = 141°$ and $219°$, respectively) have equal concavity (in magnitude). Despite the latter observation, the unfavorable nucleation of impurity cluster on a ridge compared to a groove (Fig. 6.6) explains why one twin survives and the other is poisoned, respectively. Poisoning occurs on the re-entrant groove, which explains why the high concavity seen in Fig. 6.3 is short-lived. Ultimately, the Si particle geometry determines the potency of impurity nucleation.

An interesting question is how exactly the Si crystal grows *around* the impurity clusters, once the latter have nucleated on the re-entrant groove. The termination of a twin boundary is expected to produce dislocations [205, 206] ahead of the impurity cluster in order to accommodate for the internal strain field. This question can

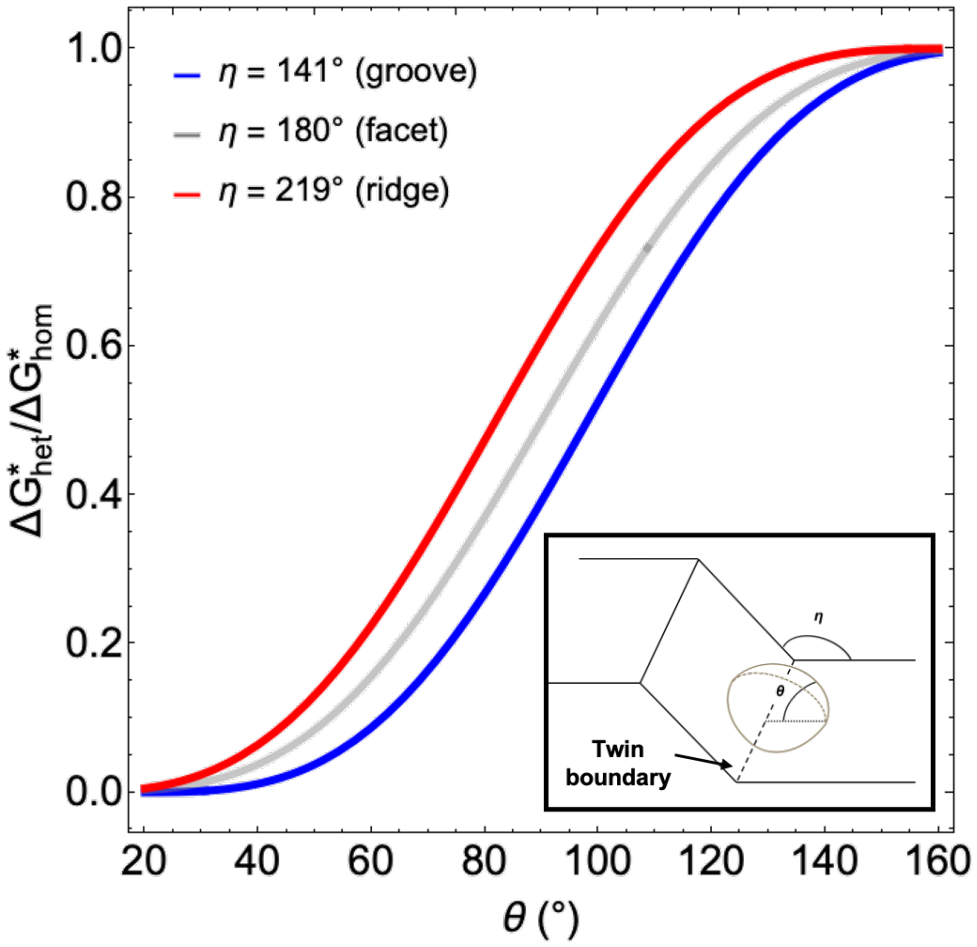

Figure 6.6: Nucleation potency of impurity clusters on the Si crystal surfaces. Ratio of heterogeneous to homogeneous nucleation barriers as a function of wetting strength (contact angle θ) is plotted for a re entrant groove, flat facet, and ridge (crystal step of angle η), computed *via* CNT [202]. For all contact angles, nucleation along the concave re-entrant groove is found to be more favorable than on the flat facet plane or along the convex ridge. Inset: Spherical droplet (light brown) nucleating with contact angle θ relative to the twin plane (dashed line) and step angle η.

be readily addressed through simulation, *e.g.,* phase field crystal, which describes atomic-scale dynamics (such as dislocation creation and annihilation) on diffusive timescales [207]. We leave this open question for further research.

6.3 Summary

We demonstrated the interplay of chemical modification, growth kinetics, and crystallographic defects that perturb the faceted solid liquid interfaces upon crystallization. By combining *in situ* and *ex situ* experiments with thermodynamic calculations, we showed that chemical modification deactivates the advantage of the twin plane re entrant edge mechanism wherein two parallel twins enable a continuous, steady state propagation of crystals from the melt. The chemically modified crystallization proceeds according to the poisoning of the twin plane re entrant groove. Consequently, the singly-twinned particles cannot grow in a steady-state fashion. These results provide insights into the relationship between the distribution of crystal defects and 'spectator' species such as dopants or impurities, with implications to a broad range of applications including metallurgy, semiconductor processing, and additive manufacturing.

6.4 Materials and Methods

6.4.1 X-Ray Microtomography

Sample preparation

Alloy buttons of nominal composition Al 32wt.%Si 15wt.%Cu 0.1wt.%Sr were cast *via* vacuum arc remelting at the Materials Preparation Center at Ames Laboratory, using 5N purity Al, 6N purity Si, 4N purity Cu, and 4N purity Sr. We note that the composition of Si (32 wt.%) in the present study is the same as that in the recent report of the unmodified alloy investigated in ref. [133]. For the synchrotron X-ray tomography (μXRT) experiments, the as prepared alloy buttons were cut in the shape of cylindrical rods of 1 mm diameter by 5 mm length *via* electrical discharge machining.

Beamline Setup

The μXRT experiments were conducted at the Beamline 2 BM of the Advanced Photon Source at Argonne National Laboratory (Lemont, IL, USA) and largely followed those of ref. [30]. Typical solidification experiments began with melting the sample by heating to 935 °C and maintaining isothermally until a fully liquid sample was observed in μXRT reconstructions. The homogenized melt was then cooled at a rate of 1 °C/min, thereby solidifying the primary Si crystals (below the liquidus temperature of 910 °C). Experiments ran for over two hours (final temperature of 808 °C). Throughout the duration of the experiments, a polychromatic 'pink' X-ray beam illuminated on the samples and a 20 μm thick LuAg:Ce scintillator converted

the transmitted X-rays to visible light. Images were recorded by a PCO Edge CMOS camera equipped with a 10x magnifying objective to provide isotropic pixel sizes of 0.65 mm x 0.65 mm. The tomographic field-of-view measured 2,560 x 600 pixels (i.e., 1,664 mm x 390 mm). The camera frame rate and exposure time were 50 Hz and 14 ms, respectively. Given the 1 mm diameter of each sample, the temperature distribution was assumed to be uniform within the sample. During acquisition, the sample was rotated continuously at a rate of 6° per second. For each 180° rotation of the sample, 1,500 projections were collected. The large number of projections (in addition to the high exposure time of 14 ms) guaranteed high quality images. This combination of acquisition parameters optimally allowed for a temporal discretization of 20 s between consecutive 3D reconstructions. In total more than 90,000 projections and over 60 total reconstructions were collected.

Data Visualization

Reconstruction of the μXRT data was performed using TomoPy, a Python based open source framework for the processing of tomographic data [182]. Within TomoPy, the X-ray projections were first normalized by the dark and white field images to account for beam instabilities. Additional correction for "ring" artefacts was made *via* combined wavelet Fourier filtering [183]. Subsequently, the data were reconstructed *via* the direct Fourier based Gridrec algorithm [184]. The reader is referred to ref. [182], and references therein, for further details. In order to enhance the contrast between the solid and liquid phases, and minimize any systematic image artefacts, reconstructions of the fully-liquefied sample were subtracted from all other recon-

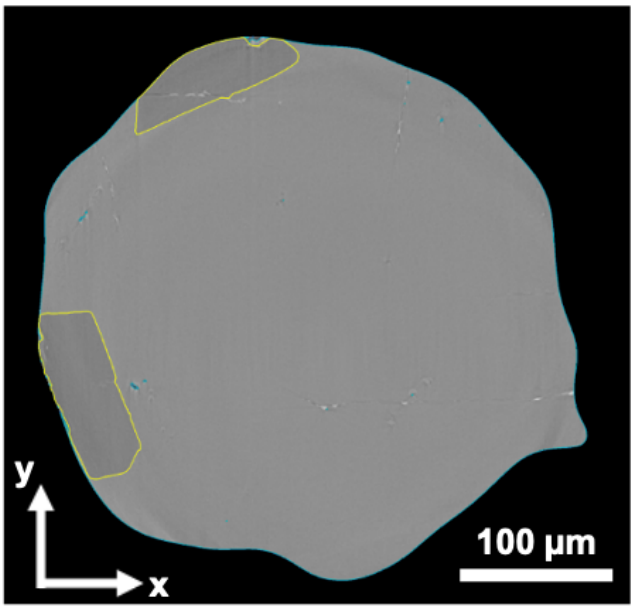

Figure 6.7: Segmentation of Si crystals in tomographic reconstructions. The edges of the segmentation output are overlaid on top of the raw (grayscale) image. Edges of Si are shown in yellow, and those the melt are shown in blue. The segmentation result shows good agreement with the reconstructed structures underneath.

structions. A representative 2D slice of 3D reconstruction, parallel to the axis of rotation of the cylinder-like sample, is given in Fig. 6.7.

The strong absorption contrast between the constituents (partition coefficient of Sr $<<$ 1) allows one to easily distinguish between the two coexisting phases: primary Si crystals (dark gray), and Al liquid matrix (light gray). Subsequently, the grayscale reconstructions of this region were segmented, i.e., transformed into a computable representation of their parts (liquid + Si crystals). Our segmentation algorithm, implemented in the Image Processing Toolbox of MATLAB R2016a, comprised of (i) multi-level thresholding, (ii) edge-based methods for finding the boundaries of 'ob-

jects' (Si and Al) within images, and (iii) morphology-based methods (*e.g.,* dilation and erosion) in order to remove speckle noise (small objects) as well as to smooth the border of large objects [208]. Figure 6.7 shows the edges of the segmentation output overlaid on the original reconstruction (edges of Si are yellow, and those of Al are blue). The results indicate excellent agreement with the crystals underneath. The segmented 2D images were then stacked along the third spatial dimension to reveal the 3D microstructures.

6.4.2 Electron Backscatter Siffraction

Sample preparation

Fresh samples with and without chemical modifier were prepared for EBSD experiments following the same solidification parameters as beamline experiments described above. The solidified samples were then mechanically ground and polished, which were then polished further by Xe plasma focused ion beam using a Thermo Fisher Helios G4 PFIB UXe.

Texture Analysis *via* EBSD

Crystallographic investigation of the fully solidified Si crystals with and without chemical modification was performed using an EBSD equipped Tescan MIRA3 scanning electron microscope. For the EBSD experiments, the beam voltage was adjusted to 30 kV; the working distance, tilt, and step size were set to 20 mm, 70° relative to normal incidence, and 0.5 to 2 μm, respectively. Analysis of the texture data was performed using the MATLAB toolbox MTEX [188] in order to generate orientation

maps and misorientation distributions.

6.5 Data Availability

The raw XRT projection data, as well as a movie of the XRT reconstructions showing the appearance of triangular mounds projecting into the melt during growth, are publicly available in the University of Michigan Deep Blue Data repository at `https://doi.org/10.7302/812m-d307`.

6.6 Acknowledgements

We gratefully acknowledge financial support from the NSF CAREER program under award number 1847855. We thank Caleb Reese and Mushfequr Rahman for assisting in the synchrotron experiments. We also acknowledge the University of Michigan College of Engineering for financial support and the Michigan Center for Materials Characterization for use of the instruments and staff assistance, in particular Drs. Robert Kerns and Nancy Senabulya Muyanja for aid in EBSD experiments. This research used resources of the Advanced Photon Source, a U.S. Department of Energy (DOE), Office of Science User Facility operated for the DOE Office of Science by Argonne National Laboratory under Contract number DE-AC02-06CH11357.

Part III

Emergence of Two-Phase Spirals *via* Multi-Step Crystallization and their Thermal Stability

Chapter 7

Multi-Step Crystallization of Self-Organized Spiral Eutectics

This chapter is based on the article published in *Small* [25].

7.1 Introduction

Solidification *via* crystallization is the seminal procedure controlling the processing of virtually all metals and alloys in use today, yet controlled crystallization can be utilized as a prototypical self-assembly strategy for synthesizing patterned structures across multiple length-scales. The centrality of crystallization phenomena in many scientific fields has spurred decades of research [20, 209, 210, 211, 212, 213, 214, 46] into this "secretive" [215] process. By tuning the growth conditions, it is possible to steer the system down different kinetic pathways to produce transient or metastable states (*e.g.,* polytetrahedral or disordered phases) on intermediate time–scales [216,

217]. In particular, non-equilibrium routes to metastable states could unveil patterns not seen in equilibrium states. Thus, an understanding of crystallization phenomena is the key to lock into place materials with morphologies and/or functionalities not present in equilibrium states [46, 216, 218, 22]. Particularly appealing are spiral eutectics [23], mixtures of two or more solid phases that grow simultaneously from a parent liquid phase and which arrange into intricate spiraling patterns, in some cases akin to a DNA helix. The intrinsic chirality of spiral eutectics offers a new strategy for rapid, bottom-up manufacturing of large-area photonic materials in the visible/infrared spectrum [23, 219], owing to the fact that conventional top-down techniques—whose speed and complexity scale up with the number of helices—sets a bottleneck for large-scale production [220].

Despite the technological promise of spiral eutectics, their adoption has been hampered largely by the lack of technical insight into their growth pathway. Thus far, spiral patterns have been observed in the Al-Th [40], Al-Ag-Cu [221], and Zn-Mg alloy systems [63, 222, 65, 223], as well as a few non-metallic systems. These reports offer competing proposals for the mechanism of spiral growth, including different growth rates of the eutectic phases,19 grain rotations along the eutectic growth direction [224], diffusional instabilities caused by a third component [54], osmotic flow-driven fingering [225], tilted growth in directional solidification [226], and thermal fluctuations [227]. Such phenomena may occur simultaneously or sequentially over the course of crystallization, and thus it is difficult to conclusively isolate the dominant factor for spiral formation. For these reasons, spiral growth is the least understood among all eutectic morphologies (including lamellar and rod [55]), yet it produces

quite dramatic effects. Unraveling spiral growth dynamics requires multiscale 3D and time-resolved measurements.

Here, we pursue a systematic investigation to uncover the origin of spiral growth in Zn-Mg alloys produced *via* directional solidification (DS). The as-solidified microstructures are chiral, faceted, and periodic with interphase spacing comparable to the wavelength of infrared light. To trace the emergence of such structures from the parent liquid, we employ correlative and multiscale microscopy encompassing fundamentally 3D measurements together with *in situ* and atomic-resolution imaging. Machine learning (random forest classification [228]) was used to analyze the 3D datasets for robust tracking of the interfaces of the complex eutectic colonies. We discovered that the metastable $MgZn_2$ Laves phase nucleates first from the liquid, with crystallographic defects (screw dislocations) that intersect its solid–liquid interfaces and catalyze the spiral growth of the two-phase microstructure. While screws are generally assumed to provide necessary step edges for crystallization [78], this work demonstrates that dislocation-driven growth is more widespread than previously imagined; it enables the simultaneous growth of two phases upon spiral eutectic crystallization. These insights open the doors to rapid fabrication and additive manufacturing of 3D chiral photonic materials.

7.2 Results and Discussion

7.2.1 Microstructure Synthesis and Informatics

Synthesis was carried out directionally by the Bridgman–Stockbarger technique, allowing for crystallization at a constant velocity V in a decoupled unidirectional thermal gradient G. In the present investigation of Zn-Mg alloys, the crystallization pathway bifurcates into two competing growth forms, depending on the combination of V and G: thermodynamically stable, rod-like Zn-Mg_2Zn_{11} and metastable, spiral Zn-$MgZn_2$ eutectics. We find a transition from the former to the latter at critical velocities, in qualitative agreement with the DS studies by Liu and Jones [223]. Rigorous analysis of this phase selection, along with microstructural informatics describing the patterns including spirals, are presented in this sub-Section. In the subsequent sub-Sections, we focus on the emergence of the spiral patterns in Zn-$MgZn_2$. Out of 195 spirals we examined, we found an equal proportion of spiral handedness (99 right- and 96 left-handed).

Competitive Growth of the Two Eutectics

Two distinct morphologies are observed in directionally-solidified samples: rod-like Zn-Mg_2Zn_{11} and predominantly spiral Zn-$MgZn_2$ (Figs. 7.1(a) and (b), respectively); compositions were determined *via* energy dispersive X-ray spectroscopy (Table 7.1).

The Zn-$MgZn_2$ microstructure also shows non-spiral regions characteristic of irregular eutectics [60], *i.e.,* varying interphase spacing and branching of the phases. Furthermore, compared to the irregular eutectic, the spiral has finer features (spiral

	Spiral eutectics		Rod eutectics	
	Zn-rich phase	Mg-rich phase	Zn-rich phase	Mg-rich phase
Mg (at.%)	3.17 ± 0.87	32.90 ± 0.81	5.26 ± 0.18	18.86 ± 0.96
Zn (at.%)	96.83 ± 0.87	67.10 ± 0.81	94.74 ± 0.18	81.14 ± 0.96
Composition	Zn	$MgZn_2$	Zn	Mg_2Zn_{11}

Table 7.1: Compositional analysis of directionally-solidified eutectics. Compositions of the eutectic phases are assigned based on elemental analysis *via* energy-dispersive X-ray spectroscopy. Values represent means and standard deviations from four measurements.

thickness ∼100 nm, ∼1 μm interphase spacing). As Fig. 7.1(b) also shows, the spirals possess either right- or left-handedness.

Phase selection can be rationalized by the competitive growth principle [60] (*cf.* 7.2.1), which states that the growth form with the highest interface temperature (lowest undercooling) dominates. Figure 7.1(c) shows the growth temperatures of the two eutectics in relation to V and G in DS experiments. The points of intersection in the temperature-velocity curves (below) match the observed transitions from rod to spiral eutectic, *e.g.,* between $V = 0.8 and 3.3 \frac{mm}{s}$ for $G = 0.5 \frac{K}{cm}$ (Fig. 7.2). This result also agrees qualitatively with that of Liu and Jones [223], who report a similar transition behavior in their metallographic observations but do not consider the influence of G in phase selection. Equations for the curves in Fig. 7.1(c) were derived from Jackson and Hunt's theory [229, 55] (*cf.* 2.3.1), which models the steady-state growth of eutectics by calculating the solutal diffusion field in the liquid. For the regular, rod-like Zn-Mg_2Zn_{11} eutectic, we use the following kinetic parameters

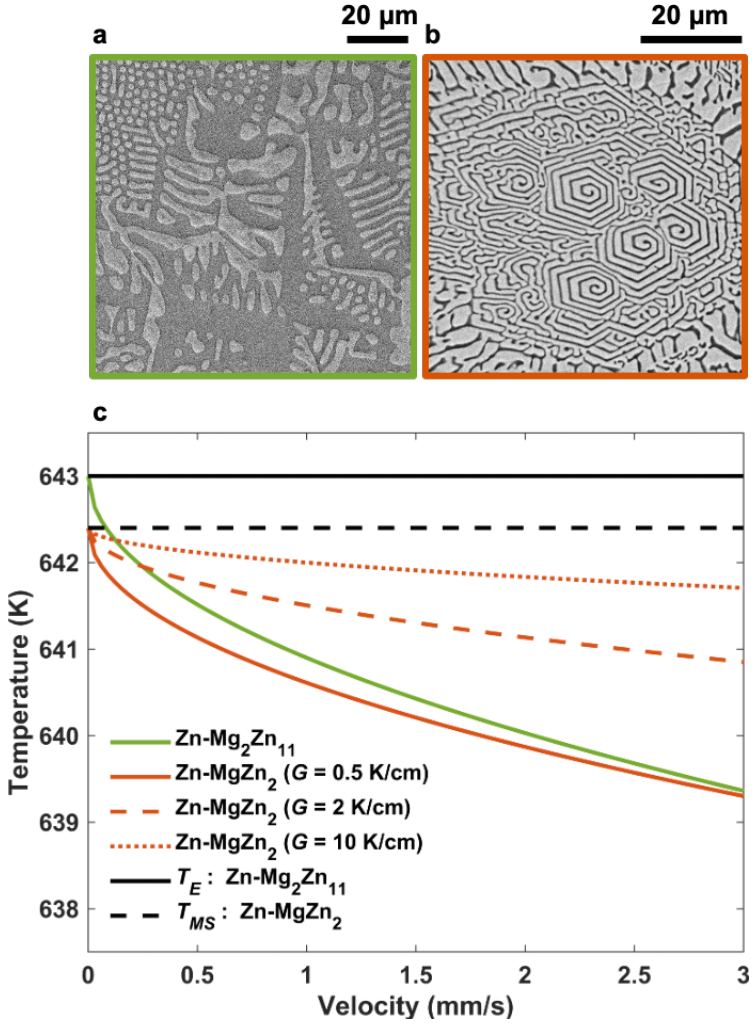

Figure 7.1: Competitive growth and morphological selection between two eutectics. (a,b) Backscattered electron micrographs of the rod-like Zn-Mg_2Zn_{11} and spiral Zn-$MgZn_2$ eutectics, respectively. In both, the Zn phase is light gray. (c) Diagram showing the growth temperatures of the two eutectics (colored lines) in relation to the growth velocity V and thermal gradient G in directional solidification experiments. The growth form with the highest interface temperature dominates, either the thermodynamically stable Zn-Mg_2Zn_{11} or metastable Zn-$MgZn_2$ eutectic. Equations for the curves were calculated based on the observed transition velocities from Fig. 7.2. The eutectic temperatures for both the equilibrium and metastable growth forms (T_E and T_{MS}) are also plotted (black lines).

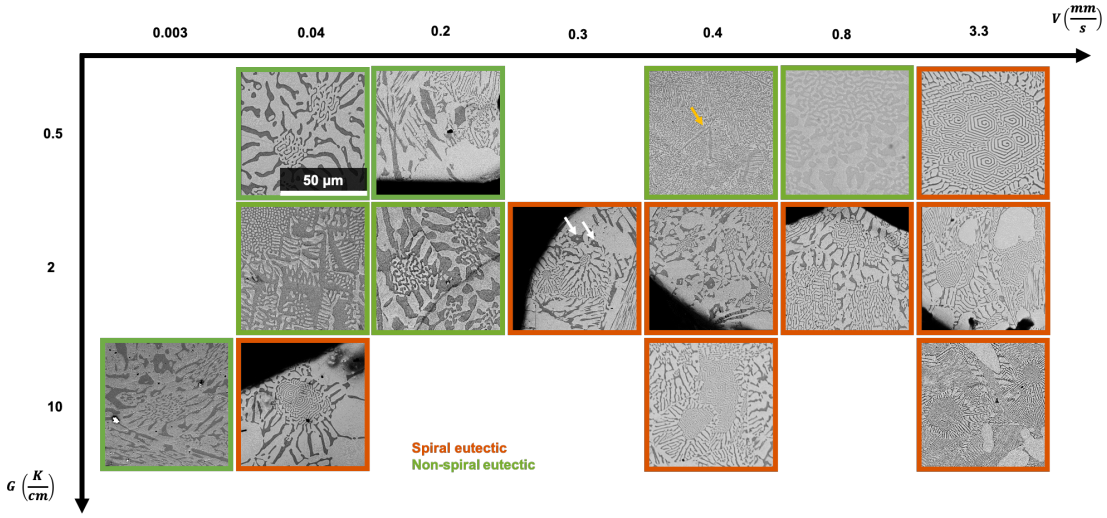

Figure 7.2: Phase selection and morphology map in the Zn-Mg eutectic alloy system. Scanning electron micrographs of samples from directional solidification (DS) experiments are shown; the imposed thermal gradient G and growth rate V in DS experiments are plotted along the vertical and horizontal axes, respectively. Samples with spiral morphology are boxed orange, while those with a non-spiral morphology are boxed green. All samples with spiral morphology have the metastable Zn-MgZn2 composition while those with rod-like morphology (e.g., V = 0.4 mm/s, G = 0.5 K/cm) have the Zn-Mg2Zn11 composition, as confirmed by elemental analysis via energy-dispersive X-ray spectroscopy (Table 7.1). White arrows on center image show open-core MgZn2 particles; yellow arrow on third image of top row shows the complex regular structure of the Zn-Mg2Zn11 eutectic (see discussion in main text).

reported by Liu and Jones [223],

$$K_1 = 13.1 \times 10^{-9} wt.\%m \tag{7.1}$$

$$K_2 = 0.58 \times 10^{9} \frac{wt.\%s}{m^2} \tag{7.2}$$

$$m = (\frac{1}{m_\alpha} + \frac{1}{m_\beta})^{-1} = 12.10 \frac{K}{wt.\%} \tag{7.3}$$

where α is the Zn phase, β is the $MgZn_2$ phase, $m_\alpha = 18.5 \frac{K}{wt.\%}$ and $m_\beta = 35 \frac{K}{wt.\%}$. The governing Jackson-Hunt equation is then expressed as

$$\frac{\Delta T}{\sqrt{V}} = \sqrt{4m^2 K_1 K_2} = 2.1 \frac{K}{\sqrt{\frac{mm}{s}}} \tag{7.4}$$

where ΔT is the total undercooling given by ${T_E}^{Zn-Mg_2Zn_{11}} - T = 643K - T$, where ${T_E}^{Zn-Mg_2Zn_{11}}$ and T are the equilibrium and growth temperatures, respectively. ${T_E}^{Zn-Mg_2Zn_{11}}$ for the stable Zn-Mg_2Zn_{11} eutectic (643 K) was found from a recent thermodynamic assessment [230] of the Zn-Mg system. Thus, upon rearrangement of Eq. 7.4, the $T - V$ plot for the rod-like eutectic shown in Fig. 7.1(c) is

$$T = 643 - 2.1\sqrt{V} \tag{7.5}$$

where T is in Kelvin and V in $\frac{mm}{s}$.

For the spiral Zn-$MgZn_2$ eutectic, we adapt the irregular growth model of Kurz

and Fisher [53] (*cf.* 2.3.2), *i.e.,* the undercooling is a function of both V and G in DS experiments, according to

$$\frac{\Delta T}{\sqrt{V}} = \frac{K_3}{\sqrt{G}} \tag{7.6}$$

where K_3 is the kinetic coefficient, and ΔT is the total undercooling (here, ${T_E}^{Zn-Mg_2Zn_{11}} - T$, where T is the growth temperature). It is reasonable to consider Zn-$MgZn_2$ as an irregular eutectic since $MgZn_2$ is a faceted phase (its Jackson α-factor is at most 5.7, *i.e.,* below the threshold value of 2). Unfortunately, the growth kinetics of the metastable Zn-$MgZn_2$ eutectic are not well-known and thus the parameter K_3 needs to be evaluated, as follows. Solving the system of equations (Eqs. 7.5 and 7.6) at the point of morphological transition (*i.e.,* between $V = 0.8$ and $V = 3.3\frac{mm}{s}$ for $G = 0.5\frac{K}{cm}$), we obtain $K_3 = 0.4\frac{K}{\sqrt{\frac{mm}{s}}}$ and ${T_E}^{Zn-Mg_2Zn_{11}} = 642.4K$. Thus, upon rearrangement of Eq. 7.6, the $T - V$ curves for the spiral eutectic (evaluated at the three thermal gradients G shown in Fig. 7.1(c)) are as follows:

$$T = 642.4 - 0.4 \times \sqrt{\frac{V}{0.05}} for G = 0.05\frac{K}{mm} \tag{7.7}$$

$$T = 642.4 - 0.4 \times \sqrt{\frac{V}{0.2}} for G = 0.2\frac{K}{mm} \tag{7.8}$$

$$T = 642.4 - 0.4 \times \sqrt{V} for G = 1\frac{K}{mm} \tag{7.9}$$

As expected, the points of intersection of Eq. 7.7- 7.9 with Eq. 7.4 follow the

morphological transitions seen in Fig. 7.2.

Probability of Spiral Handedness

Combining the scanning electron micrographs from all the DS experiments, a total of 195 spirals were observed. Among this total count N, 99 spirals were right-handed and 96 left-handed (50.8% and 49.2%, respectively). We performed statistical hypothesis testing to provide descriptive statistics for the handedness of spirals and evaluate whether it can be considered as an equal (50:50) probability event. The analysis is as follows, where we choose a confidence level of 95%.

$$N = 99 + 96 = 195 \tag{7.10}$$

where π = true proportion of left-handed spirals Null hypothesis: $H_0 : \pi = 0.5$ Alternate hypothesis: $H_a : \pi \neq 0.5$ Significance level: $\alpha = 1 - (confidencelevel) = 0.05$

$$r = \frac{96}{195} = 0.492 \tag{7.11}$$

$$Z = \frac{r - 0.05}{\sqrt{\frac{0.5 \times 0.5}{195}}} = -0.2148 \tag{7.12}$$

From statistical tables and given the above Z-score, the area of tail with $\alpha = 0.05$ is 0.4013.

$$p - value = 2 \times 0.4013 = 0.8026 > \alpha = 0.05 \tag{7.13}$$

Therefore, we cannot reject the null hypothesis; left- and right-handed spirals have equal probability with 95% confidence level.

Microstructure Informatics based on Scanning Electron Micrographs

Rigorous quantification of microstructures can help establish robust structure property processing relationships that, in turn, could identify manufacturing paths to achieve the desired material microstructure. In order to provide a complete set of statistical measures describing the spiral eutectic microstructure, we employ the recently developed stochastic framework for microstructure informatics that is based n point spatial correlations ("n-point statistics") [231, 232]. This algorithm has been demonstrated to mine the essential information in large microstructure datasets with high computational efficiently [231, 232]. The framework starts with a discretized representation of the microstructure function. In the simplest case of 1-point statistics, the algorithm takes as an input the spatial position in the microstructure and the local state of interest (*e.g.,* grain orientation or chemical composition), and the output corresponds to the volume fraction of the selected phase.

Analogously, 2-point statistics captures the probability density associated with finding local states h and h' at the tail and head, respectively, of a prescribed vector r randomly placed into the microstructure. To remove the influence of varying lamellar thickness, we implement this analysis on the skeletonized segmented image (see Fig. 7.4) of the original micrograph (Figure S4A,B; the original micrograph is shown in Fig. 7.2). The center point in the auto correlation map shown in Figure S4C corresponds to $r = 0$ and reflects the volume fraction of local state in the microstructure.

The map also captures important morphological details of the microstructure such as the hexagonal symmetry, interphase spacing (the distance between the peak at the center and the satellite peaks in its immediate vicinity), as well as the inherent isotropy in the spatial correlations present in the microstructure, corresponding to the hexagonal, faceted structure of $MgZn_2$. In going from the auto correlation map to the pair correlation function (PCF) in Fig. 7.3(d), we remove the dependence on the direction of the vector separating the two points and instead find the probability of finding local states h and h' separated by a distance $|r|$. The PCFs of two distinct microstructures are provided ($V = 0.04$ and $0.4\frac{mm}{s}$, keeping $G = 10\frac{K}{cm}$ for both; micrographs in Fig. 7.2). The peak in the PCFs at around $r \approx 0.02$ μm represents the distance between parallel spiraling arms. The data indicate that the lamellar spacing within a spiral colony is not very sensitive to the growth conditions.

7.2.2 Morphology of Spirals in 3D

Past reports have shown that eutectic spirals mostly develop a helical morphology [54, 226]. To determine if the same holds true for the Zn-$MgZn_2$ spirals (Fig. 7.1(a) and 7.2), we examined the microstructure in 3D *via* X-ray nano-tomography (nTXM). Machine learning (random forests algorithm [228]) was utilized to segment the X-ray reconstruction images into the two eutectic phases; Fig. 7.4, shows excellent agreement between the segmentation output and the eutectic structures visible in the unprocessed data. Figure 7.5(a) and Movie #1 available in the online repository (Section 7.5), show the full nTXM region-of-interest displaying multiple spiral eutectic nodules (colonies) and their pyramidal enveloping shapes (false coloring is

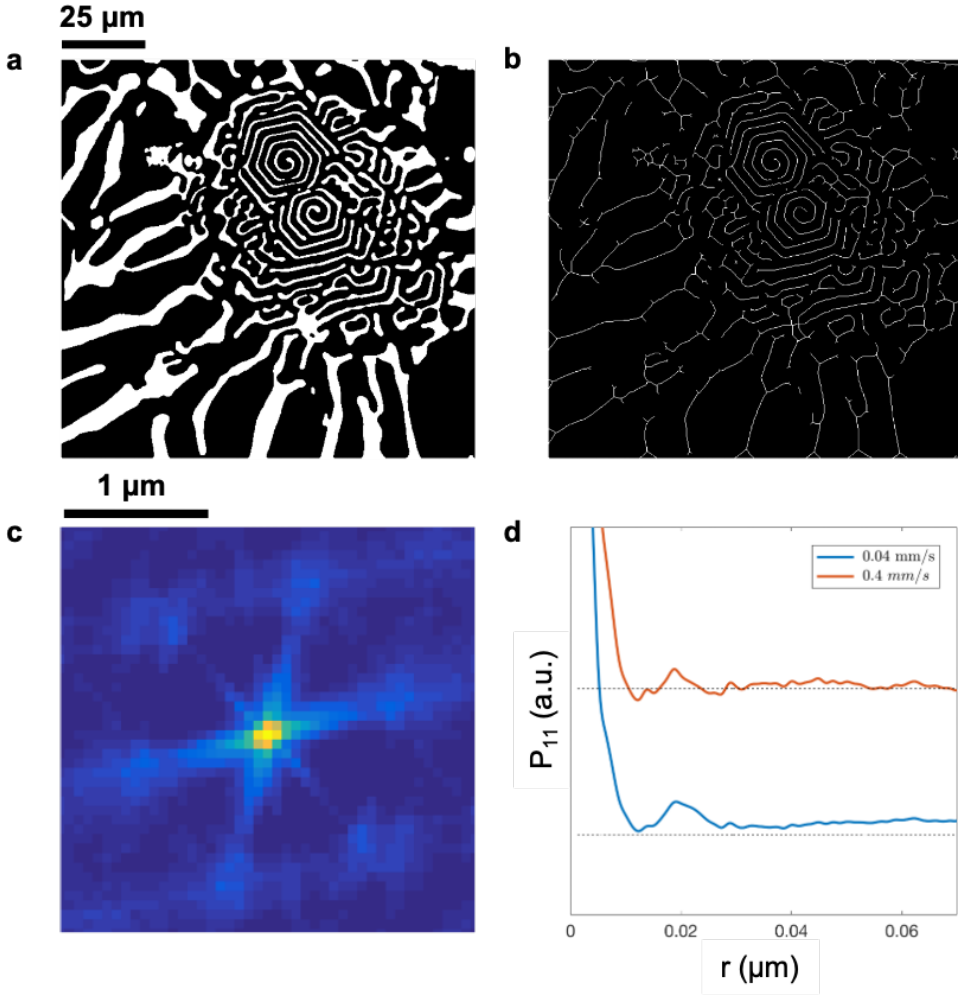

Figure 7.3: Microstructure informatics of spiral eutectics using two-point statistics and pair correlation functions. (a) Segmentation of an SEM image ($G = 10\frac{K}{cm}, V = 0.04\frac{mm}{s}$ in Fig. 7.2). The $MgZn_2$ phase is white. (b) Skeletonization of the segmented image to remove influence of varying lamellar thickness. (c) Short-range two-point autocorrelations of the $MgZn_2$ phase (white in (b,c)). The microstructure is evenly distributed in a hexagonal enveloping shape. (d) Pair-correlation function (PCF) of two spiral Zn-MgZn2 eutectics. For both, the thermal gradient $G = 10\frac{K}{cm}$; the growth rates are 0.04 and $0.4\frac{mm}{s}$. The PCFs are calculated from skeletonized segmented SEM images (similar to that shown in (b)). The peak in the PCFs around $r \approx 0.02\mu$m represents the distance between parallel spiraling arms.

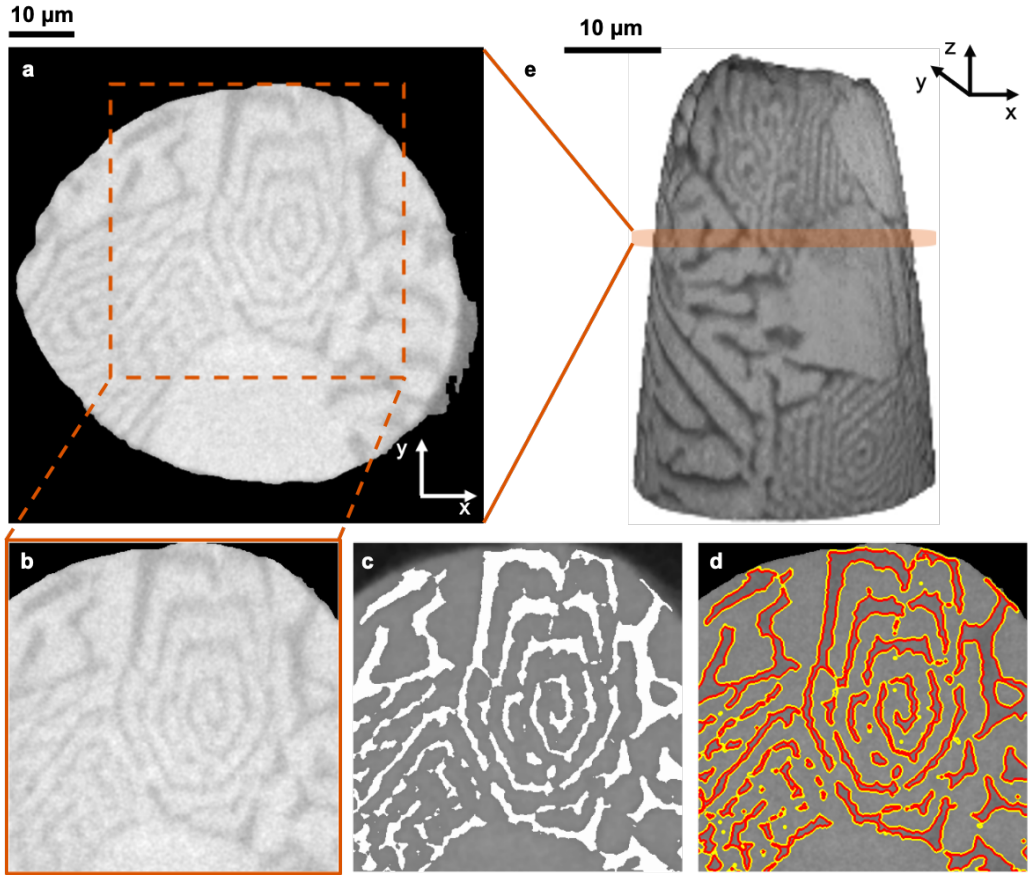

Figure 7.4: Machine learning segmentation and visualization of X-ray nano-tomographic data. (a) Representative ("raw" grayscale) 2D slice of the 3D reconstruction serves as the input for machine learning algorithm (random forests). For evaluating the robustness of the algorithm, a region-of-interest (ROI, dashed orange box) was considered. (b) The ROI containing a spiral eutectic colony is shown. The eutectic $MgZn_2$ phase is dark gray, and the eutectic Zn phase is light gray. (c) Segmented image corresponding to the same grayscale image in (b). The eutectic $MgZn_2$ phase is shown as white, and the eutectic Zn is displayed gray. (d) The edges of the segmentation output are overlaid on top of the grayscale image. Edges of eutectic $MgZn_2$ are red, and those of eutectic Zn are yellow. The segmentation result shows great agreement with the structures underneath. (e) Full 3D reconstruction of the sample. The eutectic $MgZn_2$ phase is shown in dark gray, Zn in light gray. The orange box shows the position of the 2D slice in (a).

introduced for better viewing). Outside the colonies is an irregular Zn-$MgZn_2$ eutectic, characterized by its coarser and non-periodic lamellar spacing. The nTXM reconstruction shows that the spiral colonies are randomly oriented inside the bulk volume. The internal microstructure is revealed by "cutting" the 3D rendering and displaying it orthogonally along the z-axis, as shown in Figure 7.5(b). A close-up view of the same spiral, as shown in Figure 7.5(c), provides a wealth of information: i) the outline of the colony is hexagonal (green overlay) throughout, indicating that the crystallographic anisotropy of the $MgZn_2$ phase plays an important role during solidification; ii) the spirals are characterized by an intra-facet angle $\phi = 10°$(black lines) and a dihedral angle $2\theta = 18°$; iii) the spiral is terminated at a common nucleation site (Movie #2 available in the online repository (Section 7.5); shown below to be a polytetrahedral phase); and iv) the spiraling lamellae form continuous, parallel sheets of uniform thickness, unlike the more widespread picture of a DNA helix. In general, for an n-sided cone, the two angles are related as

$$\phi = 2tan^{-1}(sin\theta tan(\frac{180°}{n})),$$

with which our nTXM results agree. These angular measurements were consistently observed on any randomly chosen spiral colony. Given the complexity of the spiral structure—two phases with nanoscale features—as well as the large volume of data from a typical tomography experiment—millions of voxels—our approach illustrates a case-study of integrating recent developments in data science with experimental techniques, here for microstructure recognition and interface tracking.

The degree of directionality of the colony in the reference (laboratory) frame is

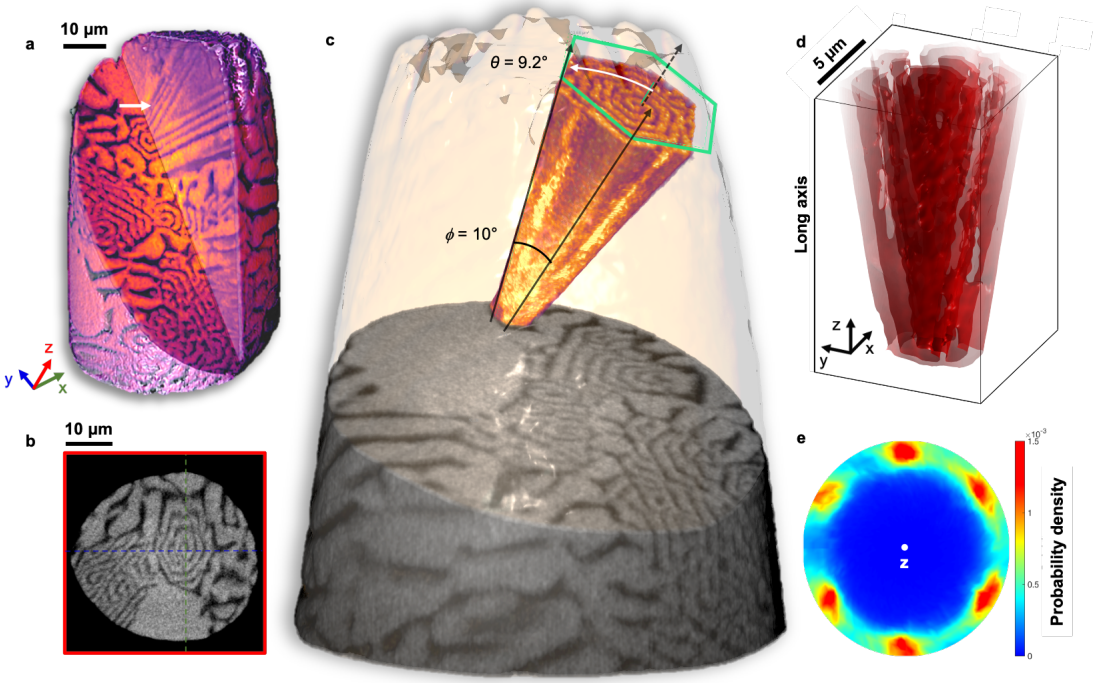

Figure 7.5: 3D morphology of spiral eutectics. (a) Full X-ray nano-tomographic region-of-interest displaying multiple spiral eutectic colonies. The white arrow shows the pyramidal shape of a spiral colony. The reconstruction is cut out to reveal the microstructure internally. The eutectic $MgZn_2$ and Zn phases are shown in dark and light false colors, respectively. (b) View along the cut seen from the y-axis. The eutectic $MgZn_2$ phase is shown in dark gray. (c) Close-up view of the spiral. The spiral colony pointed to by arrow in (a) is extracted, and its surrounding is rendered translucent orange for clarity. The gradation in the spiral's color is due to the false coloring scheme used for visual clarity. The hexagonal enveloping shape along with the inter-planar (dihedral) angle $2\theta \approx 18°$ and intra-facet angle 10° are annotated. (d,e) Solid–solid interfaces and their directionality within the spiral. The Zn-$MgZn_2$ interfaces (d) are extracted from the 3D reconstruction and are used to quantify the preferential directionality of the colony in the laboratory frame E). The interface normal distribution (defined in main text) reveals the sixfold symmetry of the solid–solid interfaces, which correspond to the sharp peaks. The sample was grown with $G = 2\frac{^\circ C}{cm}$ and $V = 3.3\frac{mm}{s}$(Fig. 7.2).

quantified by calculating the stereographic projection of the orientations (normals) of solid–solid interfacial patches, as shown in Figure 7.5(d). The resulting interface normal distribution (IND) in Figure 7.5(e) represents the superposition of all lamellar orientations present within the colony and reveals the sixfold symmetry of the Zn-$MgZn_2$ facet planes, which correspond to the sharp peaks. Overall, the nTXM results provide the first direct evidence for the hexagonal enveloping shape of the spiral Zn-$MgZn_2$ eutectic colony, terminated at an apex by a nucleation center.

7.2.3 Epitaxial Relationships Between Spiral Constituents in 3D

The complex morphology of the faceted spirals was hypothesized to be influenced by the crystallographic texture (grain rotations [224]) of the two phases. We utilized 3D-orientation microscopy (electron backscatter diffraction, EBSD) to investigate this possibility and other fundamental properties such as the heteroepitaxial relationship, crystallographic growth direction, and interphase habit plane orientation. Figure 7.6(a) shows the 3D orientation map of a spiral eutectic colony situated at the junction of three single-crystalline Zn grains (the $MgZn_2$ lamellae are rendered transparent for clarity). We find a negligible intra-lamellar misorientation ($\sim 1°$) in either phase relative to the full breadth of 3D data. Thus, the spiraling eutectic colony cannot be fully explained by grain rotations. The growth direction of the spiral (the long axis of the hexagonal pyramid, see also Figure 7.5(d)) is found to be $[0001]_{MgZn_2}$. In order to visualize the misorientation between the two eutectic phases, we focus on the orientation map of individual 2D cross-sections (Fig. 7.6(b)

and Fig. 7.7) along the specimen $\hat{z}$ direction, and superimpose the unit cell on each grain using the respective Euler angles. Both Zn and $MgZn_2$ are single-crystalline within the given colony. The inset in Figure 7.6(b) shows the misorientation between the two phases, 75° about $(\bar{2}3\bar{1}2)_{Zn}$. The two eutectic constituents maintain this epitaxial relationship, including the tilt of the solid–solid interface, across the sample volume (Figs. 7.7, 7.8, and Table 7.2). The epitaxial assignments are verified by the small ($< 3°$) angular deviation between the pairs of coincident planes between Zn and $MgZn_2$.

The 3D data also enabled us to obtain the orientation of the solid–solid interfaces by constructing a crystallographic interface normal distribution (CIND), an IND in the crystallographic frame. Specifically, the CIND is found by rotating the interface normals to the crystallographic frame of the $MgZn_2$ phase using the respective Euler angles. The CIND along $< 0001 >_{MgZn_2}$ (Figure 7.6(c)) provides a quantitative intuition into the crystallographic properties of the spiral eutectic. The six peaks in the CIND reveal that the solid–solid interfaces have the $\{70\bar{7}2\}_{MgZn_2}$ orientation. Interphase boundaries represented on opposite ends of the CIND meet at the apex of the pyramidal spiral, for instance $\{\bar{7}072\}_{MgZn_2}$ and $\{70\bar{7}2\}_{MgZn_2}$. The interplanar angle is calculated to be $\sim 18°$, corroborating the nTXM observations (*cf.* Figure 7.5). Separately, Dippenaar *et al.* used standard crystallographic formulae to arrive at the indices of the solid–solid interfaces [65], also finding that $\{70\bar{7}2\}_{MgZn_2}$ are the lowest-index planes. However, they refuted that computation, citing that "it is more likely that ... lower-index [compact] planes in the correct measure yield the average orientation" computed. This would imply the presence of an orientation gradient

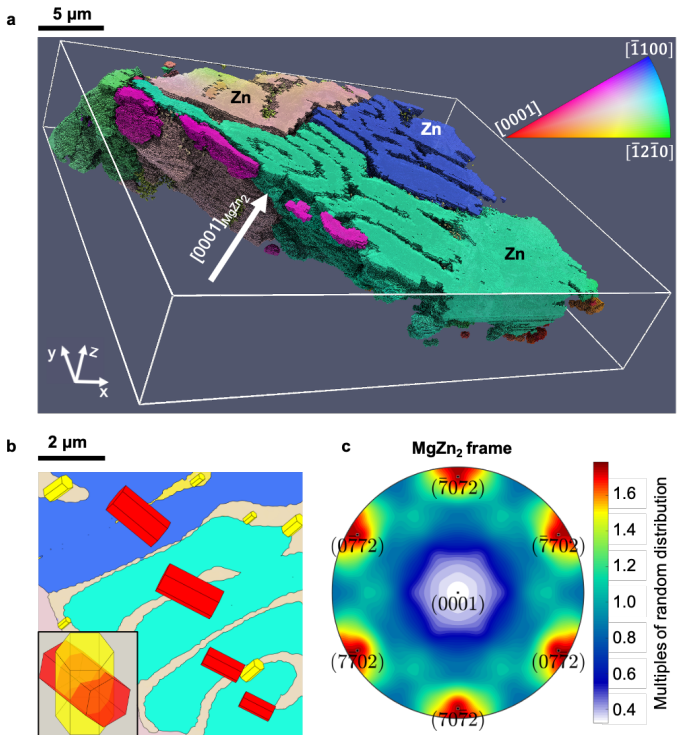

Figure 7.6: Heteroepitaxial relationship between the two spiral eutectic constituents. (a) 3D orientation map (3D EBSD) of a spiral eutectic colony. The spiral is situated at the junction of three single crystalline Zn grains (navy, turquoise, tan). The faceted $MgZn_2$ phase is rendered transparent for clarity; the Zn grains (voxels) are colored according to their orientation following the stereographic triangle on the top-right. The growth direction of the spiral is along $[0001]_{MgZn_2}$. (b) Orientation map of one representative slice with unit cells superimposed using the respective Euler angles (Zn: red; $MgZn_2$: yellow). Facets of the unit cells correspond to the $\{10\bar{1}0\}$ and $\{0001\}$ planes. Both phases are single-crystalline. The map corresponds to the transparent box shown in (a). Inset: the misorientation between the two phases. (c) Distribution of the crystallographic orientation of the solid–solid Zn-$MgZn_2$ interfaces. The plot of crystallographic interface normal distribution (defined in main text) is shown along ¡0001¿ axis of $MgZn_2$. The six crystallographically symmetric poles of high probability reveal that the solid–solid interfaces have the $\{70\bar{7}2\}_{MgZn_2}$ orientation. The interplanar angle, for example, between $\{\bar{7}072\}_{MgZn_2}$ and $\{70\bar{7}2\}_{MgZn_2}$ is $\approx 18°$, matching the observation from X-ray nano-tomography (Fig. 7.5). The sample was grown with $G = 2\frac{^\circ C}{cm}$ and $V = 3.3\frac{mm}{s}$(Fig. 7.2).

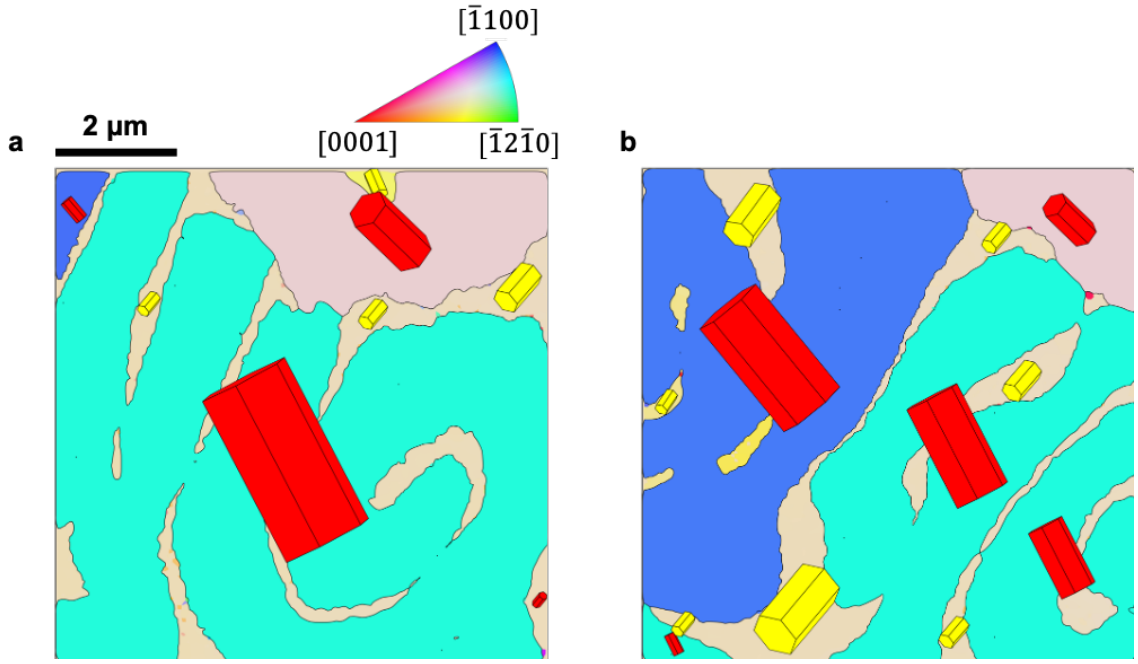

Figure 7.7: EBSD orientation map of two additional slices of the 3D EBSD dataset. (a) 1.05 μm and (b) 4.55 μm from top of sample (*cf.* Fig. 7.6(a)). Unit cells are superimposed on each grain using the Euler angles of the orientation of the grain (Zn: red; $MgZn_2$: yellow). Grains are colored according to their orientation following the standard stereographic triangle on the top-right. Both Zn and $MgZn_2$ are single crystalline. The orientation relationship is the same as that shown in Fig. 7.6.

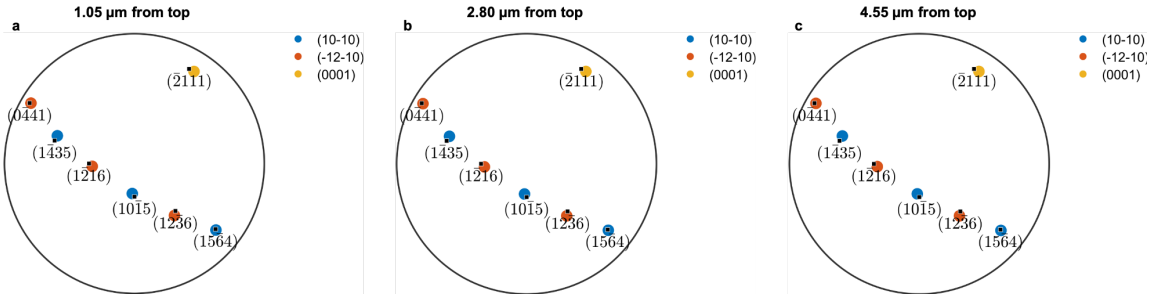

Figure 7.8: Stereographic projections of coincident planes between the Zn and $MgZn_2$ phases in spiral eutectics. (a) 1.05 μm, (b) 2.80 μm, and (c) 4.55 μm from top of sample. The three crystallographic planes of Zn (legend in stereographic projections) are plotted as colored circles, and the matching planes of $MgZn_2$ are superimposed as black squares. Same matchings are observed across volume.

across the volume of the sample, which in turn could be manifested as a change in the relative tilt of the eutectic phases. Neither of these assertions are supported by our direct 3D EBSD results (Figs. 7.7, 7.8, and Table 7.2).

Depth in sample	Angle (deg.)	h	k	i	l
1.05 μm from top	76.66	-2	3	-1	2
2.80 μm from top	76.55	-2	3	-1	2
4.55 μm from top	76.72	-2	3	-1	2

Table 7.2: Misorientation between the Zn and $MgZn_2$ phases in spiral eutectics. The angle and axis of misorientation with respect to the Zn phase (*e.g.,* inset of Fig. 7.6(b)) is uniform across the volume of the spiral examined by 3D EBSD.

7.2.4 Two-Step Crystallization Pathway

Through *in situ* synchrotron high-energy X-ray diffraction (HEXRD) under non-equilibrium conditions that favor spiral growth, we tracked the phase formation

sequence by acquiring Laue patterns as a function of diffraction angle 2θ. Synchrotron radiation is ideally suited for the detection of low-volume-fraction phases, such as the spiral nucleant. The 400 diffraction spectra collected during 200 seconds of solidification permitted resolving the fast kinetics of nucleation temporally, and the summarized results are shown in Figure 7.9 (a). The diffraction peak belonging to the first solid phase to form corresponds to $MgZn_2$ (dashed line at $\sim$ 1.0 s, $2\theta \approx 2.9°$); meanwhile, peaks belonging to the Zn phase appear $\sim$ 2 s later. Indeed, if we track the absolute intensities of the Zn (101) peak in background-subtracted spectra, shown in Fig. 7.9 (b), we can see clearly that the Zn phase forms after $\sim$ 2 s into the solidification process. These results show the sequence of phase formation and, importantly, provide direct evidence of the initial formation of $MgZn_2$ particles that serve as nucleants for the Zn-$MgZn_2$ eutectic. This observation complements the detection of seed crystals in nTXM at the apex of the pyramidal spirals (*cf.* Figure 7.5 and Movie #2 available in the online repository (Section 7.5)).

7.2.5 Atomic Visualization of Spiral Nucleant

The seed $MgZn_2$ particles are characterized by a hexagonal outer shape with an open core (white arrows in Fig. 7.2). They have a coherent lattice with the $MgZn_2$ phase of the spiral eutectics but contain more crystallographic defects, as suggested by the hollow core. Using diffraction-contrast transmission electron microscopy (TEM) under the strong two-beam conditions [233], as well as atomic-resolution scanning TEM (S/TEM) imaging, we confirm the presence of defects (screw dislocations) within seed $MgZn_2$ crystals. In the TEM images taken along the $[\bar{1}2\bar{1}0]_{MgZn_2}$ zone axis shown

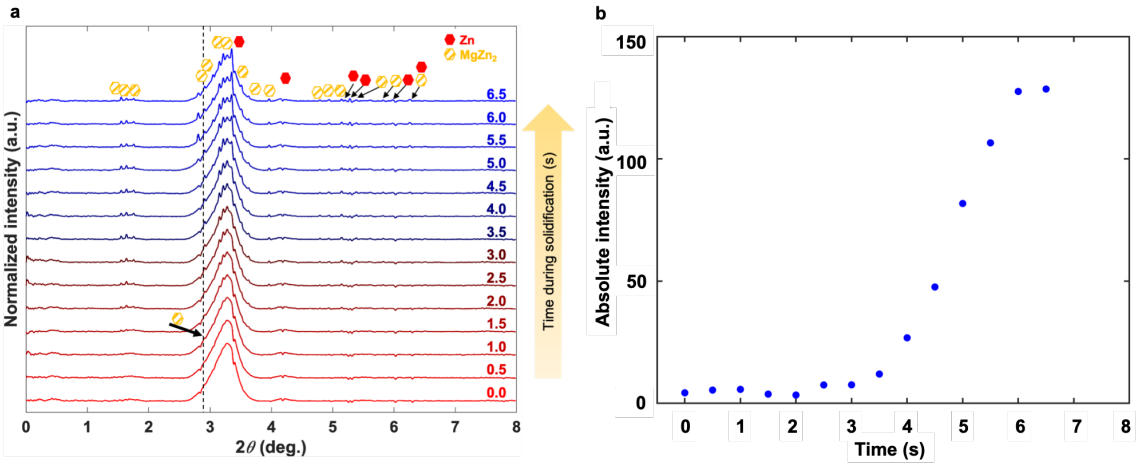

Figure 7.9: Sequence of phase formation during solidification. (a) The *in situ* high-energy X-ray diffraction (HEXRD) spectra acquired at the indicated time-steps after the start of solidification (0.0 s) show that $MgZn_2$ is the first solid phase that forms (dashed line at 1.0 s, $2\theta \approx 2.9°$). (b) HEXRD background-subtracted absolute intensities of Zn (101) peak. Absolute intensity of ~ 0 (a.u.) indicates no difference with background. The Zn phase nucleates after ~ 2.0 s.

in Figure 7.10(a,b), dislocation contrast is invisible upon exciting the $(10\bar{1}0)$ family of diffraction spots (Figure 7.10(a)). Dislocation lines become visible upon exciting a family of diffraction vectors containing a parallel component to the spiral growth axis, for example, $(\bar{1}01\bar{1})$ spot (Figure 7.10(b)). Thus, the dislocation lies along the $[0001]_{MgZn_2}$ direction, which is also the spiral growth direction (Figure 7.6(a)). Since both growth and dislocation directions are along $[0001]_{MgZn_2}$, this behavior is consistent with a dislocation of screw character. It is important to mention that the "invisibility criterion" invoked above holds for elastically isotropic materials, of which $MgZn_2$ is not [234]. Nevertheless, $MgZn_2$ has a hexagonal crystal structure, so the basal plane and all planes perpendicular to it are elastically symmetric. Consequently, all dislocations that lie on the basal plane or perpendicular to it exhibit

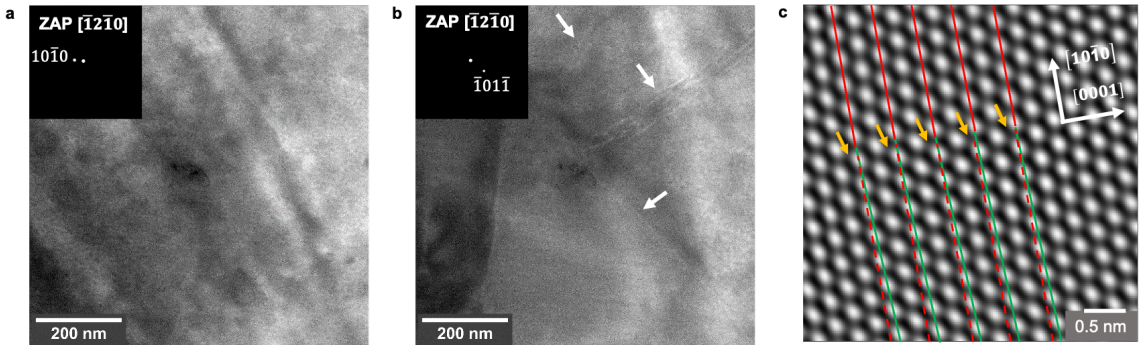

Figure 7.10: S/TEM observation of screw dislocations within "seed" $MgZn_2$ crystal. (a,b) Diffraction-contrast TEM images taken under the strong two-beam conditions defined by the diffractions as insets to the images near the $[\bar{1}2\bar{1}0]_{MgZn_2}$ zone axis. Dislocations are invisible upon excitation of diffraction vectors perpendicular to the $[0001]_{MgZn_2}$ direction, for example the $(10\bar{1}0)$ spot in (a). Dislocation lines become visible (white arrows) when the diffraction vector has a parallel component to the $[0001]_{MgZn_2}$ direction, for example, the $(\bar{1}01\bar{1})$ spot in (b). Therefore, the dislocation lies along the $[0001]_{MgZn_2}$ direction, which is also the growth direction (Figure 7.6). Since both the growth and dislocation directions are along $[0001]_{MgZn_2}$, this behavior is consistent with a dislocation of screw character. (c) Atomic-resolution high-angle annular dark-field (HAADF) image taken along $[11\bar{2}0]_{MgZn_2}$ showing screw dislocations aligned along $[0001]_{MgZn_2}$. Solid red and green lines indicate the shearing of atomic planes, characteristic of the side-view of a screw dislocation; dashed red lines indicate the position of atomic columns in the absence of screw dislocation. The orange arrows point to atomic columns around the screw dislocation core. The sample was grown with $G = 2\frac{^\circ C}{cm}$ and $V = 3.3\frac{mm}{s}$(Fig. 7.2).

pseudo-elastic isotropy, and hence the invisibility criterion is valid for dislocations which lie on such planes [233].

The atomic-resolution STEM image in Figure 7.10(c) provides a direct visualization of the screw dislocation. The STEM image shows shearing of the planes, characteristic of the side-view of a c[0001]-oriented screw dislocation in $MgZn_2$ (beam direction: $[11\bar{2}0]_{MgZn_2}$); colored lines are superimposed to guide the eye. The atomic

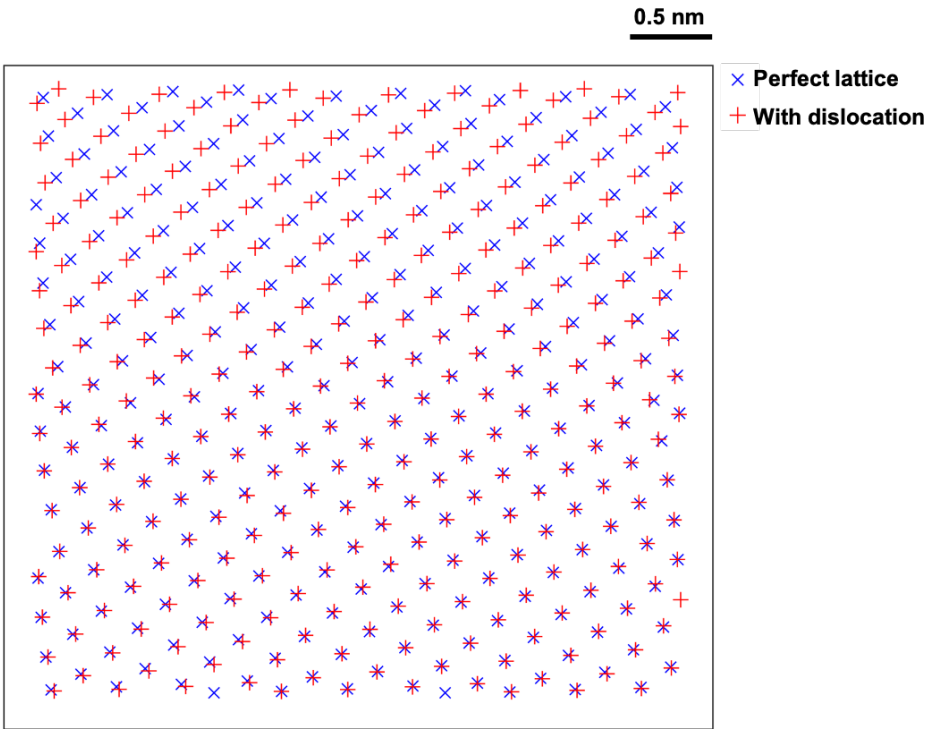

Figure 7.11: Displacement map of the $MgZn_2$ screw dislocation shown in Fig. 7.10(c). The ideal (dislocation free) lattice positions are marked with blue crosses, and the actual atomic positions from 7.10(c) are superimposed as red squares. The ideal positions were obtained from a region of the sample away from the dislocation core. The pairwise symbols represent the actual atomic displacements due to the presence of the screw dislocation.

displacements extend preferentially along the $[0001]_{MgZn_2}$ direction, as shown in Fig. 7.11.

We note that the equal probability of spiral handedness (7.2.1) implies an equal probability of the dislocation sense and, more importantly, is additional evidence of screw-mediated spiral growth.

7.2.6 Development of Spiral Patterns from Nano- to Micro-scale

Based on the results above, we propose the following mechanism, shown schematically in Figure 7.12, for the crystallization of spiral Zn-$MgZn_2$ eutectics under non-equilibrium conditions (*cf.,* Fig. 7.2). Under such conditions, $MgZn_2$ is the first phase to crystallize. The preferential nucleation of the Laves phase demonstrates that its solid–liquid interfacial energy (and hence, barrier to nucleation) is considerably less than that of the stable Mg_2Zn_{11} phase, assuming similar wetting angles [235]. Spaepen [236], Holland-Moritz [237], and others [238] have reasoned that the low interfacial energy is due to the polytetrahedral structural similarity between the melt and the $MgZn_2$ Laves phase.

The axial screw dislocation of the seed $MgZn_2$ establishes a spiral ramp that provides self-perpetuating steps which enable spiral growth (Figure 7.12(a)). Given the large Burgers vector ($\sim$4 nm; see below), as the seed crystal grows, the high strain field around the screw leads to the formation of hollow structures (open cores) in order to relieve the strain energy [78]. According to Frank's seminal theory [78], it is energetically more favorable to remove the crystalline material adjacent to the dislocation line and create an additional inner surface in the form of a hollow core, compared to retaining the strain energy of the dislocation. This is shown schematically in Figure 7.12(b). We rationalize this observation through an energy balance (below) between the dislocation strain energy and the energy required for creating the hollow core. A similar phenomenon is reported in other dislocation-prone materials [82, 239]. Here, the open-core dislocation of $MgZn_2$ is subsequently filled with

the other eutectic phase (Zn), forming the micropipes (white arrow in Fig. 7.2). As revealed by the fixed positions of HEXRD peaks in Figure 7.9, the strain field survives through the thermal contraction of the bulk volume upon solidification. Thus, our S/TEM results at room temperature are generalizable. Furthermore, in the analysis of dislocation strain relaxation as outlined below, we find only an insignificant contribution to strain relaxation from "Eshelby twist" [240] (strain-induced rotation of the crystal lattice around an axial screw):

According to elastic theory of dislocations [241], the strain energy per unit length E_{dis} due to a screw dislocation scales quadratically with the magnitude of the Burgers vector b:

$$E_{dis} = \frac{b^2 \mu}{4\pi} \ln \frac{R}{r} \tag{7.14}$$

where μ is the shear modulus of the seed crystal, and R and r are radii of the outer elastic cylinder and inner dislocation core, respectively. The energy per unit length E_{surf} for creating a new inner surface depends on the radius of the inner (hollow) core r:

$$E_{surf} = 2\pi\gamma r \tag{7.15}$$

where γ is the solid-liquid surface energy, here pertaining to the $MgZn_2$ phase. An energy balance between these competing terms establishes a relationship between

r and b:

$$b = \sqrt{\frac{8\pi^2\gamma r}{\mu}} \tag{7.16}$$

Using the literature values for $\gamma_{MgZn_2-liquid}$ and μ_{MgZn_2} (0.001 $\frac{J}{m^2}$ and 12.65x10^9 $\frac{J}{m^3}$, respectively [242, 243]), and radius of open core from SEM images (2 μm, *cf.*, white arrows in Fig. 7.2), we obtain a Burgers vector magnitude of 4 nm. Thus, the strain and surface energies can be computed using Eqs. 7.14 and 7.15: $E_{dis} = 1.8 \times 10^{-8} \frac{J}{m}$ and $E_{surf} = 1.3 \times 10^{-8} \frac{J}{m}$. Since the strain energy exceeds the energy cost of creating a new inner surface, the formation of hollow cores in primary $MgZn_2$ particles is energetically favored.

Equation 7.16 quantifies the component of the Burgers vector b due to the hollow inner tube surface energy (denoted below as b_{tube}). The total contribution b_{total} also involves the contribution b_{twist} from strain relaxation from 'Eshelby twist' [240, 82, 21], as follows:

$$b_{total} = \sqrt{\frac{8\pi^2\gamma r}{\mu}} \frac{R^2 + r^2}{R^2 - r^2} \tag{7.17}$$

Solving for b_{twist},

$$b_{twist} = b_{total} - b_{tube} \tag{7.18}$$

Thus,

$$b_{twist} = \sqrt{\frac{8\pi^2\gamma r}{\mu}} (\frac{R^2 + r^2}{R^2 - r^2} - 1) \tag{7.19}$$

From SEM images showing hollow core primary $MgZn_2$ particles (*e.g.,* white arrows in Fig. 7.2), $R \approx 3r$. Thus, with the values of other parameters noted above, we obtain

$$b_{twist} \approx 0.88nm \tag{7.20}$$

Therefore, Eshelby twist has an insignificant contribution to relaxation of the strain induced by the screw dislocation, since $b_{twist} << b_{tube}$.

As the system cools to below the metastable eutectic temperature, the Zn phase forms heteroepitaxially along the spiral growth steps of $MgZn_2$ (Figure 7.12(c)). That is, the Zn phase forms exclusively along the ledges and not on the $\{0001\}_{MgZn_2}$ terraces, assuming that the supersaturation of Zn is not too high. Only at supersaturations above the threshold of forming 2D nuclei (the kinetic roughening transition [244]) will island growth be possible on the basal plane. Once Zn has nucleated along the spiral steps, it grows in a coupled manner with the $MgZn_2$ phase. The interphase spacing (Figs. 7.2 and 7.13) is set by the undercooling for lamellar growth according to the Jackson–Hunt model [55] (*cf.,* Section 2.3.1). During the ensuing eutectic growth, low-energy solid–solid interfaces $\{70\bar{7}2\}_{MgZn_2}$ are maintained. As demonstrated in 7.2.6, these interfaces have an approximately eight-fold lower energy compared to those solid–solid interfaces in the irregular Zn-$MgZn_2$ eutectic. Phase field simulations [245] show that in these so-called "locked" eutectic grains, the interphase boundaries follow specific crystallographic growth direction such that the lamellae can be tilted relative to an imposed thermal gradient. Ultimately, the conical faceted enveloping shape of the eutectic colony is determined by the anisotropy of

the interphase boundary energy, and not the Wulff shape of $MgZn_2$ (a hexagonal rod). Within each colony, spiraling sheets of the fully faceted $MgZn_2$ phase are arranged with near-constant periodicity. This regular organization of lamellae is somewhat anomalous for an irregular eutectic (the Jackson α-factor for the $MgZn_2$ phase is at most 5.7). Given that the eutectic spirals nucleate atop axial screw dislocations, the regularity of the two phases is enforced by the spiral growth steps themselves.

The fully developed spiral colony (Figure 7.12(d)) illustrates the solid–solid interfaces, intra-facet angle, and growth direction. As the eutectic phases grow, they maintain a consistent epitaxial relationship, suggesting their interphase boundaries possess low energy. Indeed, as it has been demonstrated in ref. [246], in polycrystals (i) the most common boundary planes are those with low surface energies, and (ii) the boundary populations are inversely correlated with the boundary energy. The selection of high-index planes is due to the anisotropy of the solid-solid interfacial free energy. This anisotropy leads to a locking, and tilting, of the eutectic grains with respect to the growth front.

Estimation of Solid-Solid Interfacial Free Energy

By measuring the interphase lamellar spacings λ from Fig. 7.2, we can determine the dependence of microstructural length-scale on growth rate V. Both the spiral and irregular Zn-$MgZn_2$ microstructures exhibit a scaling law of the form $\lambda^2 V = constant$, consistent with the predictions of the Jackson-Hunt model. However, as the results in Fig. 7.13 show, only minute variations are observed in the measured lamellar spacing of the spiral Zn-$MgZn_2$ eutectic with growth velocity, as compared

to the irregular Zn-$MgZn_2$ eutectic. According to Tiller and others [247, 248, 249], the slope of $\lambda^2 - V^{-1}$ is directly proportional to the solid-solid interface free energy between the two eutectic phases (holding all else fixed, *i.e.,* assuming a negligible change in the contact angles). Thus, the ratio of the two slopes (Fig. 7.13) provides a crude estimate for the relative magnitudes of the two interfacial free energies. The slopes of the linear fits to $\lambda^2 - V$curves of the spiral and irregular eutectics are, approximately, 37 and 5 $\frac{\mu m^2}{\frac{s}{mm}}$, respectively. Thus, the spiral eutectic has an approximately 8-fold lower solid-solid interfacial free energy compared to its irregular counterpart. The implications of this relative ordering of the two solid solid interfacial free energies on the eutectic morphology may offer clues about the overall morphology of the spiral eutectic colony, as discussed above.

The nucleation behavior of the spiral Zn-$MgZn_2$ eutectic represents a surprising inversion of our conventional wisdom. It has long been thought [250] that complex regular structures arise due to morphological instabilities at the eutectic growth front, such that the solid–liquid interface is comprised of an array of macro-faceted cellular projections that enable a regular structure to develop (orthogonal to the macro-facet). This is the case for the complex regular, rod-like Zn-Mg_2Zn_{11} eutectic, wherein parallel, regularly spaced lamellae connect to a common trigonal spine. Yet this classical viewpoint cannot explain the complex regular spiral morphology of Zn-$MgZn_2$. Instead, crystallographic defects (screw dislocations) of the primary $MgZn_2$ Laves phase catalyze the heterogeneous nucleation of the eutectic phases during solidification. That is, the presence of such crystallographic defects causes the spiral growth form. While screw dislocation-driven growth has been reported in

diverse areas of crystallization [82, 251, 252, 253, 21]—and indeed extensions of the Burton–Cabrera–Frank [78] spiral growth model exist [254]—our proposed mechanism on the role of "hidden" polytetrahedral phases in assisting heterogeneous nucleation supports and expands upon recent reports [217, 255], for instance, metastable quasicrystal-induced nucleation yielding grain-refined alloys [256], among other two-step solidification pathways.

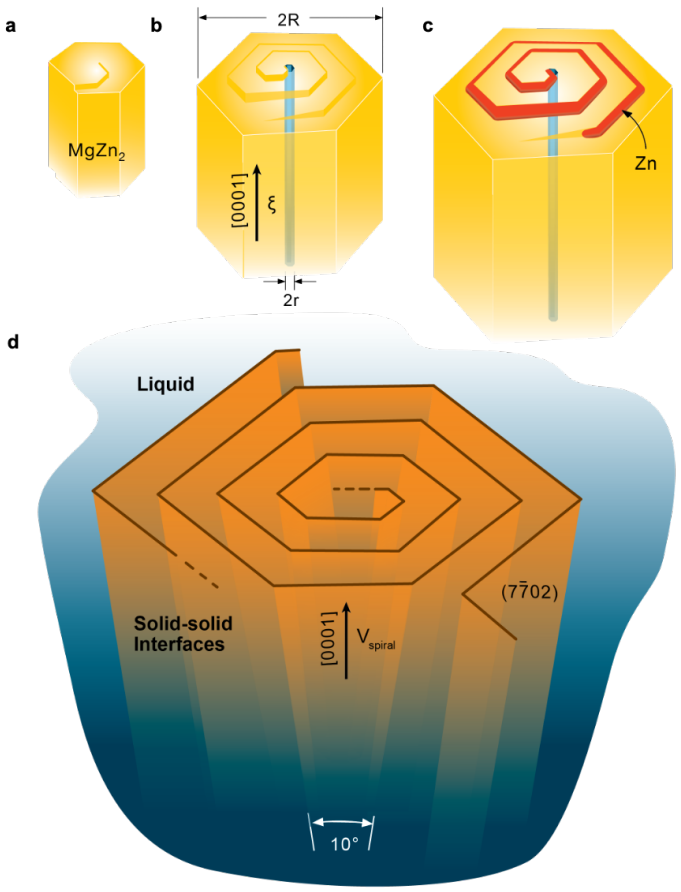

Figure 7.12: Illustration of the screw dislocation mediated growth of spiral eutectics. (a) Establishment of a spiral ramp due to axial screw dislocation on the seed $MgZn_2$ crystal. The ramp provides self-perpetuating steps that enable spiral growth. (b) Growth of the seed crystal and formation of a hollow core. The axial growth direction of the spiral is along $[0001]_{MgZn_2}$. For sufficiently large Burgers vector, the strain energy is alleviated by hollowing out the dislocation core (thin blue cylinder), in agreement with Frank's hollow-tube mechanism [78]. Radii of the seed and hollow-core are R and r, respectively; ξ is the sense vector of the dislocation. (c) Heteroepitaxial growth of Zn (red, not to scale) along the exposed MgZn2 growth steps (ledges). (d) Spiral eutectic colony during the growth process. Only solid–solid interfaces are shown for clarity. The habit planes of the spiral are $\{7\bar{7}02\}_{MgZn_2}$. The intra-facet angle is $\sim 10°$, for example, between $\{7\bar{7}02\}$ and $\{70\bar{7}2\}$.

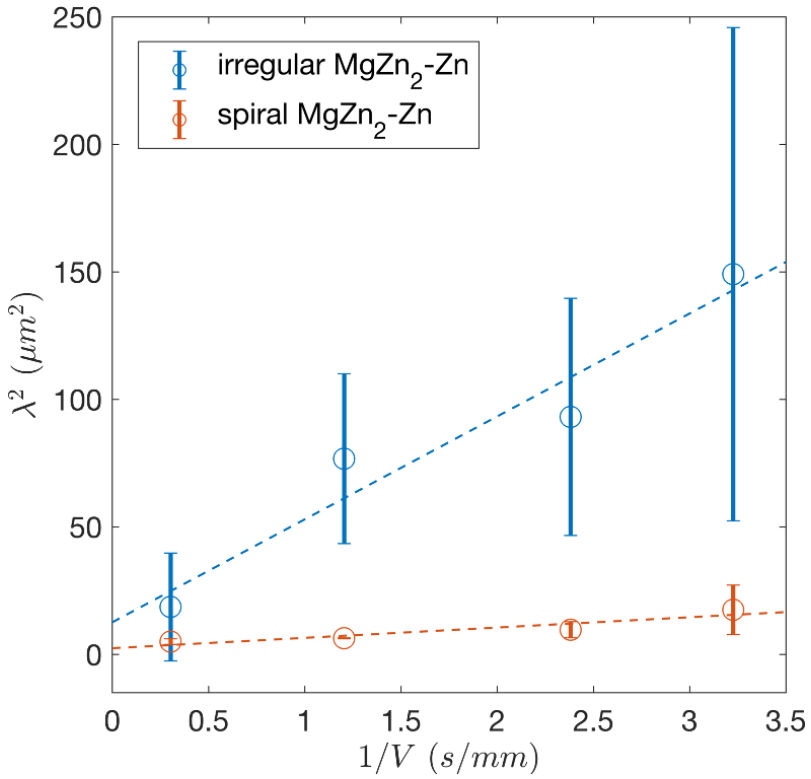

Figure 7.13: Measured eutectic interphase spacing λ as a function of growth rate V for both spiral and irregular $MgZn_2$-Zn eutectics. The interphase spacings (center-to-center distance of neighboring lamellae) were measured from SEM images of samples grown at $G = 2\frac{K}{cm}$; the average and standard deviations per image were used to construct the present figure. Both microstructures exhibit a scaling law of the form $\lambda^2 V = constant$, consistent with the predictions of the Jackson-Hunt model [55]. For spiral Zn-$MgZn_2$, only small variations in λ are observed with V, while the irregular Zn-$MgZn_2$ eutectic displays large such variations (non-uniform interphase spacing is a characteristic of irregular eutectics). The ratio of the two slopes provides a crude estimate for the relative magnitudes of the two interfacial free energies: The spiral eutectic has an ∼8-fold lower solid-solid interfacial free energy compared to its irregular counterpart.

7.3 Summary

We have synthesized spiral, two-phase microstructures that possess an intrinsic chirality and a faceted, periodic architecture. Correlative characterization facilitated by data science methods reveals the formation mechanism as well as the morphological and heteroepitaxial relationships between the phases that grant the microstructure its unique spiral pattern. We find the macroscopic spirals emerge *via* microscopic defects through a two-step crystallization process. First, polytetrahedral phases nucleate readily in the liquid owing to their low interfacial energy. These nucleation precursors provide favorable environments (screw dislocations) for crystallization of the spiral eutectic, thereby demonstrating the broad applicability of Frank's defect-driven growth mechanism to multi-phase materials. Our 3D studies provide the necessary benchmark data for simulations of complex self-organization patterns, thus expanding the horizon for the design of next-generation alloys with superior properties. Spiral self-organization may open exciting opportunities in photonics, where the resulting multi-phase structures can serve as templates for rapid fabrication or additive manufacturing of 3D chiral photonic crystals.

7.4 Materials and Methods

7.4.1 Synthesis of Eutectic Microstructures by Directional Solidification

Alloy buttons of nominal composition Zn-3 wt% Mg were cast *via* vacuum arc-remelting at the Materials Preparation Center at Ames Laboratory (Ames, IA, USA), using 99.999% purity Zn and 99.99% purity Mg. The as-prepared alloy buttons were cut in the shape of cylindrical rods of 1 mm diameter by 5 mm length *via* electrical discharge machining. In such small samples, convection effects have been shown to be negligible [257]. Two-phase eutectics were then grown by directional solidification using a three-zone vertical Bridgman furnace (MTI Corporation EQ-SKJ-BG). The temperature gradient was imposed onto the fully molten sample by independently fixing the temperatures of the three zones. The growth velocity was controlled by the upward, simultaneous movement of the zones (sample stationary). Some samples were also prepared by "gradient freeze," wherein both the sample and the heating zones remained stationary while the zone temperatures were decreased at fixed rates under the imposed thermal gradient (we note that the cooling rate is the product of the thermal gradient and growth velocity).

7.4.2 Laser Micromachining for Nano-Tomography Experiments

The directionally-solidified samples were polished to a mirror finish and imaged on an optical microscope (ZEISS Axio Imager 2, Carl Zeiss Microscopy Inc., Oberkochen, Germany) to locate the spiral regions of interest. Local features were identified as fiducials for further sample preparation. The specimens were then transferred to a picosecond laser ablation based micro-machining system (microPREP, 3D-Micromac AG, Chemnitz, Germany). The region-of-interest was registered using the built-in light microscope, and cylindrical micropillars 60 μm in diameter were milled top-down measuring nominally 100 μm in height. The pillars were extracted and mounted on tungsten needles for imaging in X-ray nano-tomography.

7.4.3 X-Ray Nano-Tomography

Non-destructive 3D imaging was performed on a ZEISS Xradia Ultra 800 (Carl Zeiss X-ray Microscopy Inc, Pleasanton CA), a nanoscale X-ray microscope with an 8.0 keV copper source. The tomography acquisition consisted of 901 X-ray projection images collected at a 130 s exposure/frame with a 64 nm/voxel resolution in the large field-of-view mode. The 3D reconstructed slices were produced by processing the projection images in the accompanying Reconstructor software, which is based on a parallel-beam filtered back projection algorithm. Output files consisted of a stack of 16-bit 3D dataset with 1024 x 1024 x 1024 pixel dimensions. The reconstructed data was rendered and analyzed using a 3D visualization software (Dragonfly 3.6,

Object Research Systems [ORS] Inc, Montreal, Canada, 2018). Additionally, two-class segmentation of reconstructed datasets was performed using an interactive pixel classifier segmentation tool based on a random forest classifier within Ilastik 1.2 (Ilastik: Interactive Learning and Segmentation Toolkit) [258].

7.4.4 Electron Backscatter Siffraction

The 3D EBSD measurements were performed on a ZEISS Crossbeam 550L focused-ion beam-scanning electron microscope (FIB-SEM) equipped with an Oxford Instrument Symmetry EBSD camera and an Oxford Instrument ULTIM MAX 170 electron dispersive spectroscopy (EDS) detector. The data were acquired using the ZEISS Atlas 5 3D software for FIB-SEM tomography. Standard Atlas 5 3D preparation with protective deposition and tracking fiducials was carried out. To avoid damage to beam-sensitive phases, an energy of 15 kV was chosen for the FIB milling with a probe current of 4 nA. SEM images were acquired using 2 kV SEM beam energy and 2 nA of beam current. Chamber secondary electrons (SE) and Inlens SE detectors were used in parallel. An isotropic voxel resolution of 10 nm was chosen for the imaging, that is, 10 nm pixel resolution within the images and 10 nm slice thickness for the FIB milling. Atlas 5 was used to measure and track the actual slice thickness and adapt the milling progress accordingly, also compensating for sample drift. A voxel resolution of 70 or 100 nm was chosen for the EBSD measurements. Thus, every 7^{th} or 10^{th} image, the sample was automatically moved to EBSD position, and the map acquisition was started. SEM conditions were changed automatically to 19 kV beam energy and 20 nA of beam current, to assure high signal-to-noise EBSD patterns.

EDS maps were acquired in parallel. Pixel resolution of the analytic maps was set to 70 or 100 nm, respectively, to achieve isotropic voxels. The Symmetry EBSD camera was set to binning mode "Speed 2" with an exposure time of 1 ms EBSD slices were registered in DREAM.3D software (BlueQuartz) using a misorientation tolerance of 5°. The registered data were subsequently rendered in 3D through the open-source visualization software ParaView (Kitware) [259]. Crystallographic analysis of the individual EBSD slices (texture data) was performed using the MATLAB (The MathWorks, Inc.) toolbox MTEX [188].

7.4.5 *In Situ* Synchrotron High-Energy X-Ray Diffraction

The HEXRD experiments were conducted at Sector 11-ID-C of the Advanced Photon Source in Argonne National Laboratory (Argonne, IL, USA). The solidification experiments were performed in sealed quartz tubes under the protection of a high-purity argon atmosphere. The sample was heated, melted, and overheated using a radio frequency induction-heating coil with a maximum heating power of 4.2 kW. Then, the power of the heating coil was switched off. The molten sample was cooled and solidified spontaneously. The cooling rate was assumed to be constant (around 20 $\frac{K}{s}$) since cooling is dominated by thermal radiation from the sample surface. The sample was melted and solidified eight times. In each cycle of melting and solidification, a monochromatic X-ray source with wavelength of 0.1173 Å was incident on the sample through a large gap between two wings of the induction coil. The diffracted X-rays were scattered in forward directions and were recorded continuously with an exposure time of 0.5 s using a Perkin-Elmer amorphous silicon detector at a distance

of about 1.8 m from the sample. The maximum active area of the detector is 409.6 mm x 409.6 mm, with 2048 x 2048 pixels and a pixel size of 0.2 mm x 0.2 mm. After the experiments, the sample-to-detector distance was calibrated using a standard sample of CeO_2 at room temperature. The recorded 2D diffraction patterns were integrated using the FIT2D software [260] (v.12.077) for phase identification. Background subtraction was performed using the High-Score software (Malvern Panalytical). Combining Braggs' law and lattice spacing of crystal structure allowed for determination of phase formation sequence.

7.4.6 Electron Microscopy

All specimens for S/TEM were prepared *via* focused-ion beam (FIB) lift-out technique in an FEI Helios 650 Nanolab SEM/FIB.

The major steps in a typical lift-out sample preparation are presented in Fig. 7.14

Lift-out samples were thinned to ∼80 nm and cleaned equally on both sides. The damage from Ga beam was limited to the top 100–120 nm of the final sample, which was avoided in all subsequent S/TEM experiments. Samples were plasma cleaned for 5 min prior to insertion into the S/TEM. The diffraction-contrast TEM experiments were performed with a JEOL 2010F microscope operating at 200 kV. All STEM experiments used a JEOL 3100R05 double-Cs corrected S/TEM with an operating voltage of 300 kV. All cross-sectional SEM and compositional maps were collected on a Tescan MIRA3 SEM on mirror-finish polished samples; the micrographs were collected using both secondary and backscattered electrons with an operating voltage

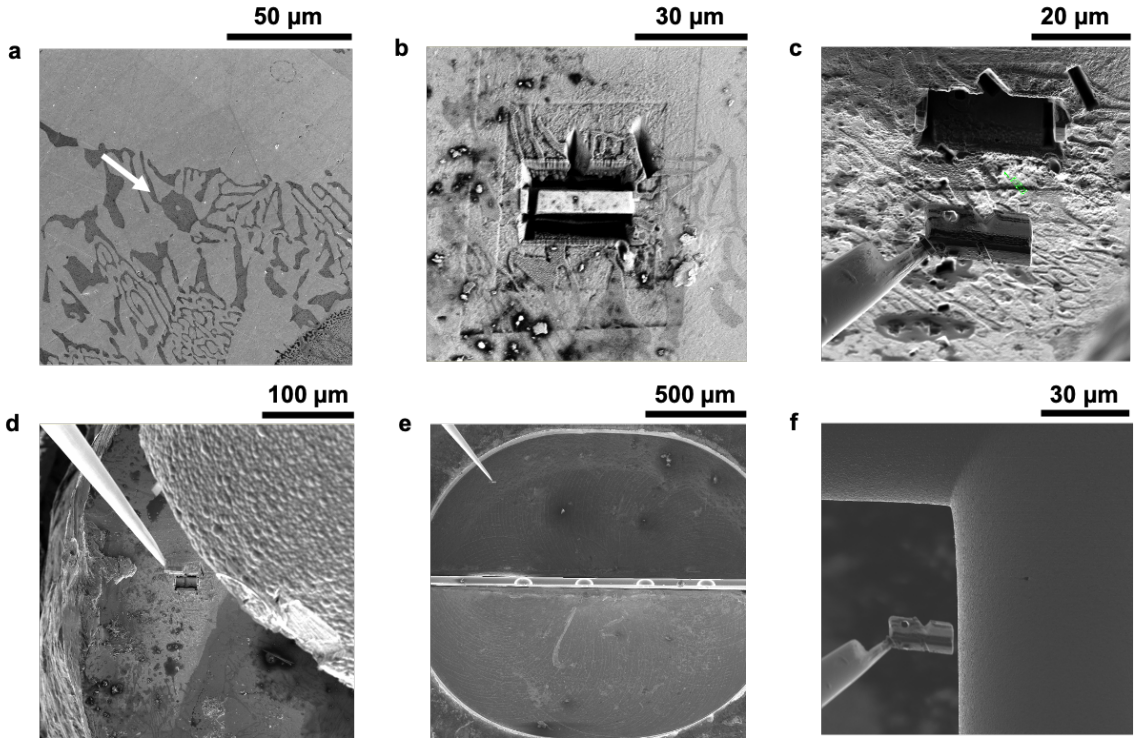

Figure 7.14: TEM sample preparation with focused ion beam (FIB). Select steps of the preparation process are shown, excluding final thinning. (a) An open-core seed particle of $MgZn_2$ (arrow). The FIB lift-out is performed across the diameter of the particle and into the depth of the sample. Given the hexagonal shape of the site, the $[0001]_{MgZn_2}$ direction points out of the page. (b) The lift-out site after U-cut. Prior to this point, protective layers of Pt (thin layer with e-beam followed by thicker layer with ion-beam) were deposited laterally across site, followed by bulk-out (trench) cuts on both sides of the region of interest. (c) Sample during lift-out. The Omniprobe was welded to a corner of the sample with Pt, and the sample was cut free from the bulk piece. (d) Migrating to the TEM grid. The lift-out sample is being transferred from the bulk piece to the TEM grid. The Pt gun is obscuring the bulk sample.(e) Lift-out sample above the TEM grid. The lift-out sample is brought into the neighborhood of the TEM grid. (f) Before welding the lift-out sample on TEM grid. The sample is brought to close proximity of the grid for welding using Pt. The lift-out sample will then be thinned equally on both sides to achieve electron transparency for best results ($\sim$ 80-100 nm).

of 10–20 kV.

7.5 Data Availability

The raw data from nTXM, 3D EBSD, and *in situ* HEXRD, as well as two movies of nTXM reconstructions, are publicly available in the University of Michigan Deep Blue Data repository at `https://doi.org/10.7302/day1-6d63`.

7.6 Acknowledgements

We gratefully acknowledge financial support from the Air Force Office of Scientific Research Young Investigator Program under award no. FA9550-18-1-0044. We also express my thanks to Professors Julia Dshemuchadse (Cornell), Sharon Glotzer, John Heron, and Amit Misra (UM) for a critical reading of the manuscript pertaining to this work [261]. We also acknowledge the University of Michigan College of Engineering for financial support and the Michigan Center for Materials Characterization for use of the instruments and staff assistance. This research used resources of the Advanced Photon Source, a U.S. Department of Energy (DOE), Office of Science User Facility operated for the DOE Office of Science by Argonne National Laboratory under Contract no. DE-AC02-06CH11357.

Chapter 8

Topological Transitions of Spiral Eutectics in Extreme Environments

This chapter is based on the article to be submitted for publication as of April 2020.

8.1 Introduction

Advances in high temperature technology have raised the need for materials with superior strength, rigidity, and ductility at elevated temperatures. To meet the challenge of higher operation temperatures, alloys based on intermetallics have been considered [26, 262, 263]. In particular, intermetallic composites have garnered recent interest as a means to improve the fracture toughness and intrinsic brittleness that

many other intermetallic-based alloys suffer from at ambient temperature [26]. A promising subset of this class of materials is *in situ* composites [26, 264], multi-phase materials where the reinforcing phase is synthesized during composite fabrication. For comparison, in *ex situ* composites the reinforcing phase is produced separately and then introduced into the matrix during a subsequent processing step such as infiltration or powder processing [265].

The strategies of synthesizing *in situ* composites can be divided into two broad groups depending on whether the reinforcements first appear in the solid or liquid state [266]. Solid-state *in situ* processes include internal oxidization [267], displacement reaction [268], reactive milling [269], mechanical alloying [270], and cryomilling [271]. Liquid-state processes include rapid solidification [272, 273], traditional casting, and directional solidification of eutectic alloys. The advantages of producing *in situ* composites by directional solidification of eutectics are multi-fold, including: (i) eutectic formation yields intrinsic thermodynamic stability and chemical compatibility between the matrix and intermetallic phases, (ii) directional solidification enables a single-stage process directly from the melt, and (iii) the microstructure can be controlled by tuning the solidification conditions (as discussed in Section 3.2).

As demonstrated in the previous chapter, directional solidification of (binary) eutectics can produce regular patterns consisting of a spiral intermetallic phase. The hierarchical nature of these spiral composites necessitated multiple experimental probes to unearth the origin of spiral growth. Collectively the results of Chapter 7 demonstrated that the spiral formation follows a two-step process, wherein the first step is mediated by the low solid–liquid interfacial energy of a precursor phase,

and the second step by crystallographic defects on the precursor. Understanding the behavior of these spirals at elevated temperature is critical to their function in extreme environments. Under such conditions these spiral *in situ* composites could degrade as a result of oxidation, reaction, and shape/size instabilities.

During isothermal annealing of eutectic composites near the eutectic temperature, the free energy associated with interfaces provides a driving force for microstructural evolution in three main ways: Rayleigh instability coarsening, Ostwald coarsening, and fault migration [39, 274]. Rayleigh instability refers to the increasing variation in the composite geometry due to periodic perturbations that grow by diffusive transport under the driving force of capillarity, as shown schematically in Fig. 8.1(a). This phenomenon somewhat resembles the breakdown of a cylinder of liquid into a row of spherical droplets, similar to that of slowly running tap water. However, the kinetics of the process in a composite are more complicated given the diffusive interaction between adjacent solid components. It has been suggested [39] that Rayleigh instabilities are less likely to occur in structures with cusps in their surface energy orientation relationship that lead to faceting, since these cusps would stabilize the structure against the diffusive perturbations resulting in pinch-off events. Ostwald coarsening, shown schematically in Fig. 8.1(b), is a bulk-diffusion process that reduces the system free energy by larger regions of the microstructure growing at the expense of the smaller ones, *via* transfer of material between the regions of different size. Fault migration and annihilation in the solid state could also lead to coarsening, as demonstrated schematically in Fig. 8.1(c). This may be the major mechanism of coarsening in highly faulted structures, where the incubation time can be very small.

Likewise, in perfect lamellar structures with alternating sheet formation, the absence of interfacial curvature prevents the operation of Rayleigh instabilities and Ostwald coarsening, and coarsening occurs almost exclusively by fault migration.

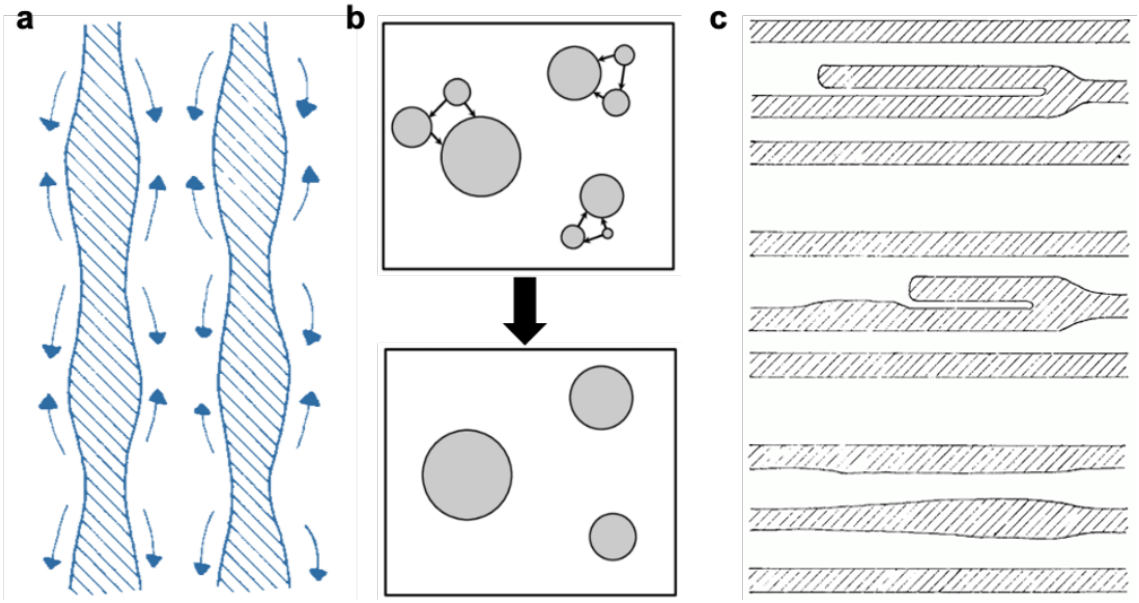

Figure 8.1: Coarsening processes. (a) Rayleigh instability coarsening. (b) Ostwald coarsening. (c) Fault migration and annihilation in a rod structure leading to coarsening. Schematics adapted from refs. [39, 275, 39], respectively.

In the present chapter, we seek to investigate the thermal stability of metastable Zn-$MgZn_2$ spiral *in situ* composites through continuous isothermal annealing near their eutectic temperature using *in situ* X-ray nano-tomography (nTXM), and further corroborated by *ex situ* crystallographic and compositional analyses. The *in situ* nTXM experiments were performed at the Full Field X-ray Imaging (FXI) beamline of the National Synchrotron Light Source II (NSLS-II) in Brookhaven National Laboratory; the *in situ* capability of performing these experiments at temperature

is a very recent addition to the beamline (fall 2019) and provides an unprecedented opportunity to probe dynamical events at high spatial and temporal resolutions. Collectively, the results identify that the structure does not evolve self-similarly, with topological breakdowns in both short- and long-term annealing due to reactive and bulk diffusion, respectively: (i) Within minutes, solid-state, reactive diffusion leads to phase transition from the metastable to the stable eutectic, which in turn causes lamellar pinch-off of the thinner portions of the intermetallic phase. (ii) During prolonged annealing (hours), bulk diffusion due to Ostwald coarsening leads to more pinch-off events and thus the formation of a greater number of disjoint components of the intermetallic phase. By unearthing the above solid-state dynamics, this study helps to generate accurate structure-performance relationships that could guide the future application of these spiral *in situ* composites in extreme environments.

8.2 Results and Discussion

8.2.1 Structural Evolution of Spirals Upon Short-Term Isothermal Annealing

In Situ Annealing *via* Synchrotron X-Ray Nano-Tomography (nTXM)

All *in situ* annealing experiments were performed using the recently-developed capability of the FXI beamline at NSLS-II in Brookhaven National Laboratory. Figure 8.2(a) shows a photo of the the beamline setup. The beamline optics allow studying the morphology of dynamic systems in 2-D and 3-D with 30 nm resolution in

a 20-40 μm field of view, and the beam energy can be tuned in the range of 6-10 keV. A complete 3D dataset for absorption-contrast tomography can be acquired in one minute [76] (as of March 2020, only absorption contrast is available). Given the beam energy and presence of a high concentration of 'heavy' element Zn in the spiral eutectics, spiral-containing 30-40 μm thick micropillars of the bulk, directionally-solidified samples were prepared by plasma focused ion beam (PFIB, Section 3.3.3) prior to arrival at the beamline. The micropillars were prepared to be tall enough so that the field-of-view could be adjusted at will along their height during beamline experiments. Images of a typical micropillar are shown in the inset of Fig. 8.2(a) and magnified in Fig. 8.2(b).

Representative 2D slices of the nTXM scans for 1, 3, 5, and 10 minutes of isothermal annealing at 270° C are shown in Figs. 8.3(a-d). Comparison of the slices reveals several instances of morphological instabilities that the spiral intermetallic phase undergoes within the first 10 minutes of annealing. Three of such pinch-off events are highlighted in Figs. 8.3(a-d). The red arrows in Figs. 8.3(a,b) point to the breakage of the $MgZn_2$ phase into disjoint components in the first three minutes of annealing. Another instance of breakage occurs upon further annealing the sample to five minutes under the same conditions, as indicated by the white arrows in Figs. 8.3(a,c). At the 10-minute mark, the lamellae show further pinch-off as well as disappearance of the thinnest portions of lamellae, demonstrated with the blue ovals in Figs. 8.3(a,d) where the lamellae have partitioned into several thinner, disjoint components during annealing.

In addition to the breakage of lamellae, the nTXM slices also show a gradual

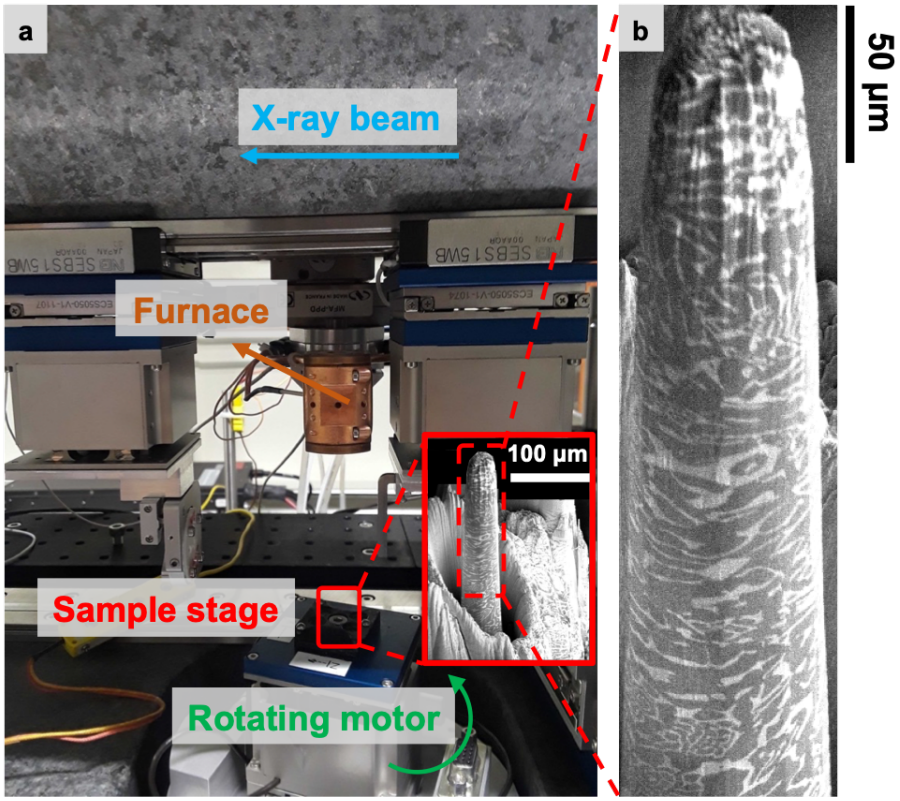

Figure 8.2: Beamline setup for *in situ* TXM at NSLS-II in Brookhaven National Laboratory. (a) Photo of the full setup at NSLS-II beamline 18-ID (FXI). A micrograph of a typical micropillar sample used in experiments is shown in the inset and magnified in (b). During the experiment, the micropillar samples are mounted on a sample holder and inserted into the furnace.

change in the signal intensity, *i.e.,* grayscale pixel value, of the scans during the first 10 minutes of annealing. Given that monochromatic X-rays are attenuated due to absorption or scattering as they pass through the sample, the concentration changes can be derived from the Beer-Lambert's law. This law relates the attenuation of incoming radiation to the properties of the material through which the radiation passes, and it is commonly applied to chemical analysis measurements from atten-

uation in physical optics [276, 277]. Furthermore, the use of monochromatic X-rays in this study helps alleviate the non-straightforward connection of intensity to composition that would be present if using a polychromatic X-ray source even when the sample thickness and the incident beam intensity are known.

The observed change in nTXM intensity suggests variations of the solutal concentration fields around the lamellae of the intermetallic phase, which could be further perturbed by the the diffusive dynamics during annealing. To evaluate the concentration changes of the lamellae experimentally, we measure the grayscale value of the pixels belonging to the intermetallic phase, averaged over five measurements for each scan in the one, three, five, and 10-minute marks. Image contrast is enhanced by normalizing each pixel using values obtained from outside the sample, where pixel values at a given spatial coordinate have the same value over the entire duration of the annealing experiment. The averaged grayscale values are plotted in Fig. 8.3(e), where the heights of the error bars represent the standard deviation of the five measurements for each scan. Since the only intensity-altering parameter is composition in this absorption–contrast tomographic dataset, equal intensities within the statistical fluctuations (error bars) indicate equivalent compositions, barring unlikely and unexpected occurrence of other events such as beam-flux variations at the beamline or intensity drop during the one-minute acquisition time of the individual scans.

Measurements of the average signal intensity for the intermetallic phase in this manner indicate an increase of grayscale values in the intermetallic lamellae. This increase in grayscale values suggests a gradual, local change of the composition of the intermetallic phase due solutal diffusion from the surrounding metallic Zn phase,

which eventually leads to a complete solid-state phase transformation of the intermetallic phase. Given the statistical fluctuations of these measurements, this solid-state phase transformation likely occurs at around 6-7 minutes into the annealing process and is complete after about 10 total minutes of annealing. These observations lead to the hypothesis, confirmed below in 8.2.1, that the $MgZn_2$ phase transforms to Mg_2Zn_{11}, and hence the eutectic from the metastable to the stable state, where the metallic Zn phase is the common phase in both eutectics. These three phases, namely Zn, $MgZn_2$, and Mg_2Zn_{11}, are distinguished in terms of differential absorption of X-rays. The heaviest phase, Zn, has the highest attenuation coefficient, 7.14 $\frac{g}{cm^3}$, and hence appears brightest in the nTXM reconstructions (*e.g.,* Figs. 8.3(a-d)). Conversely, $MgZn_2$ is the lightest phase with an X-ray attenuation coefficient of 5.09 $\frac{g}{cm^3}$, so it is the most transparent to X-ray radiation and appears darkest. The Mg_2Zn_{11} has an intermediate X-ray attenuation coefficient, 6.17 $\frac{g}{cm^3}$, and hence it appears brighter than the lighter $MgZn_2$ phase but darker than the heavier Zn phase. The color gradient in Fig. 8.3(e), from dark to light and *vice versa*, represents gradual, local change of composition due solutal diffusion that eventually leads to the solid-state phase transformation, from $MgZn_2$ (yellow) to Mg_2Zn_{11} (blue). These observations are further corroborated by chemical composition analysis *via* energy-dispersive X-ray spectroscopy (EDS) in *ex situ* annealing experiments mimicking the *in situ* nTXM experiments, as reported below.

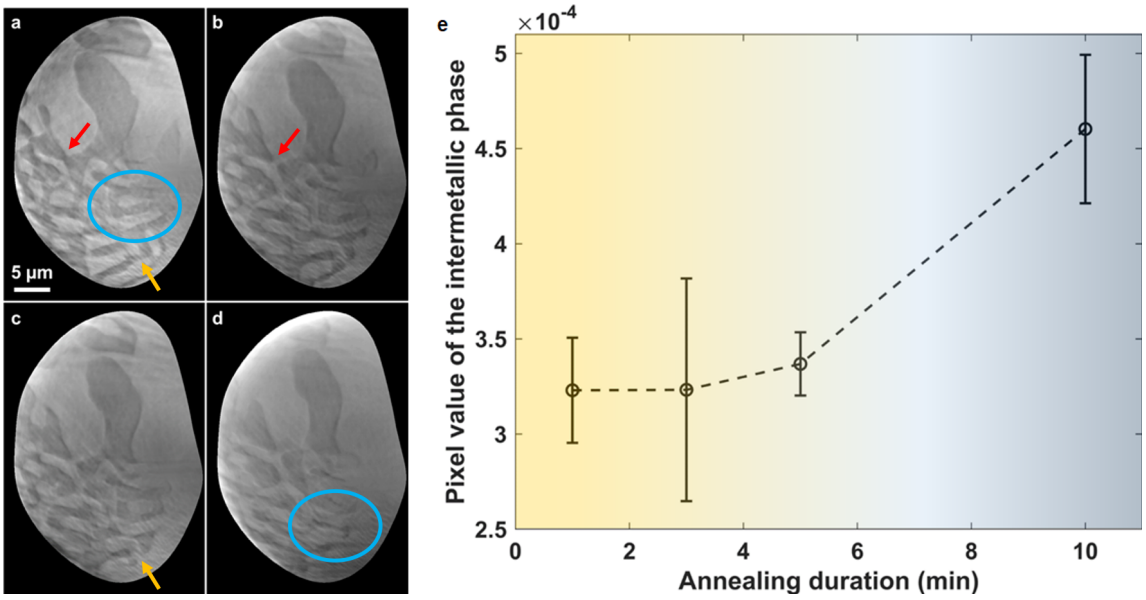

Figure 8.3: 2D representative slices of short-term annealing nTXM scans of spirals. (a-d) 1, 3, 5, and 10 minutes after isothermal annealing. Images are adjusted for brightness and contrast for clarity, and several topological transitions (pinch-off events) are marked. (e) Intensity value of the intermetallic phase (dark in (a-d) from the grayscale slices averaged over five measurements. The increase in intensity shows compositional change of the intermetallic phase.

Chemical Composition Analysis *via* Energy-Dispersive X-Ray Spectroscopy (EDS)

To confirm the occurrence of the solid-state phase transformation from the metastable Zn-$MgZn_2$ to the stable Zn-Mg_2Zn_{11} eutectic during the first 10 minutes of isothermal annealing, chemical composition of a sample annealed by mimicking the *in situ* conditions was analyzed *via* EDS. The EDS point analysis was performed on the intermetallic phase of the sample in two regions after one and 10 minutes of annealing, and the results are tabulated in Tables 8.1 and 8.2, respectively. Identical points were investigated in the two regions for the one and 10-minute annealed sample. As the

measurements in Table 8.1 show, the intermetallic phase in the one-minute annealed sample has the composition 21.68 ± 2.84 atomic percent (at.%) Mg and 78.42 ± 2.84 at.% Zn in region one, and 29.47 ± 3.72 at.% Mg and 70.53 ± 3.72 at.% Zn in region two. Therefore, at this stage the eutectic composition is Zn-$MgZn_2$.

	Region 1		Region 2	
Point number	At.% Mg	At.% Zn	At.% Mg	At.% Zn
1	23.40	76.60	26.52	73.48
2	19.53	80.47	25.87	74.13
3	24.29	75.71	25.88	74.12
4	24.71	75.24	33.14	66.86
5	18.71	81.29	32.34	67.66
6	21.59	78.41	33.05	66.95
7	18.86	81.14		
8	25.46	75.54		
9	18.56	81.44		

Table 8.1: Compositional analysis of the intermetallic phase in the one minute-annealed spiral eutectics. Compositions were determined from point EDS analysis in two distant regions of the sample. Composition of the intermetallic phase is determined to be $MgZn_2$.

After 10 minutes of annealing have passed, the compositions of the same two regions, shown in Table 8.2 based on measurements of the same points as those in Table 8.1, have changed to 11.56 ± 3.19 at.% Mg and 88.44 ± 3.19 at.% Zn in region one, and 15.83 ± 1.80 at.% Mg and 84.12 ± 1.80 at.% Zn in region two. These sets of compositions indicated that the intermetallic phase has indeed changed composition to Mg_2Zn_{11}, while the other eutectic phase remains as metallic Zn.

	Region 1		Region 2	
Point number	At.% Mg	At.% Zn	At.% Mg	At.% Zn
1	10.40	89.60	14.93	85.07
2	10.20	89.80	13.98	86.02
3	13.02	86.98	14.19	85.81
4	13.86	86.14	17.51	82.49
5	11.11	88.89	16.35	83.65
6	10.00	90.00	18.34	81.66
7	7.99	92.01		
8	18.53	81.47		
9	8.92	91.08		

Table 8.2: Compositional analysis of the intermetallic phase in the 10 minute-annealed eutectics. Compositions were determined from point EDS analysis on the same points of the same regions reported in Table 8.1. Composition of the intermetallic phase is determined to be Mg_2Zn_{11}.

8.2.2 Topological Singularities and Transitions Upon Long-Term Isothermal Annealing

In Situ Coarsening *via* nTXM

As mentioned earlier, the free energy associated with interfaces in multi-phase alloys may provide a driving force for microstructural evolution. In minimizing its total interfacial free energy through, *e.g.,* reduction of the total interfacial area of grain and interphase boundaries, a system undergoes structural evolution by transferring material from one boundary region to another *via* one or a combination of the three possible mass-transport mechanisms surveyed above (Rayleigh instability coarsening, Ostwald coarsening, and coarsening by fault migration or fault migration and annihilation). The resulting evolution of the microstructure cannot occur without topological transitions and singularities, which have been reported mostly for

multi-phase fluid systems [278]. Herein we demonstrate a distinct class of topological singularity that occurs during the long-term (1 h) solid-state coarsening (SSC) of the two-phase Zn-$MgZn_2$ spiral eutectic composites. We utilize the recent developments of the FXI beamline at NSLS II to unravel the dynamics of coarsening.

In what follows, we limit our analysis to after the completion of the solid-state phase transformation from $MgZn_2$ to Mg_2Zn_{11}, which was shown in Section 8.2.1 to occur within the first 10 minutes of annealing. During the *in situ* coarsening experiments, pinch-off occurs in the intermetallic Mg_2Zn_{11} phase of the otherwise bicontinuous, two phase eutectic composite. The loss of continuity in this phase by pinching directly impacts the properties of the composite, so understanding the dynamics that govern this process could offer key insights relevant to the processing of these materials and their microstructural control.

Segmented 3D volume renderings of a region of interest in the micropillar sample, indicated by dashed boxes in the accompanying grayscale volumes, are shown in Figs. 8.4(a,b) for the pristine and one hour-annealed sample, respectively. In the segmented volumes only the intermetallic phase is shown for clarity, which, again based on the results shown in Section 8.2.1, has the chemical composition $MgZn_2$ in Fig. 8.4(a), Mg_2Zn_{11} in Fig. 8.4(b). In the pristine sample, it can be seen that the eutectic microstructure is highly directional and bicontinuous. After one hour of SSC, not only has the intermetallic phase lost its morphological anisotropy (no longer faceted), but also it has undergone a pinch-off event, as evident from the presence of disjoint components. An example of a pinch-off event is indicated by the black arrows.

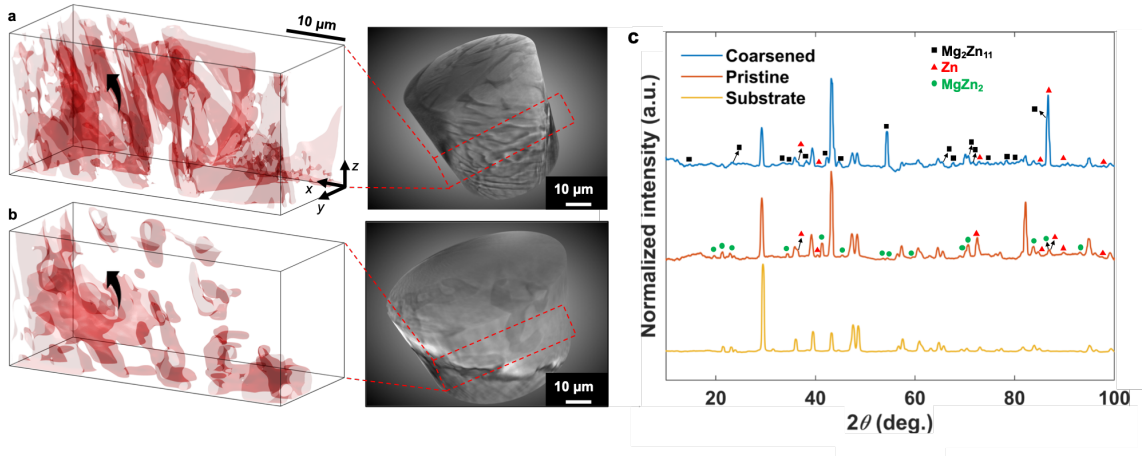

Figure 8.4: Topological evolution and spheroidization of the intermetallic lamellae upon long-term annealing. (a,b) Three-dimensional visualization of the pristine and 1-hr annealed sample, respectively. The segmented volumes correspond to the boxed regions in the corresponding grayscale volume. (c) XRD spectra of the sample before and after annealing. All non-labeled peaks belong to the substrate used during acquisition of the scans; the substrate spectrum is provided for reference.

Crystallographic Analysis *via* X-Ray Diffraction (XRD)

Given that the two intermetallic phases of interest, $MgZn_2$ and Mg_2Zn_{11}, have hexagonal and cubic crystal structures, respectively, we further corroborated the occurrence of the solid-state phase transformation by XRD. A fresh directionally-solidified sample was prepared following the same growth conditions used for the above investigations. The pristine sample was then scanned by XRD, followed by annealing at the identical conditions as above but for a total time of 10 hours. We note that the 10 hour mark ensures not only the initial solid-state phase transformation from $MgZN_2$ to Mg_2Zn_{11}, but also provides enough time for all the subsequent morphological and topological events during further annealing of the intermetallic phase.

The XRD spectra of both the pristine and the coarsened samples are presented

in Fig. 8.4(c). All peaks corresponding to the intermetallic phases have been labeled green for $MgZn_2$ and black for Mg_2Zn_{11}; the peaks belonging to the metallic Zn phase are labeled with red marks. All non-labeled peaks belong to the substrate (clay) used to support the sample during acquisition of the XRD scans. The XRD scans indicate no further phase transformation of the intermetallic phase after the initial one that shift the eutectic composition from the metastable Zn-$MgZn_2$ to the stable Zn-Mg_2Zn_{11} even after prolonged (nine hours) additional annealing under the same conditions. This observation suggests that the system reaches its steady-state chemical composition within the first few minutes of isothermal annealing, and thereafter undergoes topological singularity events and pinch-off while maintaining its composition.

8.2.3 Mechanisms of Phase and Topological Evolution

Solid-State Phase Transformation and Topological Breakdown Upon Short-Term Annealing

The results from *in situ* nTXM (Fig. 8.3) and *ex situ* EDS (Tables 8.1,8.2 show the transition from metastable $MgZn_2$ to stable Mg_2Zn_{11} phase upon annealing at 270°C. As evident from the phase diagram in Fig. 8.5, anywhere below the solid line at 364°C, Mg_2Zn_{11} is expected. The $MgZn_2$ is metastable, meaning that its free energy for all temperatures below 364°C is higher than the free energy of Mg_2Zn_{11}. Therefore, based on thermodynamic arguments alone, the transformation Zn + $MgZn_2$ = Mg_2Zn_{11} is expected for all temperatures $T < 364$°C. The EDS results suggest that short-term annealing close to but below the metastable eutectic temperature

provides the driving force for this phase transformation.

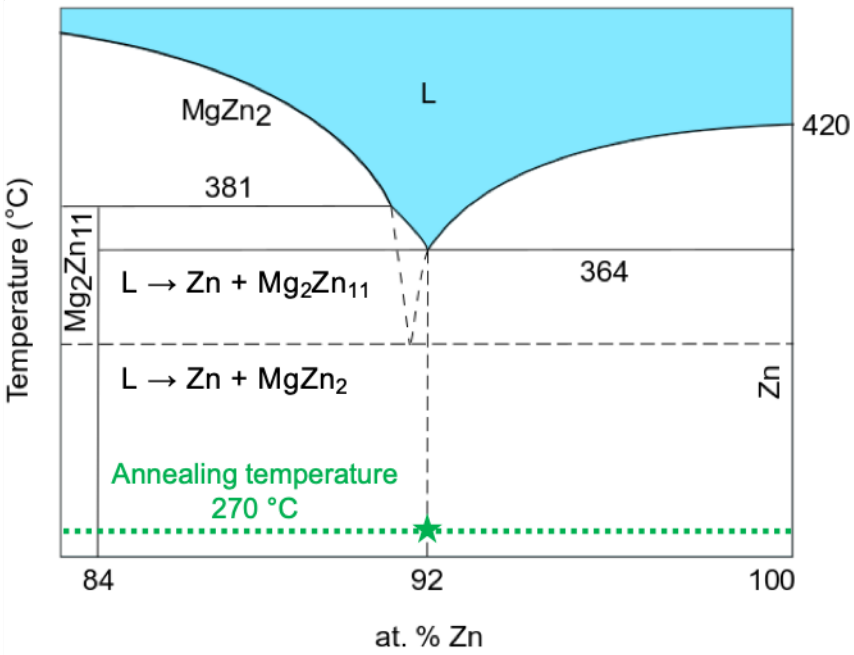

Figure 8.5: Portion of the equilibrium phase diagram of the Zn-Mg system with the two relevant intermetallic phases marked. The stable and metastable eutectic temperatures are indicated with the solid and dashed lines, respectively. The annealing temperature, 270°C, is indicated with the green dotted line.

Equilibrium thermodynamics and diffusion kinetics can be used to predict the variation of chemical composition in the diffusion zone during solid-state reactions between dissimilar materials. Indeed, a number of reactive phase formation events have been reported in metal-metal and metal-ceramic systems due to solid-state diffusion [279]. In the present case, the nTXM snapshots (Fig. 8.3(a-d)) show that the metastable phase $MgZn_2$ is consumed in the thinnest portions of lamellae. We rationalize this observation by noting that, during annealing, solutal Zn from the surrounding eutectic Zn phase accumulates around the $MgZn_2$ lamellae and eventually

diffuses into it, given that Zn is the fast diffuser compared to Mg [280]. The solutal diffusion of metallic Zn into the intermetallic phase, as shown in Fig. 8.6(a), changes the intermetallic composition locally and, within 10 minutes of annealing, the eutectic phase transformation to the stable Zn-Mg_2Zn_{11} is complete. Consumption of the $MgZn_2$ phase during this reaction-dominated process is observed to result in pinching or breaking apart of the intermetallic phase, leading to topological changes on shorter time-scales than predicted by either Rayleigh or Ostwald mechanisms.

In reacting systems that include interphase mass transport, such as the present case, the Damköhler number Da is a useful ratio for determining whether diffusion rates or reaction rates are more 'important' for defining a steady-state chemical distribution over the length and time scales of interest. Da is the ratio of the reaction to diffusion rates. The results from short-term annealing of the spiral eutectics point to a high Da number where an extremely fast reaction occurs, so that the process is limited by the solutal diffusion. Upon completion of the solid-state phase transformation, the annealing process is expected to be diffusion-dominated, as expounded below.

Topological Change at Long Time-Scales

Upon further annealing at the same conditions, the structure is observed to not evolve self-similarly. Instead, the Mg_2Zn_{11} phase undergoes topological instabilities and the formation of a greater number of disjoint components (Fig. 8.4(a,b)). Unlike the Rayleigh instability [39], where the Mg_2Zn_{11} would break down into near-spherical droplets similar to that of the slowly-running tap water, we do not observe a spectrum

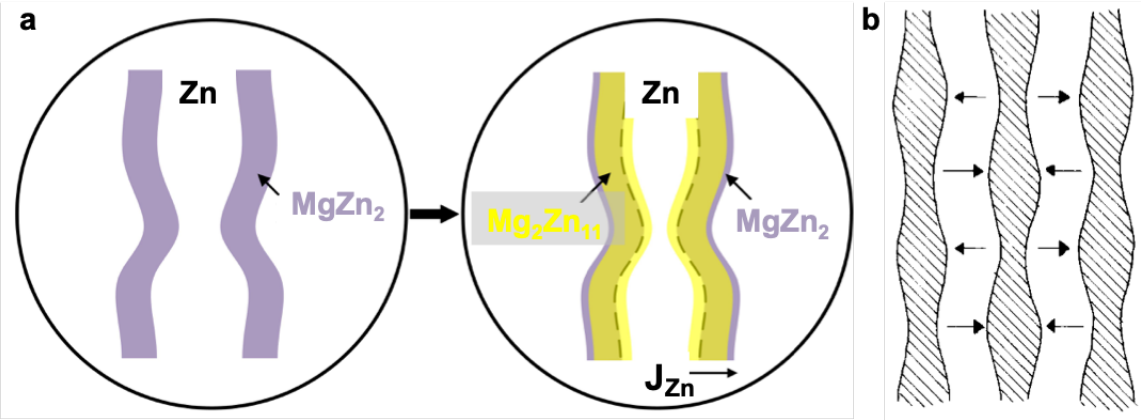

Figure 8.6: Proposed mechanism of short-term and long-term microstructural changes upon annealing. (a) Schematic illustration of reactive diffusion-mediated solid-state phase transition upon short-term annealing. (b) Schematic illustration of bulk diffusion-mediated Ostwald coarsening observed upon long-term annealing. Schematic adapted from ref. [39].

of sinusoidal perturbations that grow by diffusive transport under the driving force of capillarity.

Instead, the results from prolonged annealing experiments suggest not a surface diffusion process, but a more likely bulk diffusion process through Ostwald coarsening. During this process, the system reduces its overall interfacial free energy by the larger regions growing at the expense of the smaller ones by bulk diffusion of the material between regions of differing size, as shown schematically in Fig. 8.6(b). The results from prolonged annealing experiments point to a low Da number, where the process is dominated by bulk diffusion due to Ostwald ripening. The negative curvature of the thinnest parts of the lamellae lead to dissolution of the intermetallic phase into a greater number of disjoint components. Understanding the microstructural dynamics in this way is critical for controlling the behavior of materials at elevated

temperatures, for instance with regard to the function of materials in aerospace and automotive applications.

8.3 Summary

We investigated the behavior of thermodynamically metastable Zn-$MgZn_2$ spiral eutectics at elevated temperatures during isothermal annealing close to but below the metastable eutectic temperature. Combination of the recently developed *in situ* TXM together with *ex situ* characterization studies indicate that annealing relieves the metastable spirals from defects (screw dislocations) that were created during the formation of the material (as reported in Chapter 7). Short-term annealing, within the first few minutes, provides enough thermodynamic driving force to the system to undergo a solid-state transformation, *i.e.,* precipitation, from the metastable state to the thermodynamically stable Zn-Mg_2Zn_{11} eutectic. The precipitation process occurs under a high Damköhler number through solutal diffusion of Zn from the surrounding eutectic Zn phase into the intermetallic phase, which in turn causes the topological breakdown of the intermetallic phase on short-time scales at its thinnest sections. During prolonged annealing under the same conditions, the system operates under the dominance of bulk diffusion and hence does not evolve self-similarly. Instead, the intermetallic phase undergoes a different class of topological singularity events and divides into disjoint components through Ostwald coarsening.

8.4 Materials and Methods

8.4.1 *In Situ* nTXM for Isothermal Annealing

The nTXM experiments were conducted at beamline 18-ID (FXI) of the National Synchrotron Light Source II (NSLS-II) in Brookhaven National Laboratory (Upton, NY). Prior to the *in situ* nTXM experiments, a micropillar of the directionally-solidified, spiral-containing sample was prepared from the bulk eutectic sample by Xe plasma focused ion beam (typically 30-50 μm in diameter and 100-120 μm in height). During the *in situ* annealing experiments, the micropillar was irradiated by 8.5 keV X-ray beam and rotated continuously at 3 $\frac{^\circ}{s}$ with 30 ms exposure time for each projection image. All images were acquired with a 2 $\times$ 2 binning, resulting in a pixel size of 42.6 nm $\times$ 42.6 nm.

8.4.2 *Ex Situ* EDS for Chemical Composition Analysis

Chemical composition investigation of the samples was performed using an EDS-equipped Tescan MIRA3 scanning electron microscope. The beam voltage was adjusted to 20-30 kV. Point analysis was performed by focusing the beam onto a point of interest along the intermetallic phase of the eutectics in two distant regions. Chemical composition of 6-9 points were measured to obtain good statistical reproducibility. Sample was annealed at 270 °C for one minute, interrupted for EDS point analysis, further annealed for additional nine minutes, and followed by EDS point analysis of the same points in the same two regions.

8.4.3 *Ex Situ* XRD for Crystal Structure Characterization

The XRD scans were performed using a Rigaku Smartlab diffractometer equipped with 1.54 $\mathring{A}$ Cu Kα source and Ge-220 2-bounce monochromator. Two scans were performed, one for the pristine (non-annealed) sample, and another after annealing the sample at 270 °C for 10 hours.

8.5 Data Availability

The raw data from nTXM is publicly available in the University of Michigan Deep Blue Data repository at `https://doi.org/10.7302/v73g-tn92`.

8.6 Acknowledgements

We gratefully acknowledge the financial support from the Air Force Office of Scientific Research Young Investigator Program under award no. FA9550-18-1-0044. We thank Paul Chao, Insung Han, Geordie Lindemann, and Xianghui Xiao for assistance in nTXM, as well as Ying Qi for for assistance in XRD.

Part IV

Conclusions and Outlook

Chapter 9

Conclusions

During crystal growth the interplay of kinetics, solution or alloy chemistry, and crystallographic defects brings about a continuum across crystal formation patterns. This dissertation illustrated developments in multi-scale eutectic pattern formation during solidification from multi-component environments. Focus was put on deciphering the mechanisms that trigger micro/nanostructure selection as well as morphological and topological transitions, along with the influence of crystallographic defects on pattern formation. Both regular and irregular eutectics were considered. Part I, divided into Chapters 1-3, provides the introductory information related to the thermodynamics and kinetics of eutectic solidification patterns, as well as an overview of other key concepts that were subsequently explored in the remainder of this dissertation.

Part II, partitioned into Chapters 4-6, relates to the growth of irregular eutectics as well as primary anisotropic crystals in the presence of trace chemical modifiers. Part III, split into Chapters 7 and 8, reports the self-organization of two-phase spiral

eutectics and their behavior at elevated temperatures. These experimental findings along with their broader impacts are summarized in Sections 9.1 and 9.2, respectively.

9.1 Complexity in Crystal-Modifier Interactions During Crystallization from Multi-Component Environments

Chemical modification by the introduction of dopants or other 'spectator' species into the alloy chemistry causes drastic changes in the microstructure of the material, and the interaction of the modifier with the growing crystal could be either synergistic (Chapters 4, 5) or antagonistic (Chapter 6). The specificity of chemical modifiers for either inhibition, by poisoning the nucleation sites, or promotion, by lowering the barriers of nucleation, directly impacts the crystallization products and their defect distributions. Understanding the origins of these effects is key to tailoring the design of alloys for specific technological needs.

Chapter 4 reviewed the recent developments in our understanding of microstructure formation during eutectic solidification. Chapter 5 provided experimental results from tracking the growth behavior of a Na-modified (0.1 wt.%) irregular Al-Ge eutectic alloy and analysis of the physical characteristics of the fully-solidified specimen. The integrated characterization studies shed light on the influence of trace chemical modifiers (here Na) during the growth of the eutectic. In particular, the dynamic and 3D synchrotron-based X-ray micro-tomography results reveal the markedly dif-

ferent microstructural and, for the first time, topological properties of the eutectic constituents that arise upon modification, not fully predicted by the existing theories. Together with *ex situ* crystallographic characterization of the fully-solidified specimen, our multi-modal study provides a unified picture of eutectic modification: The modifiers selectively alter the stacking sequence of the faceted phase (here Ge), thereby inhibiting its steady-state growth. Consequently, the non-faceted phase (here Al) advances deeper into the melt, eventually engulfing the faceted phase in its wake. We present a quantitative topological framework to rationalize these experimental observations, demonstrating that interfacial topology represents a signature of the structural complexity during crystallization.

Chapter 6 focused on the growth behavior of primary Si crystals in the presence of trace chemical modifiers (here 0.1 wt.% Sr) a hypereutectic Al-Si alloy. The coherent twin boundary is widely known to catalyze growth in pristine crystals including polycrystalline Si. Much remains unknown about the impact of changing the chemical environment of the crystallization process through the deliberate addition of trace metallic species as in chemical modification. Pristine Si has been reported to grow through the classical model of two parallel twin planes acting in concert to enable steady-state propagation of the solid-liquid interfaces. Here, we achieve a new vision on the growth process *via in situ* synchrotron X-ray micro-tomography and further corroborated by *ex situ* crystallographic investigation. We find that steady-state growth is impossible in chemically-modified alloys. This is because the modifier (Sr) poisons the concave re-entrant grooves of Si, thereby de-activating the advantage of the twin plane re-entrant edge mechanism and leading to a singly-twinned interface.

This study may serve as a proxy to chemically-modified crystallization pathways of eutectic Si in Al-Si alloys and, more broadly, as a framework for the crystallization mediated-synthesis of materials.

These insights as well as experimental techniques could be extended to other materials classes, beyond Al-Si, that involve the interaction of 'spectator' species such as modifiers, dopants, and impurities, during the growth of the crystal. As an example, the newly investigated Al-Ce alloys [181] demonstrate castability, structure, and mechanical strength similar to the near-eutectic Al-Si alloys modified by Sr; as a result, the Al-Ce alloys have been rated positively for laser additive manufacturing (no cracking or porosity). In another recent report [11], it was demonstrated that chemical modification of the feedstock alloy with grain refining modifiers for additive manufacturing can achieve previously incompatible high-strength aluminum alloys that are crack-free, equiaxed, and fine-grained. In a broader context, the synergistic or antagonistic behavior reported in this dissertation may provide guidance in the search for suitable promoter, or inhibitor, combinations to control crystallization of synthetic and additive manufacturing of biomimetic materials.

9.2 Emergence of Two-Phase Spirals *via* Multi-Step Crystallization and Their Thermal Behavior

Chapter 7 focuses on the underlying mechanism and growth dynamics of two-phase spiral eutectics in the Zn-Mg alloy system. This work represents a method for the solidification of metallic alloys involving spiral self-organization as a new strategy for producing large-area chiral patterns with emergent structural and optical properties. The investigation reports discovery of a new growth mode for metastable, two-phase spiral patterns from a liquid metal. Crystallization proceeds *via* a non-classical, two-step pathway consisting of the initial formation of a polytetrahedral seed crystal, followed by ordering of two solid phases that nucleate heterogeneously on the seed and grow in a strongly-coupled fashion. Crystallographic defects within the seed provide a template for spiral self-organization. These observations demonstrate the ubiquity of defect-mediated growth in multi-phase materials and establish a pathway toward bottom-up synthesis of chiral materials with an inter-phase spacing comparable to the wavelength of infrared light. Given that liquids often possess polytetrahedral short-range order, our results are applicable to many systems undergoing multi-step crystallization.

Chapter 8 reports the behavior of these metastable spiral eutectics in extreme environments, specifically during isothermal annealing close to, but below, the metastable eutectic temperature. Results from *in situ* X-ray nano-tomography, together with *ex situ* compositional and crystallographic analyses, identify the dynamics of annealing-

mediated structural transitions in the spiral Zn-$MgZn_2$ eutectics. At short timescales (up to 10 minutes) of annealing, the faceted intermetallic phase undergoes a solid-state transformation (precipitation) to Mg_2Zn_{11}, thus transforming the eutectic to the thermodynamically stable one. Therefore, short-term annealing relieves the metastable spirals from crystallographic defects (screw dislocations) that were created during the formation of the material. At long timescales (up to 10 hours) of annealing, the structure attains this new composition but evolves non-self-similarly and proceeds, through topological transitions (pinch-off) and singularities, toward a greater number of disjoint components through Ostwald coarsening. The loss of continuity in the intermetallic phase impacts the properties of the eutectic composite. Understanding these dynamics and, more broadly, the behavior of these spiral *in situ* composites could offer key insights relevant to their processing and guide their potential application in extreme environments.

Chapter 10

Outlook

Many fundamental questions remain open relating to the growth of anisotropic systems such as irregular eutectics and certain primary crystals, as do others for the growth and chirality control of spiral eutectics. This dissertation concludes by highlighting some of these open questions, related ongoing efforts excluded from this dissertation (but to be submitted for a forthcoming publication), potential future research directions for both thrusts, and an outlook into broader context and impact.

10.1 Growth of Chemically-Modified Anisotropic Systems

Concerning anisotropy, it remains to be determined how it influences pattern selection and dynamics. More detailed information on the structure and nonlinear interface kinetics that are characteristic for faceted growth remains to be uncovered.

Key opportunities reside in integrating carefully designed *in situ* characterization studies with quantitative numerical and atomistic simulations, for instance along the lines described in ref. [281] . The parallel progress of both *in situ* experimentation and numerical phase-field simulations is highlighted in the excellent review in ref. [282]. Recent developments on both aspects show that the potential of these methods remains to be fully exploited. For *in situ* monitoring of solidification processes, and particularly for metals and alloys [283, 284, 285, 286, 287], X-ray imaging has proven to be the method of choice. Coupling X-ray imaging with controlled solidification enables exploration of how processing conditions (*e.g.,* cooling rate) influence microstructural development.

For instance, while excluded from this thesis, part of this dissertation research focused on sub-millisecond microstructure formation in chemically-modified Al-Si eutectic alloys. The distinguishing feature of this work compared to other recent studies (including *in situ* approaches) is that the latter have shed light into the late-stage growth dynamics of eutectics [141, 136, 57, 30] in both the absence and presence of modifiers, whereas in the former we aim to unearth the very formation of these structures from the parent liquid phase through fast X-ray radiography. We note that interfacial dynamics immediately following the onset of formation are characterized by much smaller time-scales (sub-milliseconds) compared to growth (seconds). Additionally, together with recently reported data processing algorithms for synchrotron X-ray imaging experiments, further quantitative information on the millisecond scale can be obtained [288, 289].

Through fast X-ray radiography and the above mentioned data processing algo-

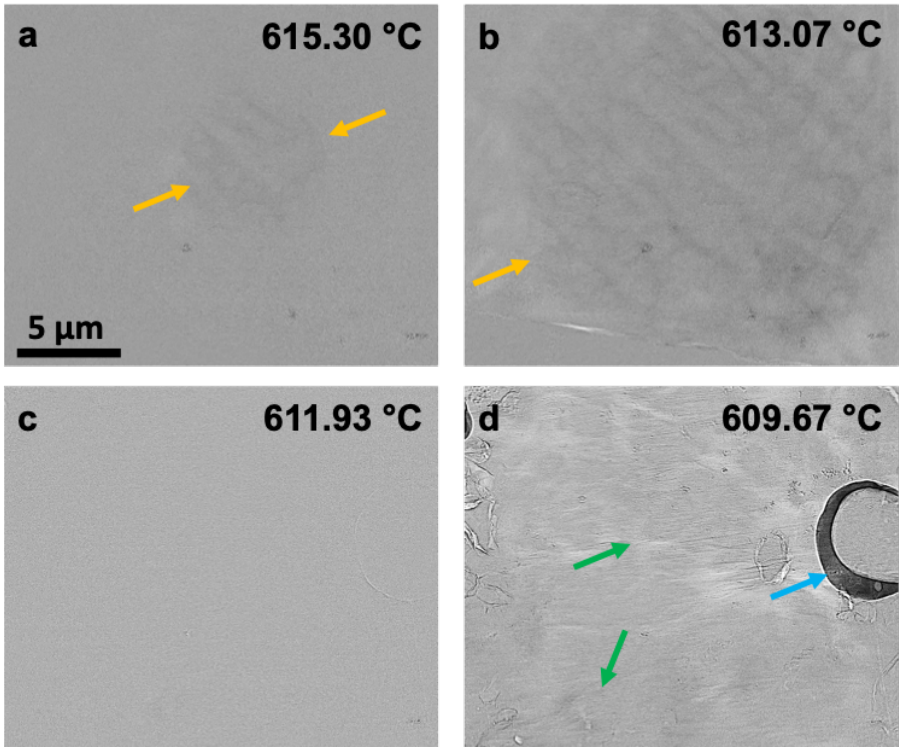

Figure 10.1: Sub-millisecond microstructure formation in chemically-modified Al-Si-based eutectic alloys. Preliminary results from synchrotron X-ray radiography during solidification of hypoeutectic Al-7Si-0.1Sr (wt. %) (a,b) and A356-0.1Sr-0.03P (c,d) alloys showing transformation of the liquid state to the eutectic. Some solid-liquid interfaces are shown by the orange and green arrows for the two alloys (the blue arrow in (d) points to a bubble). A356: Al-7Si-0.3Mg-0.2Fe-0.1Zn.

rithms (preliminary results shown in Fig. 10.1), we will be uniquely positioned to answer the following fundamental questions: (i) How do the critical undercooling, colony formation rate, and density scale with the concentration of chemical modifiers? (ii) How do the formation rate and density vary with undercooling in the presence of modifiers? (iii) Do different modifiers influence colony formation events at varying degrees? If so, can trends be rationalized in terms of easily accessible physical characteristics of the modifiers (*e.g.,* their atomic radius or solubility in the

eutectic phases, *etc.*)? We aim to utilize the results from this ongoing investigation to develop a physically consistent model for nucleation of eutectics - and crystals in general - in chemically-modified environments in order to extract correlations between the critical undercooling (*i.e.,* the thermodynamic driving force for solidification), formation rate, and density of eutectic (crystal) colonies in the presence of modifiers. Such insights can be readily extended to a vast array of other materials systems in which chemical modifiers play a critical role, *e.g.,* additive manufacturing of technologically useful multi-component alloys.

10.2 Growth and Chirality Control of Spiral Eutectics

Future avenues of research into the two-phase spiral eutectics could focus on (i) expansion upon kinetic considerations behind the formation of the metastable spirals by altering the alloy chemistry, and (ii) chirality-controlled crystallization *via* screw dislocations.

10.2.1 Impact of Alloy Chemistry

Future work into the growth of two-phase spirals could expand upon kinetic factors on the formation of the metastable spirals, for instance by consideration of alloy chemistry through minor substitution of Zn with a third component in the nominal Zn-Mg alloys. It is known that a third component can significantly alter solute distribution, interfacial energy, and interface stability of a solid/liquid interface, as

well as nucleation behavior in solidification of binary alloys [40]. Thus, investigation of changing the alloy chemistry may improve our understanding of spiral eutectic formation in the Zn-Mg system.

10.2.2 Chirality-Controlled Crystallization of Spirals

Chirality plays an important role in science and technology [239, 290]. However, the understanding of chirality amplification from chiral building blocks to spiral or helical structures remains a challenge. It has recently been demonstrated that topological defects, such as screw dislocations, can drive the chirality transfer from particle to supramolecular structure level during crystallization processes [239]. Model chiral systems have provided evidence for a screw dislocation-based mechanism to monitor, through the kinetics of crystal growth, the chiral morphology of 2D crystals from achiral to twisted structure. This recent demonstration [239] provides a framework in which screw dislocations drive the chirality amplification from constituent particles to the resulting crystalline structures, allowing for the design and elaboration of chiral functional materials of tunable helicity.

Given certain overlaps that exist with the work reported in this dissertation, namely screw-mediated two-phase spiral growth (Chapter 7), successful application of the above concept to the spiral eutectics explored herein would lead to a generalization of this chirality amplification strategy to multi-phase, hierarchical materials that are far more complex than model chiral systems explored previously. Achieving this level of predictive control is of both scientific interest and technological relevance.

10.3 Broader Context and Directions for the Future

The aim of this dissertation has been to address some of the open questions in the field through multi-modal characterization studies including the recent innovations in nanoscale X-ray tomography and aberration-corrected electron microscopy. Recent advances in these and other modalities have opened exciting opportunities in probing the materials structural parameters and various functional properties in real-space across length- and time-scales. Accompanying this progress is an exponential increase in the size and quality of data sets produced by microscopic and spectroscopic experimental techniques. The confluence of these developments necessitates adequate methods for extracting relevant physical and chemical information from the large data sets. It is envisioned that further integration of emerging data science methods will usher a new era of materials characterization studies and the associated structure-property-function relationships. Such correlative studies can also provide multifaceted experimental maps to guide computational modeling, which in turn promotes rapid discovery and design of new materials to tackle scientific questions that would otherwise be too difficult to address.

Part V

References

Bibliography

[1] In Seok Yang, Mi Rae Sohn, Sang Do Sung, Yong Joo Kim, Young Jun Yoo, Jeongho Kim, and Wan In Lee. Formation of pristine CuSCN layer by spray deposition method for efficient perovskite solar cell with extended stability. *Nano Energy*, 32:414–421, feb 2017.

[2] Jin Hyuck Heo, Dae Ho Song, and Sang Hyuk Im. Planar CH3NH3PbBr3 hybrid solar cells with 10.4% power conversion efficiency, fabricated by controlled crystallization in the spin-coating process. *Advanced Materials*, 26(48):8179–8183, dec 2014.

[3] Chang Yan, Jialiang Huang, Kaiwen Sun, Steve Johnston, Yuanfang Zhang, Heng Sun, Aobo Pu, Mingrui He, Fangyang Liu, Katja Eder, Limei Yang, Julie M. Cairney, N. J. Ekins-Daukes, Ziv Hameiri, John A. Stride, Shiyou Chen, Martin A. Green, and Xiaojing Hao. Cu2ZnSnS4 solar cells with over 10% power conversion efficiency enabled by heterojunction heat treatment. *Nature Energy*, 3(9):764–772, sep 2018.

[4] Tuncay Ozel, Benjamin A. Zhang, Ruixuan Gao, Robert W. Day, Charles M. Lieber, and Daniel G. Nocera. Electrochemical Deposition of Conformal and Functional Layers on High Aspect Ratio Silicon Micro/Nanowires. *Nano Letters*, 17(7):4502–4507, jul 2017.

[5] A.J. Malkin, Yu. G. Kuznetsov, T. A. Land, J. J. Deyoreo, and A. McPherson. Mechanisms of growth for protein and virus crystals. *Nature Structural Biology*, 2(11):956–959, nov 1995.

[6] S. D. Durbin and G. Feher. Protein Crystallization. *Annual Review of Physical Chemistry*, 47(1):171–204, oct 1996.

[7] D. T.J. Hurle and P. Rudolph. A brief history of defect formation, segregation, faceting, and twinning in melt-grown semiconductors. *Journal of Crystal Growth*, 264(4):550–564, mar 2004.

[8] R. Kern and R. Dassonville. Growth inhibitors and promoters examplified on solution growth of paraffin crystals. *Journal of Crystal Growth*, 116(1-2):191–203, jan 1992.

[9] Terry A. Land, Tracie L. Martin, Sergey Potapenko, G. Tayhas Palmore, and James J. De Yoreo. Recovery of surfaces from impurity poisoning during crystal growth. *Nature*, 399(6735):442–445, jun 1999.

[10] John E Hatch. *Aluminium: Properties and Physical Metallurgy*. ASM International, 1995.

[11] John H. Martin, Brennan D. Yahata, Jacob M. Hundley, Justin A. Mayer, Tobias A. Schaedler, and Tresa M. Pollock. 3D printing of high-strength aluminium alloys. *Nature*, 549(7672):365–369, sep 2017.

[12] J. Günther, F. Brenne, M. Droste, M. Wendler, O. Volkova, H. Biermann, and T. Niendorf. Design of novel materials for additive manufacturing - Isotropic microstructure and high defect tolerance. *Scientific Reports*, 8(1):1298, dec 2018.

[13] Andrey Vyatskikh, Stéphane Delalande, Akira Kudo, Xuan Zhang, Carlos M. Portela, and Julia R. Greer. Additive manufacturing of 3D nano-architected metals. *Nature Communications*, 9(1):593, dec 2018.

[14] Mathias Jucker and Lary C. Walker. Self-propagation of pathogenic protein aggregates in neurodegenerative diseases, sep 2013.

[15] Dimo. Kashchiev. *Nucleation: Basic theory with applications*. Butterworth Heinemann, 2000.

[16] David A. Hutchins. Oceanography: Forecasting the rain ratio. *Nature*, 476(7358):41–42, aug 2011.

[17] J. J. De Yoreo and Peter G. Vekilov. Principles of Crystal Nucleation and Growth. *Reviews in Mineralogy and Geochemistry*, 54(1):57–93, jan 2003.

[18] T. Beuvier, I. Probert, L. Beaufort, B. Suchéras-Marx, Y. Chushkin, F. Zontone, and A. Gibaud. X-ray nanotomography of coccolithophores reveals that coccolith mass and segment number correlate with grid size. *Nature Communications*, 10(1):1–8, dec 2019.

[19] Nicholas J. Greybush, Iñigo Liberal, Ludivine Malassis, James M. Kikkawa, Nader Engheta, Christopher B. Murray, and Cherie R. Kagan. Plasmon Resonances in Self-Assembled Two-Dimensional Au Nanocrystal Metamolecules. *ACS Nano*, 11(3):2917–2927, mar 2017.

[20] James J De Yoreo, Pupa U.P.A. Gilbert, Nico A.J.M. Sommerdijk, R Lee Penn, Stephen Whitelam, Derk Joester, Hengzhong Zhang, Jeffrey D Rimer, Alexandra Navrotsky, Jillian F Banfield, Adam F Wallace, F Marc Michel, Fiona C Meldrum, Helmut Cölfen, and Patricia M Dove. Crystallization by particle attachment in synthetic, biogenic, and geologic environments. *Science*, 349(6247):aaa6760, 2015.

[21] Yin Liu, Jie Wang, Sujung Kim, Haoye Sun, Fuyi Yang, Zixuan Fang, Nobumichi Tamura, Ruopeng Zhang, Xiaohui Song, Jianguo Wen, Bo Z Xu, Michael Wang, Shuren Lin, Qin Yu, Kyle B Tom, Yang Deng, John Turner, Emory Chan, Dafei Jin, robert O Ritchie, Andrew M Minor, Daryl C Chrzan, Mary C Scott, and Jie Yao. Helical van der Waals crystals with discretized Eshelby twist. *Nature*, 570(7761):358–362, 2019.

[22] John S. Bangsund, Thomas R. Fielitz, Trevor J. Steiner, Kaicheng Shi, Jack R. Van Sambeek, Catherine P. Clark, and Russell J. Holmes. Formation of aligned periodic patterns during the crystallization of organic semiconductor thin films. *Nature Materials*, 18(7):725–731, jun 2019.

[23] Ashish A. Kulkarni, Julia Kohanek, Kaitlin I. Tyler, Erik Hanson, Dong Uk Kim, Katsuyo Thornton, and Paul V. Braun. Template-directed solidification of eutectic optical materials. *Advanced Optical Materials*, 6(11):1800071, jun 2018.

[24] Ashish A. Kulkarni, Erik Hanson, Runyu Zhang, Katsuyo Thornton, and Paul V. Braun. Archimedean lattices emerge in template-directed eutectic solidification. *Nature*, 577(7790):355–358, 2020.

[25] Saman Moniri, Hrishikesh Bale, Tobias Volkenandt, Yeqing Wang, Jianrong Gao, Tianxiang Lu, Kai Sun, Robert O. Ritchie, and Ashwin J. Shahani. Multi-

Step Crystallization of Self-Organized Spiral Eutectics. *Small*, 16(8):1906146, feb 2020.

[26] H. Bei, G. M. Pharr, and E. P. George. A review of directionally solidified intermetaliic composites for high-temperature structural applications. *Journal of Materials Science*, 39(12):3975–3984, jun 2004.

[27] María F. Acosta, Sergio G. Rodrigo, Luis Martín-Moreno, Carlos Pecharromán, and Rosa I. Merino. Micropillar Templates for Dielectric Filled Metal Arrays and Flexible Metamaterials. *Advanced Optical Materials*, 5(3):1600670, feb 2017.

[28] Konrad Wysmulek, Jaroslaw Sar, Pawel Osewski, Krzysztof Orlinski, Katarzyna Kolodziejak, Anita Trenczek-Zajac, Marta Radecka, and Dorota A. Pawlak. A SrTiO3-TiO2 eutectic composite as a stable photoanode material for photoelectrochemical hydrogen production. *Applied Catalysis B: Environmental*, 206:538–546, jun 2017.

[29] Saman Moniri and Ashwin J. Shahani. Chemical Modification of Degenerate Eutectics: A review of Recent Advances and Current Issues. *Journal of Materials Research*, 34(1):20–34, 2018.

[30] Saman Moniri, Xianghui Xiao, and Ashwin J. Shahani. The mechanism of eutectic modification by trace impurities. *Scientific Reports*, 9:3381, dec 2019.

[31] J.W. Gibbs. On the equilibrium of heterogeneous substances. *Trans. Connect. Acad. Sci.*, 16:343–524, 1878.

[32] W. F. Berg. Crystal Growth from Solutions. *Proceedings of the Royal Society of London. Series A - Mathematical and Physical Sciences*, 164(916):79–95, jan 1938.

[33] Donald Pettit and Pietro Fontana. Comparison of sodium chloride hopper cubes grown under microgravity and terrestrial conditions. *npj Microgravity*, 5(1):1–7, dec 2019.

[34] Makoto Tachibana. Mechanisms of Crystal Growth from Fluxed Solutions. In *Beginner's Guide to Flux Crystal Growth*, pages 23–41. Springer, Tokyo, 2017.

[35] Frances M. Ross. Opportunities and challenges in liquid cell electron microscopy. *Science*, 350(6267):aaa9886–aaa9886, dec 2015.

[36] Federico Giberti, Gareth A. Tribello, and Michele Parrinello. Transient polymorphism in NaCl. *Journal of Chemical Theory and Computation*, 9(6):2526–2530, jun 2013.

[37] Jisoo Lee, Jiwoong Yang, Soon Gu Kwon, and Taeghwan Hyeon. Nonclassical nucleation and growth of inorganic nanoparticles. *Nature Reviews Materials*, 1(8), 2016.

[38] Gabriele C. Sosso, Ji Chen, Stephen J. Cox, Martin Fitzner, Philipp Pedevilla, Andrea Zen, and Angelos Michaelides. Crystal Nucleation in Liquids: Open Questions and Future Challenges in Molecular Dynamics Simulations. *Chemical Reviews*, 116(12):7078–7116, jun 2016.

[39] Roy Elliot. *Eutectic Solidification Processing: Crystalline and Glassy Alloys*. Butterworths, 1983.

[40] G.A. Chadwick. Eutectic alloy solidification. *Progress in Materials Science*, 12:99–182, jan 1963.

[41] P. B. Crosley and L.F. Mondolfo. The Modification of Aluminum-Silicon Alloys. *Mod. Castings*, 46:89–100, 1966.

[42] A. K. Dahle, K. Nogita, S. D. McDonald, C. Dinnis, and L. Lu. Eutectic modification and microstructure development in Al-Si Alloys. *Materials Science and Engineering A*, 413-414:243–248, dec 2005.

[43] S Terzi, J A Taylor, Y H Cho, L Salvo, M Suéry, E Boller, and A K Dahle. In situ study of nucleation and growth of the irregular α-Al/β-Al5FeSi eutectic by 3-D synchrotron X-ray microtomography. *Acta Materialia*, 58(16):5370–5380, 2010.

[44] Jihan Zhou, Yongsoo Yang, Yao Yang, Dennis S. Kim, Andrew Yuan, Xuezeng Tian, Colin Ophus, Fan Sun, Andreas K. Schmid, Michael Nathanson, Hendrik Heinz, Qi An, Hao Zeng, Peter Ercius, and Jianwei Miao. Observing crystal nucleation in four dimensions using atomic electron tomography, jun 2019.

[45] Wenchuan Ma, James F. Lutsko, Jeffrey D. Rimer, and Peter G. Vekilov. Antagonistic cooperativity between crystal growth modifiers. *Nature*, 577(7791):497–501, jan 2020.

[46] James F. Lutsko. How crystals form: A theory of nucleation pathways. *Science Advances*, 5(4):eaav7399, apr 2019.

[47] Richard P Sear. Nucleation: Theory and applications to protein solutions and colloidal suspensions, 2007.

[48] Fang Lu, Kevin G. Yager, Yugang Zhang, Huolin Xin, and Oleg Gang. Superlattices assembled through shape-induced directional binding. *Nature Communications*, 6(1):1–10, apr 2015.

[49] Evelyn Auyeung, Ting I.N.G. Li, Andrew J. Senesi, Abrin L. Schmucker, Bridget C. Pals, Monica Olvera De La Cruz, and Chad A. Mirkin. DNA-mediated nanoparticle crystallization into Wulff polyhedra. *Nature*, 505(7481):73–77, nov 2014.

[50] Brian J. Smith and William R. Dichtel. Mechanistic studies of two-dimensional covalent organic frameworks rapidly polymerized from initially homogenous conditions. *Journal of the American Chemical Society*, 136(24):8783–8789, jun 2014.

[51] Fudong Wang, Vernal N. Richards, Shawn P. Shields, and William E. Buhro. Kinetics and mechanisms of aggregative nanocrystal growth, jan 2014.

[52] Jixiang Fang, Bingjun Ding, and Herbert Gleiter. Mesocrystals: Syntheses in metals and applications, nov 2011.

[53] W Kurz and D J Fisher. Dendrite growth in eutectic alloys: the coupled zone. *International Metals Reviews*, 24(1):177–204, 1979.

[54] Silvère Akamatsu, Mikaël Perrut, Sabine Bottin-Rousseau, and Gabriel Faivre. Spiral two-phase dendrites. *Physical Review Letters*, 104(5):056101, 2010.

[55] Ka Jackson and JD Hunt. Lamellar and rod eutectic growth. *Transactions of the Metallurgical Society of AIME*, 236:1129, 1966.

[56] A. Hellawell. The growth and structure of eutectics with silicon and germanium. *Progress in Materials Science*, 15(1):3–78, jan 1970.

[57] Ashwin J. Shahani, Xianghui Xiao, and Peter W. Voorhees. The mechanism of eutectic growth in highly anisotropic materials. *Nature Communications*, 7:12953, sep 2016.

[58] R. E. Napolitano, H. Meco, and C. Jung. Faceted solidification morphologies in low-growth-rate Al-Si eutectics. *JOM*, 56(4):16–21, apr 2004.

[59] W. Kurz and D. F. Fisher. *Fundamentals of solidification*. Trans Tech Publications, 1984.

[60] J. A. Dantzig and Michel Rappaz. *Solidification*. EPFL Press, Lausanne, 2nd edition, 2017.

[61] M Timpel, N Wanderka, R Schlesiger, T Yamamoto, N Lazarev, D Isheim, G Schmitz, S Matsumura, and J Banhart. The role of strontium in modifying aluminium-silicon alloys. *Acta Materialia*, 60(9):3920–3928, 2012.

[62] P Magnin and W Kurz. Competitive Growth of Stable and Metastable Fe-C-X Eutectics: Part II. Mechanisms. *Metallurgical and Materials Transactions A*, 19A:1965–1971, 1988.

[63] R L Fullman and D.L. Wood. Origin of spiral eutectic structures. *Acta Metallurgica*, 2(2):188, 1954.

[64] R.L. Fullman and D.L. Wood. Origin of spiral eutectic structures. *Journal of Metals*, 4:1041–1041, 1952.

[65] A. Dippenaar, H.D.W. Bridgman, and G.A. Chadwick. Nucleation and growth of the spiral eutectic Zn-MgZn₂. *Journal of the Institute of Metals*, 99:137–142, 1971.

[66] D. J. Dingley. Diffraction from sub-micron areas using electron backscattering in a scanning electron microscope. *Scanning Electron Microscopy*, 2:569–575, 1984.

[67] V. Randle. Application of EBSD to the analysis of interface planes: Evolution over the last two decades. In *Journal of Microscopy*, volume 230, pages 406–413. John Wiley & Sons, Ltd, jun 2008.

[68] Valerie Randle. 'Five-parameter' analysis of grain boundary networks by electron backscatter diffraction. *Journal of Microscopy*, 222(2):69–75, 2006.

[69] D. J. Prior. Problems in determining the misorientation axes, for small angular misorientations, using electron backscatter diffraction in the SEM. *Journal of Microscopy*, 195(3):217–225, sep 1999.

[70] Brandon Runnels, Irene J Beyerlein, Sergio Conti, and Michael Ortiz. A relaxation method for the energy and morphology of grain boundaries and interfaces. *Journal of the Mechanics and Physics of Solids*, 94:388–408, 2016.

[71] H. Föll. Grain Boundaries.

[72] Oxford Instruments. EBSD Oxford Instruments - Home, 2017.

[73] Vanessa Schoeppler, Robert Lemanis, Elke Reich, Tamás Pusztai, László Gránásy, and Igor Zlotnikov. Crystal growth kinetics as an architectural constraint on the evolution of molluscan shells. *Proceedings of the National Academy of Sciences of the United States of America*, 116(41):20388–20397, oct 2019.

[74] W. Losert, B. Q. Shi, and H. Z. Cummins. Evolution of dendritic patterns during alloy solidification: Onset of the initial instability. *Proceedings of the National Academy of Sciences of the United States of America*, 95(2):431–438, jan 1998.

[75] Philip J. Withers. X-ray nanotomography. *Materials Today*, 10(12):26–34, dec 2007.

[76] Mingyuan Ge, David Scott Coburn, Evgeny Nazaretski, Weihe Xu, Kazimierz Gofron, Huijuan Xu, Zhijian Yin, and Wah Keat Lee. One-minute nano-tomography using hard X-ray full-field transmission microscope. *Applied Physics Letters*, 113(8):083109, aug 2018.

[77] J. P. Hirth, J. Lothe, and T. Mura. Theory of Dislocations (2nd ed.). *Journal of Applied Mechanics*, 50(2):476–477, jun 1983.

[78] W. K. Burton, N. Cabrera, and F. C. Frank. Role of dislocations in crystal growth. *Nature*, 163(4141):398–399, mar 1949.

[79] Evgeniya Dontsova. *Understanding of edge and screw dislocations in nanostructures by modeling and simulations*. PhD thesis, University of Minnesota, 2013.

[80] Phillip Jeffrey. X-ray Data Collection Course, 2006.

[81] Wacek Swiech, C Q Chen, Jim Mabon, and Honghui Zhou. Advanced Materials Characterization Workshop: Transmission Electron Microscopy. Technical report, Urbana, IL, 2017.

[82] Stephen A Morin, Matthew J Bierman, Jonathan Tong, and Song Jin. Mechanism and kinetics of spontaneous nanotube growth driven by screw dislocations. *Science*, 328(5977):476–480, apr 2010.

[83] H. Foll. Basics of TEM and the Contrast of Dislocations.

[84] H. Yang, J. G. Lozano, T. J. Pennycook, L. Jones, P. B. Hirsch, and P. D. Nellist. Imaging screw dislocations at atomic resolution by aberration-corrected electron optical sectioning. *Nature Communications*, 6(1):7266, dec 2015.

[85] Jianwei Miao, Peter Ercius, and Simon J L Billinge. Atomic electron tomography: 3D structures without crystals. *Science*, 353(6306):aaf2157, sep 2016.

[86] Hasse Fredriksson and Ulla Åkerlind. *Solidification and Crystallization Processing in Metals and Alloys - Fredriksson - Wiley Online Library*. Wiley, 2012.

[87] D.J. Fisher and W. Kurz. A theory of branching limited growth of irregular eutectics. *Acta Metallurgica*, 28(6):777–794, jun 1980.

[88] H. A.H. Steent and A. Hellawell. Structure and properties of aluminium-silicon eutectic alloys. *Acta Metallurgica*, 20(3):363–370, 1972.

[89] F. Yilmaz and R. Elliott. The microstructure and mechanical properties of unidirectionally solidified Al-Si alloys. *Journal of Materials Science*, 24(6):2065–2070, jun 1989.

[90] T. Hosch and R. E. Napolitano. The effect of the flake to fiber transition in silicon morphology on the tensile properties of Al-Si eutectic alloys. *Materials Science and Engineering A*, 528(1):226–232, nov 2010.

[91] T. Hosch, L. G. England, and R. E. Napolitano. Analysis of the high growth-rate transition in Al-Si eutectic solidification. *Journal of Materials Science*, 44(18):4892–4899, sep 2009.

[92] M. N. Croker, R. S. Fidler, and R. W. Smith. The Characterization of Eutectic Structures. *Proceedings of the Royal Society A: Mathematical, Physical and Engineering Sciences*, 335(1600):15–37, 1973.

[93] Aladar Pacz. Alloy, 1921.

[94] Ruyao Wang and Weihua Lu. Direct Electrolytic Al-Si Alloys (DEASA) – An Undercooled Alloy Self-Modified Structure and Mechanical Properties. In Janis Kleperis, editor, *Electrolysis*. IntechOpen, 2012.

[95] S. Shivkumar, L. Wang, and D. Apelian. Molten metal processing of advanced cast aluminum alloys. *JOM*, 43(1):26–32, jan 1991.

[96] Shu Zu Lu and A. Hellawell. The mechanism of silicon modification in aluminum-silicon alloys: Impurity induced twinning. *Metallurgical Transactions A*, 18(10):1721–1733, oct 1987.

[97] H Fredriksson, M Hillert, and N Lange. The Modification of Aluminum-Silicon Alloys by Sodium. *J. Inst. Met.*, 101:285–299, 1973.

[98] J. Campbell and M. Tiryakioğlu. Review of effect of P and Sr on modification and porosity development in Al-Si alloys, mar 2010.

[99] G. K. Sigworth. The modification of Al-Si alloys: Important practical and theoretical aspects. *International Journal of Metalcasting*, 2(2):19–40, apr 2008.

[100] C E Cross and D L Olson. Modification of Eutectic Weld Metal Microstructure. *Welding Research Supplement*, 61:381–387, 1982.

[101] M. M. Makhlouf and H. V. Guthy. The aluminum-silicon eutectic reaction: Mechanisms and crystallography. *Journal of Light Metals*, 1(4):199–218, nov 2001.

[102] Song Mao Liang and Rainer Schmid-Fetzer. Phosphorus in Al-Si cast alloys: Thermodynamic prediction of the AlP and eutectic (Si) solidification sequence validated by microstructure and nucleation undercooling data. *Acta Materialia*, 72:41–56, jun 2014.

[103] A. Darlapudi, S. D. McDonald, and D. H. StJohn. The influence of Cu, Mg and Ni on the solidification and microstructure of Al-Si alloys. *IOP Conference Series: Materials Science and Engineering*, 117, 2016.

[104] S. Farahany, A. Ourdjini, M. H. Idrsi, and S. G. Shabestari. Evaluation of the effect of Bi, Sb, Sr and cooling condition on eutectic phases in an Al-Si-Cu alloy (ADC12) by in situ thermal analysis. *Thermochimica Acta*, 559:59–68, may 2013.

[105] M.A. Savas and S. Altintas. Control of mechanical and wear properties of a commercial Al-Si eutectic alloy. *Journal of Materials Science*, 27(5):1255–1260, 1992.

[106] Thomas Hartmut Ludwig, Paul Louis Schaffer, and Lars Arnberg. Influence of some trace elements on solidification path and microstructure of Al-Si foundry alloys. *Metallurgical and Materials Transactions A*, 44(8):3783–3796, 2013.

[107] Sathyapal Hegde and K. Narayan Prabhu. Modification of eutectic silicon in Al-Si alloys. *Journal of Materials Science*, 43(9):3009–3027, 2008.

[108] A. Knuutinen, K. Nogita, S. D. McDonald, and A. K. Dahle. Modification of Al-Si alloys with Ba, Ca, Y and Yb. *Journal of Light Metals*, 1(4):229–240, nov 2001.

[109] Kazuhiro Nogita, John Drennan, and Arne Kristian Dahle. Evaluation of Silicon Twinning in Hypo-Eutectic Al-Si Alloys. *Materials Transactions*, 44(4):625–628, 2003.

[110] Kazuhiro Nogita, Stuart D. McDonald, and Arne K. Dahle. Eutectic Modification of Al-Si Alloys with Rare Earth Metals. *Materials Transactions*, 45(2):323–326, 2004.

[111] Z. M. Shi, Q. Wang, G. Zhao, and R. Y. Zhang. Effects of erbium modification on the microstructure and mechanical properties of A356 aluminum alloys. *Materials Science and Engineering A*, 626:102–107, feb 2015.

[112] T. H. Ludwig, E. Schonhovd Dæhlen, P. L. Schaffer, and L. Arnberg. The effect of Ca and P interaction on the Al-Si eutectic in a hypoeutectic Al-Si alloy. *Journal of Alloys and Compounds*, 586:180–190, feb 2014.

[113] Ussadawut Patakham, Julathep Kajornchaiyakul, and Chaowalit Limmaneevichitr. Modification mechanism of eutectic silicon in Al-6Si-0.3Mg alloy with scandium. *Journal of Alloys and Compounds*, 575:273–284, oct 2013.

[114] J. H. Li, N. Wanderka, Z. Balogh, P. Stender, H. Kropf, M. Albu, Y. Tsunekawa, F. Hofer, G. Schmitz, and P. Schumacher. Effects of trace elements (Y and Ca) on the eutectic Ge in Al-Ge based alloys. *Acta Materialia*, 111:85–95, jun 2016.

[115] Jinsong Rao, Jin Zhang, Ruxue Liu, and Jiang Zheng. Modification of eutectic Si and the microstructure in an Al-7Si alloy with barium addition. *Materials Science & Engineering A*, 728:72–79, jun 2018.

[116] J. H. Li and P. Schumacher. Modification of Eutectic Si and Refinement of Eutectic Grain in Al-Si-Mg alloys by CrB2 and Sr Addition. In *Light Metals 2016*, pages 711–714. John Wiley & Sons, Inc., Hoboken, NJ, USA, feb 2016.

[117] Paulo Eliseo Rossi. *Quantitative Classification and Assessment of Modification in Hypoeutectic Aluminum-Silicon Alloys*. PhD thesis, 2015.

[118] J H Li, M Z Zarif, G Dehm, and P Schumacher. Influence of impurity elements on the nucleation and growth of Si in high purity melt-spun Al-Si-based alloys. *Philosophical Magazine*, 92(31):3789–3805, 2012.

[119] M. D. Hanna, Shu-Zu Lu, and A. Hellawell. Modification in the Aluminum Silicon System. *Metallurgical Transactions A*, 15:459–469, mar 1984.

[120] C.B. Kim and R.W. Heine. Fundamentals of Modification in the Aluminum-Silicon System. *Journal of the Institute of Metals*, 92:367–376, 1963.

[121] Janin Eiken, Markus Apel, Song Mao Liang, and Rainer Schmid-Fetzer. Impact of P and Sr on solidification sequence and morphology of hypoeutectic Al-Si alloys: Combined thermodynamic computation and phase-field simulation. *Acta Materialia*, 98:152–163, oct 2015.

[122] Stuart D. McDonald, Kazuhiro Nogita, and Arne K. Dahle. Eutectic nucleation in Al-Si alloys. *Acta Materialia*, 52(14):4273–4280, aug 2004.

[123] M. E. Straumanis and E. Z. Aka. Lattice parameters, coefficients of thermal expansion, and atomic weights of purest silicon and germanium. *Journal of Applied Physics*, 23(3):330–334, mar 1952.

[124] Chin Yu Yeh, Z. W. Lu, S. Froyen, and Alex Zunger. Zinc-blendewurtzite polytypism in semiconductors. *Physical Review B*, 46(16):10086–10097, oct 1992.

[125] Jiehua Li, Fredrik S Hage, Xiangfa Liu, Quentin Ramasse, and Peter Schumacher. Revealing heterogeneous nucleation of primary Si and eutectic Si by AlP in hypereutectic Al-Si alloys. *Scientific reports*, 6:25244, 2016.

[126] A. Pennors, A. M. Samuel, F. H. Samuel, and H. W. Doty. Precipitation of β-Al5FeSi iron intermetallic in Al-6% Si-3.5% Cu (319) type alloys: role of Sr and P. *Transactions of the American Foundrymen's Society*, 106:251–264, 1998.

[127] Hengcheng Liao, Min Zhang, Qichang Wu, Huipin Wang, and Guoxiong Sun. Refinement of eutectic grains by combined addition of strontium and boron in near-eutectic Al-Si alloys. *Scripta Materialia*, 57(12):1121–1124, dec 2007.

[128] S. C. Flood and J. D. Hunt. Modification of Al-Si eutectic alloys with Na. *Metal Science*, 15(7):287–294, jul 1981.

[129] Ichiro Sunagawa. Growth and Morphology of Crystals . *Forma*, 14:147–166, 1999.

[130] R. S. Wagner. On the growth of germanium dendrites, jan 1960.

[131] D. R. Hamilton and R. G. Seidensticker. Propagation mechanism of germanium dendrites. *Journal of Applied Physics*, 31(7):1165–1168, jul 1960.

[132] M G Day and A Hellawell. The Microstructure and Crystallography of Aluminium-Silicon Eutectic Alloys. *Proceedings of the Royal Society of London. Series A, Mathematical and Physical Sciences*, 305(1483):473–491, 1968.

[133] Ashwin J Shahani, E Begum Gulsoy, Stefan O Poulsen, Xianghui Xiao, and Peter W Voorhees. Twin-mediated crystal growth: an enigma resolved. *Scientific Reports*, 6:28651, 2016.

[134] Ashwin J. Shahani and Peter W. Voorhees. Twin-mediated crystal growth. *Journal of Materials Research*, 31(19):2936–2947, 2016.

[135] M. Shamsuzzoha and L. M. Hogan. The crystal morphology of fibrous silicon in strontium-modified Al-Si eutectic. *Philosophical Magazine A: Physics of Condensed Matter, Structure, Defects and Mechanical Properties*, 54(4):459–477, 1986.

[136] Jiehua Li, Fredrik Hage, Manfred Wiessner, Lorenz Romaner, Daniel Scheiber, Bernhard Sartory, Quentin Ramasse, and Peter Schumacher. The roles of Eu during the growth of eutectic Si in Al-Si alloys. *Scientific reports*, 5(September):13802, sep 2015.

[137] J. H. Li, M. Albu, F. Hofer, and P. Schumacher. Solute adsorption and entrapment during eutectic Si growth in A-Si-based alloys. *Acta Materialia*, 83:187–202, 2015.

[138] Xiaorui Liu, Yudong Zhang, Benoît Beausir, Fang Liu, Claude Esling, Fuxiao Yu, Xiang Zhao, and Liang Zuo. Twin-controlled growth of eutectic Si in unmodified and Sr-modified Al-12.7%Si alloys investigated by SEM/EBSD. *Acta Materialia*, 97:338–347, jul 2015.

[139] Jeyakumar Manickaraj, Anton Gorny, Zhonghou Cai, and Sumanth Shankar. X-ray nano-diffraction study of Sr intermetallic phase during solidification of Al-Si hypoeutectic alloy. *Applied Physics Letters*, 104(7):073102, feb 2014.

[140] J. Barrirero, C. Pauly, M. Engstler, J. Ghanbaja, N. Ghafoor, J. Li, P. Schumacher, M. Odén, and F. Mücklich. Eutectic modification by ternary compound cluster formation in Al-Si alloys. *Scientific Reports*, 9(1):5506, dec 2019.

[141] M. Albu, A. Pal, C. Gspan, R. C. Picu, F. Hofer, and G. Kothleitner. Self-organized Sr leads to solid state twinning in nano-scaled eutectic Si phase. *Scientific Reports*, 6:31635, aug 2016.

[142] O. L. Krivanek, G. J. Corbin, N. Dellby, B. F. Elston, R. J. Keyse, M. F. Murfitt, C. S. Own, Z. S. Szilagyi, and J. W. Woodruff. An electron microscope for the aberration-corrected era. *Ultramicroscopy*, 108(3):179–195, feb 2008.

[143] M. Timpel, N. Wanderka, G. S. Vinod Kumar, and J. Banhart. Microstructural investigation of Sr-modified Al-15 wt%Si alloys in the range from micrometer to atomic scale. *Ultramicroscopy*, 111(6):695–700, may 2011.

[144] K. Nogita, H. Yasuda, K. Yoshida, K. Uesugi, A. Takeuchi, Y. Suzuki, and A. K. Dahle. Determination of strontium segregation in modified hypoeutectic Al-Si alloy by micro X-ray fluorescence analysis. *Scripta Materialia*, 55(9):787–790, nov 2006.

[145] J.E. Gruzleski. Aluminum-silicon eutectic modification—sodium or strontium? In *Production and Electrolysis of Light Metals*, pages 131–141. Elsevier, 1989.

[146] J. H. Li, J. Barrirero, M. Engstler, H. Aboulfadl, F. Mücklich, and P. Schumacher. Nucleation and Growth of Eutectic Si in Al-Si Alloys with Na Addition. *Metallurgical and Materials Transactions A: Physical Metallurgy and Materials Science*, 46(3):1300–1311, mar 2014.

[147] Santhana K. Eswara Moorthy and James M. Howe. Kinetic analyses of the growth and dissolution phenomena of primary Si and α-Al in partially molten Al-Si (-Cu-Mg) alloy particles using in situ transmission electron microscopy. *Metallurgical and Materials Transactions A: Physical Metallurgy and Materials Science*, 42(6):1667–1674, jun 2011.

[148] Matthew M. Schneider and James M. Howe. Observation of interface dynamics and Cu island formation at a crystalline Si/liquid Al-alloy interface. *Acta Materialia*, 133:224–229, jul 2017.

[149] Ryusuke Sagawa, Hiroki Hashiguchi, Thomas Isabell, Robert Ritz, Martin Simson, Martin Huth, Heike Soltau, Gerardo T. Martinez, Peter D. Nellist, and

Yukihito Kondo. Low Dose Imaging by STEM Ptychography Using Pixelated STEM Detector. *Microscopy and Microanalysis*, 24(S1):198–199, aug 2018.

[150] A.M. Jokisaari and K. Thornton. General method for incorporating CALPHAD free energies of mixing into phase field models: Application to the α-zirconium/δ-hydride system. *Calphad*, 51:334–343, dec 2015.

[151] U. Hecht, L. Gránásy, T. Pusztai, B. Böttger, M. Apel, V. Witusiewicz, L. Ratke, J. De Wilde, L. Froyen, D. Camel, B. Drevet, G. Faivre, S. G. Fries, B. Legendre, and S. Rex. Multiphase solidification in multicomponent alloys, nov 2004.

[152] Javier LLorca and Victor M. Orera. Directionally solidified eutectic ceramic oxides. *Progress in Materials Science*, 51(6):711–809, aug 2006.

[153] Philipp Steinmetz, Johannes Hötzer, Michael Kellner, Amber Genau, and Britta Nestler. Study of pattern selection in 3D phase-field simulations during the directional solidification of ternary eutectic Al-Ag-Cu. *Computational Materials Science*, 148:131–140, jun 2018.

[154] A. Zhang, Z. Guo, and S. M. Xiong. Quantitative phase-field lattice-Boltzmann study of lamellar eutectic growth under natural convection. *Physical Review E*, 97(5):053302, may 2018.

[155] J. J. Eggleston, G. B. McFadden, and P. W. Voorhees. A phase-field model for highly anisotropic interfacial energy. *Physica D: Nonlinear Phenomena*, 150(1-2):91–103, mar 2001.

[156] Solmaz Torabi, John Lowengrub, Axel Voigt, and Steven Wise. A new phase-field model for strongly anisotropic systems. *Proceedings of the Royal Society A: Mathematical, Physical and Engineering Sciences*, 465(2105):1337–1359, may 2009.

[157] Enzo Liotti, Carlos Arteta, Andrew Zisserman, Andrew Lui, Victor Lempitsky, and Patrick S. Grant. Crystal nucleation in metallic alloys using x-ray radiography and machine learning. *Science Advances*, 4(4):eaar4004, apr 2018.

[158] R. H. Mathiesen, L. Arnberg, H. Nguyen-Thi, and B. Billia. In situ x-ray video microscopy as a tool in solidification science. *JOM*, 64(1):76–82, jan 2012.

[159] Ken Vidar Falch, Daniele Casari, Marco Di Michiel, Carsten Detlefs, Anatoly Snigireva, Irina Snigireva, Veijo Honkimäki, and Ragnvald H. Mathiesen. In situ hard X-ray transmission microscopy for material science. *Journal of Materials Science*, 52(6):3497–3507, mar 2017.

[160] Liu Qiyang, Li Qingchun, and Liu Qifu. Modification of Al-Si alloys with sodium. *Acta metallurgica et materialia*, 39(11):2497–2502, nov 1991.

[161] P. Srirangam, S. Chattopadhyay, A. Bhattacharya, S. Nag, J. Kaduk, S. Shankar, R. Banerjee, and T. Shibata. Probing the local atomic structure of Sr-modified Al-Si alloys. *Acta Materialia*, 65:185–193, 2014.

[162] Shu-Zu Lu and A. Hellawell. Modification of Al-Si alloys: Microstructure, thermal analysis, and mechanisms. *JOM*, 47(2):38–40, feb 1995.

[163] S. G. Shabestari, M. Keshavarz, and M. M. Hejazi. Effect of strontium on the kinetics of formation and segregation of intermetallic compounds in A380 aluminum alloy. *Journal of Alloys and Compounds*, 477(1-2):892–899, may 2009.

[164] B.M. Thall and B. Chalmers. Modification in aluminium silicon alloys. *Journal of the Institute of Metals*, 77:79–97, 1950.

[165] J. H. Li, S. Suetsugu, Y. Tsunekawa, and P. Schumacher. Refinement of Eutectic Si Phase in Al-5Si Alloys with Yb Additions. *Metallurgical and Materials Transactions A*, 44:669–681, feb 2013.

[166] Kenneth A. Jackson. *Kinetic Processes: Crystal Growth, Diffusion, and Phase Transformations in Materials*. Wiley-VCH, 2004.

[167] H. M. Lu, T. H. Wang, and Q. Jiang. Surface tension and self-diffusion coefficient of liquid Si and Ge. *Journal of Crystal Growth*, 293(2):294–298, aug 2006.

[168] R. T. DeHoff, E. H. Aigeltinger, and K. R. Craig. Experimental determination of the topological properties of three-dimensional microstructures. *Journal of Microscopy*, 95(1):69–91, feb 1972.

[169] R. Mendoza, K. Thornton, I. Savin, and P. W. Voorhees. The evolution of interfacial topology during coarsening. *Acta Materialia*, 54(3):743–750, feb 2006.

[170] Emine Begum Gulsoy, Ashwin J. Shahani, John W. Gibbs, Julie L. Fife, and Peter W. Voorhees. Four-Dimensional Morphological Evolution of an Aluminum Silicon Alloy Using Propagation-Based Phase Contrast X-ray Tomographic Microscopy. *Materials Transactions*, 55(1):161–164, jan 2014.

[171] D.G. Brandon. The Structure of High-Angle Grain Boundaries. *Acta Metallurgica*, 14(11):1479–1484, 1966.

[172] Valerie Randle. The coincidence site lattice and the 'sigma enigma'. *Materials Characterization*, 47(5):411–416, 2001.

[173] Sutatch Ratanaphan, Yohan Yoon, and Gregory S Rohrer. The five parameter grain boundary character distribution of polycrystalline silicon. *Journal of Materials Science*, 49(14):4938–4945, 2014.

[174] Gregory S. Rohrer. *Structure and Bonding in Crystalline Materials*. Cambridge University Press, 2001.

[175] Madeleine N. Kelly, Krzysztof Glowinski, Noel T. Nuhfer, and Gregory S. Rohrer. The five parameter grain boundary character distribution of α-Ti determined from three-dimensional orientation data. *Acta Materialia*, 111:22–30, 2016.

[176] K. Barmak, E. Eggeling, D. Kinderlehrer, R. Sharp, S. Ta'Asan, A. D. Rollett, and K. R. Coffey. Grain growth and the puzzle of its stagnation in thin films: The curious tale of a tail and an ear. *Progress in Materials Science*, 58(7):987–1055, aug 2013.

[177] R. J. Brisley and D. J. Fray. Determination of the sodium activity in aluminum and aluminum silicon alloys using sodium beta alumina. *Metallurgical Transactions B*, 14(3):435–440, sep 1983.

[178] Hui Song and Angus Hellawell. Solidification in the system Al-Ge-Si: The phase diagram, coring patterns, eutectic growth, and modification. *Metallurgical Transactions A*, 21(2):733–740, feb 1990.

[179] J H Li, M Albu, F Hofer, and P Schumacher. Solute adsorption and entrapment during eutectic Si growth in A-Si-based alloys. *Acta Materialia*, 83:187–202, 2015.

[180] A. Politano, G. Chiarello, G. Benedek, E. V. Chulkov, and P. M. Echenique. Vibrational spectroscopy and theory of alkali metal adsorption and co-adsorption on single-crystal surfaces. *Surface Science Reports*, 68(3-4):305–389, nov 2013.

[181] A. Plotkowski, O. Rios, N. Sridharan, Z. Sims, K. Unocic, R. T. Ott, R. R. Dehoff, and S. S. Babu. Evaluation of an Al-Ce alloy for laser additive manufacturing. *Acta Materialia*, 126:507–519, mar 2017.

[182] Doğa Gürsoy, Francesco De Carlo, Xianghui Xiao, and Chris Jacobsen. TomoPy: A framework for the analysis of synchrotron tomographic data. *Journal of Synchrotron Radiation*, 21(5):1188–1193, sep 2014.

[183] Beat Münch, Pavel Trtik, Federica Marone, and Marco Stampanoni. Stripe and ring artifact removal with combined wavelet-Fourier filtering. *EMPA Activities*, 17(2009-2010 EMPA ACTIVITIES):34–35, may 2009.

[184] Betsy A. Dowd, Graham H. Campbell, Robert B. Marr, Vivek V. Nagarkar, Sameer V. Tipnis, Lisa Axe, and D. P. Siddons. Developments in synchrotron x-ray computed microtomography at the National Synchrotron Light Source. volume 3772, pages 224–236. International Society for Optics and Photonics, sep 1999.

[185] John C. Russ. *The Image processing handbook*. CRC/Taylor and Francis, Boca Raton, 2007.

[186] Mario Botsch, Leif Kobbelt, Mark Pauly, Pierre Alliez, and Bruno Levy. *Polygon Mesh Processing*. A K Peters/CRC Press, 2010.

[187] D Hilbert and S. Cohn-Vossen. *Anschauliche Geometrie*. Springer Berlin Heidelberg, Berlin, Heidelberg, 1932.

[188] F. Bachmann, Ralf Hielscher, and Helmut Schaeben. Texture Analysis with MTEX – Free and Open Source Software Toolbox. *Solid State Phenomena*, 160:63–68, feb 2010.

[189] Ivan Vesselinov Markov. *Crystal Growth for Beginners: Fundamentals of Nucleation, Crystal Growth, and Epitaxy*. World Scientific Publishing Co Pte Ltd, 3 edition, 2017.

[190] J. P. Buban, K. Matsunaga, J. Chen, N. Shibata, W. Y. Ching, T. Yamamoto, and Y. Ikuhara. Grain boundary strengthening in alumina by rare earth impurities. *Science*, 311(5758):212–215, jan 2006.

[191] Keith Thompson, John H. Booske, David J. Larson, and Thomas F. Kelly. Three-dimensional atom mapping of dopants in Si nanostructures. *Applied Physics Letters*, 87(5), 2005.

[192] Jonathan E. Allen, Eric R. Hemesath, Daniel E. Perea, Jessica L. Lensch-Falk, Z. Y. Li, Feng Yin, Mhairi H. Gass, Peng Wang, Andrew L. Bleloch, Richard E. Palmer, and Lincoln J. Lauhon. High-resolution detection of Au catalyst atoms in Si nanowires. *Nature Nanotechnology*, 3(3):168–173, 2008.

[193] Tonio Buonassisi, Andrei A. Istratov, Matthew A. Marcus, Barry Lai, Zhonghou Cai, Steven M. Heald, and Eicke R. Weber. Engineering metal-impurity nanodefects for low-cost solar cells. *Nature Materials*, 4(9):676–679, 2005.

[194] Miao Song, Gang Zhou, Ning Lu, Jaewon Lee, Elias Nakouzi, Hao Wang, and Dongsheng Li. Oriented attachment induces fivefold twins by forming and decomposing high-energy grain boundaries. *Science (New York, N.Y.)*, 367(6473):40–45, 2020.

[195] Keiji Shiga, Kensaku Maeda, Haruhiko Morito, and Kozo Fujiwara. Effect of twin boundary formation on the growth rate of the GaSb{111} plane. *Acta Materialia*, 185:453–460, 2020.

[196] Katy N. Olafson, Rui Li, Bryan G. Alamani, and Jeffrey D. Rimer. Engineering Crystal Modifiers: Bridging Classical and Nonclassical Crystallization. *Chemistry of Materials*, 28(23):8453–8465, dec 2016.

[197] S. Elhadj, J. J. De Yoreo, J. R. Hoyer, and P. M. Dove. Role of molecular charge and hydrophilicity in regulating the kinetics of crystal growth. *Proceedings of the National Academy of Sciences of the United States of America*, 103(51):19237–19242, dec 2006.

[198] James J. De Yoreo. Physical mechanisms of crystal growth modification by biomolecules. In *AIP Conference Proceedings*, volume 1270, pages 45–59, 2010.

[199] B. Cai, A. Kao, P. D. Lee, E. Boller, H. Basevi, A. B. Phillion, A. Leonardis, and K. Pericieous. Growth of β intermetallic in an Al-Cu-Si alloy during directional solidification via machine learned 4D quantification. *Scripta Materialia*, 165:29–33, may 2019.

[200] Xinbo Yang, K. Fujiwara, K. Maeda, J. Nozawa, H. Koizumi, and S. Uda. Crystal growth and equilibrium crystal shapes of silicon in the melt. *Progress in Photovoltaics: Research and Applications*, 22(5):574–580, may 2014.

[201] H. Gleiter. Microstructure. In *Physical Metallurgy*, pages 843–942. Elsevier, 1996.

[202] C. A. Sholl and N. H. Fletcher. Decoration criteria for surface steps. *Acta Metallurgica*, 18(10):1083–1086, 1970.

[203] Nancy Senabulya and Ashwin J Shahani. Growth interactions between icosahedral quasicrystals. *Physical Review Materials*, 3(9):93403, 2019.

[204] Andrew D. Gamalski, Peter W. Voorhees, Caterina Ducati, Renu Sharma, and Stephan Hofmann. Twin plane re-entrant mechanism for catalytic nanowire growth. *Nano Letters*, 14(3):1288–1292, mar 2014.

[205] J. G. Zheng, Xiaoqing Pan, M. Schweizer, F. Zhou, U. Weimar, W. Göpel, and M. Rühle. Growth twins in nanocrystalline SnO2 thin films by high-resolution transmission electron microscopy. *Journal of Applied Physics*, 79(10):7688–7694, may 1996.

[206] S. Xue, Z. Fan, Y. Chen, J. Li, H. Wang, and X. Zhang. The formation mechanisms of growth twins in polycrystalline Al with high stacking fault energy. *Acta Materialia*, 101:62–70, dec 2015.

[207] N. Pisutha-Arnond, V. W.L. Chan, K. R. Elder, and K. Thornton. Calculations of isothermal elastic constants in the phase-field crystal model. *Physical Review B*, 87:014103, 2013.

[208] Russ. Segmentation and Thresholding. *The Image Processing Handbook*, pages 398–441, 2016.

[209] Jens Baumgartner, Archan Dey, Paul H.H. Bomans, Cécile Le Coadou, Peter Fratzl, Nico A.J.M. Sommerdijk, and Damien Faivre. Nucleation and growth of magnetite from solution. *Nature Materials*, 12(4):310–314, apr 2013.

[210] Wouter J.E.M Habraken, Jinhui Tao, Laura J Brylka, Heiner Friedrich, Luca Bertinetti, Anna S Schenk, Andreas Verch, Vladimir Dmitrovic, Paul H.H. Bomans, Peter M Frederik, Jozua Laven, Paul Van Der Schoot, Barbara Aichmayer, Gijsbertus De With, James J. DeYoreo, and Nico A.J.M. Sommerdijk. Ion-association complexes unite classical and non-classical theories

for the biomimetic nucleation of calcium phosphate. *Nature Communications*, 4:1507, 2013.

[211] R. Lee Penn and Jillian F. Banfiel. Imperfect Oriented Attachment: Dislocation Generation in Defect-Free Nanocrystals. *Science*, 281(5379):969–971, aug 1998.

[212] N. Duane Loh, Soumyo Sen, Michel Bosman, Shu Fen Tan, Jun Zhong, Christian A. Nijhuis, Petr Král, Paul Matsudaira, and Utkur Mirsaidov. Multistep nucleation of nanocrystals in aqueous solution. *Nature chemistry*, 9:77–82, jan 2017.

[213] Mark C. Weidman, Detlef M. Smilgies, and William A. Tisdale. Kinetics of the self-assembly of nanocrystal superlattices measured by real-time in situ X-ray scattering. *Nature Materials*, 15(7):775–781, jul 2016.

[214] Zhengrong R. Tian, James A. Voigt, Jun Liu, Bonnie Mckenzie, Matthew J. Mcdermott, Mark A. Rodriguez, Hiromi Konishi, and Huifang Xu. Complex and oriented ZnO nanostructures. *Nature Materials*, 2(12):821–826, dec 2003.

[215] Veselina Uzunova, Weichun Pan, Vassiliy Lubchenko, and Peter G. Vekilov. Control of the nucleation of sickle cell hemoglobin polymers by free hematin. *Faraday Discussions*, 159:87–104, mar 2012.

[216] V A Stoica, N Laanait, C Dai, Z Hong, Y Yuan, Z. Zhang, S Lei, M. R. McCarter, A Yadav, A R Damodaran, S Das, G A Stone, J Karapetrova, D A Walko, X Zhang, L W Martin, R Ramesh, L. Q. Chen, H Wen, V Gopalan, and J W Freeland. Optical creation of a supercrystal with three-dimensional nanoscale periodicity. *Nature Materials*, 18(4):377–383, 2019.

[217] Güven Kurtuldu, Karl F Shamlaye, and Jörg F Löffler. Metastable quasicrystal-induced nucleation in a bulk glass-forming liquid. *Proceedings of the National Academy of Sciences*, 115(24):6123–6128, jun 2018.

[218] T. Yang, Y. L. Zhao, Y. Tong, Z. B. Jiao, J. Wei, J. X. Cai, X. D. Han, D. Chen, A. Hu, J. J. Kai, K. Lu, Y. Liu, and C. T. Liu. Multicomponent intermetallic nanoparticles and superb mechanical behaviors of complex alloys. *Science*, 362(6417):933–937, nov 2018.

[219] Iwona Jozwik-Biala, Andrzej Klos, Johann Toudert, Hancza B Surma, Marcin Gajc, Piotr Dluzewski, Kamil Sobczak, Katarzyna Sadecka, Krzysztof Orlinski, and Dorota A Pawlak. When eutectics meet plasmonics: Nanoplasmonic,

volumetric, self-organized, silver-based eutectic. *Advanced Optical Materials*, 3(3):381–389, 2014.

[220] C.M. Soukoulis and M. Wegener. Past achievements and future challenges in the development of three-dimensional photonic metamaterials. *Nature Photonics*, 5:523–530, sep 2011.

[221] Philipp Steinmetz, Saurabh Gadkari, and Amber Genau. Post-solidification effects in directionally solidified ternary eutectic Al-Ag₂Al-Al₂Cu. *Journal of Crystal Growth*, 507:425–436, feb 2019.

[222] J.D. Hunt and P. Chilton. An Investigation of the Zinc-3% Magnesium Eutectic. *Journal of the Institute of Metals*, 93:146–148, 1966.

[223] H.Y. Liu and H. Jones. Solidification microstructure selection and characteristics in the zinc-based Zn-Mg system. *Acta Metallurgica et Materialia*, 40(2):229–239, feb 1992.

[224] D. D. Double, P. Truelove, and A. Hellawell. The development of preferred orientations in eutectic alloys. *Journal of Crystal Growth*, 2(4):191–198, aug 1968.

[225] György Tegze and Gyula I. Tóth. Osmotic convection-driven instability and cellular eutectic growth in binary systems. *Acta Materialia*, 60(4):1689–1694, feb 2012.

[226] Johannes Hötzer, Philipp Steinmetz, Marcus Jainta, Sebastian Schulz, Michael Kellner, Britta Nestler, Amber Genau, Anne Dennstedt, Martin Bauer, Harald Köstler, and Ulrich Rüde. Phase-field simulations of spiral growth during directional ternary eutectic solidification. *Acta Materialia*, 106:249–259, 2016.

[227] Tamás Pusztai, László Rátkai, Attila Szállás, and László Gránásy. Spiraling eutectic dendrites. *Physical Review E*, 87(3):032401, 2013.

[228] L E O Breiman. Random Forests. *Machine Learning*, 45(1):5–32, 2001.

[229] P. Magnin and R. Trivedi. Eutectic growth: A modification of the Jackson and Hunt theory. *Acta Metallurgica Et Materialia*, 39(4):453–467, apr 1991.

[230] Chunju Niu, Miao Liu, Changrong Li, Zhenmin Du, and Cuiping Guo. Thermodynamic description on the miscibility gap of the Mg-based solid solution in the MgZn, MgNd and MgZnNd systems. *Calphad*, 34(4):428–433, dec 2010.

[231] Ali Khosravani, Ahmet Cecen, and Surya R. Kalidindi. Development of high throughput assays for establishing process-structure-property linkages in multi-phase polycrystalline metals: Application to dual-phase steels. *Acta Materialia*, 123:55–69, jan 2017.

[232] Abhik Choudhury, Yuksel C. Yabansu, Surya R. Kalidindi, and Anne Dennstedt. Quantification and classification of microstructures in ternary eutectic alloys using 2-point spatial correlations and principal component analyses. *Acta Materialia*, 110:131–141, may 2016.

[233] J. W. Edington. Interpretation of Transmission Electron Micrographs. In *Interpretation of Transmission Electron Micrographs*, pages 1–112. Macmillan Education UK, London, 1975.

[234] Anubhav Jain, Shyue Ping Ong, Geoffroy Hautier, Wei Chen, William Davidson Richards, Stephen Dacek, Shreyas Cholia, Dan Gunter, David Skinner, Gerbrand Ceder, and Kristin A. Persson. Commentary: The materials project: A materials genome approach to accelerating materials innovation. *APL Materials*, 1(1):011002, jul 2013.

[235] John Russo and Hajime Tanaka. The microscopic pathway to crystallization in supercooled liquids. *Scientific Reports*, 2(1):505, dec 2012.

[236] Frans Spaepen. Five-fold symmetry in liquids. *Nature*, 408(6814):781–782, dec 2000.

[237] D Holland-Moritz, D M Herlach, and K Urban. Observation of the undercoolability of quasicrystal-forming alloys by electromagnetic levitation. *Physical Review Letters*, 71(8):1196–1199, 1993.

[238] H. Reichert, O. Klein, H. Dosch, M. Denk, V. Honkimäki, T. Lippmann, and G. Reiter. Observation of five-fold local symmetry in liquid lead. *Nature*, 408(6814):839–841, dec 2000.

[239] Baeckkyoung Sung, Alexis De La Cotte, and Eric Grelet. Chirality-controlled crystallization via screw dislocations. *Nature Communications*, 9(1):1405, dec 2018.

[240] J. D. Eshelby. Screw dislocations in thin rods. *Journal of Applied Physics*, 24(2):176–179, feb 1953.

[241] D Hull and D J Bacon. 1 - Defects in Crystals. In *Introduction to Dislocations (Fourth Edition)*, pages 1–21. 2001.

[242] Jan Fransaer, Andrew V. Wagner, and Frans Spaepen. Solidification of Ga-Mg-Zn in a gas-filled drop tube: Experiments and modeling. *Journal of Applied Physics*, 87(4):1801–1818, feb 2000.

[243] Ping-li Mao, Bo Yu, Zheng Liu, Feng Wang, and Yang Ju. Mechanical properties and electronic structures of MgCu₂, Mg₂Ca and MgZn₂ Laves phases by first principles calculations. *Transactions of Nonferrous Metals Society of China*, 24(9):2920–2929, sep 2014.

[244] D.E. Temkin. *Crystallization Processes*. Consultants Bureau, New York, 1966.

[245] Supriyo Ghosh, Abhik Choudhury, Mathis Plapp, Sabine Bottin-Rousseau, Gabriel Faivre, and Silvère Akamatsu. Interphase anisotropy effects on lamellar eutectics: A numerical study. *Physical Review E*, 91(2):22407, 2015.

[246] Gregory Andrew S. Rohrer. The distribution of grain boundary planes in polycrystals. *JOM*, 59(9):38–42, sep 2007.

[247] W.A. Tiller. *Liquid metals and solidification (ASM Cleveland)*. 1958.

[248] H. Fredriksson. On the mechanism of eutectic solidification. *Materials Letters*, 5(11-12):457–459, oct 1987.

[249] George Kaptay. A method to estimate interfacial energy between eutectic solid phases from the results of eutectic solidification experiments. *Materials Science Forum*, 790-791:133–139, may 2014.

[250] Roy Elliott. Growth in anomalous eutectic solidification. In *Eutectic Solidification Processing*, pages 120–156. 2013.

[251] Zina Zhu, David S Goldfarb, Michael D Ward, Jeffrey D Rimer, Jeffrey A Wesson, Zhihua An, and Michael H Lee. Crystal growth inhibitors for the prevention of L-cystine kidney stones through molecular design. *Science*, 330(6002):337–341, oct 2010.

[252] Matthew J Bierman, Y K Albert Lau, Alexander V Kvit, Andrew L Schmitt, and Song Jin. Dislocation-driven nanowire growth and Eshelby twist. *Science*, 320:1060–1063, 2008.

[253] Feng Ding, Avetik R Harutyunyan, and Boris I Yakobson. Dislocation theory of chirality-controlled nanotube growth. *Proceedings of the National Academy of Sciences*, 106(8):2506–2509, feb 2009.

[254] Ryan C Snyder and Michael F Doherty. Predicting crystal growth by spiral motion. *Proceedings of the Royal Society A: Mathematical, Physical and Engineering Sciences*, 465(2104):1145–1171, 2009.

[255] Wolfgang Hornfeck, Raphael Kobold, Matthias Kolbe, Matthias Conrad, and Dieter Herlach. Quasicrystal nucleation and Z module twin growth in an intermetallic glass-forming system. *Nature Communications*, 9(1):4054, dec 2018.

[256] Güven Kurtuldu, Alberto Sicco, and Michel Rappaz. Icosahedral quasicrystal-enhanced nucleation of the fcc phase in liquid gold alloys. *Acta Materialia*, 70:240–248, may 2014.

[257] J. H. Lee, Shan Liu, and R. Trivedi. The effect of fluid flow on eutectic growth. *Metallurgical and Materials Transactions A: Physical Metallurgy and Materials Science*, 36(11):3111–3125, nov 2005.

[258] Christoph Sommer, Christoph Straehle, Ullrich Kothe, and Fred A. Hamprecht. Ilastik: Interactive learning and segmentation toolkit. In *IEEE International Symposium on Biomedical Imaging*, pages 230–233, 2011.

[259] James Ahrens, Berk Geveci, and Charles Law. ParaView: An end-user tool for large-data visualization. In *Visualization Handbook*, pages 717–731. Elsevier, 2005.

[260] Andy Hammersley. The FIT2D Home Page, 2004.

[261] Saman Moniri, Hrishikesh Bale, Tobias Volkenandt, Yeqing Wang, Jianrong Gao, Tianxiang Lu, Kai Sun, Robert O. Ritchie, and Ashwin J. Shahani. Multi-Step Crystallization of Self-Organized Spiral Eutectics. *Small*, page 1906146, jan 2020.

[262] M. Yamaguchi, H. Inui, and K. Ito. High-temperature structural intermetallics. *Acta Materialia*, 48(1):307–322, jan 2000.

[263] R. Tewari, N. K. Sarkar, D. Harish, B. Vishwanadh, G. K. Dey, and S. Banerjee. Intermetallics and Alloys for High Temperature Applications. In *Materials Under Extreme Conditions: Recent Trends and Future Prospects*, pages 293–335. Elsevier Inc., feb 2017.

[264] H. Bei, E. P. George, and G. M. Pharr. Effects of composition on lamellar microstructures of near-eutectic Cr-Cr3Si alloys. *Intermetallics*, 11(4):283–289, apr 2003.

[265] R. M. Aikin. The mechanical properties of in-situ composites. *JOM*, 49(8):35–39, aug 1997.

[266] S.G. Fishman. In-situ Composites: Science and Technology. pages 1–19. Warrendale, PA, 1994.

[267] S. Guruswamy, S. M. Park, J. P. Hirth, and R. A. Rapp. Internal oxidation of Ag-in alloys: Stress relief and the influence of imposed strain. *Oxidation of Metals*, 26(1-2):77–100, aug 1986.

[268] C. H. Henager, J. L. Brimhall, and J. P. Hirth. Synthesis of a MoSi2-SiC composite in situ using a solid state displacement reaction. *Materials Science and Engineering A*, 155(1-2):109–114, jun 1992.

[269] B. S. Murty and S. Ranganathan. Novel materials synthesis by mechanical alloying/milling. *International Materials Reviews*, 43(3):101–141, 1998.

[270] C. Suryanarayana. Nanocrystalline materials. *International Materials Reviews*, 40(2):41–63, 1995.

[271] C. C. Koch. Intermetallic matrix composites prepared by mechanical alloying - A review. *Materials Science and Engineering A*, 244(1):39–48, mar 1998.

[272] Nam P. Suh. Method for Forming Metal, Ceramic or Polymer Compositions, feb 1981.

[273] A. Mortensen and S. Suresh. Functionally graded metals and metal-ceramic composites: Part 1 processing. *International Materials Reviews*, 40(6):239–265, 1995.

[274] Malcolm McLean. Directionally solidified materials for high temperature service. London : Metals Society, 1983.

[275] Ladan Zoheidi. *Flow Characterization of Milk Protein Foam Transport in Inner Geometries*. PhD thesis, Friedrich-Alexander-Universitat Erlangen-Nurnberg, 2018.

[276] M. Becker, S. Klein, and F. Kargl. In-situ solute measurements with a laboratory polychromatic microfocus X-ray source during equiaxed solidification of an Al-Ge alloy. *Scripta Materialia*, 124:34–37, nov 2016.

[277] W. U. Mirihanage, K. V. Falch, I. Snigireva, A. Snigirev, Y. J. Li, L. Arnberg, and R. H. Mathiesen. Retrieval of three-dimensional spatial information from fast in situ two-dimensional synchrotron radiography of solidification microstructure evolution. *Acta Materialia*, 81:241–247, dec 2014.

[278] Larry Kenneth Aagesen. Phase-Field Simulation of Solidification and Coarsening in Dendritic Microstructures. 2010.

[279] F. J.J. Van Loo, M. R. Rijnders, K. J. Rönkä, J. H. Gülpen, and A. A. Kodentsov. Solid state diffusion and reactive phase formation. *Solid State Ionics*, 95(1-2):95–106, feb 1997.

[280] Sarah Brennan, Katrina Bermudez, Nagraj Kulkarni, and Yongho Sohn. Diffusion couple investigation of the Mg-Zn system. In *Magnesium Technology*, pages 323–327. Springer, Cham, 2012.

[281] Sida Ma, Adam J. Brown, Rui Yan, Ruslan L. Davidchack, Paul B. Howes, Chris Nicklin, Qijie Zhai, Tao Jing, and Hongbiao Dong. Atomistics of prenucleation layering of liquid metals at the interface with poor nucleants. *Communications Chemistry*, 2(1):1–12, dec 2019.

[282] Silvère Akamatsu and Mathis Plapp. Eutectic and peritectic solidification patterns, feb 2016.

[283] Amy J. Clarke, Damien Tourret, Seth D. Imhoff, Paul J. Gibbs, Kamel Fezzaa, Jason C. Cooley, Wah Keat Lee, Alex Deriy, Brian M. Patterson, Pallas A. Papin, Kester D. Clarke, Robert D. Field, and James L. Smith. X-ray imaging and controlled solidification of Al-Cu alloys toward microstructures by design. *Advanced Engineering Materials*, 17(4):454–459, apr 2015.

[284] Ragnvald H. Mathiesen, Lars Arnberg, Kjell Ramsøskar, Timm Weitkamp, Christoph Rau, and Anatoly Snigirev. Time-resolved X-ray imaging of aluminum alloy solidification processes. *Metallurgical and Materials Transactions B: Process Metallurgy and Materials Processing Science*, 33(4):613–623, 2002.

[285] R. H. Mathiesen, L. Arnberg, F. Mo, T. Weitkamp, and A. Snigirev. Time resolved X-ray imaging of dendritic growth in binary alloys. *Physical Review Letters*, 83(24):5062–5065, jan 1999.

[286] H Nguyen Thi, H Jamgotchian, J Gastaldi, J H rtwig, T Schenk, H Klein, B Billia, J Baruchel, and Y Dabo. Preliminary in situ and real-time study of directional solidification of metallic alloys by x-ray imaging techniques. *Journal of Physics D: Applied Physics*, 36(10A):A83–A86, 2003.

[287] Hideyuki Yasuda, Itsuo Ohnaka, Koichi Kawasaki, Akira Sugiyama, Tetsutaro Ohmichi, Jun Iwane, and Keiji Umetani. Direct observation of stray crystal formation in unidirectional solidification of Sn-Bi alloy by X-ray imaging. *Journal of Crystal Growth*, 262(1-4):645–652, feb 2004.

[288] Francisco García-Moreno, Paul Hans Kamm, Tillmann Robert Neu, Felix Bülk, Rajmund Mokso, Christian Matthias Schlepütz, Marco Stampanoni, and John Banhart. Using X-ray tomoscopy to explore the dynamics of foaming metal. *Nature Communications*, 10(1):1–9, dec 2019.

[289] Yang Yang, Zhengrui Xu, James D. Steiner, Yijin Liu, Feng Lin, and Xianghui Xiao. Quantitative probing of the fast particle motion during the solidification of battery electrodes. *Applied Physics Letters*, 116(8):081904, feb 2020.

[290] Jiao Yan, Wenchun Feng, Ji Young Kim, Jun Lu, Prashant Kumar, Zhengzhi Mu, Xiaochun Wu, Xiaoming Mao, and Nicholas A. Kotov. Self-Assembly of Chiral Nanoparticles into Semiconductor Helices with Tunable near-Infrared Optical Activity. *Chemistry of Materials*, 32(1):476–488, jan 2020.